UNIVERSIDAD COMPLUTENSE DE MADRID

FACULTAD DE CIENCIAS QUÍMICAS

Departamento de Química Inorgánica

TESIS DOCTORAL

1212-Molybdo-Cuprates: synthesis, structure and properties

MEMORIA PARA OPTAR AL GRADO DE DOCTOR

PRESENTADA POR

Sourav Marik

Directores

M. A. Alario Franco
Olivier Toulemonde

Madrid, 2014

UNIVERSIDAD COMPLUTENSE DE MADRID

FACULTAD DE CIENCIAS QUÍMICAS
Departamento de Química Inorgánica I

1212 – Molibdocupratos: Síntesis, estructura y propiedades

1212 – Molybdocuprates: Synthesis, structure and properties

TESIS DOCTORAL

Sourav Marik

Madrid, 2014

1212 – Molybdo-Cuprates: Synthesis, structure and properties

by

Sourav Marik

A dissertation submitted in partial satisfaction of the
requirements for the degree of
Doctor of Philosophy
in
Chemistry

in the
Departamento de Química Inorgánica
of the
Universidad Complutense de Madrid, Spain

Supervisors:

Professor M. A Alario-Franco (UCM, Madrid, Spain)
Professor Emilio Moran (UCM, Madrid, Spain)
Dr. Olivier Toulemonde (ICMCB, CNRS, Bordeaux, France)

Madrid, 2014

UNIVERSIDAD COMPLUTENSE DE MADRID

FACULTAD DE CIENCIAS QUÍMICAS
DEPARTAMENTO DE QUÍMICA INORGÁNICA

1212 – Molybdo-Cuprates: Synthesis, structure and properties

THESIS DOCTORAL

Sourav Marik

Directores:

Professor M. A Alario-Franco (UCM, Madrid, Spain)
Professor Emilio Moran (UCM, Madrid, Spain)
Dr. Olivier Toulemonde (ICMCB, CNRS, Bordeaux, France)

Madrid, 2014

Contents

Abstract

A systematic study on the composition-structure-property correlations is presented here for the (Mo,Cu)-1212 materials. The aim of the present studies is to investigate the detail structure-property correlation of the interesting molybdo-cuprate compounds with composition $Mo_xCu_{1-x}Sr_2RECu_2O_y$ (RE = rare earth cations). Concurrently, the effect of oxygenation on the structure and property of the above mentioned compounds has also been investigated. The detailed crystal structure determination is carried out using the combination of X-ray powder diffraction patterns, neutron powder diffraction (NPD) patterns and Electron Microscopy. The physical properties were obtained using the combination of ac and dc magnetic measurements, resistivity and thermoelectric power (TEP) measurements.

High temperature superconductivity in cuprates arises from doping of a Mott-Hubbard insulator. The understanding of metal-insulator transitions of doped Mott-Hubbard insulators is one of the outstanding challenges occupying modern Solid State Physics. In particular, in the doped cuprates, there exist a variety of complex interplay between lattice, charge, and spin degrees of freedom. Therefore, beside the investigation of the effect of Mo – substitution in the $CuSr_2RECu_2O_y$ (RE-123, Cu-1212) crystal structure, it is the aim of this thesis to study the electronic states of the present materials. In the present thesis, in order to understand the evolution with oxygen doping from a Mott insulator and furthermore, the doping evolution (oxygen doping) of physical properties and their consequences in the electronic states has been investigated in a large set of materials. X-ray photo electron spectroscopy (XPS), which is indeed a powerful tool in studying the 3d element doping in the Cu site and can provide the information on the electronic structure of the system has been employed to investigate the electronic states.

A systematic study of the range of stability of molybdenum substituted Sr-based Cu - 1212 ($CuSr_2YCu_2O_y$) compounds within the $Mo_xCu_{1-x}Sr_2YCu_2O_y$ system, synthesized under ambient pressure showed that all the materials crystallize in a tetragonal symmetry with the space group: *P4/mmm*. It shows the ability of this phase to incorporate foreign cations. It also observed that the square-planar copper [Cu-O_4] in the chains in the $CuSr_2YCu_2O_y$ (YSCO, Cu-1212, Y-123) structure is not completely replaced by [Mo-O_6] octahedra at ambient pressure. The observed solubility limit of Mo is rather low in this structure and secondary phases start to form as soon as $x > 0.3$ in the nominal composition is reached. On the other hand it is demonstrated that the anti-ferromagnetic property in all superconducting multiphase samples are due to the secondary phase $Y_2Cu_2O_5$.

The Cu/Mo cationic distribution in plane chain copper site is established using a combination of X-ray/Neutron powder diffraction refinement for the pure $Mo_{0.3}Cu_{0.7}Sr_2RECu_2O_y$ materials (RE = Y, Er and Tm). The chemical substitution of the Mo ions for the Cu ions in the $CuYSr_2Cu_2O_y$ structure is found to occur in both of copper sites for the as-prepared (AP) samples but up to a limited extent. Interestingly, no trace of Mo substitution in the copper plane site is found to occur after oxygenation. A model for the Mo diffusion to the copper chain site during the oxidation process is presented and discussed. The splitting observed in the NPD patterns of the oxygen annealed (OA) $Mo_{0.3}Cu_{0.7}Sr_2TmCu_2O_y$ sample is due to the increased c/a ratio after oxygenation.

Magnetic measurements on the AP $Mo_{0.3}Cu_{0.7}Sr_2ErCu_2O_y$ sample indicate the existence of ferromagnetic interactions. However, the magnetic state of the AP $Mo_{0.3}Cu_{0.7}Sr_2TmCu_2O_y$ material experiences Paramagnetic (PM) – Weak anti-ferromagnetic (WAFM) – Spin glass (SG) transitions in lowering the temperature. However, instead of a classical individual spin freezing, we suggest a cluster by cluster freezing model to explain the SG nature in this material. The complex magnetic behaviours in these AP materials have been discussed in the frame of cation disordering.

On the other hand, all the oxygenated materials are superconducting. The material oxygenated using high pressure shows the highest superconducting transition temperature (T_C = 84 K). Structural analyses show the tendency of short-range oxygen ordering in the $(Mo/Cu)O_{1+\delta}$ chain after oxygenation, at mesoscopic scale. A short-range oxygen ordering model at mesoscopic scale in the $(Mo/Cu)O_{1+\delta}$ chain site is proposed and discussed here. This increases the effectiveness in the charge transfer to the superconducting layer (CuO_2), resulting in superconductivity. A peak has been observed in the critical current density plot and can be explained on the basis of field induced pins.

The influence of oxygenation in the electronic states for the $Mo_{0.3}Cu_{0.7}Sr_2YCu_2O_y$ and $Mo_{0.3}Cu_{0.7}Sr_2ErCu_2O_y$ systems associated with the oxidation reaction from a semiconducting to a superconducting state has been investigated by means of X-ray photoelectron spectroscopy (XPS). The XPS studies show the predominance of the Mo^V state over the Mo^{VI} one in the AP samples. Yet, annealing under an oxygen atmosphere enhances the Mo^{VI} state. Quite interestingly, at the same time, a reduction in the copper species is observed. An interesting self doping mechanism is proposed here for the 1212-molybdo-cuprate compounds, after oxygenation. Equally, the presence of a high amount of magnetic Mo^V is found to be a reason to originate incipient magnetic interactions within the charge reservoir layer. The detailed studies of the electronic states for the $Mo_{0.3}Cu_{0.7}Sr_2YCu_2O_y$ and

$Mo_{0.3}Cu_{0.7}Sr_2ErCu_2O_y$ systems are also presented here. The hole concentration (P_h) on the copper plane is calculated using the room temperature TEP value; this shows an increasing tendency in parallel to an increasing T_C, after oxygenation. Following our experimental results, we have found that charge transfer energy is the key factor to tune the superconducting transition temperature (T_C). We have observed that T_C increases with decreasing charge transfer energy. This is occurring in parallel with the shortening of the apical Copper-Oxygen distance (Cu2–O2) and increasing CuO_2 plane buckling.

In an attempt to increase the amount of Mo dopant in the charge reservoir layer (copper chain, Cu1), a new family of 1212-molybdo-cuprate materials, with composition $Mo_{0.5}Cu_{0.5}Sr_2RECu_2O_{7.5}$ (RE = Gd, Y, Ho and Er) has been prepared at High Pressure and High Temperature. None of these new materials do show superconducting behaviour. Nevertheless, they show interesting features. Structural analyses using the joint refinement of room temperature (RT) NPD and room temperature XRD showed that the chain oxygen ions are randomly distributed in two different oxygen sites, which are partially filled. Moreover, the defect induced by the oxygen vacancies makes the chain fragmented and disordered. This disordering could then be a reason for the absence of superconductivity in these materials. A remarkable micro-domain texture has been identified using electron microscopy. The microstructure of these compounds is interpreted by a well-known diagonal cell $\sqrt{2}a_p \times \sqrt{2}a_p \times 3a_p$, distributed in three dimensional domains, as confirmed by selected area electron diffraction (SEAD) and high resolution transmission electron microscopy (HRTEM), while an ideal triple perovskite structure with a "simple" $a_p \times a_p \times 3a_p$ cell is supported from the results found by the RT NPD/XRD joint refinements; this is due to the absence of the long-range ordering in the octahedral tilt due to the random distribution of the equal amount of Mo and Cu in the copper chain site.

XPS studies on the sample with RE = Ho show the predominance of the non magnetic Mo^{VI} state over the Mo^{V} one. At the same time oxidation state of copper is found to be dominated by Cu^{II}. The presence of higher amount of nonmagnetic Mo^{VI} is found to be a reason for the absence of the magnetic interaction in these materials. Specific heat measurements indicate the magnetic ordering at 2.13 K for the $Mo_{0.5}Cu_{0.5}Sr_2GdCu_2O_{7.5}$ material is due to the 3-dimentional AFM ordering of the Gd cation. $Mo_{0.5}Cu_{0.5}Sr_2HoCu_2O_{7.5}$ material shows a flat maximum at 5 K due to the separation of the two lowest-lying singlet levels of Ho^{III} ions at that temperature. A systematic structure-property correlation for these new 1212-molybdo-cuprate compounds is also presented here.

Resumen

En este trabajo se presenta un estudio sistemático de las correlaciones entre composición-estructura y propiedades para compuestos del tipo (Mo, Cu).1212. El objetivo de este estudio es investigar con detalle las correlaciones entre estructura y propiedades de materiales de composición $Mo_xCu_{1-x}Sr_2TRCu_2O_y$ (TR = cationes de tierras raras), de gran interés. Además se ha investigado a fondo el efecto que tienen distintas condiciones de oxigenación sobre estos compuestos. La determinación detallada de la estructura cristalina se ha llevado a cabo combinando distintas técnicas de difracción sobre polvo policristalino: rayos X (XRD), neutrones (NPD) y electrones (ED). Por otra parte se han estudiado propiedades físicas combinando medidas magnéticas ac y dc, medidas de resistividad y de poder termoeléctrico (TEP).

La superconductividad a alta temperatura en los cupratos surge como consecuencia de un dopado adecuado de un aislante Mott-Hubbard. El comprender la naturaleza de las transiciones metal-aislante en los aislantes Mott-Hubbard dopados, es uno de los retos más importantes en la Física del Estado Sólido moderna. En particular, en los cupratos dopados, hay una gran variedad de interacciones complejas entre la red cristalina, la carga y los grados de libertad para los espines. Así pues, además de la investigación del efecto que tiene la sustitución de cobre por molibdeno en la estructura $Cu\ Sr_2TRCu_2O_y$ (denominada unas veces TR-123, y otras Cu-1212), es un objetivo de esta tesis el estudio de los estados electrónicos en estos materiales. En la presente tesis se ha investigado, en un elevado número de materiales, el efecto que tiene el dopado con oxígeno sobre las propiedades físicas y sus consecuencias en los estados electrónicos, con el fin de comprender la transición inducida por el dopado con oxígeno en un aislante de Mott. Por otro lado, para investigar los estados electrónicos, se ha utilizado la espectroscopia de fotoelectrones de rayos X (XPS), una herramienta muy potente para el estudio de sustituciones por elementos 3d en la posición del Cu y que suministra información muy valiosa de la estructura electrónica del sistema.

El estudio sistemático del margen de estabilidad de los compuestos $Mo_xCu_{1-x}Sr_2YCu_2O_y$ sintetizados a presión ambiente, mostró que todos los materiales cristalizan con una estructura de simetría tetragonal y grupo espacial P4/mmm, lo que muestra la capacidad que tiene esta fase para incorporar distintos cationes. Se observó

además que, en la estructura Cu $Sr_2YCu_2O_y$ (YSCO, Cu-1212 o Y-123), a presión ambiente no se sustituye completamente al cobre situado en coordinación plano cuadrada en las cadenas [Cu-O_4] por molibdeno en coordinación octaédrica [MoO_6]. El límite de solubilidad observado para el Mo es bastante bajo en esta estructura y comienzan a aparecer fases secundarias a partir de valores de x superiores a 0.3 en la composición nominal. Por otra parte, se demuestra aquí que el antiferromagnetismo observado en toda los materiales multifásicos superconductores, se sebe a una fase secundaria $Y_2Cu_2O_5$.

La distribución catiónica Cu/Mo en los planos y cadenas se ha establecido utiizando una combinación de refinamientos de datos de difracción (Rayos X y neutrones) en polvo utilizando materiales puros de composición $Mo_{0.3}Cu_{0.7}Sr_2TRCu_2O_y$ (TR = Y, Er y Tm). Se ha encontrado que la sustitución química del cobre por molibdeno en esta estructura sucede, para las fases "as prepared" (AP), en ambas posiciones (planos Cu-1 y cadenas Cu-2) aunque hasta un cierto límite. Es interesante señalar que, después de la oxigenación, no quedan trazas de sustitución del cobre por molibdeno en los planos cobre-oxígeno. En este sentido se propone y discute un modelo para la difusión del Mo en las cadenas de cobre durante el proceso de oxidación.

Las medidas magnéticas de la muestra de erbio: $Mo_{0.3}Cu_{0.7}Sr_2ErCu_2O_y$-AP indican la existencia de interacciones ferromagnéticas. Sin embargo, la muestra análoga con tulio $Mo_{0.3}Cu_{0.7}Sr_2TmCu_2O_y$-AP muestra transiciones paramagnética (PM)-antiferromagnetimo débil (WAFM) – vidrio de espín (SG) al bajar la temperatura. Sin embargo, en lugar del clásico congelamiento individual de espines, sugerimos un modelo de congelamiento "cluster" (agregados) a cluster para explicar la naturaleza de vidrio de espín de este material. Estos comportamientos magnéticos complejos en los materiales "as prepared" se han discutido en el contexto de desorden catiónico.

Por otro lado, todos los materiales oxigenados son superconductores. El material oxigenado mediante alta presión muestra la transición superconductora a temperatura más alta (Tc = 84 K). El análisis estructural muestra la tendencia a un orden corta distancia de los oxígenos en las cadenas $(Mo/Cu)O_{1+\delta}$ después de la oxigenación a una escala mesoscópica. Se propone y discute un modelo para el orden a corta distancia de los oxígenos en dichas

posiciones a la escala mesoscópica. Se ha observado un pico en la gráfica de la densidad de corriente crítica que puede ser explicado sobre la base de "pins" inducidos por el campo.

Se ha investigado la influencia de la oxigenación sobre los estados electrónicos para los sistemas $Mo_{0.3}Cu_{0.7}Sr_2TRCu_2O_y$ (TR = Y y Er) asociado a un cambio desde el estado semiconductor a otro superconductor y se ha hecho por medio de espectroscopía de fotoelectrones (XPS). Estos estudios muestran la predominancia del estado de oxidación (V) sobre el (VI) para el molibdeno en las muestras "as prepared" (AP). Además, el recocido en una atmósfera de oxígeno aumenta el estado Mo^{VI} y, almismo tiempo, se observa una reducción en las especies de cobre, lo que es muy interesante. Se propone en este sentido un mecanismo de autodopado promovido por la oxidación para los molibdocupratos 1212. Igualmente, la presencia de una alta cantidad de Mo^{V}, magnético, es la razón para que se originen interacciones magnéticas incipientes dentro de la capa de reserva de carga. Se presentan así mismo estudios detallados de los estados electrónicos para los sistemas $Mo_{0.3}Cu_{0.7}Sr_2TRCu_2O_y$ (TR = Y y Er). Se ha calculado la concentración de huecos (P_h) en el plano cobre-oxígeno usando el valor TEP de temperatura ambiente; éste muestra una tendencia creciente en paralelo con el incremento de T_C tras la oxigenación. Siguiendo con nuestros resultados experimentales, hemos encontrado que la energía para la transferencia de carga es el factor clave para modular la temperatura de la transición superconductora (T_C). Hemos observado que T_C aumenta al disminuir dicha energía de transferencia de carga. Esto ocurre en paralelo con el acortamiento de la distancia apical cobre-oxígeno (Cu2-O2) y un incremento en el plegamiento de los planos CuO_2.

Tratando de incrementar la cantidad de molibdeno en la capa de reserva de carga (cobre en cadenas, Cu1), hemos preparado, en condiciones de alta presión y alta temperatura, una nueva familia de molibdocupratos 1212, de composición $Mo_{0.5}Cu_{0.5}Sr_2TRCu_2O_{7.5}$ (TR = Gd, Y, Ho y Er). Ninguno de estos nuevos materiales presenta comportamiento superconductor aunque presentan características muy interesantes. Los análisis estructurales utilizando conjuntamente refinamientos a temperatura ambiente de difracción de rayos X (XRD) y de neutrones (NPD) muestran que los iones óxido de las cadenas están distribuidos en dos posiciones distintas y parcialmente ocupadas. Más aún, estos defectos inducidos por las vacantes oxígeno hacen que las cadenas estén fragmentadas y desordenadas. Este

desorden podría ser la razón para la ausencia de superconductividad en estos materiales. Mediante microscopía electrónica se ha identificado una textura en microdominios muy notable. La microestructura de estos compuestos se interpreta mediante la bien conocida celda diagonal $\sqrt{2}a_p$ x $\sqrt{2}a_p$ x $3a_p$ distribuida en dominios tridimensionales, como se confirma utilizando difracción de electrones de área seleccionada (SAED) y microscopía electrónica de transmisión de alta resolución (HRTEM), mientras que los resultados conjuntos a temperatura ambiente de neutrones y Rayos X (NPD / XRD) muestran una "simple" estructura perovskita triple a_p x a_p x $3a_p$; esto es debido a la ausencia de orden a larga distancia en el giro de los octaedros, lo que se debe a la distribución al azar y en igual proporción de Mo y Cu en las posiciones de las cadenas.

Los estudios XPS para la muestra con TR = Ho muestran el predominio del estado Mo^{VI} no magnético sobre el Mo^{V}. Al mismo tiempo, el estado de oxidación del cobre que se encuentra es Cu^{II}. La presencia de una mayor cantidad de Mo^{VI} no magnético parece ser la razón para la ausencia de interacciones magnéticas en estos materiales. Las medidas de calor específico indican un orden magnético a 2.13 K para el material $Mo_{0.5}Cu_{0.5}Sr_2GdCu_2O_{7.5}$ debido al ordenamiento antiferromagnético tridimensional de los cationes gadolinio. El compuesto $Mo_{0.5}Cu_{0.5}Sr_2HoCu_2O_{7.5}$ muestra un máximo aplanado a 5 K debido a la separación entre los dos niveles singletes de más baja energía de los iones Ho^{III} a esa temperatura. Se presenta también aquí un estudio sistemático de la correlaciones entre estructura y propiedades para estos nuevos molibdocupratos 1212.

Chapter 1

Introduction

1.1. Superconductivity and Conventional Superconductors

"*The experiment left no doubt that, as far as accuracy of measurement went, the resistance disappeared. At the same time, however, something unexpected occurred. The disappearance did not take place gradually but abruptly. From 1/500 the resistance at 4.2K, it could be established that the resistance had become less than a thousand-millionth part of that at normal temperature. Thus the mercury at 4.2K has entered a new state, which, owing to its particular electrical properties, can be called the state of superconductivity*." Heike Kamerlingh Onnes

Soon, after achieving the liquefaction of helium, the phenomenon of superconductivity was first discovered in mercury by Kamerlingh Onnes[1] in 1911. At first, he attributed the sudden drop and vanishing of dc electrical resistivity to an experimental error, such as an accidental short circuit. But careful repetition showed that he had indeed discovered a stunning electronic phase. The discovery of zero resistivity in several other elements soon followed.

In 1933, Meissner and Ochsenfeld discovered another, equally surprising characteristic of superconductivity, the expulsion of the magnetic flux from a material in the superconducting state. Over the next several decades, the theory of superconductivity was one of the most intriguing puzzles in solid state physics. Major advances were made with the London theory[3] in 1935 and the Ginzburg-Landau[4] theory in 1950.

Nevertheless, it took almost 50 years to achieve a microscopic theory: In 1957, 46 years after the original experimental discovery of superconductivity, Bardeen, Cooper, and Schrieffer put forth a universally accepted microscopic theory of the phenomenon of superconductivity.[5] They proposed that electrons could overcome their mutual electrostatic repulsion to bind in pairs (Cooper pairs) due to the coupling to vibrations of the crystal lattice, which is called a phonon coupling. Unlike the normal electrons, these pairs can condense to a single coherent ground state which allows the electrons to move cooperatively through the crystal without losing their forward momentum and therefore carry current without loss of energy.

1.2. High T_C Superconductivity

Prior to 1986, the highest observed critical temperature (T_C) was 23 K for the inter-metallic compound Nb_3Ge. Quite unexpectedly, in 1986, J. G. Bednorz and K. A. Müller[6] discovered that under certain conditions, a particular layered copper oxide ($La_{2-x}M_xCuO_4$, M = Sr and Ba) become superconducting. It was indeed a surprise that a very poor conductor

could become a superconductor and even more that the T_C was higher than any other by then known material. This discovery sparked a frenzy of research to find new cuprate compounds with higher T_C, as well as to understand the phenomenology of the materials, and to develop a theoretical understanding of the mechanism of *high temperature superconductivity* (*HTSC*). In less than one year after the discovery of superconductivity in cuprates, an enormous amount of research all over the world pushed the transition temperature above the liquid Nitrogen temperature (77 K) with the discovery of $YBa_2Cu_3O_{7-\delta}$ (YBCO)[7], reaching as high as 135 K in a mercury based cuprate compound (T_C = 164 K at high pressure).[8,9] Figure 1.1 shows the time evolution of the superconducting critical temperature since the discovery of superconductivity in 1911.

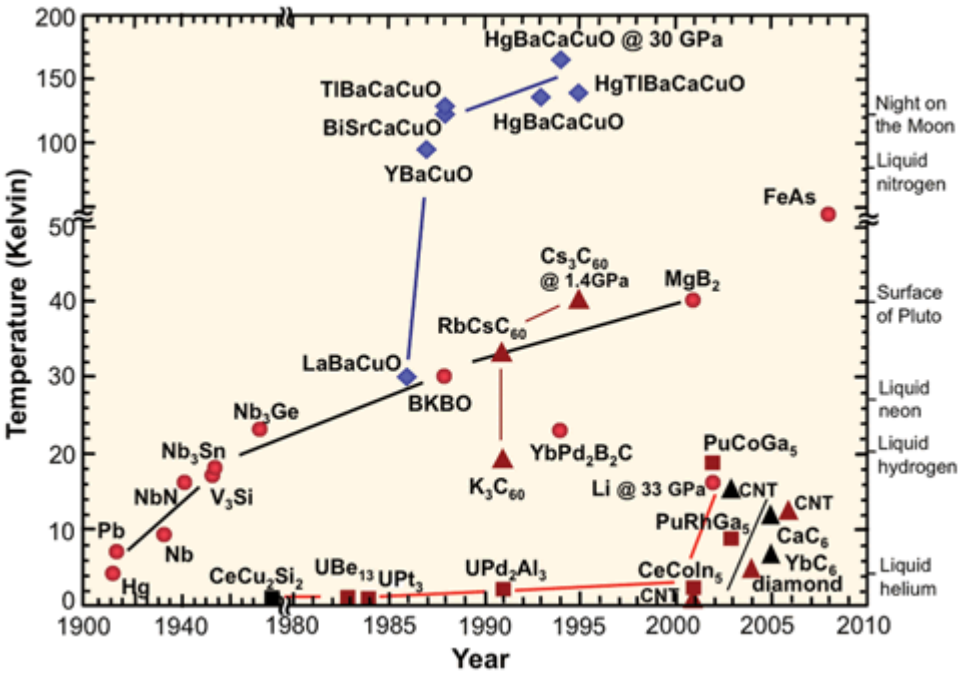

Figure 1.1. Time evolution of superconducting materials (taken from the Wikipedia, http://en.wikipedia.org/wiki/Superconductivity).

The high-T_C cuprate superconductors belong to a wide class of materials named strongly correlated materials, which are characterized by strong interactions or correlations between electrons. The unconventional and exotic behaviours of highly correlated electron system, in particular transition-metal oxides, have been widely investigated in recent years. Especially, since the discovery of the high-T_C superconductors by Bednorz and Muller, the world started the synthesis of ceramics of almost every imaginable combination and many investigations were performed trying to understand the mechanism of high-T_C superconductivity beyond the conventional BCS theory. However, the complete

understanding of the high-T_C superconductivity mechanism has not yet been achieved. In the last thirty-five years, following the discovery of superconductivity in the cuprates, a large number of related cuprate compounds with high superconducting transition temperatures have been found. Nevertheless, most of the work devoted to the search of high temperature superconductors has relied upon the synthesis of new materials derived from $YBa_2Cu_3O_{7-\delta}$ ($CuBa_2YCu_2O_{7-\delta}$, Cu - 1212) and, in particular, upon the substitution of one of the copper atoms located in the so-called charge reservoir layer (CRL) or copper chain site. The most common feature of these high-temperature superconductors (HTSC's) is a layered-perovskite crystal structure containing CuO_2 planes (see the following chapters, in particular chapter 2) separated by block layers. This famous cuprate system drastically changes their behaviour depending on the electron density in the two-dimensional CuO_2 planes, which are the platform of the high-T_C superconductivity and related physics. The basic behaviour of the CuO_2 plane is common to all the cuprate superconductors; it goes from an antiferromagnetic Mott insulator to the superconducting state.

1.3. General overview of the thesis

In this thesis, we have tried to extend the knowledge of the interesting 1212-molybdo-cuprate family. We will present here a systematic study of the crystal structure, electronic states and physico-chemical properties of the 1212-type molybdo-cuprate compounds. We have investigated the detailed electronic states of these molybdo-cuprate compounds with a large set of samples using the X-ray photoelectron spectroscopy techniques. A detailed study of the structure-composition-properties correlation is then presented.

The thesis is organised as follows: The detailed background, motivation and scope for the present work is described in *chapter 2*.

The detailed experimental set ups and conditions are described in *chapter 3*.

In *chapter 4*, we have described the solubility range of Mo in YSCO ($CuYSr_2Cu_2O_{7-\delta}$) structure and demonstrated contrarily to previous assertions, the non-co-existence of magnetism and superconductivity in that system.

In *chapter 5*, we have described, systematically, the detailed crystal structure, as well as the physical properties of three compounds with nominal composition $Mo_{0.3}Cu_{0.7}Sr_2RECu_2O_y$ (RE = Y, Er and Tm). An interesting composition-structure-property correlation is shown in this chapter.

The evolution with doping from an insulator and furthermore, the evolution of the physical properties with oxygen doping and its consequences in the electronic states has been

investigated in a large set of materials ($Mo_{0.3}Cu_{0.7}Sr_2RECu_2O_y$ with RE = Y and Er) and is discussed in *chapter 6*. The correlation between the charge transfer mechanism and some structural peculiarities are also discussed in this chapter.

In *chapter 7*, we have described, the synthesis, structure and microstructure and magnetic properties of a new family of molybdo-cuprates with nominal composition $Mo_{0.5}Cu_{0.5}Sr_2RECu_2O_{7.5}$ (RE = Gd, Y, Ho and Er.), obtained at high pressure and high temperature.

Taking into account all these results, the summary and concluding remarks are presented in *chapter 8*.

References

[1]H. K. Onnes. *Communications from the Physical Laboratory of the University of Leiden* (1911).

[2]W. Meissner and R. Ochsenfeld, "Ein neuer Effekt bei Eintritt der Supraleitf¨ahigkeit." *Naturwissenschaften* **21**, 787–788 (1933).

[3]F. and H. London. *Proceedings of the Royal Society of London* **A149**, 71 (1935).

[4]V. L. Ginzburg and L. D. Landau. *Zh. Eksperim. i Teor. Fiz.* **20**, 1064 (1950).

[5]J. Bardeen, L. N. Cooper and J. R. Schrieffer, "Theory of Superconductivity." *Physical Review* **108**, 1175–1204 (1957).

[6]J. G. Bednorz and K.A. M¨uller, Z. Phys. B **64**, 189 (1986).

[7]M. K. Wu, J. R Ashburn, C. J. Torng, P. H. Hor, R. L. Meng, L. Gao. Z. J. Huang, Y. Q. Wang, C. W. Chu, Phys. Rev. Lett. **58**, 908 (1987).

[8]A. Schilling, M. Cantoni, J. D. Guo and H. R. Ott, Nature **363**, 56 (1993).

[9]C. W. Chu, L. Gao, F. Chen, Z. J. Huang, R. L. Meng, and Y. Y. Xue, Nature **365**, 323 (1993).

Chapter 2

High T_C Cuprates: Background

2.1. Strongly correlated systems

The high-T_C cuprate superconductors (HTSC)[1] belong to the class of strongly correlated materials, which are characterized by the strong interactions or correlations between electrons. The science of strongly correlated materials opened up in the early days of modern Solid State Physics. In 1930's, the band theory was developed by Bloch[2] and Wilson[3], which explained the metallic behaviour in some materials and the insulating character of others. Boer and Verweij[4] soon pointed out that the Bloch and Wilson's band theory fails to explain a large number of insulating 3d transition metal compounds, such as NiO and CoO, which were predicted to be metals. Peierls pointed out that the strong Coulomb interaction between the d-electrons overcame the energy gain by delocalization of the electrons. Mott[5] and Hubbard[6] imputed the insulating behaviour to electron-electron correlation. Nowadays, the Hubbard model is the most used one to study strong correlated systems. Meanwhile, Anderson[7,8] introduced a model, which is virtually identical to the Hubbard model, by introducing super-exchange in a model with a strong d-d Coulomb interaction of local 3d electrons caused by energy lowering via hopping. He introduced the famous "Anderson Hamiltonian"[9] to address the phenomena like the Kondo effect[10-12] and heavy Fermion materials, where Coulomb interaction between the local d electrons or f electrons from the magnetic impurities plays an important role and determines whether local magnetic moments exist or not. However, from a two-body or three-body problem to a many body problem, correlation effects give rise to a wide number of complex and often surprising phenomena. And understanding the correlated electron systems has been the most challenging subject, in recent years, in condensed matter physics due to the difficulties, immanent in the many-body character of electron correlations and their manifestation in a large variety of phenomena: Metal Insulator transitions, insulator-superconductor transition, Kondo effects, heavy Fermion phenomena, high-T_C superconductivity, mixed valence, quantum Hall effect, colossal magneto-resistance, charge ordering, and so on. Some of them have been interpreted in the framework of the above theoretical models.

2.2. Crystal structure and phase diagram

In the last thirty seven years, following the discovery of HTSC in $La_{2-x}Ba_xCuO_4$ (LBCO) by Bednorz and Muller[13], a large number of related cuprate compounds with increasingly higher superconducting transition temperatures have been found. In the year following the unearthing of superconductivity in cuprates, the discovery of $YBa_2Cu_3O_{7-\delta}$ (YBCO, Y-123)[14,15]pushed the transition temperature (T_C) above the boiling point liquid Nitrogen (77 K,

at ambient pressure). And this trend has attained transition temperature as high as 135 K (164 K under very high pressure) in Hg based cuprate compounds[16,17]

The most common feature of these high-temperature superconductors (HTSC) is a layered perovskite-type crystal structure containing CuO_2 planes separated by block layers. Electrons are added / withdrawn from the CuO_2 planes by replacing or adding ions and the transport properties of cuprates change drastically by the introduction of charge carriers to the CuO_2 planes. This is done by chemical doping that varies for each family of cuprates.[18] For instance, in the case of LBCO, the chemical doping is done by the substitution of some of the La^{3+} ions by Ba^{2+} which introduces holes to the CuO_2 plane. Figure 2.1 shows the crystal structure of LBCO.

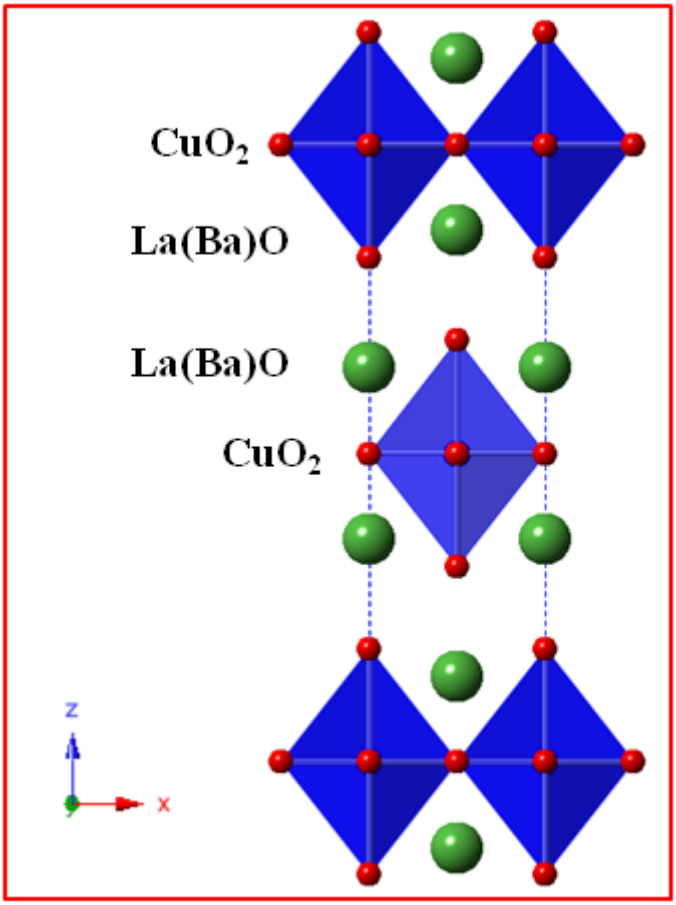

Figure 2.1. Crystal structure of $La_{2-x}Ba_xCuO_4$, the first high-temperature cuprate superconductor. The La(Ba)O and CuO_2 layers are highlighted in the figure and the red spheres indicate the oxygen ions.

Figure 2.2 shows the most studied cuprate compounds. The figure is taken from review of Eshaki et. al.[19] Their study showed that T_C tends to increase both for the increasing number of neighbouring CuO_2 planes (although this seems limited to 3; afterwards T_C decreases) and reducing the disorder.

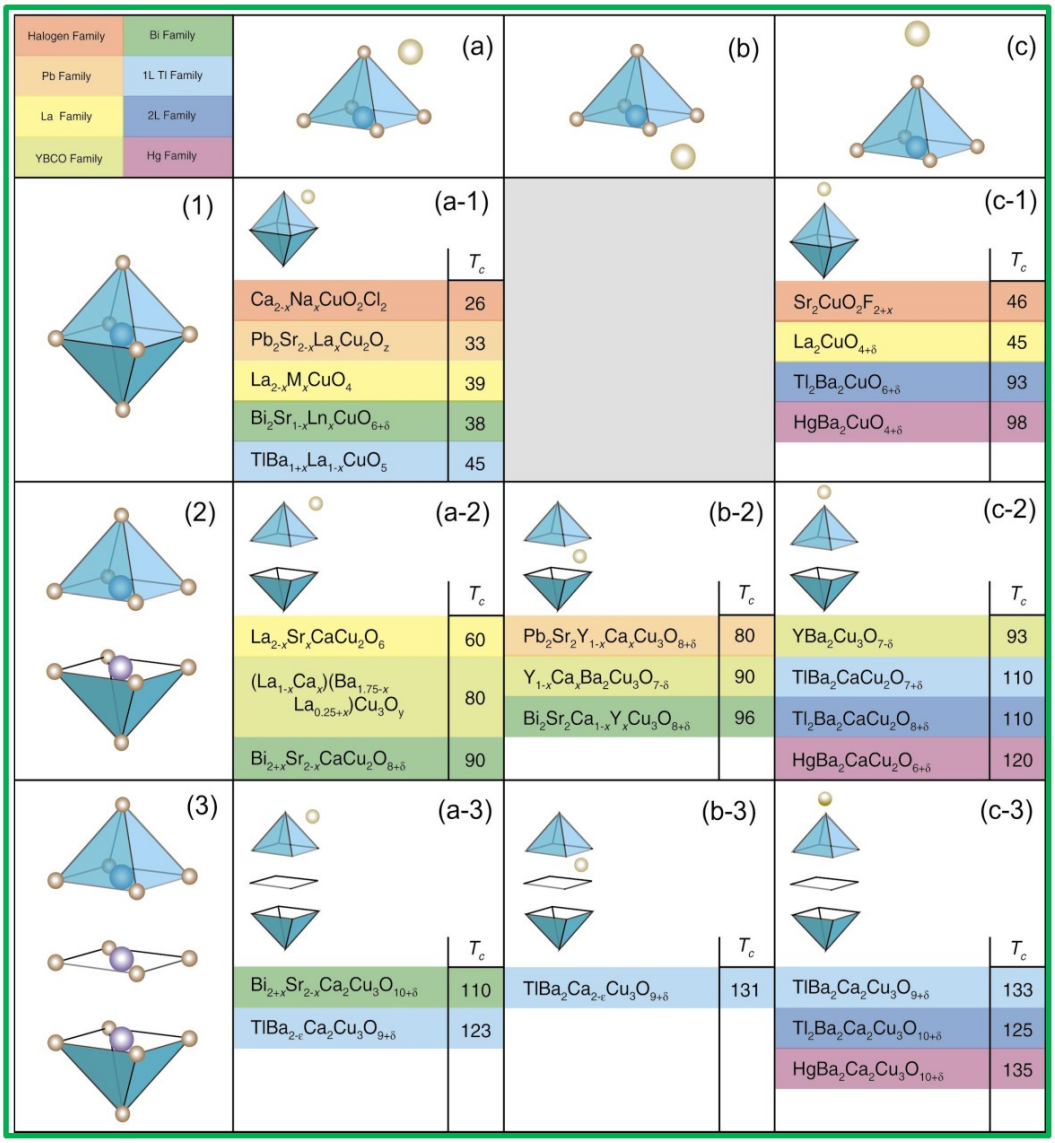

Figure 2.2. The most studied cuprate HTSC materials. The figure shows the classification in terms of number of CuO_2 layers and disorder site. The figure is taken from the study of *Eisaki et al.*[19]

Indeed, the most famous compound in the cuprate family is $YBa_2Cu_3O_{7-\delta}$; better formulated as $CuBa_2YCu_2O_{7-\delta}$, so as to stress the fact that there are two copper sites, which have different but complementary roles in the compound. YBCO and the related '123' materials having $T_C \sim 90$ K are not toxic and are readily synthesized in bulk form; on the other hand, a large number of new materials have been prepared with higher critical

temperatures (for instance, in Bi–Sr–Ca–Cu–O[20] and Tl–Ba–Ca–Cu–O[21] systems T_C reached up to 110-120 K and in $HgBa_2Ca_2Cu_3O_{8+\delta}$[16,17] T_C is 135 K). After the discovery of superconductivity in the Bi–Sr–Ca–Cu–O and Tl–Ba–Ca–Cu–O materials, the following comment appeared in Nature:

"as thallium is highly toxic and bismuth is in short supply, both materials may be of greater Scientific than technological importance"[18,22]

This does indeed remain true for the Hg-based compounds. The easy synthesis method of YBCO and other 123 materials makes them good parent compounds for substitution studies. In this thesis I will restrict the discussion to the YBCO and related cuprate materials.

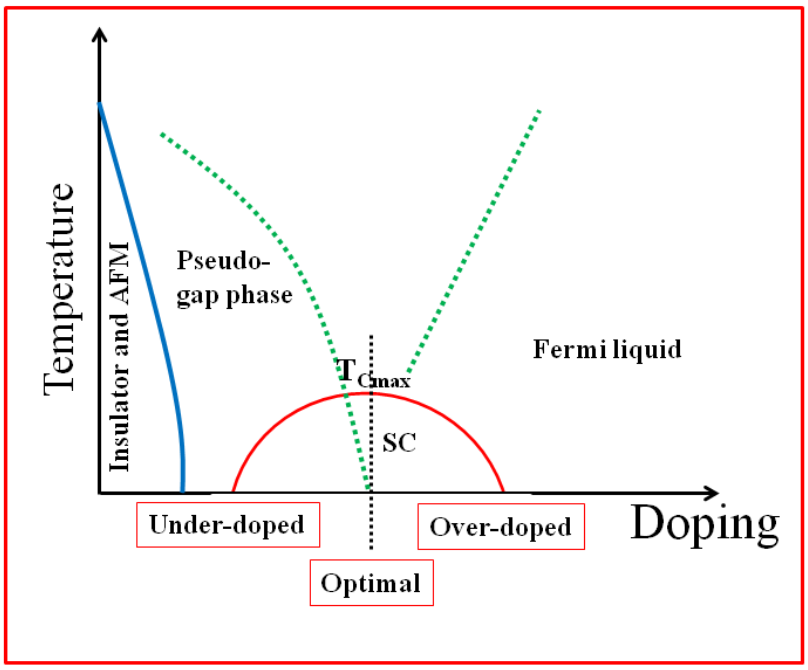

Figure 2.3. The schematic phase diagram of HTSC cuprate materials is shown here. At half filling or undoped, they are antiferromagnetic insulators (AFI). With increasing *hole concentration*, the system shows the pseudogap behavior. At very large hole doping, more typical metallic properties associated with a Fermi liquid appear. At low temperature, the system shows superconductivity (SC).

Figure 2.3 shows a schematic phase diagram of the cuprate materials. Half filled or undoped (hole concentration $P_h = 0$) cuprates are antiferromagnetic insulators (AFI). As the number of holes increases, the antiferromagnetic phase is quickly destroyed and the cuprates become a pseudogap phase. With further hole doping, the metallic phase turns to more conventional behavior expected from Fermi-liquid theory. And below a certain temperatures, for $0.07 < P_h < 0.25$, the system becomes superconducting. The maximum T_C ($T_{C,max}$) is achieved at $P_h \sim 0.15$, referred to as optimal doping, whereas the lower and higher hole doping are referred to

as underdoped and overdoped, respectively. The $T_{C,max}$ of different families of cuprates are different, the T_C roughly scales with $T_{C,max}$ and follows an universal curve as a function of hole concentration according to the following equation.[23,24]

$$T_C / T_{C,max} = 1-82.6(P_h-0.16)^2 \quad (2.1)$$

2.3. Electronic structure

In the CuO_2 plane (shown in figure 2.1 and in figure 2.5), Cu has five d orbitals and the $d_{x^2-y^2}$ has the highest energy among them as shown in figure 2.4 (a). The $d_{x^2-y^2}$ band originated as the Cu $d_{x^2-y^2}$ orbital well hybridizes with the oxygen p orbitals through the in-plane Cu-O bonds, which have a shorter length than the out-of-plane Cu-O bonds.[18,25]

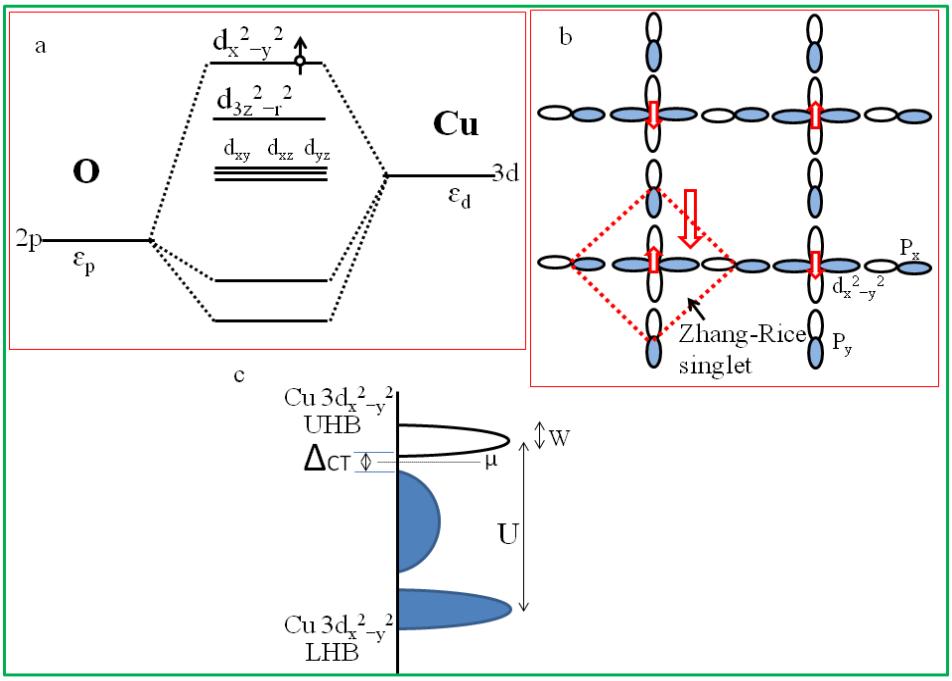

Figure 2.4. Schematic picture for the (a) energies of the Cu 3d and O 2p, (b) electronic orbital and (c) electronic structure of cuprates, highlight the hybridization of copper with the oxygen in CuO_2 plane.

Therefore, the $d_{x^2-y^2}$ band is half-filled and each Cu atom has spin ½ in the parent compound with nine d electrons (and one d hole). At half-filling, the electrons tend to avoid the double occupancy of the $d_{x^2-y^2}$ orbital and the electrons are localized as a Mott insulator as the on-site Coulomb repulsion U between the $d_{x^2-y^2}$ electrons is stronger than the band width W (the kinetic energy of the electrons) in the cuprates. Previous photoemission experiments have shown that the Cu d^8 state is 8 eV below the Cu d^9L state, where L refers to a hole in the ligand orbital (in this case are the oxygen orbitals).[26] U is large compared to the charge-transfer energy (Δ) in the parent cuprate compounds, which in fact classifies the parent

compounds of the cuprates as charge-transfer type insulator.[25] Optical conductivity studies show that the transfer gap (Δ_{CT}) is about 1.5 eV for undoped parent insulators.[27,28] Thus, it is not possible to construct an effective Hamiltonian to study the low energy physics by neglecting the oxygen sites. According to the three band Hubbard model proposed by Emery.[29]

$$H = \varepsilon_d \sum_{i\sigma} n^d_{i\sigma} + \varepsilon_p \sum_{j\sigma} n^p_{j\sigma} + t_{pd} \sum_{\sigma(ij)} (p^{\uparrow}_{j\sigma} d_{i\sigma} + H.c.) + t_{pp} \sum_{\sigma(jj'')} (P^{\uparrow}_{j\sigma} dp_{j''\sigma} + H.c.)$$

$$+ U_d \sum_{i\sigma} n^d_{i\uparrow} n^d_{i\downarrow} + U_p \sum_{j\sigma} n^d_{j\uparrow} n^d_{j\downarrow} + U_{pd} \sum_{\sigma(ij)} n^d_{i\sigma} n^p_{i-\sigma} \qquad (2.2)$$

p and d refer to oxygen p and copper d orbitals, respectively. Figure 2.4(b) and (c) show the three bands in the CuO_2 plane ($d_{x^2-y^2}$, P_x and P_y) and their energies relative to the chemical potential μ, respectively. However, Zhang and Rice consider a single CuO_4 plaquette containing one or two holes and found that the hole located at the Cu site is hybridized most strongly with a hole in a molecular orbital of a linear combination of the four surrounding oxygen ions, forming a singlet, a nonbonding, and a triplet state.[30] Therefore, the P_h hole in the Zhang-Rice singlet (ZRS) carries another spin 1/2 in the opposite direction to the spin of the d hole of Cu. However, if one ignores the upper-Hubbard band (UHB), the effective Hamiltonian becomes the t-J model, which was also an effective Hamiltonian for the single Hubbard model.

2.4. YBCO and YBCO based compounds

2.4.1. YBCO and YSCO

As already mentioned, the most widely studied high T_C superconducting cuprate is YBCO, which is in fact the first superconductor with the T_C above the boiling point of liquid nitrogen. Figure 2.5 shows the crystal structure of $YBa_2Cu_3O_{7-\delta}$ material. It is an oxygen-deficient triple perovskite, $A_3B_3O_{9-x}$, where Y and Ba are the central A cations and Cu the B cation.[31] Oxygen ions are missing from the central Y layer and from the a-axis of the basal plane. The structure of $YBa_2Cu_3O_{7-\delta}$ and related phases contains two crystallographic distinct Cu sites: the chain site (Cu1, CuO chain) and the square-pyramidal or planar site (Cu2, CuO_2 planes) with the CuO_5 unit corner-sharing to form buckled sheets in the a-b plane.

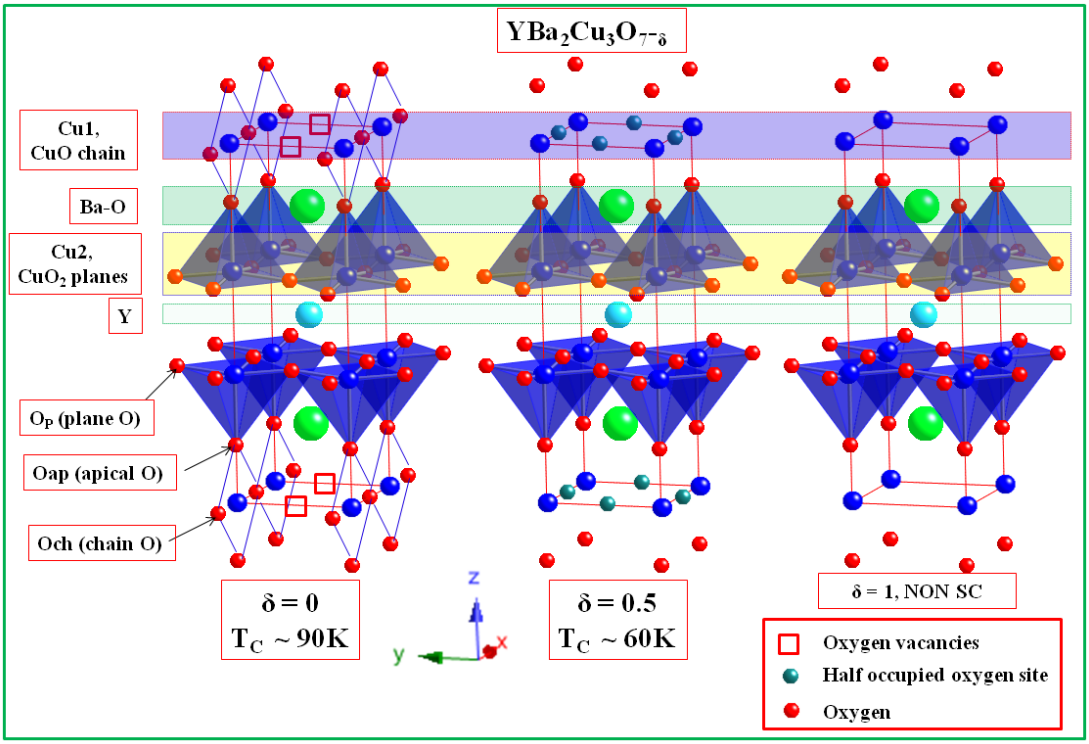

Figure 2.5. Crystal structures of $YBa_2Cu_3O_{7-\delta}$ material with (a) δ= 0, (b) δ = 0.5, (c) δ = 1.0 are compared here.

The oxygen stoichiometry of $YBa_2Cu_3O_{7-\delta}$ can vary over the range 6 to 7 retaining the triple perovskite structure[18,32] with a semiconducting to superconducting phase transformation (figure 2.5). From the structural point of view, $YBa_2Cu_3O_7$ is orthorhombic, but as the oxygen content decreases, the structure undergoes a phase transformation to tetragonal symmetry. Afterwards, the whole class of compounds with $REBa_2Cu_3O_{7-\delta}$ structure where RE = Y, La, Nd, Sm, Eu, Gd, Ho, Er, and Lu were discovered with similar physical properties and T_C ~ 90Kwith an exception of Pr-123 compound, which is neither metallic nor superconducting.[14,18] However, the highest value of superconducting temperature, T_C = 92 K, occurred at the optimal doping in metallic phase at δ = 0.08. And with oxygen content 0.4, T_C goes down and the metallic phase transforms into the semiconducting phase.[18,33-35] In the highly oxygen deficient structure with δ = 1, long-range AF order appears.[18] Previous studies showed that the short-range ordering in the copper chain site ($Cu1–O_{ch}$) has an essential effect on the electronic properties of this superconductor.[36-54] This indeed point out to the local nature of the doping of the conducting CuO_2 plane due to charge (hole) transfer from the copper chain site ($Cu1–O_{ch}$). The charge transfer from the chains to the plane site after oxygenation was confirmed later in the photoemission experiments. Cava et al.[46] showed that

for samples with a fixed oxygen content, the transition temperature T_C can vary considerably depending on the oxygen ordering in the Cu1–O_{ch} chains. It also explains why the short-range ordering of oxygen ions in chains is so important for proper hole doping in CuO_2 planes.

Despite the chemical similarity between Sr and Ba, the 123 structure can only be stabilized at ambient pressure using the standard and simple solid-state reaction technique for the Ba-based $REBa_2Cu_3O_{7-\delta}$ (REBCO) compounds but not for the Sr-based $RESr_2Cu_3O_{7-\delta}$ (RESCO) ones, when RE =Y, La, or any of the other rare-earth elements except Ce and Tb. Pure $YSr_2Cu_3O_{7-\delta}$ (YSCO, tetragonal, $T_{C,onset}$ = 60 K), the strontium analog of $YBa_2Cu_3O_{7-\delta}$ (YBCO), can only be prepared at high pressure.[55] The superconducting properties of $YSr_2Cu_3O_{7-\delta}$ (YSCO) are of particular interest due to the shorter distance between CuO_2-planes and the absence of the orthorhombic superconducting phase compared to the isomorphous YBCO. Besides the shorter distance between the CuO_2 planes, the copper chain layer seems to be more tolerant than the CuO layer in the YBCO.[56] As a matter of fact not only the substitution of Cu by transition metal elements such as Li, Al, Ti, V, Cr, Fe, Co, Ga, Ge, Mo, W, Re, Rh, Ir [*ref 18 and the references therein*] have been executed but also several anion groups such as CO_3^{2-}, PO_4^{3-}, SO_4^{2-} and NO_3^- have been inserted in the YSCO structure.[57-63]

2.4.2 M–1212

Since the discovery of YBCO, many substitution effects for every possible position have been done on the parent compound. Indeed, the majority of the chemical elements, excluding noble gases and actinides, are reported to substitute to some extent into the YBCO structure.[18] However, as we discussed in the previous section, the CuO chain layer in YBCO seems to be more tolerant than the CuO layer in YBCO. The YSCO phase can be stabilized at ambient pressure by substituting Pb, Li, Al, Ti, V, Cr, Fe, Co, Ga, Ge, Mo, W, Re, Rh and Ir partially or completely for the Cu in the chains [*ref 18 and the references therein*]. Clearly, since the beginning, the effect of chemical substitution in the layered cuprate structure is one of the most important areas of research in quest for the mechanism of high T_C superconductivity. However, as alrealy mentioned, by modifying the formula of the YBCO or YSCO as $Cu(Ba/Sr)_2YCu_3O_{7-\delta}$, it is called as 1212-type (Cu–1212) structure. Any replacement of CuO chain layer in Y-123 (or Cu-1212) structure by other metal oxide (MO_x) layers results in the M – 1212 structure (figure 2.6). The M-1212–type layered cuprates, having general formula $MA_2RECu_2O_{8-\delta}$ or M – 1212 (where M is commonly a transition metal element, A is an alkaline earth metal, and RE is a rare earth ion) are iso-structural with the classical

$YBa_2Cu_3O_y$ (YBCO or Cu-1212) in which Y, Ba, and Cu1 (the chain copper site) are completely or partially replaced with rare earth elements, alkaline earth metals, and transition metal ions, respectively. The δ signifies the oxygen deficiency, which is dependent on the synthesis conditions and the oxidation state of the transition metal element, and is the key tool for controlling the oxidation state of the copper planes and inducing superconductivity. The flexibility of this structural design has lead to an explosion of new materials with interesting properties, other than, indeed, superconductivity.

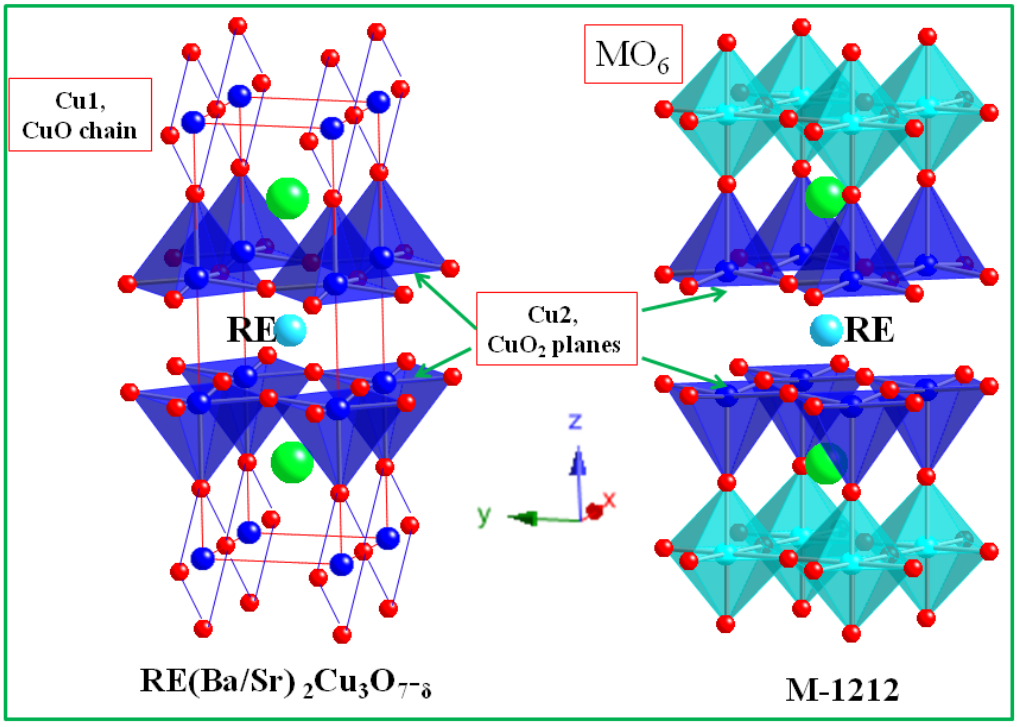

Figure 2.6. Crystal structure of Cu-1212 ($Cu(Ba/Sr)_2YCu_3O_{7-\delta}$) and M-1212 ($MA_2RECu_2O_{8-\delta}$) are compared. It shows the replacement of the CuO chain layer in Y-123 (or Cu-1212) structure by metal oxide (MO_6) layers.

Analogues incorporating M-site ions vary from: first-row transition metals such as Sc, Ti, V, Cr, Mn, Cu, Fe, Co;[18,64-66] second-row transition metals such as Ru[67], Mo[68], third-row transition metals such as Ta, Hg, as well as p-block elements such as Ga and Tl.[69,70] This wide and interesting variation in chemical composition leads to an equally wide diversity of electronic properties. Besides the superconductivity, the fine electronic balance in many of these materials leads to novel and unexpected phenomena. Till now the most interesting and widely studied compound in the 1212 family is magneto-superconducting Ru-1212 with nominal composition $RuSr_2GdCu_2O_8$.[67]

However, at room pressure, not all the members of M-1212 type compounds can be prepared. The use of high pressure has proven very useful in this context. And also for the bigger and smaller rare earth cations, high pressure and high temperature synthesis technique proved to be an effective one. It has been already demonstrated that along with Ir-1212 and Cr-1212, for the adequate formation of Ru-1212, as majority phases, the synthesis can only be performed in a particular and relatively narrow window of pressure and temperature, outside which they cannot be obtained pure or not even obtained at all.[71] According to that study these "optimum conditions" bear a remarkable Gaussian correlation with the rare earth ion size, the rare earth cation being at the center of the unit cell in the YBCO setting, and they do not follow the classic lanthanide contraction so often observed in the chemistry of those elements. Instead, they suggested that inter-electronic repulsion seems to play a major role in fixing the synthesis conditions.

2.4.3. 1212 Magneto-Superconductors

1212-Rutheno-Cuprates: According to early views manifested particularly by Ginzburg[1], superconductivity and long-range magnetic ordering do not co-exist within a single phase. The topic has been widely discussed in condensed matter science over decades. Nevertheless, the coexistence of weak ferromagnetism (WFM) and superconductivity (SC) have been observed in the ruthenocuprate with nominal composition $RuSr_2GdCu_2O_{8-\delta}$[72,73], due to a double-exchange interaction, promoted by the mixed valence state of the Ru ions (Ru^{IV} and Ru^{V}). In the case of conventional superconductors, long-range ferromagnetic ordering and superconductivity usually exclude each other. The structures of the Ru-1212 compound can be also viewed as modifications of Cu-1212 (Y-123) structures. In Ru-1212, retaining the CuO_2–RE–CuO_2 block (RE = Gd), the charge reservoir of square planer copper (CuO chains) in figure 2.5 are replaced by RuO_2 octehedral layers (figure 2.6).

The Ru-1212 compounds have tetragonal structures (space group *P4/mmm*) with lattice parameters: $a = b = 3.838$ Å $c = 11.573$ Å.[67] The presence of Ru makes the oxygen content equal to eight ions per unit cell, instead of seven as in YBCO or nine as in a triple perovskite $A_3B_3O_9$. In fact, microstructural studies by means of electron diffraction and microscopy have shown that the real cell is often tetragonal and sometimes orthorhombic but corresponds, in all cases, to the so-called diagonal cell: $\sqrt{2}a_p \times \sqrt{2}a_p \times 3a_p$.[67]

Previous studies showed that this material exhibit ferromagnetic ordering of the Ru moments on a microscopic scale below 133 K and becomes superconducting at a lower temperature T_C = 16K, which can reach 46 K depending on the sample preparation.[67,72-74]

Although the bulk magnetism in RuO_2 layers of Ru-1212 compounds was confirmed by μSR and ESR studies on the microscopic scale, the exact type of magnetic structure is still controversial. Neutron diffraction experiments (antiferromagnetic ordering) and magnetization studies (ferromagnetic) appear to contradict each other. A recent magnetization study in a pulsed field up to 47 T proposed that the magnetic sub-lattice of the Ru moment is predominantly antiferromagnetic involved by Ru^V ions, interrupted by ferromagnetic stripes due to the charge transfer between Ru^{IV} and Ru^V ions.[75] At the same time the bulk nature of superconductivity has been confirmed by specific heat measurements and a recent report argues that bulk superconductivity exists in this compound within a magnetically ordered state.[74,76]

1212-Molybdo-Cuprates: Five years after the discovery of co-existing magnetism and superconductivity in Ru-1212, it has been claimed that "Mo–1212" would also a member in the 1212-type magneto-cuprate family.[68,77-79] The studies on "Mo–1212" claimed that the full substitution of copper in the chain by molybdenum cations in Sr-based Cu-1212 ($CuSr_2YCu_2O_{7-\delta}$) is possible at ambient pressure. Also, according to those works, Y-containing "Mo–1212" would show the coexistence of superconductivity (SC, T_C = 20 K) and antiferromagnetism (AFM, T_N = 12 K). Even more, this would appear to be an interesting compound as it seemed to show the magnetic ordering below the superconducting transition temperature, which is opposite to the case of Ru-1212. We will see in chapter 4 that this is not really the case. Yet, it is worth mentioning that, up to now; less attention has been given to the Mo substituted "Mo–1212" phases in comparison with the widely studied coexistence of SC and weak-ferromagnetism (WFM) in Ru-1212.

Besides the "Mo–1212" phases, partial doping of Mo in the Cu-1212 structure is also very interesting. As molybdenum can exists in several-oxidation states (commonly IV, V, VI), it is of interest to investigate the effect of Mo substitution for copper in the crystal structure, magnetic properties and superconductivity in "123" (Cu-1212) type superconductors. It is proven than partial doping of Mo for Cu in the chain site of Cu-1212 structures can stabilize the structure at ambient pressure.[18] Mo substituted Cu-1212 compounds have the tetragonal P4/mmm structure. Previous crystal structure studies on superconducting $Mo_{0.3}Cu_{0.7}Sr_2YCu_2O_y$ ((Mo,Cu)-1212) are somehow controversial: *Hu et al*[80] found that the majority of the molybdenum substitution occurs at the square-pyramidal Cu2 site, while *Harlow et al*[81] found the opposite result by single crystal X-ray and neutron diffraction studies. They found that the majority of molybdenum substitutes the chain (Cu1)

site and discussed the correlation between the copper valence and superconductivity by assuming a Mo^{VI} state.

Concerning the electronic properties, previous works on Mo-stabilized Cu-1212 phases clearly stated that these compounds display a superconducting transition centring around 30 K associated to an oxidation reaction from a semiconducting state, within the exception for the bigger rare earth cations = La, Pr and Nd, which are not superconducting.[80-88] And the superconducting transition temperature of $Mo_{0.3}Cu_{0.7}Sr_2RECu_2O_y$ ((Mo,Cu)-1212) materials can be almost as high as YBCO, when the materials were oxygenated under high pressure.[85-88] Along with the superconductivity, the oxygenated (Mo,Cu)-1212 compounds show interesting magnetic properties.[83,89] However, the as-prepared phases and their electronic modification after oxygenation have not been studied in details.

In 2010, *Chmaissem et al.*[85,86] published the structural refinements of the non superconducting and oxidized superconducting phases for the $(Mo_{0.25}Cu_{0.75})Sr_2YCu_2O_{7+\delta}$ by powder neutron diffraction. Their structural results showed that the apical Cu2–O_{ap} distance decreases after oxygenation with increasing T_C, while the in plane Cu-O_P distance remain same, in fact appears to contradict the two-orbital model of *Sakakibara et al*[90] that find T_C increases with increasing apical copper-Oxygen (Cu2–O_{ap}) distance. Moreover, all the first four members of the homologous series of $(Cu_{0.75}Mo_{0.25})Sr_2(Ce,Y)_SCu_2O_{5+2s+\delta}$ (s = 1 - 4)[85,86] compounds also show the trend of shortening apical oxygen distances after oxygenation. Then, the shortening of apical oxygen distance in the molybdo-cuprate materials, in contradiction with the current theory, could suggest the possibility of a different approach to superconductivity in cuprates. Also, the out-of-plane buckling angle (in plane O_P-Cu-O_P angle) increases with oxygenation in disagreement with the common belief that maximum T_C's are achieved when perfectly flat CuO_2 planes are synthesized. All these findings turn this molybdo cuprate family in an interesting topic of research.

2.5. Motivation and scope

Yet, as we discussed previously the molybdo–cuprate family including "Mo–1212", have not been well studied; this prompted us to investigate systematically the 1212-molybdo-cuprate compounds, including the as-prepared phases. Also, due to a existence of debate concerning the Mo site selection, it is important to re-investigate the structure of these interesting compounds. At the same time, there are no reported data dealing with the systematic study of the structure, magnetic ordering and superconductivity for the materials with small rare earth

cations having composition $Mo_xCu_{1-x}Sr_2RECu_2O_y$ (RE = Er, Tm, Yb and Lu). Therefore, it is the purpose of the present thesis to investigate and trying to understand the origin of the magnetic correlation in the "Mo–1212" compounds. Equally, in the light of the several unresolved but remarkable properties observed in the previous cases, we aim to investigate the detailed structure-property correlation of the compounds with composition $Mo_xCu_{1-x}Sr_2RECu_2O_y$ (RE = rare earth cations). Concurrently, the effect of oxygenation on the structure and properties of the above mentioned compounds has been dealt with.

In high T_C cuprates, the doping evolution of the electronic structure and its relevance to the properties is, indeed, an interesting field of research. Since the discovery, high temperature superconductivity in the cuprates is considered to arise from doping of a Mott-Hubbard insulator. The understanding of metal-insulator transition in doped Mott-Hubbard insulators is one of the outstanding challenges occupying modern Solid State Physics. In particular, in the doped cuprates, there exist a complex interplay between lattice, charge, and spin degrees of freedom. The lack of studies on the electronic structure on this interesting molybdo-cuprate family supported us to investigate the electronic states of 1212-type molybdo-cuprate materials. Therefore, beside the investigation of the effect of Mo – substitution on the crystal structure, it is another purpose of this thesis to study the electronic states of the present materials. In order to understand the evolution with doping from a Mott insulator and, furthermore, the influence of oxygen doping in the physical properties and their consequences on the electronic states have to be investigated with a large set of materials. With this in mind, the X-ray photo electron spectroscopy (XPS), which is indeed a powerful tool in studying the influence of 3d element doping in Cu site and can provide the information on the electronic structure of the system, has been employed to investigate the electronic states.

References

[1]V. L. Ginzburg, On surface superconductivity Phys Lett, **13**,101 (1964).

[2]F. Bloch, Z. Phys. **57**, 545 (1929).

[3]A. H. Wilson, Proc. Roy. Soc. A **133**, 458 (1931).

[4]H. J. De Boer and E. J. W. Verwey, Proc. Roy. Soc. A **49**, 59 (1937).

[5]N. F. Mott, Proc. Roy. Soc. A **62**, 416 (1949).

[6]J. Hubbard, Proc. Roy. Soc. A **277**, 237 (1964).

[7]P. W. Anderson, Phys. Rev. **115**, 2 (1959).

[8]P.W. Anderson, Solid State Physics **14**, 99 (1963).

[9]P. W. Anderson, Phys. Rev. **124**, 41 (1961).

[10]J. Kondo, Prog. Theoret. Phys. **28**, 846 (1962).

[11]J. Kondo, Prog. Theoret. Phys. **32**, 37 (1964).

[12]J. Kondo, Prog. Theoret. Phys. **34**, 204 (1965).

[13]J. G. Bednorz and K.A. M¨uller, Z. Phys. B **64**, 189 (1986).

[14]M. K. Wu, J. R Ashburn, C. J. Torng, P. H. Hor, R. L. Meng, L. Gao. Z. J. Huang, Y. Q. Wang, C. W. Chu, Phys. Rev. Lett. **58**, 908 (1987).

[15]R. J. Cava, B. Batlogg, R. B. Van Dover, D. W. Murphy, S. Sunshine, T. Siegrist, J. P. Remeika, E. A. Rietman, S. Zahurak and G. P. Espinosa, Phys. Rev. Lett. **58**, 1676, (1987).

[16]A. Schilling, M. Cantoni, J. D. Guo and H. R. Ott, Nature **363**, 56 (1993).

[17]C. W. Chu, L. Gao, F. Chen, Z. J. Huang, R. L. Meng, and Y. Y. Xue, Nature **365**, 323 (1993).

[18]J. M.S. Skakle, Materials Science and Engineering, **R23**, 1-40, (1998).

[19]Eisaki et al. Phys. Rev. B, **69 (6)**, 064512, (2004).

[20]Y. Koike, M. Masuzawa, T. Noji, H. Sunagawa, H. Kawabe, N. Kobayashi and Y. Saito, Physica C **170**, 130, (1990).

[21]S. S. P. Parkin, V. Y. Lee, A. I. Nazzal, R. Savoy, R. Beyers, and S. J. La Placa, Phys. Rev. Lett. **61**, 750, (1988).

[22]L. Garwin, Nature **332**, 103 (1988).

[23]H. Zhang and H. Sato, Phys. Rev. Lett. **70**, 1697, (1993).

[24]M. R. Presland et al. Physica C **176** , 95 (1991).

[25]"Electronic Structure Of Cuprate Perovskites: High Tc Superconductors: Study of Electronic Structure on substitution, orientation, & temperature in High Tc cuprate perovskites", Saurabh Dalela, LAP LAMBERT Academic Publishing (June 14, 2012).

[26]Z. X. Shen, J. W. Allen, J. J. Yeh, J. S. Kang, W. Ellis, W. Spicer, I. Lindau, M. B. Maple, Y. D. Dalichaouch, M. S. Torikachvili, J. Z. Sun and T. H. Geballe, Phys. Rev. B **36**, 8414 (1987).

[27]S. Uchida, T. Ido, H. Takagi, T. Arima, Y. Tokura and S. Tajima, Phys. Rev. B **43**, 7942 (1991).

[28]Y. Tokura, S. Koshihara, T. Arima, H. Takagi, S. Ishibashi, T. Ido and S. Uchida, Phys. Rev. B **41**, 11657 (1990).

[29]V. J. Emery, Phys. Rev. Lett. **58**, 2794 (1987).

[30]F. C. Zhang and T. M. Rice, Phys. Rev. B **37**, 3759 (1988).

[31]W. L. F. David, W. T. A. Harrison, J. M. F. Gunn, O. Moze, A. K. Soper, P. Day, J. D. Jorgensen. D. G. f1inks, M. A. Beno. L. Soderholm, D. W. Capone II, L. K. Schuller, C.U. Segre, K. Zhang and J.D. Grace, Nature **327**, 310, (1987).

[32]P. K. Gallagher, H. M. O'Bryan, S. A Sunshine and D. W. Murphy, Mater. Res. Bull. **22**, 995 (1987).

[33]J. D. Jorgensen, B. W. Veal, W. K. Kwok, G. W. Crabtree, A. Umezawa. L. J. Nowicki, A. P. Paulikas. Phys. Rev. B **36**, 5731 (1987).

[34]R. I. Cava, A. W. Hewat, E. A. Hewat, B. Batlogg, M. Marezio. K. M. Rabe. J. J. Krajewski. W. F. Peck Jr.. L. W. Rupp Jr., Physica C **165**, 419 (1990).

[35]J. D. Jorgensen, B. W. Veal, A. P. Paulikas, L. J. Nowicki, G. W. Crabtree, H. Claus and W. Kwok, Phys. Rev. B **41**, 1863 (1990).

[36]J. D. Jorgensen, M. A. Beno, D. G. Hinks, L. Soderholm, K. J. Volin, R. L. Ritterman, D. G. Grace, I. K. Schuller, C.U. Segre, K. Z. Zhang and M. S. Kleefisch, Phys. Rev. B **36**, 3608 (1987).

[37]G. Uimin, Phys. Rev. B **50**, 9531 (1994).

[38]A. A. Aligia and J. Garcés, Phys. Rev. B **49**, 524 (1994).

[39]H. Haugerud, G. Uimin and W. Selke, Physica C **275**, 93 (1997).

[40]H. Claus, S. Yang, A. P. Paulikas, J. W. Downey and B. W. Veal, Physica C **171**, 205 (1990).

[41]B. W. Veal, A. P. Paulikas, H. You, H. Shi, Y. Fang and J. W. Downey, Phys. Rev. B **42**, 6305 (1990).

[42]S. Libbrecht, E. Osquiguil, B. Wuyts, M. Maenhoudt, Z.X. Gao and Y. Bruynseraede, Physica C **206**, 51 (1993).

[43]J. Madsen, N. H. Andersen, M. V. Zimmermann and Th. Wolf, Risø Report **R-933** (EN), 1997 (unpublished).

[44]P. Schleger, R. Hadfield, H. Casalta, N. H. Andersen, H. F. Poulsen, M. von Zimmermann, J. R. Schneider, R Liang, P. Dosanjh and W. N. Hardy, Phys. Rev. Lett. **74**, 1446 (1995).

[45]M. Käll, M. V. Zimmermann, N. H. Andersen, J. Madsen, T. Frello, H. F. Poulsen, J. R. Schneider, and Th. Wolf, Europhys. Lett. **51**, 447 (2000).

[46]R. J. Cava, A. W. Hewat, E. A. Hewat, B. Batlogg, M. Marezio, K. M. Rabe, J. J. Krajewski, W. F. Peck, Jr. and L. W. Rupp, Jr., Physica C **165**, 419 (1990)

[47]Th. Zeiske, D. Hohlwein, R. Sonntag, F. Kubanek and Th. Wolf, Physica C **194**, 1, (1992).

[48]J. Grybos, D. Hohlwein, Th. Zeiske, R. Sonntag, F. Kubanek, K. Eichhorn and Th. Wolf, Physica C **220**, 138 (1994).

[49]P. Burlet, V. P. Plakthy, C. Marin and J. Y. Henry, Phys. Lett. A **167**, 401, (1992).

[50]Th. Zeiske, D. Hohlwein, R. Sonntag, J. Grybos, K. Eichhorn and Th. Wolf, Physica C **207**, 333 (1993).

[51]D. Hohlwein, in *Materials and Crystallographic Aspects of* HT_C*-Superconductivity*, edited by E. Kaldis (Kluwer Academic, The Netherlands, 1994), p. 65.

[52]E. Straube, D. Hohlwein and F. Kubanek, Physica C **295**, 1, (1998).

[53]W. Schwarz, O. Blaschko, G. Collin and F. Marucco, Phys. Rev. B **48**, 6513, (1993).

[54]R. A. Hadfield, P. Schleger, H. Casalta, N. H. Andersen, H. F. Poulsen, M. von Zimmermann, J. R. Schneider, M. T. Hutchings, D. A. Keen, Ruixing Liang, P. Dosanjh and W. N. Hardy, Physica C **235-240**, 1267, (1994).

[55]B. Okai, Jpn. J. Appl. Phys., **29**, L2180, (1990).

[56]O. Milat et al., Physica C, **217**, 444-454, (1993)

[57]Y. Miyazaki, H. Yamane, N. Ohnishi, T. Kajitani, K. Hiraga, Y. Morii, S. Funahashi and T. Hirai, Physica C, **198**, 7-131, (1992).

[58]B. Domengès, M. Hervieu and B. Raveau, Physica C, **207**, 65-78, (1993).

[59]N. Ohnishi, Y. Miyazaki, H. Yamane, T. Kajitani, T. Hirai and K. Hiraga, Physica C, **207**, 175-184, (1993).

[60]Y. Miyazaki, H. Yamane, N. Kobayashi, T. Hirai, H. Nakata, K. Tomimoto and J. Akimitsu, Physica C, **202**, 162-166, (1992).

[61]J. Akimitsu, M. Uehara, M. Ogawa, H. Nakata, K. Tomimoto, Y. Miyazaki, H. Yamane, T. Hirai, K. Kinoshita and Y. Matsui, Physica C, **201**, 320-324, (1992).

[62]P. R. Slater, C. Greaves, M. Slaski and C. M. Muirhead, Physica C, **208**, 193-196, (1993)

[63]A. Maignan, M. Hervieu, C. Michel and B. Raveau, Physica C, **208**, 116-120, (1993)

[64]G. V. M. Williams and J. L. Tallon, Physica C **258**, 41 (1996).

[65]L. Rukang, Z. Yingjie, Z. Daoyuang, X. Chen, Q. Yitai, C. Zuyao and Z. Guien, J. Alloy Compd. **185**, 45 (1992).

[66]A. C. Mclaughlin, D. Morrice and F. Sher, J. Solid State Chem. **178**, 2274 (2005).

[67]A. C. McLaughlin, W. Zhou, J. P. Attfield, A. N. Fitch and J. L. Tallon, Phys. Rev. B **60**, 7512 (1999).

[68]I. Felner and E. Galstyan, Phys. Rev. B, **69**, 024512 (2004).

[69]S. Adachi, K.-I. Kubo, S. Takano and H. Yamauchi, Physica C, **191**, 174 (1992).

[70]M. H. Eder and G. Gritzner, Supercond. Sci. Technol. **18**, 87 (2005).

[71]M. A Alario-Franco, R. Ruiz-Bustos and A. J. Dos Santos-Garcia, Inorg chem **47**, 6475, (2008).

[72]L. Bauernfeind, W. Widder and H. F. Braun, Physica C **254**, 151-158, (1995).

[73]J. W. Lynn, B. Keimer, C. Ulrich, C. Bernhard and J. L. Tallon, Phys Rev. B. **61**, R14964, (2000).

[74]V. P. S. Awana, M. Karppinen, and H. Yamauchi, Magneto–superconductivity in rutheno-cuprates

$RuSr_2GdCu_2O_{8-\delta}$ (Ru-1212) and $RuSr_2(Gd_{0.75}Ce_{0.25})_2Cu_2O_{10-\delta}$ (Ru-1222): A critical review.

[75]T. P. Papageorgiou, E. Casini, Y. Skourski, T. Herrmannsdo, J. Freudenberger, H. F. Braun and J. Wosnitza Physica C, **460–462**, 390–391 (2007).

[76]Y. Tokunaga, H. Kotegawa, K. Ishida, Y. Kitaoka, H. Takigawa and J. Akimitsu, Phys. Rev. Lett. **86**, 5767 (2001).

[77]N. Balchev, K. Nenkov, G. Mihova, B. Kunev, J. Pirov and D. A. Dimitrov JMMM **321**, 388–391 (2009).

[78]N. Balchev, K. Nenkov, V. Antonov, J. Pirov, B. Kunev, Physica C, **470**, 2040-2046 (2010).

[79]N. Balchev, K. Nenkov, G. Mihova, J. Pirov and B. Kunev, Physica C, **470**, 178-182 (2010),

[80]S. F. Hu, R. S. Liu, S. C. Su, D. S. Shy and D. A. Jefferson, J. Solid State Chem. **112**, 203, (1994).

[81]R. L. Harlow, G. H. Kwei, R. Suryanarayanan and M. A. Subramanian, Physica C, **257** 125-136 (1996).

[82]P. H. Hor, J. W. Chu, Y. Wang, H. H. Feng, Y. Y. Sun, K. Matsuishi, Q. Xiong and C. W. Chu, in Proceedings of the l992 TCSUH workshop on HTS Materials, Bulk Processing, and Bulk Applications, edited by C W Chu, W K Chu, P H Hor and K Salama (World Scientific, Singapore).

[83]H. L. Tsay, Y. C. Chen, S. S. Weng,. C. F. Chang and H. D. Yang Phys. Rev. B, **59,** 636 (1999).

[84] Q. Xiong, Y. Y. Xue, J. W. Chu, Y. Y. Sun, Y. Q. Wang, P. H. Hor and C. W. Chu Phys. Rev. B **47**, 11337 (1993-I).

[85]I. Grigoraviciute, H. Yamauchi, M. Karppinen and M. Marezio, Phys. Rev. B **82**, 104507 (2010).

[86]I. Grigoravicute, M. Karppinen, T. –S. Chan, Ru-Shi Liu, Jin-Ming Chen, O. Chmaissem and H. Yamauchi, JACS, **132**, 838-841, (2010).

[87]V. P. S. Awanaa, A. Gupta, H. Kishan, E. Takayama-Muromachi, T. Watanabe, M. Karppinen, H. Yamauchi, S. K. Malik, W. B. Yelon, V. Ganesan and A. V. Narlikar, Solid State Commun. **129**, 117-121, (2003).

[88]B. Dabrowski, K. Rogacki, J. W. Koenitzer, K. R. Poeppelmeier and J. D. Jorgensen, Physica C, **277**, 24-35, (1997).

[89]H. L. Tsay, C. R. Shih, Y. C. Chen, W. H. Lee, T. H. Meen and H. D. Yang, Physica C, **252**, 79-86, (1995**)**.

[90]H. Sakakibara, H. Usui, K. Kuroki, R. Arita and H. Aoki, Phys. Rev. Lett. **105**, 057003, (2010).

Chapter 3

Experimental Section

3.1. Synthesis, annealing and oxygenation procedures

3.1.1. Solid state reaction route

Polycrystalline samples of nominal composition $Mo_{1-x}Cu_xSr_2RECu_2O_y$ (RE = Y, Er and Tm) were synthesized by the standard solid state reaction method from the starting products Mo metal powder, RE_2O_3, $SrCO_3$ and CuO with purity above 99.9%. They were mixed, homogenized, pressed into pellets and pre-heated at 1023 K for 24 hours in air and then sintered and annealed at 1273 K for 48 hours with intermediate grindings. Box furnaces and tubular furnaces (for oxygenation) with PID controller have been used for the solid state reaction route.

3.1.2. High pressure and High temperature (HPHT) route

The samples with composition $Mo_{0.5}Cu_{0.5}Sr_2RECu_2O_{7.5}$ (RE = Gd, Y, Ho and Er) were prepared using the HPHT synthesis process. And the $Mo_{0.3}Cu_{0.7}Sr_2ErCu_2O_y$ material has been oxygenated using this process. The description of the equipments and the preparation details are as follows.

Equipment description: Synthesis and the oxygenation have been carried out in a "Conac" and a "Belt" presses located in the High Pressure Laboratory of Universidad Complutense de Madrid (http://www.ucm.es/info/labcoap/index.htm). Figure 3.1 shows both the high pressure equipments; the belt type press can work with two different pressure chambers, the largest is 17mm in length, could reach 40 Kbar of pressure, and can store 300-500 mg of reactants mixture, depending of its density.

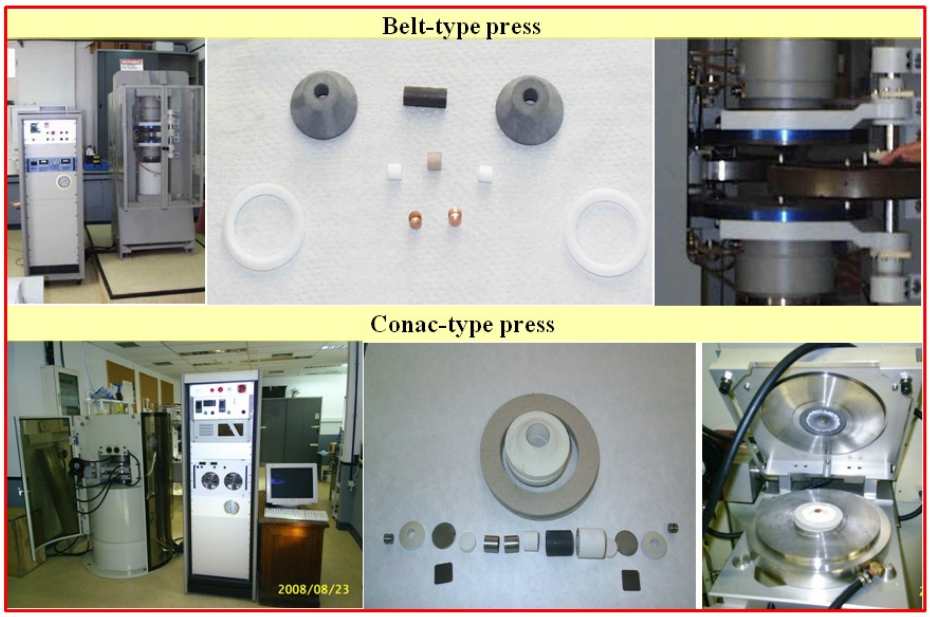

Figure 3.1. Belt and Conac-type presses with the capsules and oven assemblies.

The 12.5 mm chamber can reach 80 Kbar and store 50 mg of reactants mixture. The heating is generated by a graphite oven by means of Joule effect, the maximum temperature it can reach is 1100ºC and 1400ºC for Au and Pt crucibles, respectively. The reactants, grounded and mixed are pressed manually in to a crucible, and then placed inside the cylindrical graphite oven, separated by an cylinder insulator of Al_2O_3; two MgO tops are placed at the ends of the previous cylinder; two phyrophylite cones (used as quasi-hydrostatic pressure transmitter) close the new cylinder, with two teflon rings (to avoid losses of phyrophylite), from the belt plate. Once the crucible pack has been mounted, pressure is applied at a rate of 300 tons/hr, when the value of pressure needed is reached, the machine is left to stabilize for 5 minutes; then heating is applied at a constant rate reaching the required temperature; then temperature is kept constant in a fixed time; at the end of this period the temperature is switched off, the machine is left to stabilize for 5 minutes allowing the quenching of sample and finally pressure is released.

The Concac Press has a different design; here two plates can accommodate a toroidal $CaCO_3$ carrier where the internal volume is occupied by a cylindrical graphite furnace, Al_2O_3 insulator cylinder and Pt crucible containing the reactants mixture.

Synthesis and oxygenation procedures: The synthesis procedures were carried out in a two step process. The first step corresponds to the synthesis of $SrCuO_2$, which is in fact a very useful precursor for the synthesis of 1212-type cuprates in high pressure and high temperature synthesis method. $SrCuO_2$ have been synthesized by the standard solid state reaction method from the starting $SrCO_3$ and CuO products with purity above 99.9%. A mixture of these well homogenized reagents were pressed into pellets and heated at 1273 K for 72 hours in air with further intermediate grindings.

In the second step, this precursor was mixed with the appropriate amount of MoO_3, CuO and corresponding RE_2O_3, which were decarbonized by heating at 1123 K, were placed in a platinum container and heated at 1323 K under a pressure of 50 kbar in a Belt-type apparatus, according to the following equation:

$$2SrCuO_2 + 0.5CuO + 0.5MoO_3 + 0.5RE_2O_3 = Mo_{0.5}Cu_{0.5}Sr_2RECu_2O_{7.5} \qquad (1)$$

The reaction pathway was as follows: (i) rising the pressure up to 50 kbar, (ii) increasing the temperature up to 1323 K in 15 minutes, (iii) maintaining the temperature and pressure for 5-30 min, (iv) quenching to room temperature. Afterwards, the pressure was decreased to ambient pressure. The best result was obtained with a reaction time of 15 min.

In order to increase the oxygen content of the as-prepared $Mo_{0.3}Cu_{0.7}Sr_2ErCu_2O_y$ sample, it was oxygenated high pressure conditions. The high pressure oxygenation was carried out in a Belt Press and also in a Conac type apparatus at 50 kbar and 773 K for 30 min in the presence of 33 mol % $KClO_3$. The $KClO_3$ has been used at the top and bottom end of the platinum crucible with the powder of the AP sample. Under high pressure and high temperature, $KClO_3$ decomposes to KCl and oxygen and acts as an oxygen source.

3.2. Characterization techniques

Three types of radiations are used for the crystal structure studies: X-rays, electrons and neutrons; of these, X-rays are the most used technique but electron and neutron diffraction has important specific applications. By electron diffraction, the wave properties of electrons and its high scattering efficiency, it is possible to carry out the experiments in the same condition of single crystal diffraction but in a micrometric scale, using crystals of few of thousands of Å; moreover, by electron diffraction it is possible to have information about some symmetry properties not available with other techniques, for instance, to know the existence or not of the inversion center (Friedel's law is not valid in electron diffraction). The role of neutron diffraction is clear when it is mandatory to know the magnetic structure of a sample; since neutrons possess a magnetic dipole moment they can interact with unpaired electrons of d and f orbitals, giving rise to an additional scattering effect. Beside the magnetic structure, neutron diffraction is a very useful method to determine the oxygen content.

3.2.1. Powder X-ray diffraction

Powder samples were characterized by the X-ray powder diffraction (XRD) at room temperature performed in a PANalytical X'Pert PRO ALPHA1 diffractometer (Cu $K\alpha_1$-radiation, λ=1.5406 Å). Working conditions was of 45 kV and 40 mA. The measurement scan program was in the range between $5° \leq 2\theta \leq 90°$ with a step of 0°,017' , the recording time was variable in function of each sample due to its characteristics and established from a first trial measurement, usually established that the number of counts for the highest peak was not lower than $2x10^4$ counts.

3.2.2. Electron microscopy

Microstructure characterization of samples is one important point in the study of materials. All microstructural characterization have been carried out in the "Centro Nacional de Mircoscopia Electronica" Luis Bru in the Universidad Complutense of Madrid (http://www.ucm.es/info/vinvest/sic/cais/bru.htm).

Transmission Electron Microscopy and High Resolution Transmission Electron Microscopy (TEM and HRTEM): The sample preparation for electron transmission microscopy starts with the grinding of sample in a mortar, then the powder is dispersed in *n-butanol* using an ultrasonic bath; after that, a few drops of the suspension are placed in a Ni TEM grid covered by a carbon layer; once the solvent is evaporated, the grid is ready for TEM experiments.

Selected Area Electron Diffraction (SAED) experiments have been carried out in a transmission microscope JEOL 2000FX with an accelerating voltage of 200 keV with a resolution between points of 0.31 nm; the microscope is equipped with a double tilting ± 45°, in two directions, sample holder and a microanalysis system for Energy-dispersive X-ray spectroscopy (EDS), Link ISIS 300; Further experiments have been carried out with a JEOL JEM 2100 with an accelerated voltage of 200 kV; LaB_6 electron gun; a resolution of 0.25nm between points; STEM unit with clear field detector; CCD ORIUS SC 1000 camera (model 832); the grid of microscope can tilt in one direction ±42, or in two directions ±42/±30; or until ±80 in tomography mode; the microanalysis has been carried out by means of EDS (OXFORD INCA).

Experiments of high resolution TEM have been performed in a Field Emission Gun (FEG) microscope JEOL-3000F with a accelerate voltage of 300 keV, a resolution of 0.17 nm and a spherical aberration Cs = 0.6 mm; the sample holder can rotate of ±25° in two directions and microanalysis was carried out by the LINK ISIS 300. High resolution images have collected by means of a CCD multiscan camera.

For images processing Digital Micrograph Gatan software 3.10.0 (Gatan Inc. 5933 Colorado Lane Pleasantone, CA, Usa, 94588-3334) is used. Calculated images have made by Mac Tempas software (Kilaas, R. MacTempas Software, version 2.3.7; Total Resolution Inc.: Berkeley, CA, 1988), starting from lattice, space group and atomic position of desired structure.

Energy-dispersive X-ray Spectroscopy (XEDS): Cationic composition of samples have been checked in every microscope by EDS; detector record photon energies emitted from the sample due to electron beam, each emission line recorded by the detector is characteristic of an element.

3.2.3. Neutron diffraction

Neutron diffraction is a key technique to investigate the properties of materials at the atomic scale. This technique is complementary to the X-ray experiment as neutrons can interact strongly with light elements. The uniqueness of this method is based on the fact that the

wavelength and energy of thermal neutrons ideally match with inter-atomic distances and excitation energies in condensed matter.. In addition, neutrons carry magnetic moment, which makes them a unique probe for detecting magnetic structures. Long scan of neutron powder diffarction (NPD) at room temperature (RT) and at low temperatures (1.5 K, 12 K and 50 K) were recorded for the AP and OA powder samples (~2 g) using the D2B diffractometer (Optimum wavelength, λ=1.59 Å) at the Institute Laue Langevin (ILL), France. For the HPO $Mo_{0.3}Cu_{0.7}Sr_2ErCu_2O_y$ the NPD data was recorded only at 1.5 K. Long scan of NPD data for the $Mo_{0.5}Cu_{0.5}Sr_2YCu_2O_{7.5}$ and $Mo_{0.5}Cu_{0.5}Sr_2HoCu_2O_{7.5}$ samples (~250 mg) were recorded at RT. The high resolution diffraction patterns were refined with the Rietveld procedure following the Fullprof suite program.

3.2.4. Thermogravimetric methods

Thermal analysis may be defined as the measurement of physical and chemical properties of materials as a function of temperature. The two main thermal analysis techniques are thermogravimetric analysis (TGA), which automatically records the change in weight of a sample as a function if either temperature or time; the differential thermal analysis (DTA), which measures the difference in temperature, ΔT, between a sample and an inert reference material as a function of temperature; DTA therefore detects changes in heat content.

We have used 5% H_2/N_2 reducing conditio. The samples were heated to 973 K then isothermally maintained for 15 h, and cooled down to room temperature. The oxygen contents were calculated assuming that the final products were RE_2O_3, SrO, $SrMoO_4$ and Cu, as observed by X-ray diffraction.

3.3. Physical property measurements

Magnetic property measurements: Direct current (dc) magnetization and alternating current (ac) magnetic susceptibility measurements have been performed in a Magnetic Properties Measurement System-superconducting Quantum Interference Device, Quantum Design (MPMS-SQUID). A small piece (~30 mg – 100 mg) of sample has been used for the measurements.

DC magnetization measurements, as a function of temperature have been carried out warming from 2 to 300 K after a zero magnetic field cooling (ZFC) and/or after an applied magnetic field cooling (FC) using an external applied magnetic field. In ZFC mode, the sample has been cooled to 2 K in absence of the magnetic field and then, by applying a magnetic field the measurements were carried out. In FC mode the sample has been cooled to 2 K in presence of a magnetic field and then the measurement has been carried out.

The temperature dependence of the ac susceptibility measured at different frequencies and in presence of different ac and dc magnetic fields.

Magnetization vs. applied field measurements (M-H) has been performed at several constant temperatures in ZFC mode. Once the required temperature is reached, the applied magnetic field is increased up to 5T after that decreased to -5T and increased again to close the cycle.

Heat capacity measurements: Specific heat measurements have been performed using a Quantum Design Physical property measurement system (PPMS) at constant pressure in the absence of a magnetic field. All the measurements were performed with a square piece of sample with < 30 mg mass, followed by the addenda measurements. The addenda measurement consists of measuring the heat capacity of the sample holder. The addenda measurements were performed prior to mounting a sample for the purpose of separating the sample's heat capacity contribution from the total heat capacity.

Resistivity and Thermo electric power (TEP) measurements: Resistivity and thermo electric power (TEP) measurements have been performed using a standard four-lead dc method in a He-cryostat.

3.4. X-ray photoelectron spectroscopy

The X-ray photoelectron spectroscopy (XPS) is carried out on a Thermo-VG Scientific ESCALAB 220 iXL spectrometer, equipped with a monochromatic Al K_α X-ray source (1486.6 eV) at Centre de Caractérisation des Matériaux Avancés" – CeCaMA, Bordeaux. Figure 3.2 shows the spectrometer.

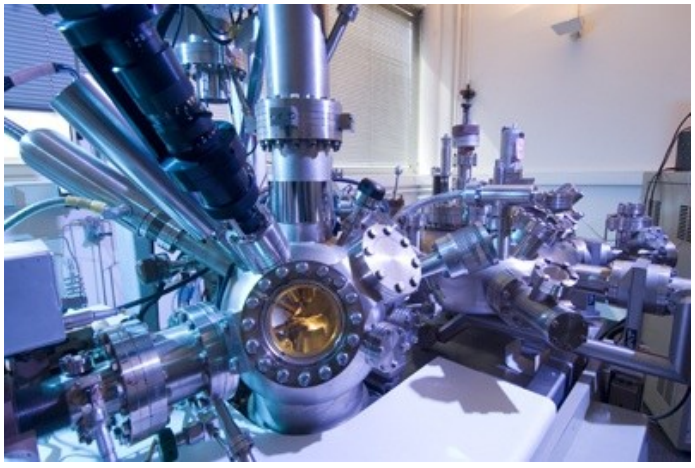

Figure 3.2. Thermo-VG Scientific ESCALAB 220 iXL spectrometer, apparatus for the chemical and morphological characterization of submicron scale. The picture is taken from the ICMCB-CNRS, Bordeaux website.

The samples are scraped in ultra-high vacuum (UHV; 10^{-9} mbar) at room temperature with a stainless steel blade until strong attenuation of the C ls signal is achieved. We estimate that less than 5% of C is left on the surface after cleaning for all cases. The spectra are collected with 20 eV constant pass energy. The collected XPS data are fitted with a combination of Gaussian-Lorentzian line shapes, after correction for the Shirley background, by using the AVANTAGE software from THERMOFISHER SCIENTIFIC.

Chapter 4

Solubility limit of Mo, magnetism and superconductivity in the $Mo_xCu_{1-x}Sr_2YCu_2O_y$ compounds

General Overview

This chapter describes the solubility range of Mo in YSCO ($CuYSr_2Cu_2O_{7-\delta}$) structure and demonstrates the non-co-existence of magnetism and superconductivity in the $Mo_xCu_{1-x}Sr_2YCu_2O_y$ (x = 0.3, 0.4, 0.6, 1.0) compounds prepared at ambient pressure.

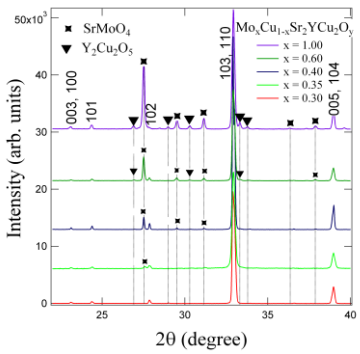

Publication from this chapter

1. Marik S, Moran E, Labrugere C, Toulemonde O and Alario-Franco M A *"$Mo_xCu_{1-x}Sr_2YCu_2O_y$ (0.3≤x≤1) revisited: Superconductivity, magnetism and the molybdenum oxidation state"* 2012 *J. Solid State Chem.* **191** 40.

4.1. Introduction

Charge transport and high temperature superconductivity (HTSC) resides in the CuO_2 planes of all known HTSC cuprates, [1] except that $CuO_{1+\delta}$ chains have been reported to participate in the *b*-axis transport of $YBa_2Cu_3O_{7-\delta}$ (also denoted as YBCO, Y-123 or Cu-1212) [2]. The structure of $YBa_2Cu_3O_{7-\delta}$ and related phases contains two crystallographically distinct Cu sites: the chain site (Cu1, CuO chain) and the square-pyramidal or planar site (Cu2, CuO_2 planes). The connecting layer (CuO chain) can act as a charge reservoir by supplying the carriers necessary for superconductivity in the CuO_2 planes. Pure $YSr_2Cu_3O_{7-\delta}$ (YSCO, $T_{C,onset}$ = 60K), the strontium analog of "123" superconductor $YBa_2Cu_3O_{7-\delta}$ (YBCO), can only be prepared at high pressure [3]. However, these phases can be stabilized at ambient pressure by substituting Pb, Li, Al, Ti, V, Cr, Fe, Co, Ga, Ge, Mo, W and Ir partially or completely for the Cu in the chains[4, 5, 6].

Recently it has been claimed that the full substitution of copper in the chains by molybdenum cations in Sr-based Cu-1212 ($CuSr_2YCu_2O_{7-\delta}$) is possible at ambient pressure [7, 8]. Also, according to this work, Y-containing "Mo–1212" would show the coexistence of superconductivity (SC) and antiferromagnetism (AFM). It is worth mentioning that, up to now, less attention has been given to the Mo substituted "Mo–1212" phases in comparison with the widely studied coexistence of SC and weak-ferromagnetism (WFM) in Ru–1212 [9]. The coexistence of these presumed antagonistic properties in Ru–1212 are due to a site selective substitution of all the Cu in the chain by Ru cations resulting in a layered magnetic structure.

This chapter carefully describes the solubility range of Mo in YSCO ($CuYSr_2Cu_2O_{7-\delta}$) structure and demonstrates the non-co-existence of magnetism and superconductivity in the $Mo_xCu_{1-x}Sr_2YCu_2O_y$ (x = 0.3, 0.4, 0.6, 1.0) compounds prepared at ambient pressure.

4.2. Experimental Details

***Sample preparation*:** All polycrystalline samples of nominal composition $Mo_xCu_{1-x}Sr_2YCu_2O_y$ (x = 0.3, 0.4, 0.6, 1.0) have been synthesized by the standard solid state reaction method from the starting products Mo metal powder, Y_2O_3, $SrCO_3$ and CuO with purity above 99.9%. They were mixed, homogenized, pressed into pellets and pre-heated at 750°C for 24 h in air and then sintered and annealed under various conditions. The sample with nominal composition $MoSr_2YCu_2O_8$ was first sintered at 950 °C for 48h in air and then annealed it under flowing oxygen at 900°C for 24h with a cooling rate of 50°C/hr. And also a series of samples with nominal composition $Mo_xCu_{1-x}Sr_2YCu_2O_8$ where x = 0.3, 0.35, 0.4, 0.6, 1.0 were sintered and annealed under flowing oxygen for 48 hour at 950°C with a cooling rate of 50°C/hr.

X-ray Powder Diffraction (XRD): Powder samples were initially characterized by X-ray powder diffraction (XRD) at room temperature performed in a PANalytical X'Pert PRO ALPHA1 diffractometer (Cu $K\alpha_1$-radiation, λ=1.5406 Å). The diffraction patterns were refined with the Rietveld procedure following the Fullprof suite program. Backgrounds are fitted using a linear interpolation, and peak shapes are modelled by a pseudo–Voight function.

Electron Microscopy: Transmission electron microscope (TEM) images are obtained on a Jeol JEM 3000EX microscope. Sample compositions are checked by energy-dispersive spectrometry (EDS, Link Pentafet 5947 Model, Oxford Microanalysis Group) analysis.

Physical Properties: DC magnetic susceptibility measurements are performed over the temperature range 2–300 K, using a Squid Quantum Design XL-MPMS magnetometer in zero-field-cooling (ZFC) and field-cooling (FC) conditions.

4.3. Results and discussion

4.3.1. Structural analyses: Figure 4.1 shows the XRD pattern of the compound with nominal composition $MoSr_2YCu_2O_8$. This is similar to the early reported one [7, 8]. However, a large number of secondary phases detected in the XRD measurements. In previous studies [7, 8] they were identified as $SrMoO_4$ and Y_2CuO_4, where $SrMoO_4$, is Pauli–paramagnetic [10] and RE_2CuO_4, the second impurity, reveals the magnetism (AFM, T_N = 265 K [11]) of CuO_2 sheets only when it is synthesized under high pressure.

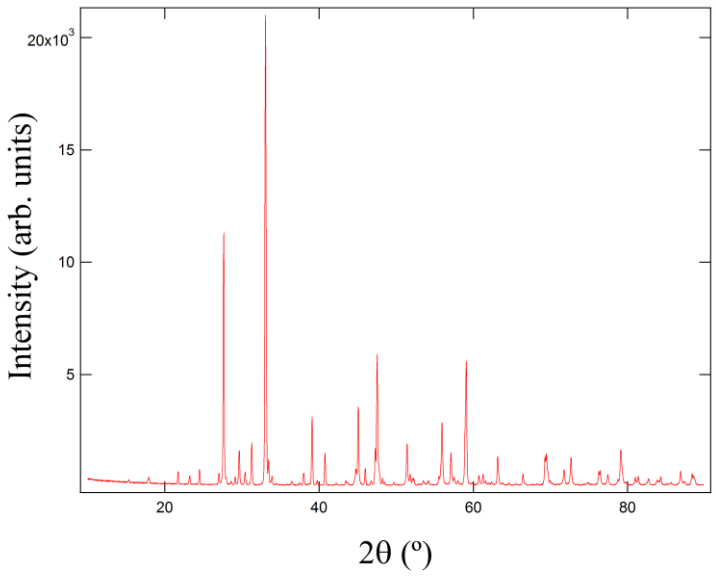

Figure4.1. XRD pattern of the compound with nominal composition $MoSr_2YCu_2O_8$

Figure 4.2 shows the Le-Bail fitting of the X-ray powder diffraction pattern of the same sample having composition $MoSr_2YCu_2O_8$. XRD measurement confirms the tetragonal structure with space group *P4/mmm*: a triple superstructure of the perovskite type structure. In fact contrary to the previous studies [7, 8] we did identify the secondary phases as $SrMoO_4$ and $Y_2Cu_2O_5$ (Figure 4.2). The secondary phases were also confirmed in electron microscopy studies. Moreover, the EDS analyses suggest that in this composition ($MoSr_2YCu_2O_8$), not all the copper in the chain site has been replaced by molybdenum. A molybdenum content of ~ 0.36 is found in the EDS studies.

To know more about the solubility of Mo in "(Mo,Cu)–1212" phase, we prepared a series of compounds with nominal composition $Mo_xCu_{1-x}Sr_2YCu_2O_y$ for x = 0.3, 0.35, 0.4, 0.6, 1.0. Final annealing was done under flowing oxygen at 900°C for 24h with a cooling rate of 50°C/hr. Representative region of the XRD patterns of this series are shown in figure 4.3.

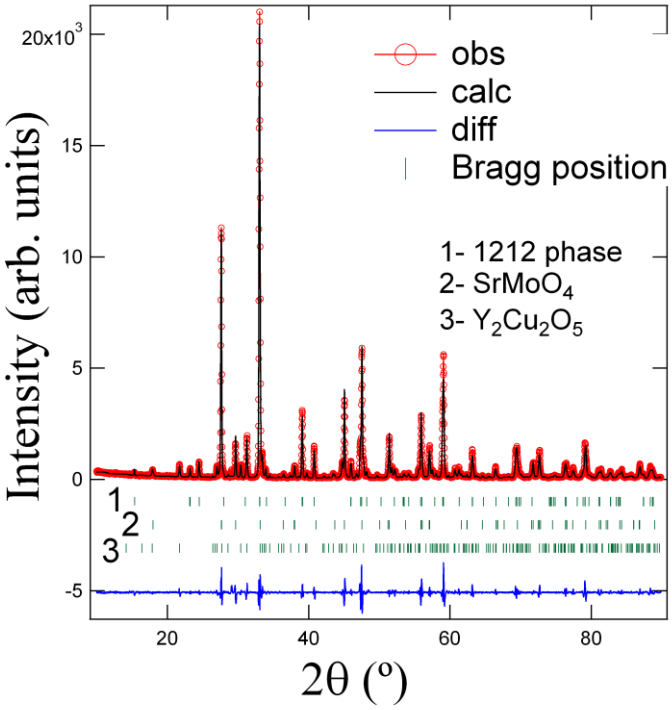

Figure 4.2. Le-Bail fit of the X-ray powder diffraction of nominal composition "$MoSr_2YCu_2O_8$". The upper set of Bragg ticks correspond to reflections from this type of structure (1212 type); the lower ticks locate reflections from secondary phases $SrMoO_4$ (2) and $Y_2Cu_2O_5$ (3) respectively.

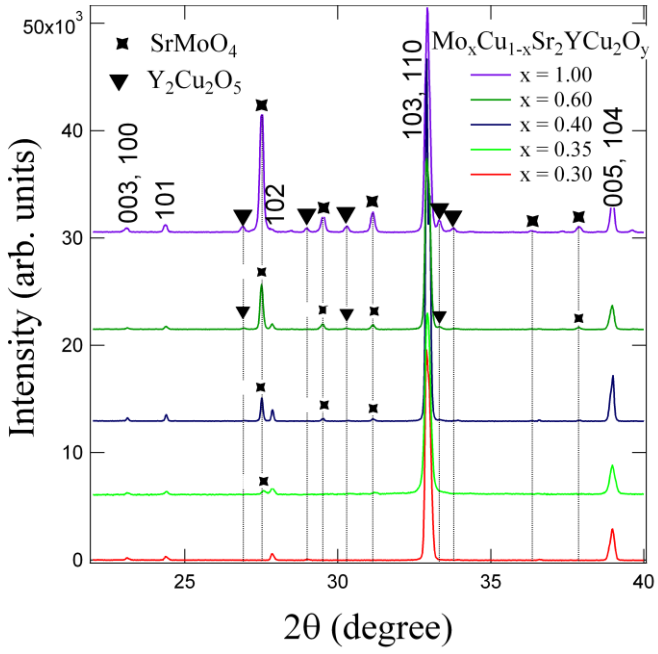

Figure 4.3. X-ray powder diffraction patterns for $Mo_xCu_{1-x}Sr_2YCu_2O_y$ (x = 0.3, 0.35, 0.4, 0.6, 1.0). They show the growing intensity of secondary phase's reflections with increasing the Mo content in the nominal composition.

All attempts to completely get rid of the impurities were unsuccessful for $x \geq 0.35$ as shown on the XRD patterns of this series in figure 4.3. The amount of secondary phases increases with increasing the amount of Mo in the nominal composition. Moreover, the solubility limit of Mo for this series is also confirmed by our EDS analyses (Table 4.1) suggesting that, in every case, not all the copper in the chain site has been replaced by molybdenum. A molybdenum content of ~ 0.36 is found for all the compounds (except for x = 0.3) in this series. Finally, for x = 0.3 no impurity peaks are detected in XRD measurements, thus a truly monophasic sample is obtained at ambient pressure for x = 0.3.

Table4.1. EDS analysis of the samples having different nominal composition.

Nominal composition	Mo	Cu
$MoSr_2YCu_2O_y$	0.36	2.62
$Mo_{0.3}Sr_2YCu_{2.7}O_y$	0.29	2.69
$Mo_{0.4}Sr_2YCu_{2.6}O_y$	0.35	2.72
$Mo_{0.6}Sr_2YCu_{2.4}O_y$	0.38	2.75

4.3.2. Magnetism and Superconductivity: Figure 4.4 illustrates the magnetization of the compound having nominal composition "$MoSr_2YCu_2O_8$", annealed at 900°C (see experimental section), as a function of temperature in zero field-cooled (ZFC) and field-cooled (FC) modes at 10 Oe. It shows a superconducting state (T_C~20 K) along with the antiferromagnetic ordering (AFM, T_N ~ 12 K), which matched well with the previously reported one [7]. Figure 4.5 illustrates the change of the magnetic susceptibility as a function of temperature in both ZFC and FC mode measured at 10 Oe for oxygen annealed (at 950°C for 48 hour) $Mo_xCu_{1-x}Sr_2YCu_2O_y$ compounds with x = 0.3, 0.4, 0.6, 1.0. All the compounds are superconducting at the same temperature (T_C = 29K). The superconducting fraction is continually lowered in relation with the continuous increase of the intensity of the peak obtained at 10.3K in FC mode. This indicates an AFM ordering fraction for the samples with x = 0.4, 0.6, 1.0. However, one notes that although one of the observed impurities $SrMoO_4$ is Pauli-paramagnetic, the second impurity, $Y_2Cu_2O_5$ shows a sharp AFM ordering at 10-12 K [10, 11].

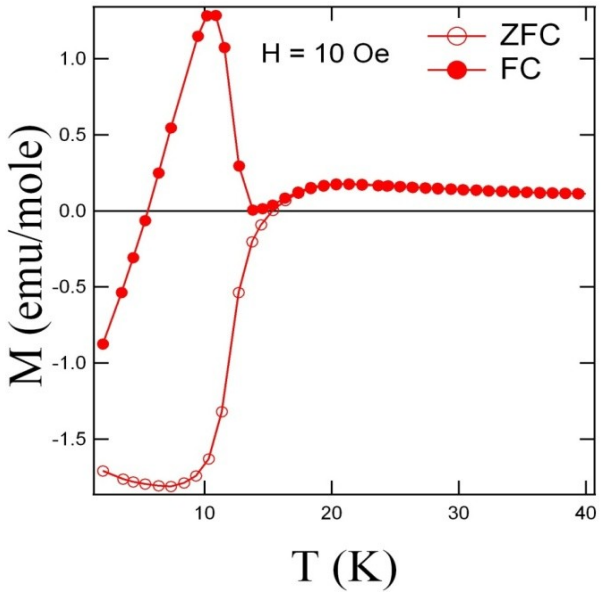

Figure 4.4. ZFC and FC magnetization curves of "Mo-1212Y" measured at 10 Oe

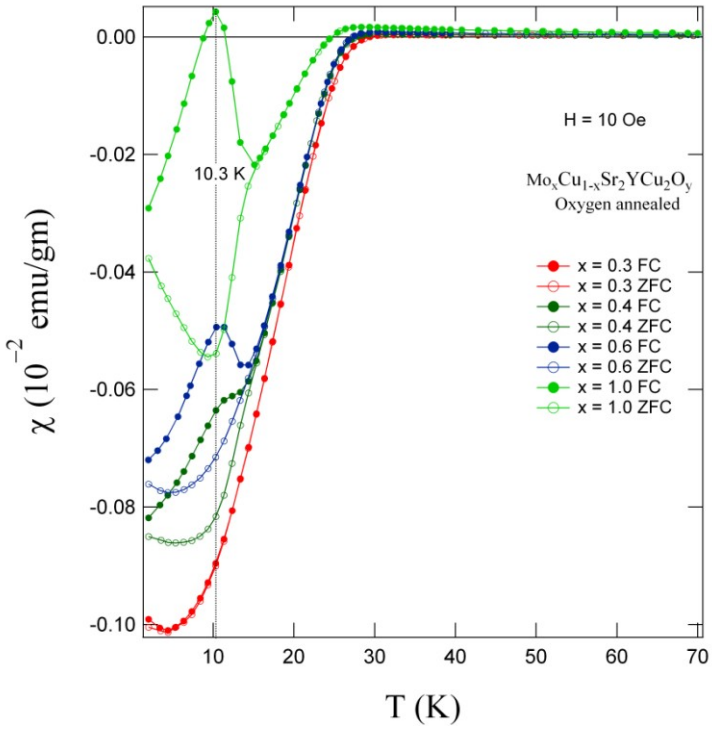

Figure 4.5. Temperature dependence of the magnetic susceptibility (ZFC and FC) of $Mo_xCu_{1-x}Sr_2YCu_2O_y$ (Sample B, x = 0.3, 0.4, 0.6, 1.0) at 10 Oe. It shows the evolution of the magnetic peak at 10.3 K with the increasing content of secondary phases in the compound.

Since no AFM peak is detected in the magnetic susceptibility data of the pure sample with x = 0.3, the superconductivity observed in all these multiphase samples has to be attributed to the $Mo_{0.3}Cu_{0.7}Sr_2YCu_2O_y$ phase and the AFM peak at 10.3 K corresponds to the $Y_2Cu_2O_5$.

4.4. Conclusion

The present study of the $Mo_xCu_{1-x}Sr_2YCu_2O_y$ samples emphasizes the ability of this phase to incorporate foreign cations. However, it also clearly shows that the secondary phases start to form when $x \geq 0.35$ and the AFM ordering is due to the $Y_2Cu_2O_5$ secondary phase. In fact, a material of composition "$MoSr_2YCu_2O_8$" does not exist at room pressure and indeed, can not show any coexistence of antiferromagnetism and superconductivity contrary to what has been previously suggested [7, 8].

References

[1] J. M. Tarascon and B. G. Bagley, in *Chemistry of High Temperature Superconductors*, edited by A. Vanderaha (Noyes, NewYork 1993), pp. 310, and references therein.

[2] R. Gagnon, C. Lupien, and L. Taillefer, Phys. Rev. B 50 (1994) 3458.

[3] B. Okai, Jpn. J. Appl. Phys, 29 (1990) L2180.

[4] Tohru Den and Tamaki Kobayashi, Physica C 196 (1992) 141-152.

[5] S. F. Hu, R. S. Liu, S. C. Su, D. S. Shy and D. A. Jefferson, J. Solid State Chem. 112 (1994) 203.

[6] R. L. Harlow, G. H. Kwei, R. Suryanarayanan, and M. A. Subramanian, Physica C 257 (1996) 125-136.

[7] I. Felner, E. Galstyan, I. Felner, E. Galstyan, Phys. Rev. B, 69 (2004), p. 024512..

[8] N. Balchev, K. Nenkov, V. Antonov, Journal of Superconductivity and Novel Magnetism 26 (2013) 59-63

[9] L. Bauernfeind, W. Widder, H.D. Braun, Physica C 254 (1995) 151.

[10] S.I. Ikeda and N. Shirakawa, Physica C 785 (2000) 341-348.

[11] B.L. Ramakrishna, E.W. Ong and Z. Iqbal, Solid State Communications 68 (8) (1988) 775-779.

Chapter 5

$Mo_{0.3}Cu_{0.7}Sr_2RECu_2O_y$ (RE = Y, Er and Tm)

General Overview

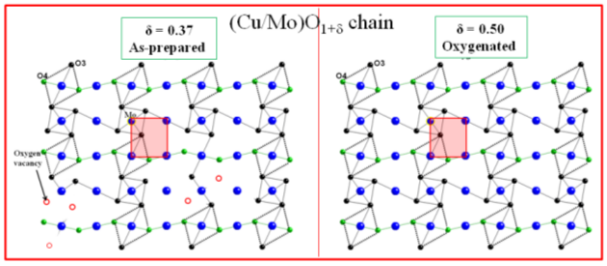

This chapter describes the detailed crystal structure, as well as the physical properties of three compounds with nominal composition $Mo_{0.3}Cu_{0.7}Sr_2RECu_2O_y$ (RE = Y, Er and Tm). The detailed crystal structure is determined using the combination of X-ray/Neutron powder diffraction and electron microscopy techniques. A detailed composition-structure-property correlation is presented here.

Publications from this chapter

1. Marik S, Moran E, Labrugere C, Toulemonde O and Alario-Franco M A *"$Mo_xCu_{1-x}Sr_2YCu_2O_y$ $(0.3\leq x\leq 1)$ revisited: Superconductivity, magnetism and the molybdenum oxidation state"* 2012 *J. Solid State Chem.* **191** 40.

2. Marik S, Dos santos-Garcia A J, Moran E, Toulemonde O and Alario-Franco M A "*Spin glass to superconducting phase transformation by oxidation of a molybdo-cuprate: $Mo_{0.3}Cu_{0.7}Sr_2TmCu_2O_y$*" 2013 *J. Phys.: Condens. Matter* **25** 165704**.**

3. Marik S, Dos santos-Garcia A J, Moran E, Toulemonde O and Alario-Franco M A *"Unusual charge transfer, magnetism and superconductivity in $Mo_{0.3}Cu_{0.7}Sr_2ErCu_2O_y$"* (will be submitted in J. Chemistry C)

5.1. Introduction

In recent years, layered cuprates have attracted much interest in the scientific community for their ability to host a variety of functional properties, especially high temperature superconductivity (HTSC). The 1212–type layered cuprates, having general formula $MA_2RECu_2O_{8-\delta}$ or M – 1212 (where M is commonly a transition metal element, A is an alkaline earth metal, and RE is a rare earth ion) are iso-structural with the classical $YBa_2Cu_3O_y$ (YBCO or Cu-1212) in which Y, Ba, and Cu1 (the chain copper site) are completely or partially replaced with rare earth elements, alkaline earth metals, and transition metal ions, respectively. In the case of YBCO, the copper chain layers are alternatively stacked along the c direction and act as a charge reservoir block by supplying the carriers necessary for superconductivity to the CuO_2 planes (Cu2 site).[1]

The interactions of the magnetic rare-earth sublattice with the superconducting CuO_2 planes and the magnetic behaviour of the heavy rare-earth ions (RE) in $CuBa_2RECu_2O_y$ (REBCO or Cu-1212) is an interesting topic of research. Although, the rare earth planes in REBCO and related phases are well isolated from each other and sandwiched between two CuO_2 planes, three-dimensional (3D) magnetic ordering has been discovered in the compounds with RE =Er, Gd, Dy, and Nd.[2,3] $CuBa_2TmCu_2O_y$ (TmBCO)[4] shows relatively strong paramagnetism compared to other $CuBa_2RECu_2O_y$ [2,3] compounds (RE =Er, Gd, Dy, and Nd); such behaviour has been mainly attributed to the strong Tm-magnetic anisotropy that operates in both paramagnetism (PM) and superconductivity.[4] Coexistence of weak ferromagnetism (WFM) and superconductivity (SC) have even been discovered in the ruthenocuprate with nominal composition $RuSr_2GdCu_2O_{8-\delta}$[5,6], due to a double-exchange interaction, promoted by the mixed valence state of the Ru ions (Ru^{IV} and Ru^{V}). A recent magnetization study in a pulsed field up to 47 T proposed that the magnetic sub-lattice of the Ru moment is predominantly antiferromagnetic originated by Ru^{V} ions, interrupted by ferromagnetic stripes due to the charge transfer between Ru^{IV} and Ru^{V} ions.[7] Depending on the magnetic state of the substituted transition metal ion, other 1212 compounds show a wide diversity of electronic properties.[5-14]

As molybdenum can exists in several-oxidation states (commonly IV, V, VI in oxides), it is of interest to investigate the effect of Mo substitution for copper in the crystal structure, magnetic properties and superconductivity in “123” type superconductors. Also, it is important to examine the effect of Mo–substitution on the oxidation state of copper to understand the superconductivity on these types of materials. Previous work on Mo-stabilized

$RESr_2Cu_3O_{7-\delta}$ (RE = Rare earth, [15]) phases clearly stated that these compounds display a superconducting transition centring around 30 K, with the exception of the bigger R = La, Pr and Nd lanthanide-compounds, which are not superconducting.[15] Recently, and contrary to previous claims of coexistence of anti-ferromagnetism (AFM) and SC in Mo−1212 compounds, as suggested by several groups,[16,17] we have shown in the previous chapter that there is no coexistence of magnetism and superconductivity in these compounds, with our work on $Mo_xCu_{1-x}Sr_2YCu_2O_y$.[18] In fact, full replacement of Mo for the copper chain site is not possible at ambient pressure; a pure compound can only form with $x \leq 0.3$ nominal composition. Previous crystal structure studies on superconducting $Mo_{0.3}Cu_{0.7}Sr_2YCu_{2.7}O_y$ are somehow controversial: *Hu et al*[19] found that the majority of the molybdenum substitution occurs at the square-pyramidal Cu2 site, while *Harlow et al*[20] found the opposite result by single crystal X-ray and neutron diffraction studies. They found that the majority of molybdenum substitutes the chain (Cu1) site and discussed the correlation between the copper valence and superconductivity by assuming a Mo^{VI} state.

As it well known that Tm and Er have a strong magnetic anisotropy, it is the aim of this work to investigate the effect of these magnetic cation substitution for non magnetic Y in the $Mo_{0.3}Cu_{0.7}Sr_2YCu_2O_y$ compound. Changes in the crystallographic structure, the presence of superconductivity and/or magnetic ordering and a correlation among them are expected. Also, according to our literature survey, there are no reported data dealing with the systematic study of the structure, magnetic ordering and superconductivity for $Mo_{0.3}Cu_{0.7}Sr_2RECu_2O_y$ (RE = Er and Tm).

In this chapter, we have described systematically, the detailed crystal structure, as well as the physical properties of three compounds with nominal composition $Mo_{0.3}Cu_{0.7}Sr_2RECu_2O_y$ (RE = Y, Er and Tm). This chapter is divided in two sub-chapters. First part (5.2a) carefully describes the structural, magnetic, specific heat and detailed X-ray photoelectron spectroscopy (XPS) studies for the $Mo_{0.3}Cu_{0.7}Sr_2YCu_2O_y$, having different oxygen content. The second part (5.2b) describes and compares the detailed crystal structure using the combination of X-ray/Neutron powder diffraction and electron microscopy techniques, as well as the magnetic and superconducting properties for the as-synthesized and oxygenated $Mo_{0.3}Cu_{0.7}Sr_2ErCu_2O_y$ and $Mo_{0.3}Cu_{0.7}Sr_2TmCu_2O_y$ materials.

5.2a. $\underline{Mo_{0.3}Cu_{0.7}Sr_2YCu_2O_y}$

5.2a.1. Experimental Details

Sample preparation: Polycrystalline samples of nominal composition $Mo_{0.3}Cu_{0.7}Sr_2YCu_2O_y$ were synthesized by the standard solid state reaction method from the starting products Mo metal powder, Y_2O_3, $SrCO_3$ and CuO with purity above 99.9%. They were mixed, homogenized, pressed into pellets and pre-heated at 1023 K for 24 hours in air and then annealed at 1273 K for 48 hours with intermediate grindings. We denote this sample as the as-prepared (AP or as-synthesized) one. A part of the as-prepared sample was annealed under an oxygen flow at 873 K (48 hours) followed by slow cooling (0.5 K/min) in a tubular furnace, we named this sample as oxygen annealed (OA). A sample, named OA1, was prepared and sintered at 1223 K under oxygen atmosphere for 48 hour.

X-ray Powder Diffraction (XRD): Powder samples were characterized by the X-ray powder diffraction (XRD) at room temperature performed in a PANalytical X'Pert PRO ALPHA1 diffractometer (Cu $K\alpha_1$-radiation, λ=1.5406 Å). The diffraction patterns are refined with the Rietveld procedure following the Fullprof suite program.[21] Backgrounds are fitted using a linear interpolation, and peak shapes are modelled by a pseudo–Voight function.

Physical properties: Direct current (dc) magnetic susceptibility measurements are performed over the temperature range 2–300 K, using a Squid Quantum Design XL-MPMS magnetometer in zero-field-cooling (ZFC) and field-cooling (FC) conditions. Specific heat measurements are performed using a Quantum Design PPMS.

X-ray photoelectron spectroscopy: The X-ray photoelectron spectroscopy (XPS) is carried out on a Thermo-VG Scientific ESCALAB 220 iXL spectrometer. The details of the experiments and data treatment are discussed in the experimental chapter (*chapter 3*).

5.2a.2. Results and discussion

Structure and Microstructure: Figure 5.1 shows the Rietveld refinement of the XRD data for the AP and OA $Mo_{0.3}Cu_{0.7}Sr_2YCu_2O_y$ material. The refinement indicates that for both samples the crystal structure is tetragonal (space group: P4/mmm) with the parameters a = b = 3.8247 (1) Å and c = 11.5443 (1) Å for the AP material. The lattice parameters and cell volumes decrease for the oxygen annealed compound (OA). Table 5.1 gives the parameters of fitting as well as the fit agreement factors for the AP and OA material, respectively.

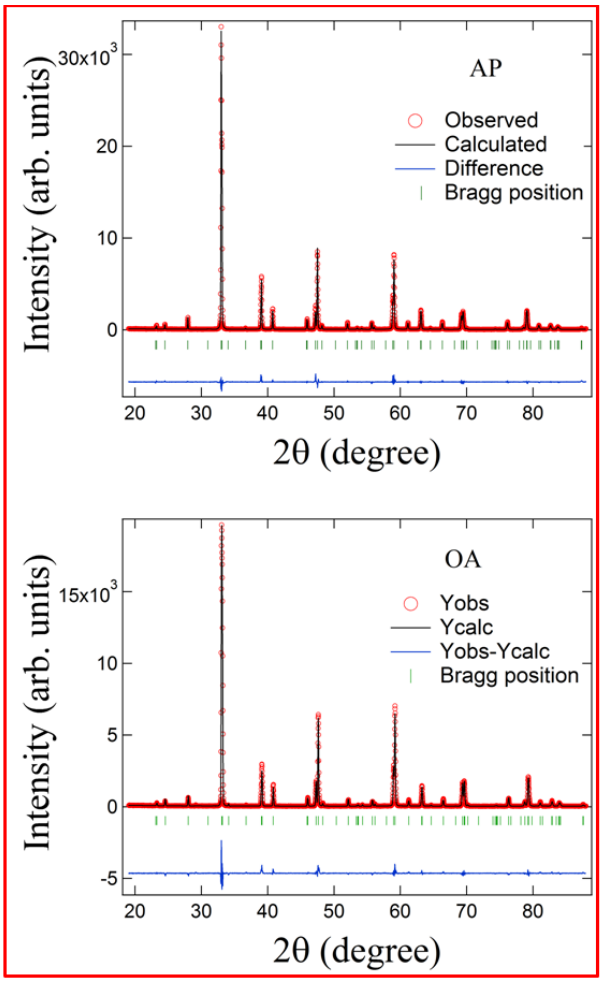

Figure 5.1. Rietveld refinement patterns of the X-ray powder diffraction pattern for the AP and OA $Mo_{0.3}Cu_{0.7}Sr_2YCu_2O_y$ material.

Table 5.1. Cell and Atomic Parameters and Agreement Factors for the $Mo_{0.3}Cu_{0.7}Sr_2YCu_2O_y$ materials as suggested by the room temperature XRD refinements.

Samples	**AP**	**OA**
a (Å)	3.82467 (4)	3.81565 (3)
c (Å)	11.5443 (1)	11.5250 (1)
V (Cell Volume, $Å^3$)	168.871 (3)	167.795 (3)
Y [1d, (0.5, 0.5, 0.5)]		
Mo1/Cu [1a, (0, 0, 0)]		
Occupancy	0.20 (2)/0.80(2)	0.19 (1)/0.81(1)
B	2.4 (1)	1.5 (1)
Mo2/Cu2[2g, (0, 0,z)]		
z	0.3569 (2)	0.3548 (2)
Occupancy	0.10 (3)/1.90(3)	0.08 (1)/1.92(1)
B	1.58 (6)	1.10 (6)
Sr [2h, (0.5, 0.5, z)]		
z	0.1962 (1)	0.1922 (1)
B	2.21 (5)	1.5 (5)
O(1) [4i, (0, 0.5, z)]		
z	0.3749 (4)	0.3750 (4)
B	0.8 (1)	0.5 (1)
O(2) [2g, (0, 0, z)]		
z	0.1597 (7)	0.1609 (7)
B	2.3 (2)	1.9 (2)
O (3) [4n, (x, 0.5, 0)]		
x	0.191 (4)	0.160 (4)
B	6.2 (2)	7.5 (9)
R_P	6.19	7.53
R_{wp}	8.86	9.00
R_F	2.29	2.08
χ^2	2.66	2.39

Site occupancy refinement for all samples indicates that the chemical substitution of the Mo ions for the Cu ions in the $CuYSr_2Cu_2O_{7-\delta}$ structure is found to occur in both Cu sites. We have determined that the majority of the Mo substitution in these samples occurs for the copper in the [Cu1] chain sites in the 123–type parent structure, which is in a good agreement with *Harlow et. al.*[20] The initial model used for our refinements is based on the structure proposed by *Harlow et al*.[20] in which the chain site (Cu/Mo)-O_6 octahedron are rotated. As a consequence of these rotations, the chain oxygen position O(3), as refined using XRD data, is displaced from its ideal position (0, 0.5, 0) in this structure type to a (±x, 0.5, 0) site, with x = 0.191 for the as prepared sample. After annealing under oxygen atmosphere a decrease in the displacement of chain oxygen position (x = 0.16 for OA sample) is observed.

Magnetic, superconducting and specific heat studies: Figure 5.2 shows the temperature variation of magnetic susceptibility for the AP and OA samples, measured at 10 Oe. The AP sample is not superconducting (SC), rather, it shows an irreversibility between FC and ZFC magnetic susceptibility starting from 15 K. On the other hand, both the oxygenated samples (OA and OA1, Figure 5.2 and 5.3) are superconducting. The onset of the SC transition occurs at 29 K and 36 K for the OA1 and OA materials, respectively.

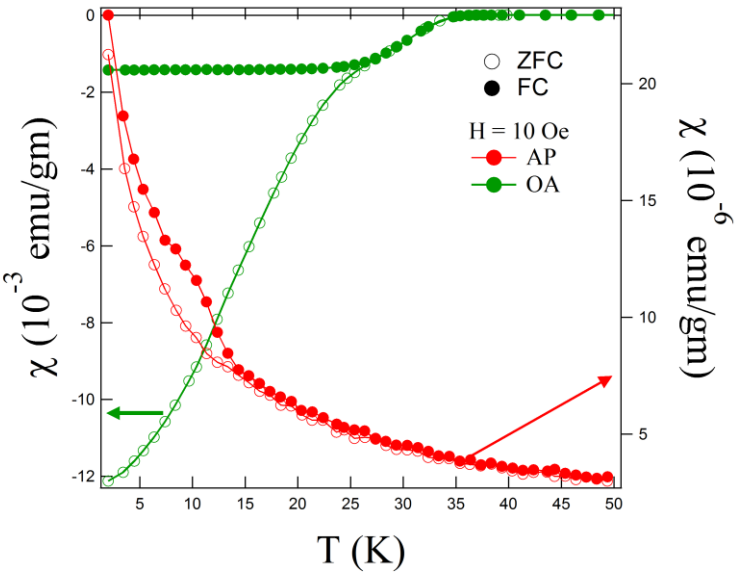

Figure 5.2. Zero field cooled and field cooled magnetic susceptibility as a function of temperature for as prepared (AP) and oxygen annealed (OA) $Mo_{0.3}Cu_{0.7}Sr_2YCu_2O_y$ samples taken at 10 Oe. The onset of superconducting transition in oxygen annealed sample occurs at 36 K

Nevertheless, above T_C, the dc susceptibility curves measured at 100 Oe for all samples (figure 5.4) have the typical paramagnetic shape. A best fit to Curie-Weiss law [$\chi = C/(T-\theta)$ (C = Curie constant, θ = CW temperature)] above T_C, yields the effective magnetic moment

P_{eff} = 1.09μ_B for the AP material. P_{eff} value is calculated by assuming the oxygen occupancy y = 7.4.

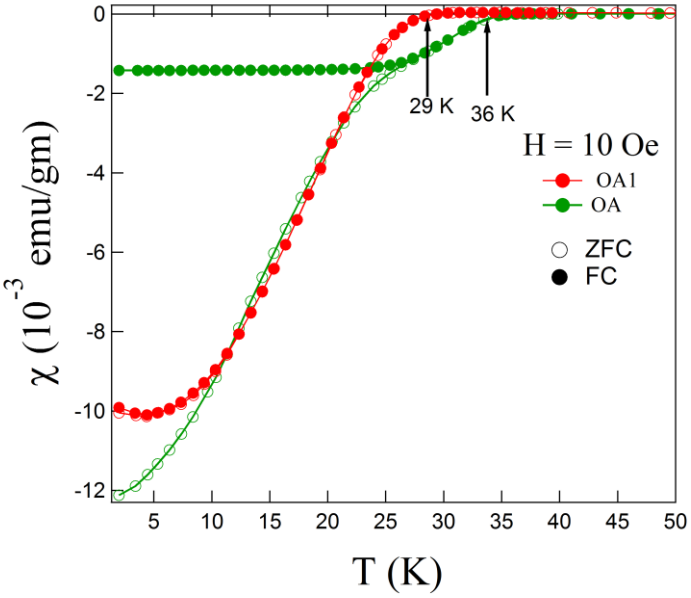

Figure 5.3. Zero field cooled and field cooled magnetic susceptibility as a function of temperature for oxygen annealed (OA and OA1) $Mo_{0.3}Cu_{0.7}Sr_2YCu_2O_y$ samples taken at 10 Oe. The onset of the superconducting transition occurs at 29 K and 36 K for OA1 and OA, respectively.

Before fitting, we subtracted the temperature independent susceptibility of the Cu ions [(1.8 × 10^{-4} emu/mol Oe) (Ref. 22)] from our susceptibility data. So there must be some Molybdenum in 5+ state (P_{eff} of Mo^{5+} = 1.73 μ_B, $4d^1$, S = 1/2) and the P_{eff} value obtained corresponds to the Mo^{5+} ion.

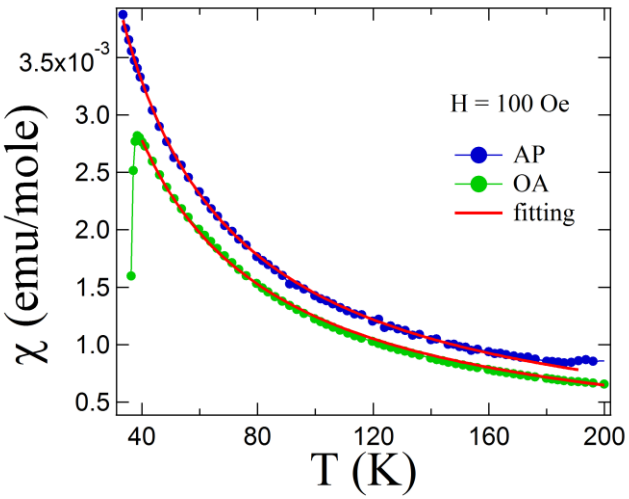

Figure 5.4. FC magnetic susceptibility along with Curie-Weiss fitting as a function of temperature for the AP and OA $Mo_{0.3}Cu_{0.7}Sr_2YCu_2O_y$ samples taken at 100 Oe.

This is indeed both interesting and surprising since non magnetic Mo^{VI} has always been assumed in all previous works with this type of compounds.[19,20,23-27] It is possible that the magnetic anomaly (irreversibility between FC and ZFC susceptibility) in the AP $Mo_{0.3}Cu_{0.7}Sr_2YCu_2O_y$ sample originated from the Mo^{V} paramagnetic cations that are better aligned on the FC mode. We have also performed specific heat measurements in absence of magnetic field. Neither any cusp at superconducting transition temperature nor any magnetic anomalies are observed down to 4.2K in the C vs. T measurement. These results are consistent with those previously observed.[24]

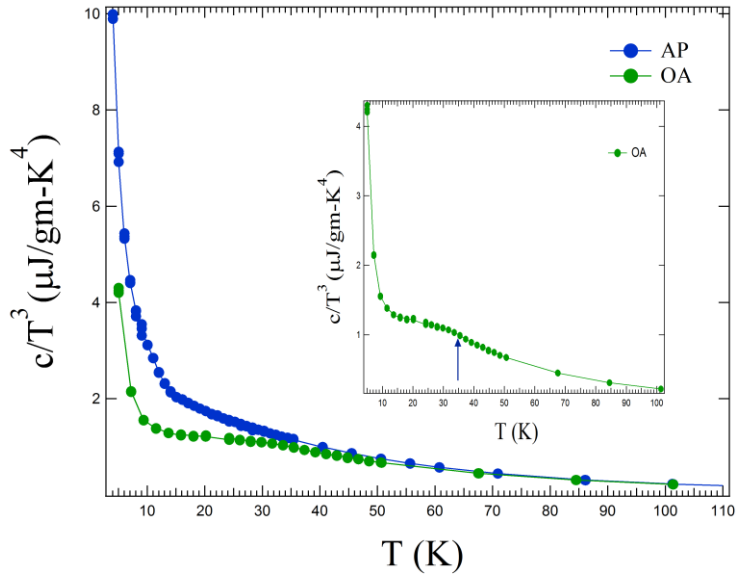

Figure 5.5. C/T^3 vs T plot of as prepared (AP) and oxygen annealed (OA) samples. The OA sample shows a clear bump at the superconducting transition temperature (T_C). Inset shows c/T^3 vs T plot of the OA sample with an arrow indicating the bump at T_C

Figure 5.5 shows C/T^3 vs. T plot for the as prepared (OA) and the oxygen annealed (OA) samples. The specific-heat curves for these two samples merge together at higher temperature. This merging indicates that these compounds have the same electronic and lattice contributions to specific heat at high temperature. But irreversibility started below 50 K and the oxygen annealed superconducting sample (OA) shows a clear bump at T_C in C/T^3 – T curve (figure 5.5). In order to get further knowledge about the unusual Mo oxidation state obtained from the Curie-Weiss law formalism, we have investigated the electronic structure by means of X-ray photoelectron spectroscopy (XPS).

XPS measurements: In what follows, we do analyse and discuss the XPS core level spectra of the Mo 3d, Cu 2p and O 1s energy region, which are concerned with the oxidation state

related problems, we have encountered earlier. The detailed XPS studies are discussed in *chapter 6*.

Figure 5.6 compares the XPS spectra of the Mo 3d core levels for the as prepared sample before and after annealing under oxygen atmosphere for 48 hours at 873 K (AP and OA). As OA compound exhibits the highest T_C among the oxygen annealed $Mo_{0.3}Cu_{0.7}Sr_2YCu_2O_y$ samples, we choose this sample for XPS measurement. We have observed peak broadening for the OA sample compared to the AP one. A spin-orbit splitting of 3.1 eV[28] and a $3d_{5/2}$:$3d_{3/2}$ intensity ratio of 3:2 have been used for the fitting after appropriate correction of the background with a single Shirley (Gaussian-step) function. The fitting parameters are shown in table 5.2. Fitting of the XPS spectra of Mo 3d core levels allows us to confirm the large content of Mo^V. The presence of Mo^V and Mo^{VI} is identified by the energy shifts of their core levels assigning the doublet at 232 eV & 235.1 eV ($3d_{5/2}$ and $3d_{3/2}$) to Mo^V and the one's at 233.3 eV & 236.4 eV ($3d_{5/2}$ and $3d_{3/2}$) to Mo^{VI} as previously proposed.[29] Annealing under oxygen atmosphere is enhancing the Mo^{VI} state.

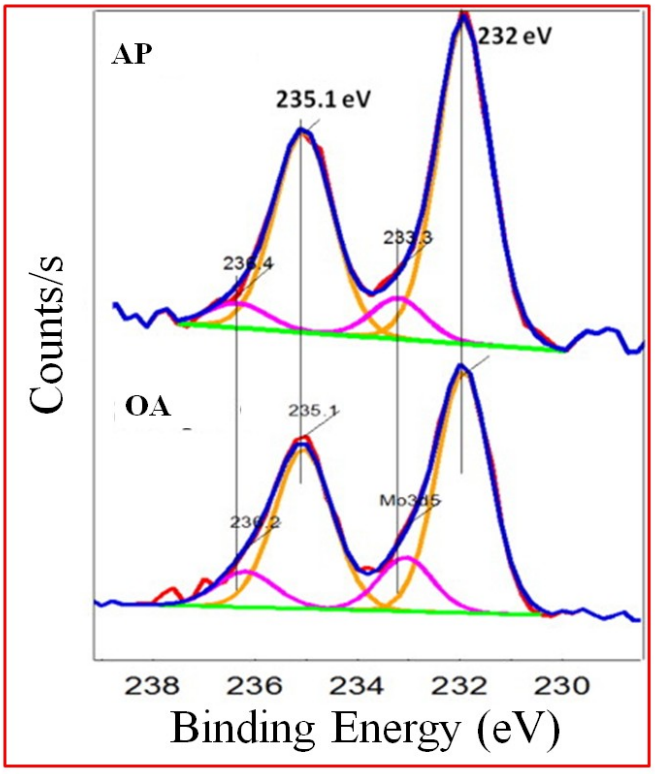

Figure 5.6. Core level XPS spectra of Mo 3d energy region for both the AP and OA $Mo_{0.3}Cu_{0.7}Sr_2YCu_2O_y$ materials. It shows the co-existence of Mo^V and Mo^{VI}. The amount of Mo^{VI} is increasing by annealing under oxygen.

We have found that the ratios between Mo^V and Mo^{VI} are 0.92:0.08 and 0.80:0.20 for the AP and OA material, respectively. This is accompanied by a contraction of the cell parameters as Mo^{VI} (0.59Å for VI coordination) is smaller in radius than Mo^V (0.61Å for VI coordination).

The Cu 2p core level spectra are shown in figure 5.7. The Cu $2p_{3/2}$ spectra for all the $Mo_{0.3}Cu_{0.7}Sr_2YCu_2O_y$ samples are typical of Cu^{II} compounds. The main peak near 933.5 eV is attributed to the well-screened $\underline{2p}^5 3d^{10}\underline{L}$ final states resulting from ligand-to-metal (O $2p \rightarrow$ Cu $3d$) charge transfer and the satellite at higher binding energy corresponds to a multiplet of $\underline{2p}^5 3d^9\underline{L}$ states, underbar denotes a hole and L denotes the oxygen ligand.[30-33]

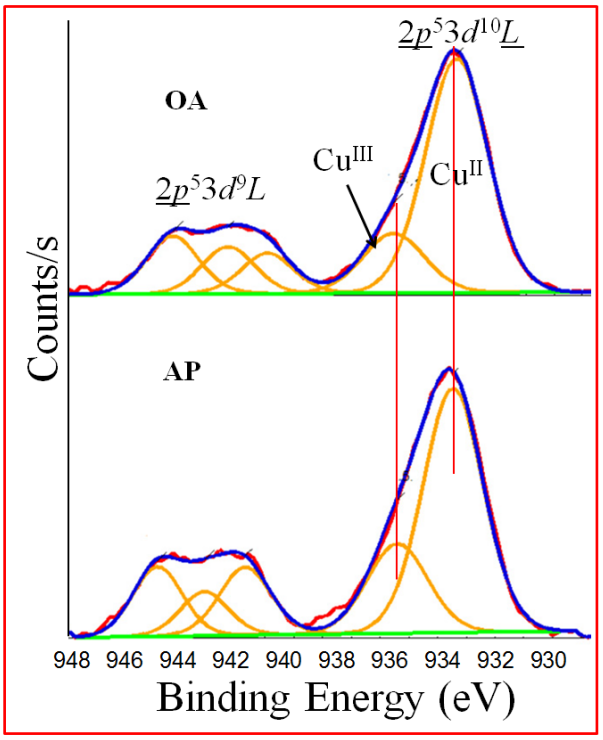

Figure 5.7. Core level XPS spectra of Cu 2p energy region for both the as prepared and oxygen annealed $Mo_{0.3}Cu_{0.7}Sr_2YCu_2O_y$ materials.

Quite interestingly, in parallel to the oxidation of the molybdenum species a reduction of the copper is observed on the XPS spectra of the Cu $2p$ core levels. As shown in figure 5.7, fitting of the XPS spectra of Cu 2p core level shows that the average oxidation state of copper in our superconducting sample (OA) is 2.20, which is within the usual superconducting range of copper (2.05–2.25).[34]

In materials of the same family, such as $RuSr_2RECu_2O_8$ (RE=rare earth cation) a self doping mechanism is usually considered. That is, partially reducing the cation in the charge reservoir layer (chain site) and oxidizing the copper in the superconducting plane (Cu2) give

a copper oxidation state within the usual superconducting range.[34], [35] In the case of the present molybdo-cuprates, after annealing under an oxygen atmosphere a different self-doping mechanism is suggested by the XPS measurements:

$$Mo^{V}_{x}Mo^{VI}_{(0.3-x)} + Cu^{III}_{y}Cu^{II}_{(2.7-y)} \leftrightarrow Mo^{V}_{(x-m)}Mo^{VI}_{(0.3-x+m)} + Cu^{III}_{(y-n)}Cu^{II}_{(2.7-y+n)}$$

Where $0 \leq (x-m) \leq 0.3$ and $0 \leq (y-n) \leq 2.7$

Table 5.2. Parameters of fitting for the Mo3d and Cu2p XPS core level spectra.

Sample name	Core level spectra	B.E (eV)	FWHM (eV)	Mo^{V}/Mo^{VI} Ratio
AP	Mo^{V} $3d_{5/2}$	232	1.28	0.89/0.11
	$3d_{3/2}$	235.1	1.39	
	Mo^{VI} $3d_{5/2}$	233.3	1.28	
	$3d_{3/2}$	236.4	1.39	
OA	Mo^{V} $3d_{5/2}$	232	1.26	0.80/0.20
	$3d_{3/2}$	235.1	1.38	
	Mo^{VI} $3d_{5/2}$	233.1	1.26	
	$3d_{3/2}$	236.2	1.38	
Sample name	Core level spectra	B.E (eV)	FWHM (eV)	Cu^{II}/Cu^{III} Ratio
AP	Cu^{II} $2p_{3/2}$	933.5	2.56	0.73/0.27
	Cu^{III} $2p_{3/2}$	935.4	2.56	
OA	Cu^{II} $2p_{3/2}$	933.5	2.73	0.80/0.20
	Cu^{III} $2p_{3/2}$	935.8	2.73	

It is apparent in figure 5.8a that the O 1s spectra exhibit two broad peaks. The O 1s spectra show two components: a main line at 529 eV is ascribed to O 2p–Cu 3d bonding, consistent with the studies of other cuprate superconductor[33] while the shoulder at about 530.9 eV is ascribed to O 2p–Mo 3d bonding.

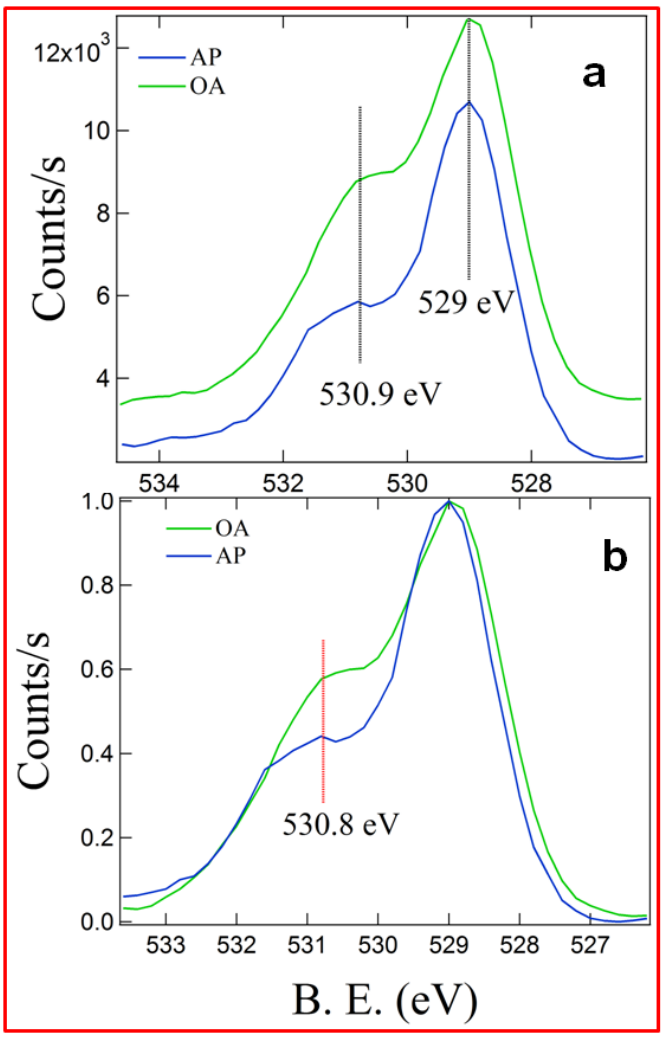

Figure 5.8. (a) Core level XPS spectra of O1s energy region for both the as prepared (AP) and oxygen annealed (OA) $Mo_{0.3}Cu_{0.7}Sr_2YCu_2O_y$ samples. (b) The data have been normalized to the area under the main peak at 529 eV. It shows that an oxidation is taking place during annealing under oxygen.

In figure 5.8b, the data have been normalized to the area under the main peak at 529 eV. It shows that the shoulder at 530.8 eV is increased after oxygen annealing, i,e, oxygen annealing introduces the extra oxygen into the layer, this enhances Mo^{VI} state and leads to a splitting of the O 1s line shapes related to the O 2p–Mo 3d bonding.

5.2b. $Mo_{0.3}Cu_{0.7}Sr_2RECu_2O_y$ (RE = Er and Tm)

5.2b.1. Experimental Details

Sample preparation: Polycrystalline samples of nominal composition $Mo_{0.3}Cu_{0.7}Sr_2RECu_2O_y$ (RE = Er and Tm) were synthesized by the standard solid state reaction method from the starting products Mo metal powder, RE_2O_3, $SrCO_3$ and CuO with purity above 99.9%. They were mixed, homogenized, pressed into pellets and pre-heated at 1023 K for 24 hours in air and then annealed at 1273 K for 48 hours with intermediate grindings. We denote these samples the as-prepared (AP or as-synthesized) one. In order to increase the oxygen content of the AP samples, these were oxygenated at ambient pressure as well as high pressure condition. A part of the AP samples were annealed under an oxygen flow at 873 K (48 hours) at ambient pressure followed by slow cooling (0.5 K/min) and named as OA. The AP $Mo_{0.3}Cu_{0.7}Sr_2ErCu_2O_y$ sample was oxygenated also at high pressure condition, which was carried out in a Belt Press type apparatus at 5 GPa and 773 K for 30 min in the presence of 33 mol % $KClO_3$. These conditions appear to be the optimal conditions[36] used for these types of samples and this sample is named as HPO.

Structural characterization: Powder samples were characterized by the X-ray powder diffraction (XRD) at room temperature performed in a PANalytical X'Pert PRO ALPHA1 diffractometer (Cu $K\alpha_1$-radiation, λ=1.5406 Å). Further Neutron powder diffraction (NPD) data allow us to determine, more precisely the extra oxygen position and oxygen occupancies. Long scan of NPD at room temperature (RT) and at lower temperature (1.5 K, 12 K and 50 K) were recorded for the AP and OA samples (~2 g) using the D2B diffractometer (Optimum wavelength, λ=1.59 Å) at the Institute Laue Langevin (ILL), France. For the HPO $Mo_{0.3}Cu_{0.7}Sr_2ErCu_2O_y$ the NPD data was recorded only at 1.5 K. The high resolution diffraction patterns were refined with the Rietveld procedure following the Fullprof suite program.[21]

Selected Area Electron diffraction patterns (SAED) and transmission electron microscope (TEM) images were obtained on a Jeol JEM 2000FX microscope. Sample cationic compositions were checked at the electron microscope by *in-situ* Energy Dispersive X-Ray Spectroscopy (EDS) analysis.

Physical properties: Direct current (dc) magnetization and alternating current (ac) susceptibility measurements were performed over the temperature range 2–300 K, using a Squid Quantum Design XL-MPMS magnetometer. Resistivity and thermo electric power

(TEP) measurements have been performed using a standard four-lead dc method in a He-cryostat.

X-ray photoelectron spectroscopy: The X-ray photoelectron spectroscopy (XPS) is carried out on a Thermo-VG Scientific ESCALAB 220 iXL spectrometer, equipped with a monochromatic Al K_α X-ray source (1486.6 eV). The details of the experiments are described in the experimental chapter (*chapter 3*)

5.2b.2. Results and discussion

5.2b.2.1. Structure, microstructure and oxygen content

Figure 5.9a and 5.9b show the NPD data for the as-prepared and oxygenated phases at 1.5 K for the $Mo_{0.3}Cu_{0.7}Sr_2ErCu_2O_y$ and $Mo_{0.3}Cu_{0.7}Sr_2TmCu_2O_y$ materials, respectively. The right side of both the figures (5.9a and 5.9b) compare a part of the 1.5 K NPD data for the as-prepared and oxygenated samples.

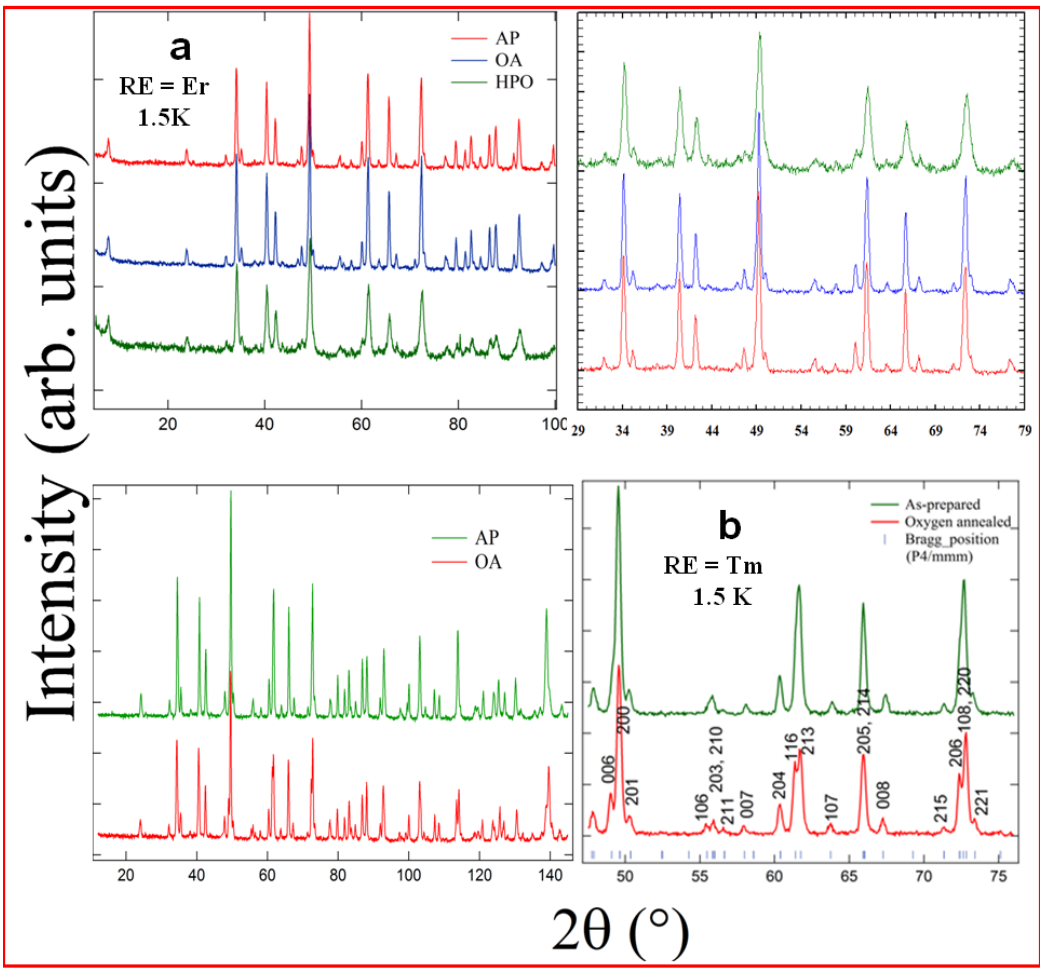

Figure 5.9. NPD patterns of (a) AP, OA and HPO $Mo_{0.3}Cu_{0.7}Sr_2ErCu_2O_y$ and (b) AP and OA $Mo_{0.3}Cu_{0.7}Sr_2TmCu_2O_y$ materials collected at 1.5 K. Right side of each figure compare a part of 1.5K NPD patterns of AP and oxygenated materials.

Neither significant changes nor any splitting is observed between the NPD patterns of AP and oxygenated (OA and HPO) samples for the $Mo_{0.3}Cu_{0.7}Sr_2ErCu_2O_y$ material. Nevertheless, splitting of the diffraction peaks is clearly observed for the OA $Mo_{0.3}Cu_{0.7}Sr_2TmCu_2O_y$ sample, shown in the right side of figure 5.9b. Figure 5.10a and 5.10b compare the room temperature (RT) and 1.5 K NPD data for the $Mo_{0.3}Cu_{0.7}Sr_2ErCu_2O_y$ samples and figure 5.11 shows the NPD patterns for the AP and OA $Mo_{0.3}Cu_{0.7}Sr_2TmCu_2O_y$ recorded at different temperatures.

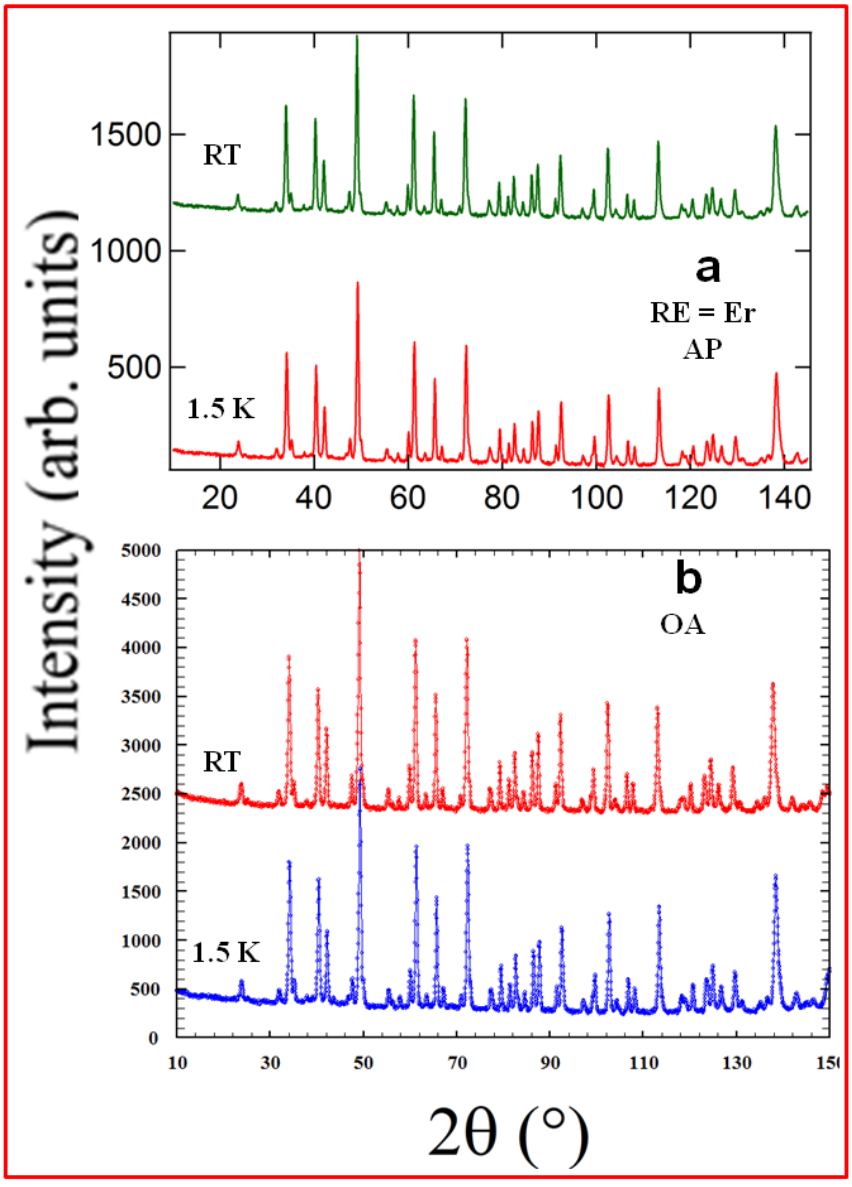

Figure 5.10. NPD patterns collected at 1.5 K and at RT are compared for the (a) AP $Mo_{0.3}Cu_{0.7}Sr_2ErCu_2O_y$ and (b) OA $Mo_{0.3}Cu_{0.7}Sr_2ErCu_2O_y$ material.

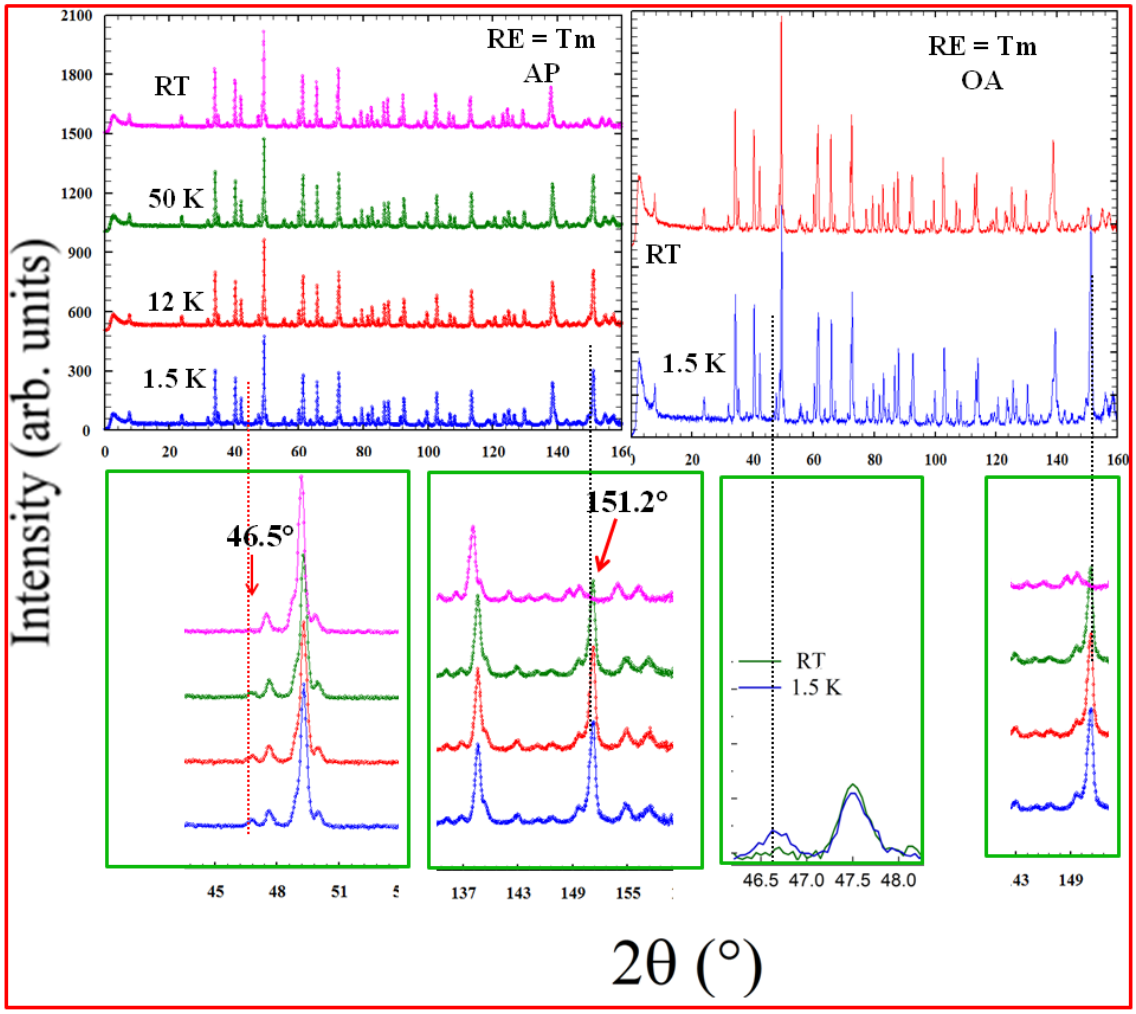

Figure 5.11. NPD patterns collected at different temperatures are compared for the AP $Mo_{0.3}Cu_{0.7}Sr_2TmCu_2O_y$ (1.5 K, 12 K, 50 K and RT, left side) and OA $Mo_{0.3}Cu_{0.7}Sr_2TmCu_2O_y$ (1.5 K and RT, right side) materials. Lower panels of the figure highlight the cryostat peak at 2θ = 46.5° and at 151.2° in all the low temperature NPD measurements.

The raw data do not show any impurity phases. The lower panels of the figure 5.11 highlight the appearance of extra peaks (at 2θ = 45.5° and 151.2°) in the low temperature NPD data due to the cryostat. However, no significant structural changes have been found between the 1.5 K and RT NPD preliminary refinements; in the rest of this paper, we will use the data for the 1.5 K NPD refinements for all the samples in order to minimize the long-thermal vibrations with increasing temperature. Furthermore, comparing with the RT NPD pattern, neither magnetic reflections nor a change in the intensities are observed in any of the low temperature diffraction patterns for both the materials. This situation clearly indicates that neither the Mo and Cu nor the Tm magnetic sub-lattices show long range magnetic ordering in the studied temperature range. We will see a correspondence between the absence of long range magnetic ordering and magnetic results in section 5.2b.2.3.

The structural analysis using the combination of XRD/NPD and ED for both the samples is as follows.

Strategy of the refinement: As a starting model, we used the atomic parameters taken from the recent study of $Mo_{0.25}Cu_{0.75}Sr_2YCu_2O_y$[36] material, in which the chemical substitution of the Mo ions for the Cu ions in $CuYSr_2Cu_2O_{7-\delta}$ structure is assumed to occur only in the chain site (Cu1). And the structure refinement of that material was based on the NPD patterns only. However, no reliable Cu/Mo populations can be established for the Cu1 and Cu2 sites from the neutron data alone. The lack of sensitivity results from the relative similarity in coherent neutron scattering lengths for Cu and Mo (0.772×10^{-12} and 0.695×10^{-12} cm, respectively). As neutron data are highly sensitive to oxygen-atom positions, occupancies and their thermal motions and XRD data provides greater sensitivity in determining the Mo and Cu population over the Cu1 and Cu2 sites, we have used a joint refinement using RT NPD and RT XRD patterns. In the refinement, Mo is allowed to share both copper sites. Finally, 1.5 K NPD data is refined using the results of joint RT refinement, without varying the Cu/Mo occupancies. A similar joint powder neutron/X-ray refinement on $Mo_{0.3}Cu_{0.7}Sr_2HoCu_2O_y$[25] provided significant information on Mo population over Cu1 and Cu2 sites, compared to neutron-only measurements on the same phase.

As-prepared materials: Figure 5.12 shows the final observed, calculated and difference profiles (Joint Rietveld refinement pattern) of the RT XRD patterns and RT neutron powder diffractions (NPD) for the AP $Mo_{0.3}Cu_{0.7}Sr_2ErCu_2O_y$ and $Mo_{0.3}Cu_{0.7}Sr_2TmCu_2O_y$ materials.

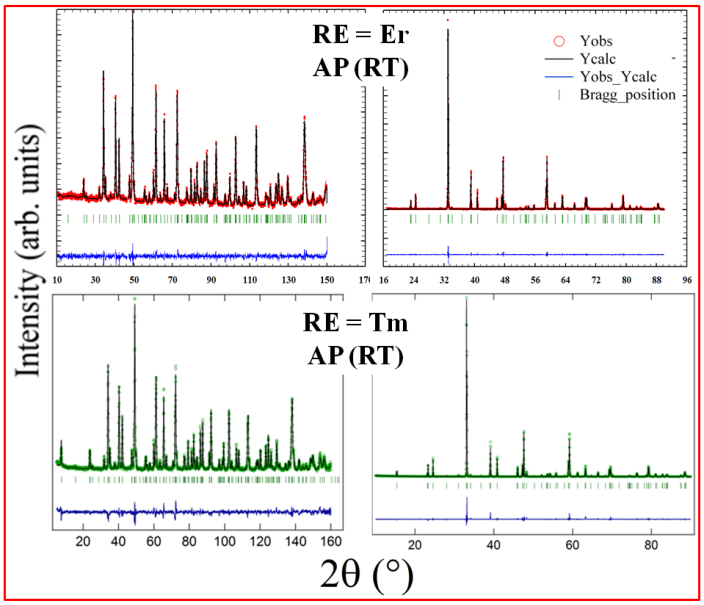

Figure 5.12. Final observed, calculated and difference profiles (Joint Rietveld refinement pattern) of the RT XRD patterns and RT neutron powder diffractions (NPD) for the AP $Mo_{0.3}Cu_{0.7}Sr_2ErCu_2O_y$ and $Mo_{0.3}Cu_{0.7}Sr_2TmCu_2O_y$ materials.

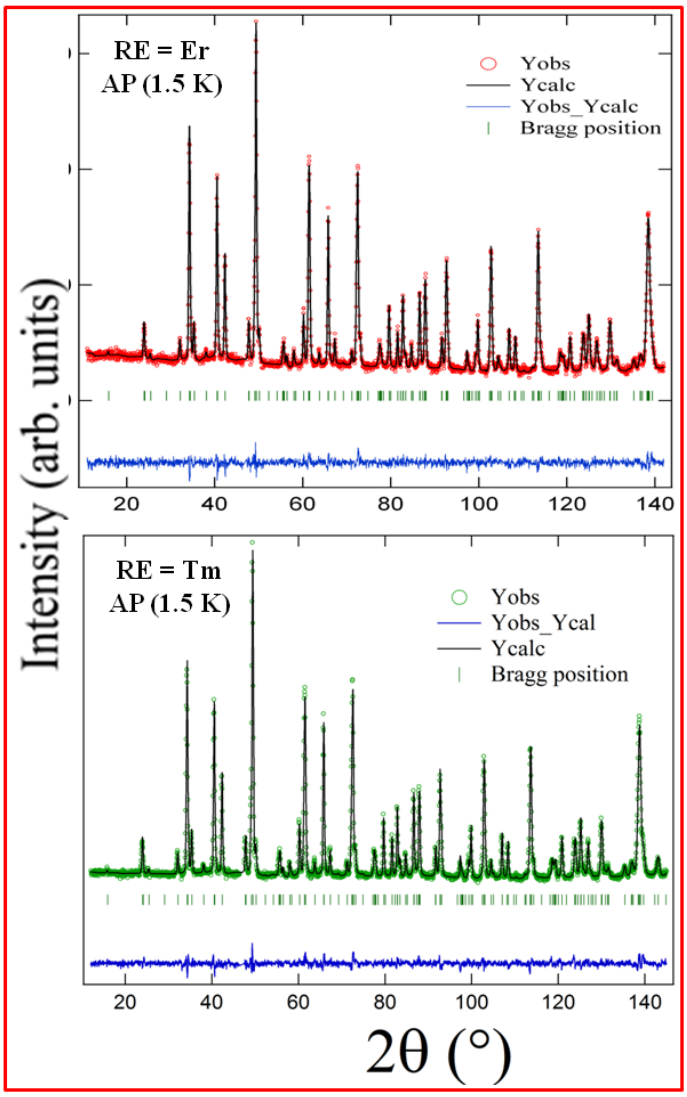

Figure 5.13. Best fitted Rietveld refinement patterns of neutron powder diffraction (NPD) collected at 1.5 K for the AP $Mo_{0.3}Cu_{0.7}Sr_2ErCu_2O_y$ (upper figure) and AP $Mo_{0.3}Cu_{0.7}Sr_2TmCu_2O_y$ (Lower figure) materials. 2θ = 46.5–47° is excluded in the refinement due to the appearance of a cryostat peak in 1.5 K NPD data.

The best fitted Rietveld refinement of NPD data at 1.5 K for both the as-prepared samples are shown in figure 5.13.The obtained structural parameters from the joint refinement are provided in the table 5.3. The refined structural parameters using 1.5 K NPD patterns are given in table 5.4. Some selected bond lengths and angles as suggested from the refinement of the 1.5 K NPD data are given in table 5.5.

Table 5.3. Refined structural Parameters and Agreement Factors (from RT NPD/RT XRD joint refinement) for the AP and OA samples of the $Mo_{0.3}Cu_{0.7}Sr_2RECu_2O_y$ (RE = Er and Tm) materials.

	RE = Er (AP)	RE = Er (OA)	RE = Tm (AP)	RE = Tm (OA)
a (Å)	3.8205 (1)	3.81288 (1)	3.8121 (1)	3.8034 (1)
c (Å)	11.5378 (1)	11.5227 (2)	11.5236 (1)	11.5387 (1)
V (Cell Volume, Å^3)	168.407 (2)	167.518 (2)	167.462 (3)	166.914 (2)
RE (0.5, 0.5, 0.5)				
Biso	0.68 (4)	0.81 (5)	0.25 (4)	0.45 (4)
Mo/Cu[Cu1,(0,0,0)]				
Occupancy	0.25 (2)/0.75 (2)	0.30/0.70	0.23 (2)/0.77 (2)	0.30/0.70
Biso	0.8 (1)	1.1 (1)	1.69 (6)	1.39 (4)
Mo/Cu[Cu2,(0,0,z)]				
z	0.3569 (2)	0.3540 (1)	0.3578 (2)	0.3569 (1)
Occupancy	0.07 (1)/0.93 (1)	0/1.00	0.05 (1)/0.95 (1)	0/1.00
Biso	0.32 (5)	0.48 (4)	0.1 (1)	0.30 (2)
Sr (0.5, 0.5, z)				
z	0.1968 (1)	0.1958 (1)	0.1965 (2)	0.1968 (1)
Biso	0.48 (2)	0.9 (1)	1.19 (5)	1.19 (4)
O1 (0.5, 0, z)				
z	0.3748 (2)	0.3734 (1)	0.3753 (2)	0.3755 (1)
Biso	0.37 (3)	0.62 (2)	0.55 (4)	0.61 (2)
O2 (x, y, z)				
x	0.041 (3)	0.037 (4)	0.040 (2)	0.035 (1)
y	0.041 (3)	0.037 (4)	0.040 (2)	0.035 (1)
z	0.1626 (2)	0.1607 (2)	0.1608 (2)	0.1594 (2)
Biso	0.7 (1)	0.52 (7)	0.5 (2)	0.41 (7)
O3 (x, y, 0)				
x	0.74 (1)	0.72 (1)	0.750 (7)	0.734 (3)
y	0.403 (3)	0.401 (2)	0.414 (6)	0.409 (3)
Biso	1.6 (1)	1.7 (2)	1.8 (2)	2.0 (2)
Occupancy	0.086 (4)	0.10 (1)	0.087 (5)	0.106 (3)
O4 (0.5, y, 0)				
y	0.10 (1)	0.11 (1)	0.112 (6)	0.107 (4)
Biso	1.6 (1)	1.7 (2)	1.8 (2)	2.0 (2)
Occupancy	0.163 (9)	0.161 (6)	0.166 (11)	0.150 (6)
Total oxygen content	7.34 (3)	7.44 (2)	7.36 (4)	7.45 (2)
R_P	7.33	6.60	5.22	4.23
R_{wp}	8.39	8.52	6.72	5.21
R_F	3.26	4.81	2.88	2.41
χ^2	3.82	4.71	3.33	2.24

Table 5.4. Refined structural Parameters and Agreement Factors (from 1.5 K NPD refinement) for the AP $Mo_{0.3}Cu_{0.7}Sr_2RECu_2O_y$ (RE = Er and Tm) materials.

	RE = Er (AP)	RE = Tm (AP)
a (Å)	3.8095 (1)	3.8061 (1)
c (Å)	11.4999 (1)	11.4943 (1)
V (Cell Volume, $Å^3$)	166.891 (2)	166.514 (2)
RE (0.5, 0.5, 0.5)		
Biso	0.3 (1)	0.44 (5)
Mo/Cu [Cu1, (0, 0, 0)]		
Occupancy	0.25/0.75	0.23/0.77
Biso	1.19 (3)	1.59 (6)
Mo/Cu [Cu2, (0, 0, z)]		
z	0.3577 (2)	0.3588 (1)
Occupancy	0.07/0.93	0.05/0.95
Biso	0.2 (1)	0.1 (1)
Sr (0.5, 0.5, z)		
z	0.1971 (2)	0.1972 (1)
Biso	0.67 (4)	0.93 (4)
O1 (0.5, 0, z)		
z	0.3752 (1)	0.3756 (1)
Biso	0.1 (1)	0.34 (4)
O2 (x, y, z)		
x	0.039 (2)	0.035 (2)
y	0.039 (2)	0.035 (2)
z	0.1618 (2)	0.1615 (2)
Biso	0.1 (1)	0.35 (9)
O3 (x, y, 0)		
x	0.726 (4)	0.734 (4)
y	0.402 (3)	0.413 (3)
Biso	0.7 (2)	1.7 (2)
Occupancy	0.093 (3)	0.094 (3)
O4 (0.5, y, 0)		
y	0.114 (4)	0.106 (5)
Biso	0.7 (2)	1.7 (2)
Occupancy	0.15 (1)	0.149 (6)
Total oxygen content	7.34 (2)	7.35 (3)
R_P	4.74	4.98
R_{wp}	5.87	6.28
R_F	2.26	2.10
χ^2	1.55	2.02

Table 5.5. Selected bond lengths (Å), angles (°) and the relevant distances (Å) for the AP $Mo_{0.3}Cu_{0.7}Sr_2RECu_2O_y$ (RE = ER and Tm) materials, as suggested by the 1.5 K NPD refinement.

Bond length and angle and relevant distances	RE = Er (AP)	RE = Tm (AP)
Cu1-O2	1.873 (2)	1.866 (2)
Cu1-O3	1.85 (1)	1.87 (1)
Cu1-O3	2.51 (1)	2.45 (1)
Cu1-O4	1.954 (5)	1.945 (4)
Cu2-O1	1.9153 (3)	1.9128 (2)
Cu2-O2	2.272 (4)	2.276 (3)
Tm-O1	2.3851 (1)	2.381 (1)
Sr-O1	2.797 (1)	2.797 (2)
$Sr\text{-}O2_{avg}$	2.727 (1)	2.725 (6)
Sr-O3	2.454 (2)	2.458 (6)
Sr-O4	2.702 (1)	2.718 (2)
O1-Cu2-O1 (angle)	168.267 (1)	168.45 (1)
Cu1-O2-Cu2 (angle)	168.21 (1)	169.367 (4)
Cu1-Cu2	4.114 (1)	4.124 (3)
d(intra)	3.272 (2)	3.245 (2)
d(inter)	8.2279 (2)	8.25 (1)
d(apical)	2.272 (4)	2.276 (3)
d(block)	3.746 (1)	3.732 (4)

Site occupancy refinement for both the as-prepared samples indicates that the chemical substitution of the Mo ions for the Cu ions occur in both Cu sites (Cu1 and Cu2). We have found that the majority of the Mo [0.25 (2), ~83% of the total Mo content and 0.23 (2), ~77% of the total Mo content for the samples with RE = Er and Tm, respectively] substitution in these samples occur for the copper in the chain sites (Cu1), which is in a good agreement with previous works.[20,25]

The apical oxygen atom O2 has been refined using a displacement from its initial position [from (0, 0, z) to (x, y, z) where x = y] to reduce the initially observed high thermal

factor (initial B_{iso} = 1.76 (6) for both samples). The oxygen atoms in the CuO_2 plane (O1) show a typical displacement (0.201 (1) Å and 0.193 (1) Å for the samples with RE = Er and Tm, respectively) towards the rare earth site. We have found full occupancies for O1 (occupancy = 1.00), O2 (occupancy = 0.25), Sr (occupancy = 1.00) and RE (occupancy = 1.00).

The $(Mo/Cu)O_{1+\delta}$ chain is situated between two Sr-O layers in the intermediate region of the structure (figure 5.14). The extra oxygen atoms in the chain layer have several possible site preferences. In analogy to the as-prepared $Mo_{0.25}Cu_{0.75}Sr_2YCu_2O_y$[36] compound, we have also found the best fit using two different chain oxygen positions O3 (x y 0) and O4 (0.5 y 0), to give a minimum thermal factor. These two positions are partially occupied. The crystal structure of the $Mo_{0.3}Cu_{0.7}Sr_2RECu_2O_y$ materials, which is similar to the $Mo_{0.25}Cu_{0.75}Sr_2YCu_2O_y$[36] compound, is shown in figure 5.14. The joint refinement using the RT NPD and RT XRD patterns for both materials (RE = Er and Tm) show nearly equal distributions of relative O3/O4 (~51%/49%) oxygen contents, indicating the random distribution of chain oxygen in both the O3 and O4 crystallographic sites. However, a redistribution of oxygen in the chain site has been observed at the low temperature (1.5 K) refinement.

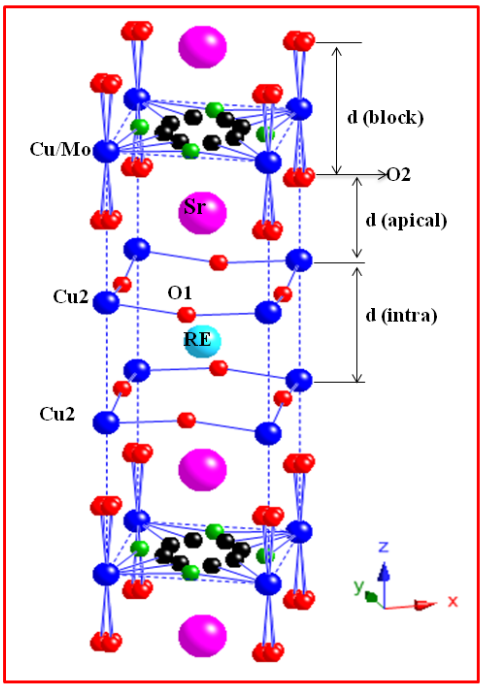

Figure 5.14. Crystal structure of the $Mo_{0.3}Cu_{0.7}Sr_2RECu_2O_y$ material (Tetragonal, *P4/mmm*) as suggested by NPD refinement. Blue spheres indicate Cu and Mo sites. Chain oxygens O3 (x, y, 0) and 4 (0.5, y, 0) are shown as black and green sphere, respectively. Remaining oxygen positions (O1, O2) are indicated by red spheres. The chain oxygen sites are partially occupied.

More oxygen is found to freeze around the O3 crystallographic sites in the 1.5 K NPD refinement for both cases. The relative O3/O4 oxygen contents have changed to ~ 55%/45% and 56%/44% at 1.5 K for the AP $Mo_{0.3}Cu_{0.7}Sr_2ErCu_2O_y$ and $Mo_{0.3}Cu_{0.7}Sr_2TmCu_2O_y$, respectively.

The total oxygen content obtained from the refined oxygen occupancy is y = 7.34 (3) and 7.35 (3) for the as-prepared $Mo_{0.3}Cu_{0.7}Sr_2ErCu_2O_y$ and $Mo_{0.3}Cu_{0.7}Sr_2TmCu_2O_y$ material, respectively.

Electron diffraction (ED) patterns of the AP $Mo_{0.3}Cu_{0.7}Sr_2ErCu_2O_y$ sample along [100]/ [001] has revealed a primitive tetragonal cell with a = b = 3.8 Å and c = 11.5Å (Figure 5.15).

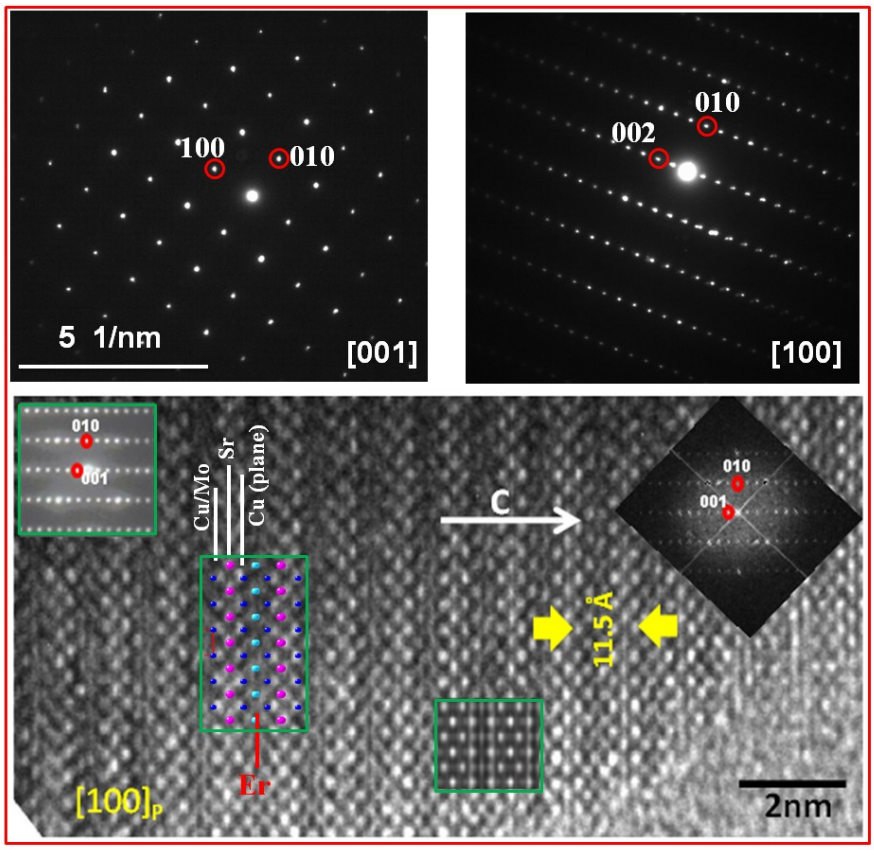

Figure 5.15. ED patterns (upper panels) along [001] and [100] directions and the TEM micrograph (lower panel) of the as-prepared $Mo_{0.3}Cu_{0.7}Sr_2ErCu_2O_y$ along $[100]_P$ with the simulated image over imposed. Inset of the lower panel shows the Fourier transform (FET) of the image that fitted the ED pattern. FET (top-right part of the lower panel) from the images that appears rather well with the corresponding ED pattern along [100] direction.

No superlattice spots were detected in the ED pattern which means that the materials are basically homogeneous without any extra ordering and there is no presence of twining domains as has been observed in other 1212 compounds [for instance Ir-1212, ref. 13, 14].

The microstructure of these compounds can then be interpreted as that of an ideal triple perovskite structure with a "simple" $a_p \times a_p \times 3a_p$ cell, which is also supported from the results found by the NPD/XRD refinements. The c/a value is almost 3 for this case. The HRTEM image (Figure 5.15) confirms that the layers are regularly stacked along the c direction according to the expected 1212 model. There is a good correlation between the calculated and the experimental image (see Figure 5.15).

Oxygen annealed materials: On the light of splitting, observed in the NPD pattern of the OA $Mo_{0.3}Cu_{0.7}Sr_2TmCu_2O_y$ material (Figure 5.9b); the sample is also analyzed by ED and TEM. Figure 5.16a and 5.16b show the electron diffraction patterns of the oxygen annealed $Mo_{0.3}Cu_{0.7}Sr_2TmCu_2O_y$ phase taken along the [001] and [010] zone axes. A mismatch between a (3.78 Å) and b (3.82 Å) parameter (for $YSr_2Cu_3O_{6.92}$[37] a = b = 3.7903 Å, c = 11.3992 Å) has been observed in the ED patterns of a few crystals, taken along the [001] direction. This indicates a slight orthorhombic distortion in the oxygen annealed $Mo_{0.3}Cu_{0.7}Sr_2TmCu_2O_y$ sample which is reminiscent of the behaviour of YBCO under similar annealing conditions.[38–43]

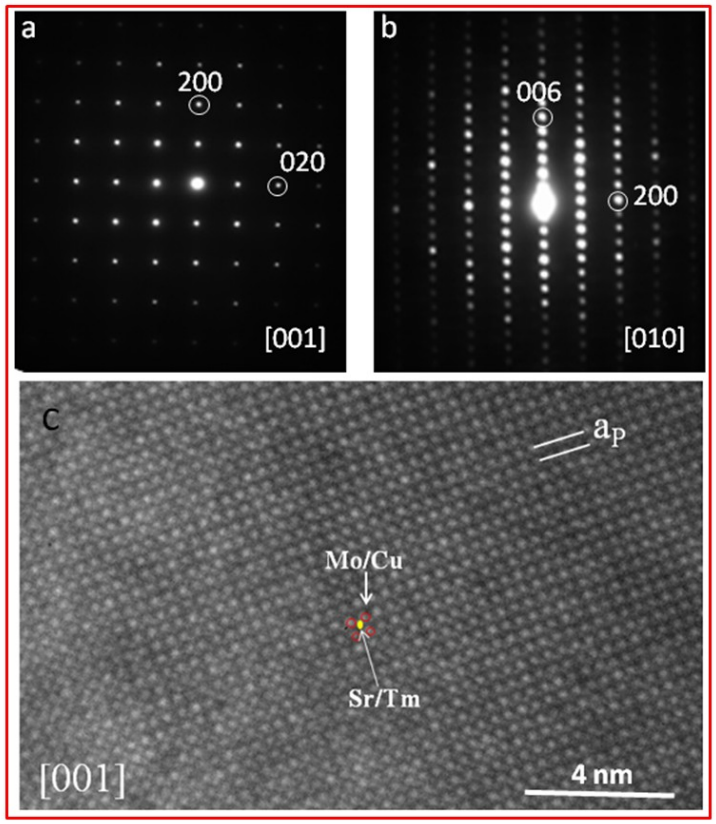

Figure 5.16. Electron diffraction patterns for the oxygen annealed $Mo_{0.3}Cu_{0.7}Sr_2TmCu_2O_y$ material recorded along (a) [001] and (b) [010] direction. (c) TEM micrograph of the same sample taken along $[001]_p$ direction.

Figure 5.16c shows the corresponding TEM image of the same sample taken along $[001]_P$ direction; good correlation [deviations [100×[a (NPD) – a (TEM)] / a (NPD)] for a and b parameters are 0.43% and 0.63% respectively] is observed with the expected structure. As discussed previously, splitting of the diffraction peaks is clearly observed for the $Mo_{0.3}Cu_{0.7}Sr_2TmCu_2O_y$ material after it has been annealed in flowing oxygen at 873 K for 48 hours and the appearance of double peaks (left panel in figure 5.9b) in some of (hkl) and (khl) reflections in the oxygen annealed sample clearly indicates a structural distortion. But these splitting are not related to the orthorhombic splitting. In fact no orthorhombic splitting has been observed in the any of the NPD patterns of the OA $Mo_{0.3}Cu_{0.7}Sr_2TmCu_2O_y$ sample. However, as we have observed the mismatch between a and b parameter in the ED pattern, we have refined the NPD of OA $Mo_{0.3}Cu_{0.7}Sr_2TmCu_2O_y$ material using both the tetragonal (P4/mmm) and orthorhombic (Pmmm) symmetries. Figure 5.17 compares the refined 1.5 K NPD pattern using both the symmetries. The refined parameters and agreement factors are compared in table 5.6. The orthorhombicity, defined as $\delta = (b-a)/(b+a)$,[42] found for this oxygen annealed sample is 1.32×10^{-4}, which is in fact lower than the resolution limit of D2B diffractometer (5×10^{-4}) and one order of magnitude lower than the orthorhombic YBCO ($\delta = 7.7\times10^{-3}$ (*ref 38*)).

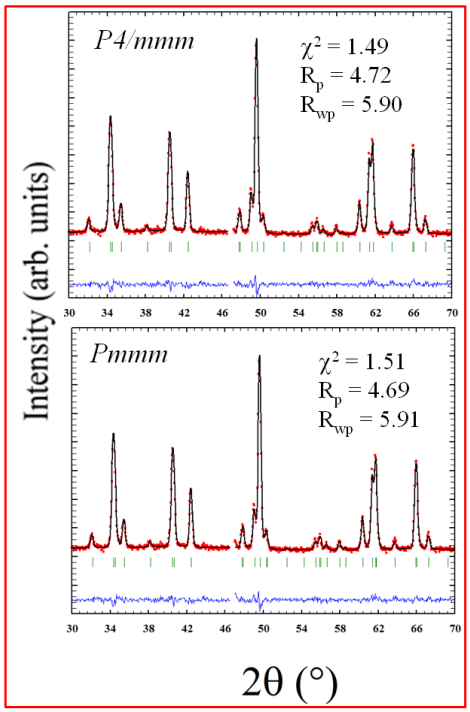

Figure 5.17. Best fitted Rietveld refinement patterns of neutron powder diffraction (NPD) collected at 1.5 K using the tetragonal *P4/mmm* and orthorhombic *Pmmm* space group are compared for the oxygen annealed $Mo_{0.3}Cu_{0.7}Sr_2TmCu_2O_y$.

Table 5.6. Refined structural Parameters and Agreement Factors of the NPD pattern collected at 1.5 K using the tetragonal *P4/mmm* and orthorhombic *Pmmm* space group are compared for the oxygen annealed $Mo_{0.3}Cu_{0.7}Sr_2TmCu_2O_y$.

	RE = Tm (OA) *P4/mmm*	RE = Tm (OA) *Pmmm*
a (Å)	3.79611 (1)	3.79555 (3)
b (Å)	3.79611 (1)	3.79655 (3)
c (Å)	11.5091 (1)	11.5090 (1)
V (Cell Volume, Å^3)	165.849 (2)	165.844 (3)
Tm (0.5, 0.5, 0.5)		
Biso	0.26 (4)	0.37 (8)
Mo/Cu [Cu1, (0, 0, 0)]		
Occupancy	0.30/0.70	0.30/0.70
Biso	1.10 (5)	1.1 (1)
Mo/Cu [Cu2, (0, 0, z)]		
z	0.3573 (1)	0.3573 (1)
Occupancy	0/1.00	0/1.00
Biso	0.27 (3)	0.56 (4)
Sr (0.5, 0.5, z)		
z	0.1969 (2)	0.1969 (1)
Biso	0.81 (4)	0.86(5)
O1 (0.5, 0, z)		
z	0.3755 (1)	0.3737 (9)
Biso	0.36 (2)	0.4 (1)
O1a (0.5, 0, z)		
z		0.3774 (9)
Biso		0.6 (1)
O2 (x, y, z)		
x	0.026 (1)	0.030 (1)
y	0.026 (1)	0.031 (1)
z	0.1615 (2)	0.1614 (2)
Biso	0.20 (5)	0.23 (8)
O3 (x, y, 0)		
x	0.715 (3)	0.718(3)
y	0.398 (3)	0.402 (2)
Biso	2.0 (2)	2.6 (2)
Occupancy	0.107 (3)	0.114 (4)
O4 (0.5, y, 0)		
y	0.119 (5)	0.114 (5)
Biso	2.0 (2)	2.6 (2)
Occupancy	0.147 (6)	0.138 (3)
Total oxygen content	7.44 (2)	7.46 (2)
R_P	4.72	4.69
R_{wp}	5.90	5.91
R_F	2.21	2.18
χ^2	1.49	1.51

The refined patterns and the agreement factors (χ^2, R_p, R_{wp}, R_F) show similar results in both cases. Yet, the isotropic temperature factors (B_{iso}), especially for the oxygen atoms show better results with the tetragonal (S.G. P4/mmm) symmetry. As a result, we choose to model this sample using the tetragonal P4/mmm symmetry, the same model used to refine the as-prepared material. Though the ED patterns of few crystals indicate a local orthorhombic distortion, NPD analyses suggest that the orthorhombic distortion is lost on average in this ($Mo_{0.3}Cu_{0.7}Sr_2TmCu_2O_y$) oxygen annealed sample.

The same strategy, like the as-prepared samples, is employed to refine the oxygen annealed samples. The obtained structural parameters from the joint refinement using the RT XRD/RT NPD for the OA $Mo_{0.3}Cu_{0.7}Sr_2RECu_2O_y$ (RE = Er and Tm) materials are compared in table 5.3 with the structural parameters of the AP $Mo_{0.3}Cu_{0.7}Sr_2RECu_2O_y$ (RE = Er and Tm) materials. However, the HPO $Mo_{0.3}Cu_{0.7}Sr_2ErCu_2O_y$ sample is refined using only the 1.5 K NPD data. Refined structural parameters and the agreement factors obtained from 1.5 K NPD refinements for the OA and HPO $Mo_{0.3}Cu_{0.7}Sr_2ErCu_2O_y$ samples and for the OA $Mo_{0.3}Cu_{0.7}Sr_2TmCu_2O_y$ sample are shown in table 5.7 and 5.8, respectively. The structural parameters of the AP sample are compared with the oxygenated materials in every case. And some selected bond lengths and angles, compared with the as-prepared samples, are shown in table 5.9 and 5.10 for the $Mo_{0.3}Cu_{0.7}Sr_2ErCu_2O_y$ and $Mo_{0.3}Cu_{0.7}Sr_2TmCu_2O_y$ materials, respectively. The splitting in the NPD pattern for OA $Mo_{0.3}Cu_{0.7}Sr_2TmCu_2O_y$ sample (Figure 5.9b) is observed due to the increased c/a ratio (c/a = 3.02 and 3.03 for the as-prepared and oxygen annealed sample, respectively, see table 5.8) after oxygen annealing. Figure 5.18 illustrates the joint refinement patterns using the RT XRD/RT NPD for the OA $Mo_{0.3}Cu_{0.7}Sr_2ErCu_2O_y$ and $Mo_{0.3}Cu_{0.7}Sr_2TmCu_2O_y$ samples. The 1.5 K NPD refinement patterns for the OA $Mo_{0.3}Cu_{0.7}Sr_2ErCu_2O_y$ and $Mo_{0.3}Cu_{0.7}Sr_2TmCu_2O_y$ samples are shown in figure 5.19. And the 1.5 K NPD refinement pattern for the HPO $Mo_{0.3}Cu_{0.7}Sr_2ErCu_2O_y$ sample is shown in figure 5.20.

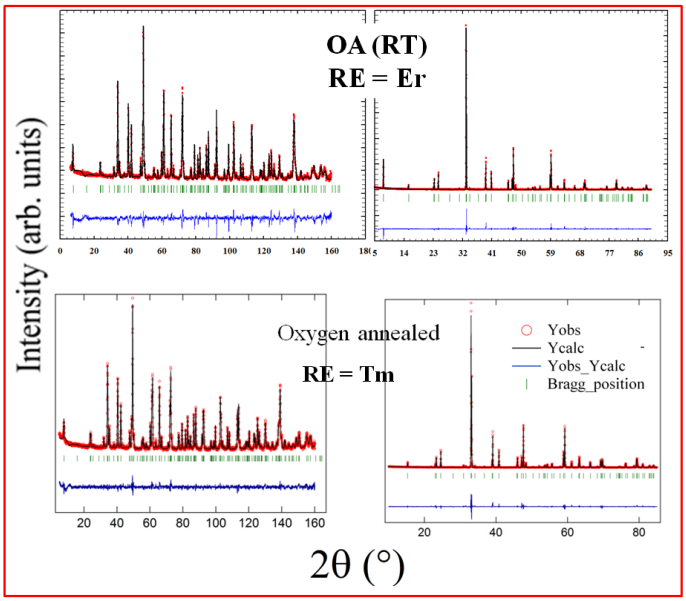

Figure 5.18. Final observed, calculated and difference profiles (Joint Rietveld refinement pattern) of the RT XRD patterns and RT neutron powder diffractions (NPD) for the OA $Mo_{0.3}Cu_{0.7}Sr_2ErCu_2O_y$ and $Mo_{0.3}Cu_{0.7}Sr_2TmCu_2O_y$ materials.

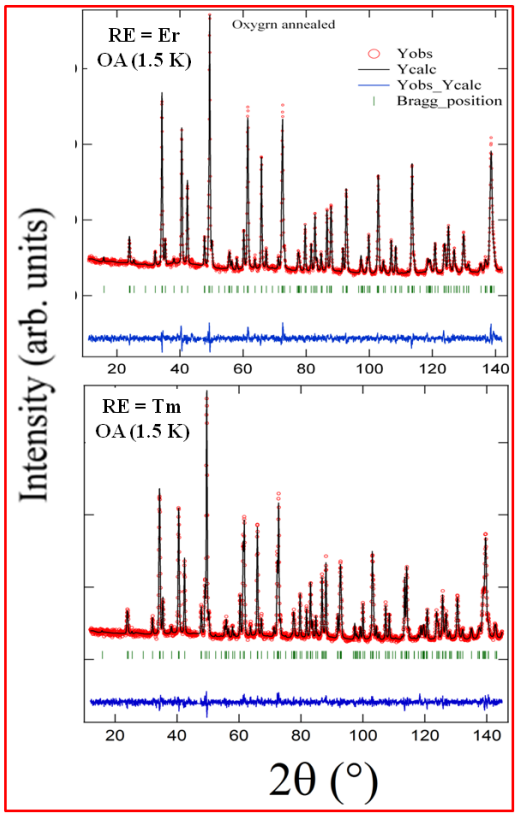

Figure 5.19. Best fitted Rietveld refinement patterns of the neutron powder diffraction (NPD) collected at 1.5 K for the OA $Mo_{0.3}Cu_{0.7}Sr_2ErCu_2O_y$ (upper figure) and OA $Mo_{0.3}Cu_{0.7}Sr_2TmCu_2O_y$ (Lower figure) materials. 2θ = 46.5–47° is excluded in the refinement due to the appearance of a cryostat peak in 1.5K NPD data.

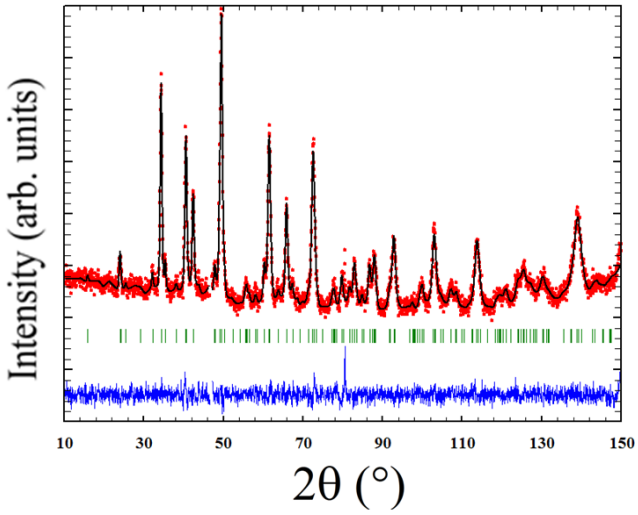

Figure 5.20. Best fitted Rietveld refinement patterns of the NPD pattern collected at 1.5 K for the HPO $Mo_{0.3}Cu_{0.7}Sr_2ErCu_2O_y$ material. 2θ = 46.5–47° is excluded in the refinement due to the appearance of a cryostat peak in 1.5K NPD data.

Table 5.7. Refined structural Parameters and Agreement Factors for the AP, OA and HPO $Mo_{0.3}Cu_{0.7}Sr_2ErCu_2O_y$, refined using the 1.5 K NPD patterns.

	AP	OA	HPO
a (Å)	3.8095 (1)	3.80815 (2)	3.8019 (5)
c (Å)	11.4999 (1)	11.4944 (1)	11.4887 (1)
c/a	3.02 (1)	3.02 (1)	3.02 (1)
V (Cell Volume, Å^3)	166.891 (2)	166.692 (3)	166.058 (4)
Er (0.5, 0.5, 0.5)			
Biso	0.3 (1)	0.39 (2)	0.49(2)
Mo1/Cu1 (0, 0, 0)			
Occupancy	0.25/0.75	0.30/0.70	0.30/0.70
Biso	1.19 (3)	1.32 (1)	0.98 (1)
Mo2/Cu2 (0, 0, z)			
z	0.3577 (2)	0.3580 (2)	0.3578 (2)
Occupancy	0.07/0.93	0.00/1.00	0.00/1.00
Biso	0.2 (1)	0.11 (5)	0.35 (4)
Sr (0.5, 0.5, z)			
z	0.1971 (2)	0.1963 (2)	0.1947 (2)
Biso	0.67 (4)	0.92 (3)	0.49 (2)
O1 (0.5, 0, z)			
z	0.3752 (1)	0.3750 (1)	0.3753 (3)
Biso	0.1 (1)	0.18 (2)	0.32 (1)
O2 (x, y, z)			
x=y	0.039 (2)	0.035 (2)	0.033 (2)
z	0.1618 (2)	0.1616 (2)	0.1617 (5)
Biso	0.1 (1)	0.15 (8)	0.36 (5)

O3 (x, y, 0)			
x	0.726 (4)	0.722 (4)	0.728 (7)
y	0.402 (3)	0.392 (3)	0.389 (5)
Occupancy	0.093 (3)	0.101 (3)	0.114 (3)
Biso	0.7 (2)	1.9 (1)	1.46 (6)
O4 (0.5, y, 0)			
y	0.114 (4)	0.118 (5)	0.10 (1)
Occupancy	0.15 (1)	0.16 (2)	0.16 (1)
Biso	0.7 (2)	1.9 (1)	1.46 (6)
Total oxygen content	7.34 (2)	7.45 (2)	7.55 (2)
R_P	4.74	4.20	2.78
R_{wp}	5.87	5.17	3.54
R_F	2.26	3.06	2.10
χ^2	1.55	1.96	1.46

Table 5.8. Refined structural Parameters and Agreement Factors for the AP and OA $Mo_{0.3}Cu_{0.7}Sr_2TmCu_2O_y$, refined using the 1.5 K NPD pattern.

	As-prepared (*P4/mmm*)	Oxygen annealed (*P4/mmm*)
a (Å)	3.8061 (1)	3.79611 (1)
c (Å)	11.4943 (1)	11.5091 (1)
c/a	3.019 (1)	3.032 (1)
V (Cell Volume, $Å^3$)	166.514 (2)	165.849 (2)
Tm (0.5, 0.5, 0.5)		
Biso	0.44 (5)	0.26 (4)
Mo/Cu [Cu1, (0, 0, 0)]		
Occupancy	0.23/0.77	0.30/0.70
Biso	1.59 (6)	1.10 (5)
Mo/Cu [Cu2, (0, 0, z)]		
z	0.3588 (1)	0.3573 (1)
Occupancy	0.05/0.95	0/1.00
Biso	0.1 (1)	0.27 (3)
Sr (0.5, 0.5, z)		
z	0.1972 (1)	0.1969 (2)
Biso	0.93 (4)	0.81 (4)
O1 (0.5, 0, z)		
z	0.3756 (1)	0.3755 (1)
Biso	0.34 (4)	0.36 (2)
O2 (x, y, z)		
x	0.035 (2)	0.026 (1)
y	0.035 (2)	0.026 (1)
z	0.1615 (2)	0.1615 (2)
Biso	0.35 (9)	0.20 (5)

O3 (x, y, 0)		
x	0.734 (4)	0.715 (3)
y	0.413 (3)	0.398 (3)
Biso	1.7 (2)	2.0 (2)
Occupancy	0.094 (3)	0.107 (3)
O4 (0.5, y, 0)		
y	0.106 (5)	0.119 (5)
Biso	1.7 (2)	2.0 (2)
Occupancy	0.149 (6)	0.147 (6)
Total oxygen content	7.35 (3)	7.44 (2)
R_P	4.98	4.72
R_{wp}	6.28	5.90
R_F	2.10	2.21
χ^2	2.02	1.49

Table 5.9. Selected bond lengths, angles and the relevant distances for the AP, OA and HPO samples of the $Mo_{0.3}Cu_{0.7}Sr_2ErCu_2O_y$ material obtained from 1.5 K NPD refinements.

Bond length and angle and relevant distances	AP	OA	HPO
(Cu1,Mo1)-O2	1.873 (2)	1.867 (2)	1.8653 (1)
(Cu1,Mo1)-O3	1.85 (1)	1.83 (1)	1.8057 (1)
(Cu1,Mo1)-O3	2.51 (1)	2.54 (1)	2.5209 (1)
(Cu1,Mo1)-O4	1.954 (5)	1.956 (4)	1.9325 (1)
Cu2-O1	1.9153 (3)	1.9141 (2)	1.912 (1)
Cu2-O2	2.272 (4)	2.264 (3)	2.255 (2)
Er-O1	2.3851 (1)	2.3852 (1)	2.3804 (1)
Sr-O1	2.797 (1)	2.801 (1)	2.8142 (1)
$Sr\text{-}O2_{avg}$	2.727 (1)	2.724 (1)	2.717 (1)
Sr-O3	2.454 (2)	2.444 (2)	2.4399 (1)
Sr-O4	2.702 (1)	2.684 (1)	2.7227 (2)
O1-Cu2-O1	168.267 (1)	168.225 (1)	167.84 (1)
Cu1-O2-Cu2	168.21 (1)	169.44 (1)	170.033 (1)
Cu1-Cu2	4.114 (1)	4.115 (1)	4.109 (1)
d(intra)	3.272 (2)	3.263 (1)	3.268 (1)

d(inter)	8.2279 (2)	8.2314 (1)	8.221 (1)
d(apical)	2.272 (4)	2.264 (3)	2.255 (2)
d(block)	3.746 (1)	3.734 (1)	3.731 (1)

Table 5.10. Selected bond lengths, angles and the relevant distances for the AP, and OA samples of the $Mo_{0.3}Cu_{0.7}Sr_2TmCu_2O_y$ material obtained from 1.5 K NPD refinements.

Bond length and angle and relevant distances	RE = Tm (AP)	RE = Tm (OA)
Cu1-O2	1.866 (2)	1.864 (2)
Cu1-O3	1.87 (1)	1.86 (1)
Cu1-O3	2.45 (1)	2.53 (1)
Cu1-O4	1.945 (4)	1.95 (1)
Cu2-O1	1.9128 (2)	1.9096 (3)
Cu2-O2	2.276 (3)	2.258 (3)
Tm-O1	2.381 (1)	2.378 (1)
Sr-O1	2.797 (2)	2.798 (2)
$Sr\text{-}O2_{avg}$	2.725 (6)	2.716 (1)
Sr-O3	2.458 (6)	2.440 (5)
Sr-O4	2.718 (2)	2.687 (1)
O1-Cu2-O1 (angle)	168.45 (1)	167.391 (1)
Cu1-O2-Cu2 (angle)	169.367 (4)	172.201 (1)
Cu1-Cu2	4.124 (3)	4.112 (2)
d(intra)	3.245 (2)	3.284 (2)
d(inter)	8.25 (1)	8.224 (1)
d(apical)	2.276 (3)	2.258 (3)
d(block)	3.732 (4)	3.728 (4)

The relative O3/O4 occupancy changes from 55%/45% in the AP sample to 57%/43% in OA material and to 60%/40% after the HP oxygenation (HPO) for the

$Mo_{0.3}Cu_{0.7}Sr_2ErCu_2O_y$ material. And the relative O3/O4 occupancy changes to 59%/41% (55%/45% in the AP sample) after oxygen annealing for the $Mo_{0.3}Cu_{0.7}Sr_2TmCu_2O_y$ material. The chain oxygen occupancy refinements then suggest that along the oxidation process oxygen within O3 and O4 crystallographic sites, although randomly distributed become more ordered at the mesoscopic scale. After the oxygenation, the extra oxygen prefers the O3 crystallographic site. The total oxygen contents obtained from the refined oxygen occupancies are y = 7.44 (2) and 7.45 (2) for the OA $Mo_{0.3}Cu_{0.7}Sr_2ErCu_2O_y$ and $Mo_{0.3}Cu_{0.7}Sr_2TmCu_2O_y$ material, respectively. And the total oxygen content is 7.55 (2) for the HPO $Mo_{0.3}Cu_{0.7}Sr_2ErCu_2O_y$ material.

The copper polyhedron is elongated along the apical direction (something usually attributed to a Jahn-Teller distortion), where the equatorial d_{Cu2-O1} distances (~1.91 Å for all the samples) are comparable to those observed in the common HTSC superconductors (1.88-1.97 Å).[34,35] On the other hand, the out of plane O1-Cu2-O1 buckling angle (Figure 5.21) becomes larger for the oxygen annealed material. A similar type of result was observed in $Mo_{0.25}Cu_{0.75}Sr_2YCu_2O_y$[36] compound after oxygen annealing and interpreted as an evidence for a direct competition between the electronic and nuclear structures of superconducting materials.

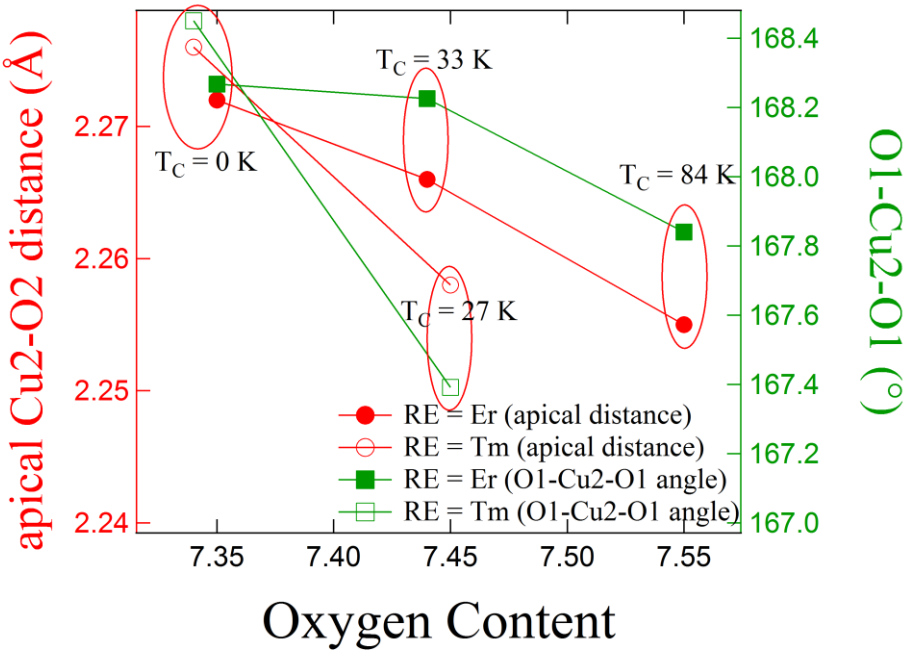

Figure 5.21. Variation of apical Cu2-O2 distances and O1-Cu2-O1 angles with the oxygen content for the $Mo_{0.3}Cu_{0.7}Sr_2RECu_2O_y$ (RE = Er and Tm) materials as obtained from 1.5 K NPD refinements. The superconducting transition temperatures (T_C) are also marked for different samples.

We have observed a contraction in the apical Cu2–O2 (Figure 5.21) bond length after oxygenation in all cases, contrary to the two-orbital model[44]. But the equatorial Cu2-O1 bond length remains unchanged. Similar kind of decreased apical oxygen distance has also been observed in the previously studied 1212-type molybdo-cuprate compounds after oxygen annealing.[18,36,45]

Interestingly, no trace of Mo substitution at the Cu2 site is observed in the Joint RT XRD/RT NPD refinement for both the oxygen annealed samples (occupancy becomes negative when Mo is allowed to share Cu2 site). This means that Mo diffusion to the copper chain site is taking place during the oxidation process. In figure 5.22, we have proposed a possible mechanism for the diffusion process. It seems that during the oxidation process, at 873 K, the Cu1-O2-Cu2 angle becomes greater due to the thermal vibration and that makes the apical oxygen away from the c axis. Under these circumstances Mo may diffuse due to the relatively easy opening of the "tunnel" to go from [Cu2/Mo2-O] layer to [Cu1/Mo1-O] plane.

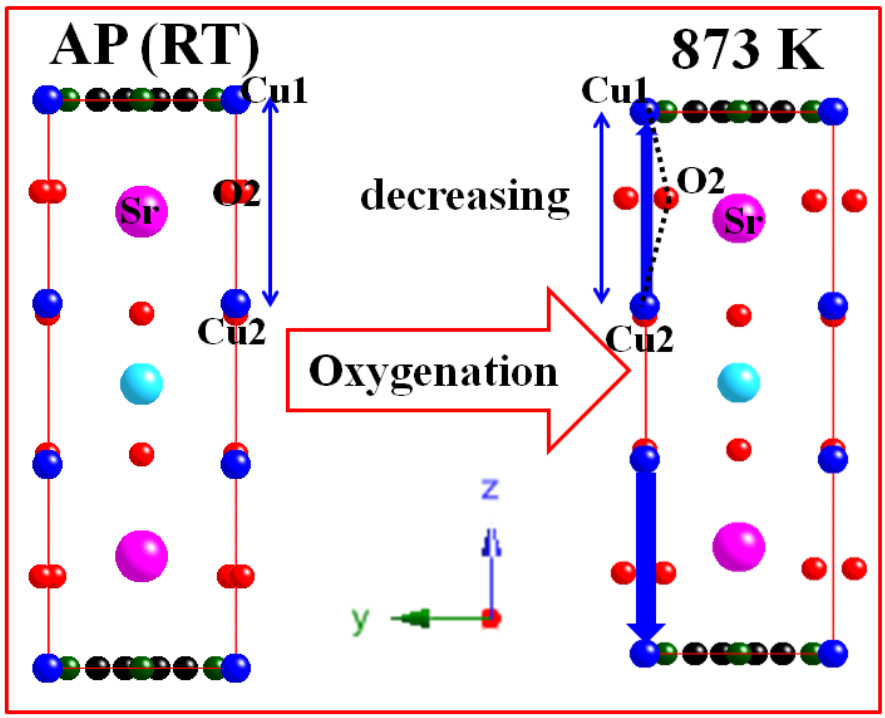

Figure 5.22. The possible mechanism of the Mo diffusion to the copper chain site during the oxidation process for the $Mo_{0.3}Cu_{0.7}Sr_2RECu_2O_y$ (RE = Er and Tm) materials.

5.2b.2.2. XPS measurements

Figure 5.23 compares the XPS spectra of the Mo 3d core levels for the AP, OA and HPO $Mo_{0.3}Cu_{0.7}Sr_2ErCu_2O_y$ samples. We have observed both peak broadening and peak shifting for the oxygenated samples comparing to the AP one. The details of the fitting

strategy are described in the previous section. Fitting of the XPS spectra of Mo 3d core levels allow us to confirm the large content of Mo^V. As one could expect, annealing under an oxygen atmosphere increases the amount of the Mo^{VI} state. This is indeed what happens and we have observed that the Mo^V/ Mo^{VI} is 0.76:0.24, 0.71:0.29 and 0.60:0.40 for the AP, OA and HPO samples respectively.

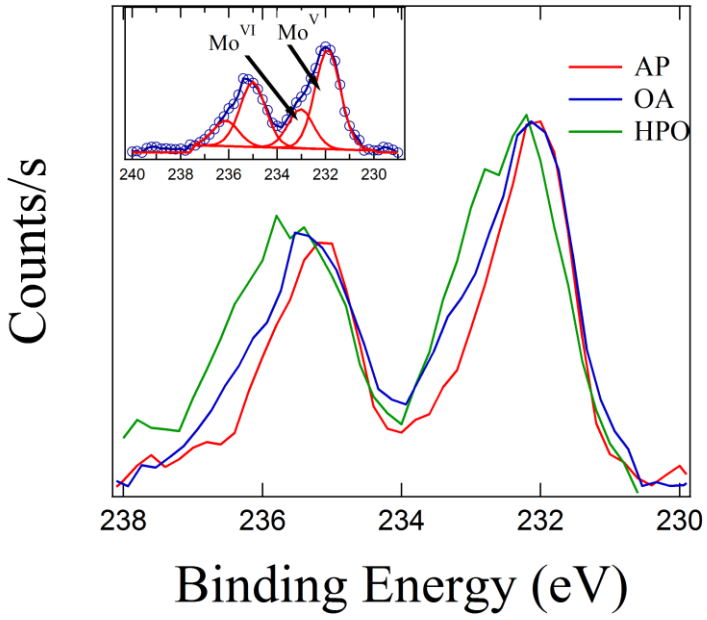

Figure 5.23. Core level XPS spectra of Mo 3d energy region for the AP, OA and HPO $Mo_{0.3}Cu_{0.7}Sr_2ErCu_2O_y$ material. Inset shows the fitted Mo 3d spectrum of the OA sample. It shows the co-existence of Mo^V and Mo^{VI}. The Mo^{VI} /Mo^V increases after oxygenation.

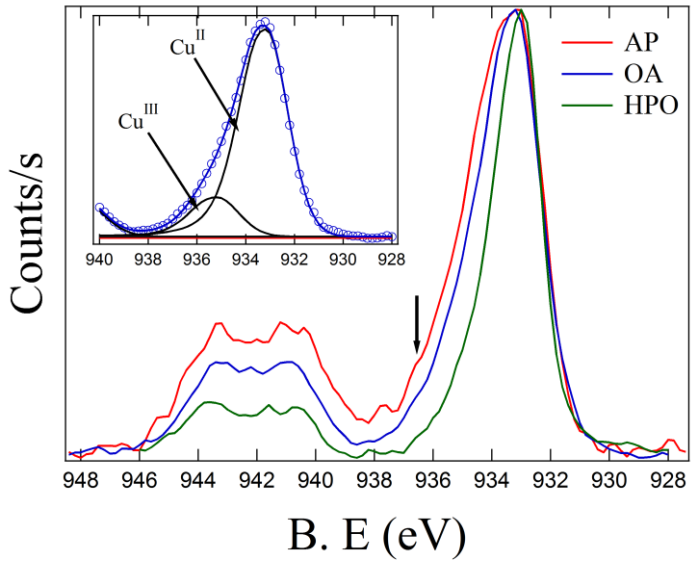

Figure 5.24. Core level XPS spectra of Cu2p energy region for the AP, OA and HPO $Mo_{0.3}Cu_{0.7}Sr_2ErCu_2O_y$ material. The data has been normalized under the $Cu2p_{3/2}$ main peak. A Cu^{III} characteristic shoulder is shown by an arrow. Inset shows the fitted Cu2p spectrum of the OA sample.

The Cu 2p core level spectra are shown in figure 5.24. Data has been normalized to the area under Cu $2p_{3/2}$ main line. The Cu $2p_{3/2}$ spectra for all the $Mo_{0.3}Cu_{0.7}Sr_2ErCu_2O_y$

samples are typical of Cu^{II} compounds. Quite interestingly, similar to the $Mo_{0.3}Cu_{0.7}Sr_2YCu_2O_y$ material, in parallel to the oxidation of the molybdenum species a reduction of the copper is observed on the XPS spectra of the Cu 2*p* core levels. As shown in figure 5.24, one could see a clear shoulder (shown by an arrow) and broadening of the Cu $2p_{3/2}$ main peak at higher binding energy side for the AP sample, which is characteristic feature of Cu^{III}.[46] The fitting parameters for the Mo 3d and Cu 2p core level spectra are presented in table 5.11. The self doping redox mechanism proposed earlier is also acting here according to the present XPS measurements:

$$Mo^{V}_{x}Mo^{VI}_{(0.3-x)} + Cu^{III}_{y}Cu^{II}_{(2.7-y)} \leftrightarrow Mo^{V}_{(x-m)}Mo^{VI}_{(0.3-x+m)} + Cu^{III}_{(y-n)}Cu^{II}_{(2.7-y+n)}$$

We will see in what follows a clear correspondence between the XPS and magnetic results and its relevance for the superconducting properties.

Table 5.11. Fitting parameters of the Mo 3d and Cu 2p core level XPS spectra for the AP, OA and HPO $Mo_{0.3}Cu_{0.7}Sr_2ErCu_2O_y$ material.

Sample name	Core level spectra	B.E (eV)	FWHM (eV)	Mo^{V}/Mo^{VI} Ratio
AP	Mo^{V} $3d_{5/2}$	232	1.08	0.76/0.24
	$3d_{3/2}$	235.1	1.12	
	Mo^{VI} $3d_{5/2}$	232.9	1.08	
	$3d_{3/2}$	236	1.12	
OA	Mo^{V} $3d_{5/2}$	231.9	1.28	0.71/0.29
	$3d_{3/2}$	235	1.30	
	Mo^{VI} $3d_{5/2}$	233	1.28	
	$3d_{3/2}$	236.1	1.30	
HPO	Mo^{V} $3d_{5/2}$	231.9	1.26	0.60/0.40
	$3d_{3/2}$	235	1.30	
	Mo^{VI} $3d_{5/2}$	233	1.26	
	$3d_{3/2}$	236.1	1.30	

Sample name	Core level spectra	B.E (eV)	FWHM (eV)	Cu^{II}/Cu^{III} Ratio
AP	Cu^{II} $2p_{3/2}$	933.1	2.00	0.80/0.20
	Cu^{III} $2p_{3/2}$	934.8	2.00	
OA	Cu^{II} $2p_{3/2}$	933.2	2.17	0.85/0.15
	Cu^{III} $2p_{3/2}$	935.2	2.17	
HPO	Cu^{II} $2p_{3/2}$	933.0	1.80	1.00/0.00
	Cu^{III} $2p_{3/2}$	–	-	

5.2b.2.3. Magnetism and superconductivity

***Physical Properties of the AP samples*:** Figure 5.25 shows the temperature dependence of the FC and ZFC susceptibility (χ) curves for the AP $Mo_{0.3}Cu_{0.7}Sr_2ErCu_2O_y$ (left side) and $Mo_{0.3}Cu_{0.7}Sr_2TmCu_2O_y$ (right side) materials, respectively.

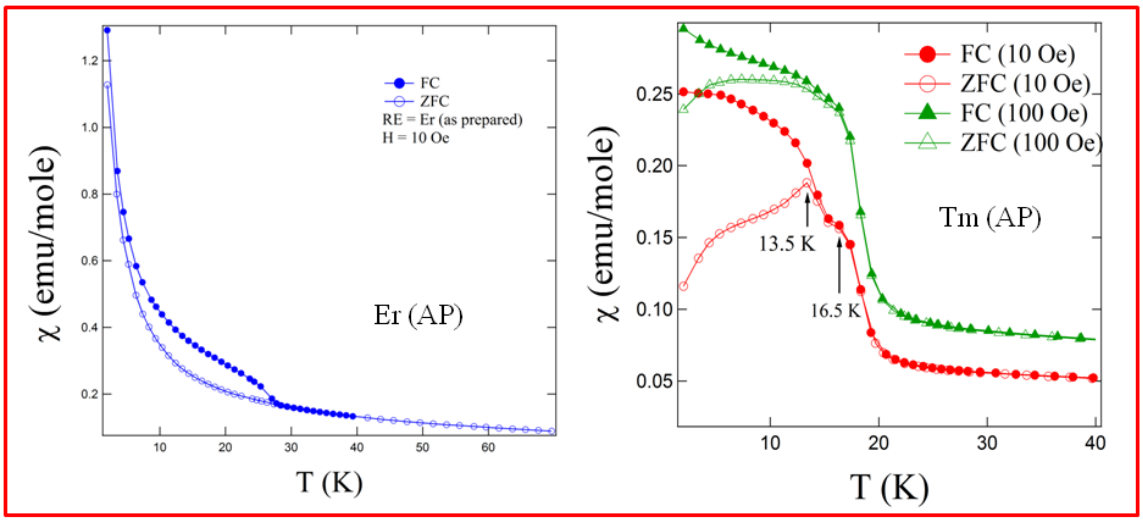

Figure 5.25. Zero field cooled (ZFC) and field cooled (FC) magnetic susceptibility as a function of temperature for the AP $Mo_{0.3}Cu_{0.7}Sr_2ErCu_2O_y$ (10 Oe, left side) and $Mo_{0.3}Cu_{0.7}Sr_2TmCu_2O_y$ (10 Oe and 100 Oe, right side) materials.

The Curie-Weiss [$\chi = C/(T-\theta)$, C = Curie constant, θ = Curie-Weiss temperature] fitting of the inverse of the FC magnetic susceptibility measured at 100 Oe, performed in the paramagnetic regime (figure 5.26, 250 K-300 K), leads to an effective paramagnetic moment P_{eff} = 9.53μ_B and 7.70μ_B, with $\theta = -17$ (1) K and -36.4 (0.2) K for the AP $Mo_{0.3}Cu_{0.7}Sr_2ErCu_2O_y$ and $Mo_{0.3}Cu_{0.7}Sr_2TmCu_2O_y$ samples, respectively. The observed paramagnetic moments are then a little higher than expected for Er^{III} (P_{eff} = 9.5 μ_B) and Tm^{III} (P_{eff} = 7.61 μ_B) ion because of the existence of other magnetic (Mo^{V} ($4d^1$, 1.73μ_B), Cu^{II} ($3d^9$, 1.83μ_B)) cations. By considering the ratio of Mo^{V} and Mo^{VI}, suggested by the XPS in the AP samples (that is 0.76/0.24 for AP $Mo_{0.3}Cu_{0.7}Sr_2ErCu_2O_y$ material), a better agreement is obtained between the experimental and calculated value of P_{eff} (9.54μ_B and 7.62μ_B for the AP $Mo_{0.3}Cu_{0.7}Sr_2ErCu_2O_y$ and $Mo_{0.3}Cu_{0.7}Sr_2TmCu_2O_y$ samples, respectively.

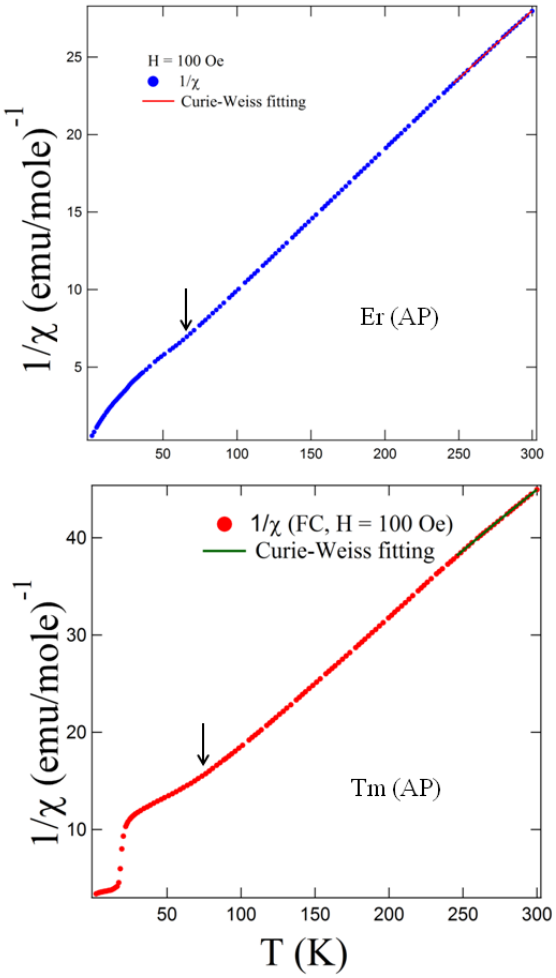

Figure 5.26. The temperature dependence of reciprocal FC susceptibility measured at 100 Oe along with Curie-Weiss fitting for the AP $Mo_{0.3}Cu_{0.7}Sr_2ErCu_2O_y$ (upper panel) and $Mo_{0.3}Cu_{0.7}Sr_2TmCu_2O_y$ (lower panel) materials. The starting of non linearity in the reciprocal FC susceptibility is indicated by an arrow.

The negative values of Curie-Weiss temperature indicate that the magnetic interactions should be of an anti-parallel nature. It is important to notice here on figure 5.26 that a short range magnetic ordering starts to occur at a temperature ~60K for the AP $Mo_{0.3}Cu_{0.7}Sr_2ErCu_2O_y$ compound. For the AP $Mo_{0.3}Cu_{0.7}Sr_2TmCu_2O_y$ compound the short range ordering starts at ~85 K, followed by a broad maximum (marked by an arrow in Figure 27) at 60 K. The beginning of the magnetic ordering for AP $Mo_{0.3}Cu_{0.7}Sr_2TmCu_2O_y$, can be observed from the local minimum, seen in the temperature dependence of the derivative of the FC susceptibility ($d\chi/dT$ vs T) measured at 100 Oe (inset in Figure 5.27).

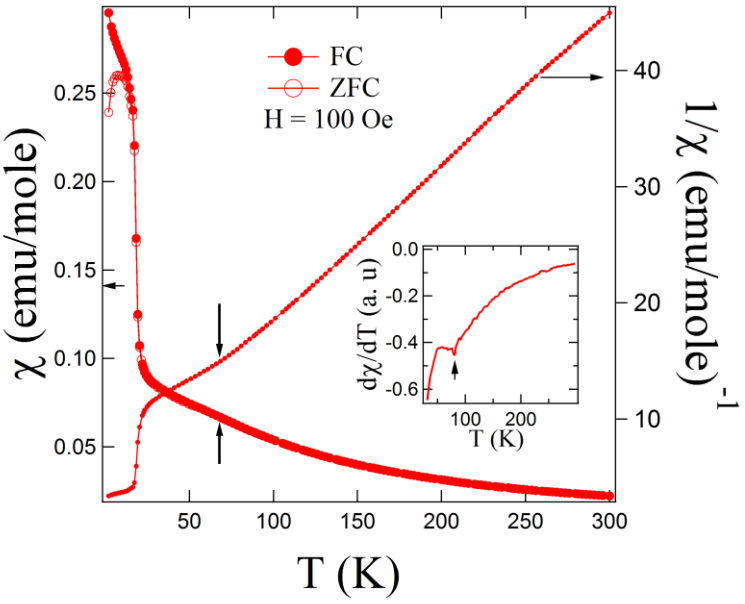

Figure 5.27. Temperature dependence of FC and ZFC magnetic susceptibility for the AP $Mo_{0.3}Cu_{0.7}Sr_2TmCu_2O_y$ sample measured at 100 Oe. The broad maximum is indicated by an arrow. Inset shows the ordering temperature at 85 K, indicated by the presence of a local minimum in the temperature dependence of derivative of the FC susceptibility ($d\chi/dT$ vs T) plot.

On further cooling, for the AP $Mo_{0.3}Cu_{0.7}Sr_2ErCu_2O_y$ material irreversibility between FC and ZFC is observed at 27 K (left panel of figure 5.25). Along with the irreversibility at 27 K, the high value of susceptibility at lower temperature indicates the presence of ferromagnetic interactions.

For the AP $Mo_{0.3}Cu_{0.7}Sr_2TmCu_2O_y$ sample, at ~ 20 K, a sharp rise in both the ZFC and FC susceptibility curve is observed. Figure 5.25 compares the low temperature region of the $\chi(T)$ behaviour measured at 10 Oe and 100 Oe for the AP $Mo_{0.3}Cu_{0.7}Sr_2TmCu_2O_y$ sample. A pronounced peak at 13.5 K is seen in the ZFC measurement ($\chi_{ZFC}(T)$) at 10 Oe. The presence of another peak at 16.5 K is also observed at low field measurement (figure 5.25)

but, at higher field, this peak is vanished. The amplitude of the magnetization is increased in higher field measurement. The cusp-like (peak) shape at 13.5 K and the strong irreversibility between the FC and ZFC magnetization below this temperature is suggestive of spin glass behavior[47] in the AP $Mo_{0.3}Cu_{0.7}Sr_2TmCu_2O_y$ compound. In order to get a deeper insight about the cusp like behaviour seen at 13.5 K for the Tm compound, we studied the temperature dependence of the ac susceptibility measured at different frequencies in an excitation field (ac field) of 2 Oe. Figure 5.28a and 5.28b show the temperature dependence of the real (χ') and imaginary (χ") parts of the ac susceptibility, respectively.

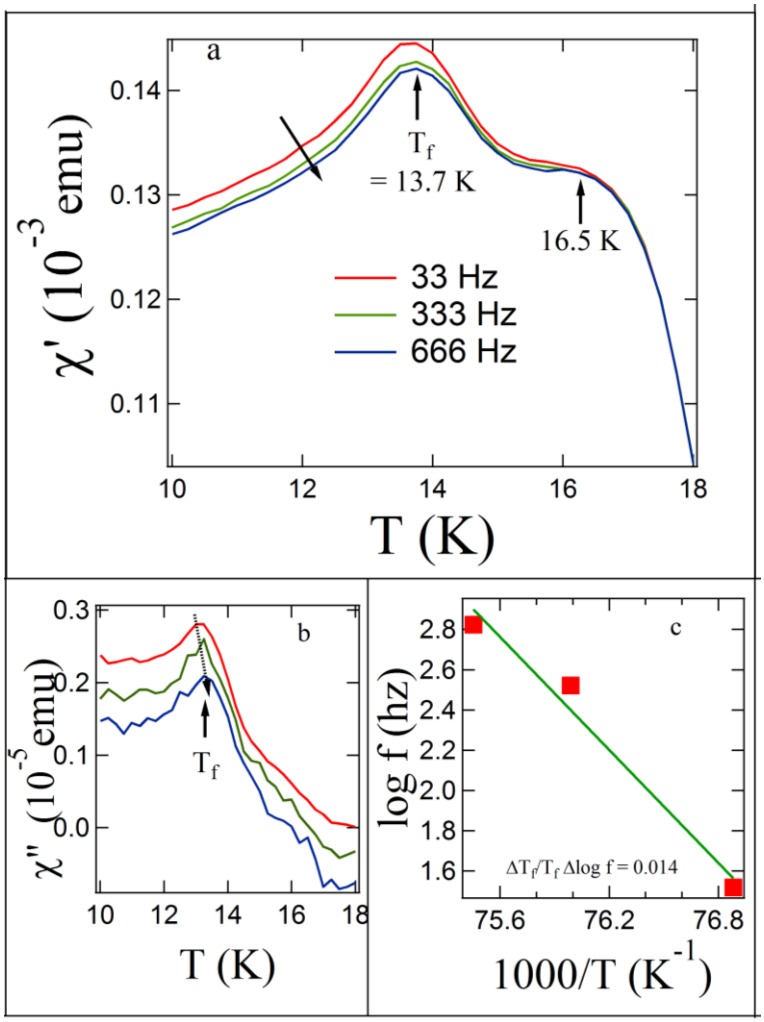

Figure 5.28. Temperature dependence of the (a) real (χ') and (b) imaginary (χ″) part of ac magnetic susceptibility measured at different frequencies for the AP $Mo_{0.3}Cu_{0.7}Sr_2TmCu_2O_y$ material. (c) Frequency dependence of the freezing temperature is plotted as log f vs 1000/T used to estimate the k value.

The real part of the ac susceptibility shows the existence of a peak at 13.7 K which is defined as the freezing temperature (T_f). This peak is slightly displaced to higher temperatures and decreases in intensity with the increasing frequency; this is better seen in the χ'' component. This is a typical feature of spin glass systems.[47-49] The maxima are not cusped, but rather rounded. It is also interesting to observe that the shoulder at 16.5 K also appears in the χ' (T) curve and is independent of the frequency within the probed range but does vanish in the χ'' component, which can be an indication of the absence of long range ordering (LRO); this is also supported by the NPD measurements. However, in the absence of NPD measurements at the freezing temperature (13.7 K) we can not rule the possibility of longer range ordering (or detectable short range ordering) at that temperature. A quantitative measurement of the frequency shift is usually estimated from the $k = \Delta T_f/T_f\Delta(\log_{10}f)$, where Δ refers to the difference in the corresponding quantity and f refers to the frequency. This k varies in the range of 0.004–0.018 for spin-glass systems.[47] Taking T_f as the temperature corresponding to the maxima from the imaginary part of the ac susceptibility, we have obtained a value of k = 0.014 from the fitting shown in figure 5.28c. Therefore, our data are consistent with the spin glass hypothesis.

Magnetization measurements as a function of magnetic field (M-H) at different fixed temperatures for the AP $Mo_{0.3}Cu_{0.7}Sr_2ErCu_2O_y$ compound is shown in figure 5.29. The M-H curves are typical isothermal magnetization curves for a soft-ferromagnetic material, having very low coercivity, below the Curie (transition) temperature.

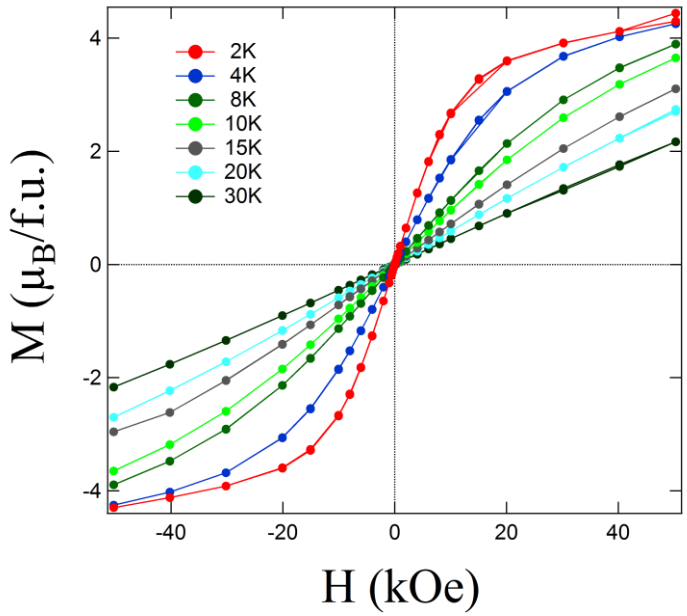

Figure 5.29. Change of magnetization as a function of magnetic field measured at different temperatures for the AP $Mo_{0.3}Cu_{0.7}Sr_2ErCu_2O_y$ sample.

Along with the high values of magnetization at lower temperature, the M-H measurements on the AP $Mo_{0.3}Cu_{0.7}Sr_2ErCu_2O_y$ material indeed indicate the existence of ferromagnetic (FM) correlation that is best reflected in the FC mode.

And for AP $Mo_{0.3}Cu_{0.7}Sr_2TmCu_2O_y$ material M-H show typical unsaturated AFM type hysteresis loops (Figure 5.30) at lower temperatures. It can also be seen that, at the low-field region, the magnetization becomes a nonlinear function of field and also displays a tiny hysteresis (inset in the figure 5.30). And this feature is also characteristic of spin-glass-like phases.[47,51]

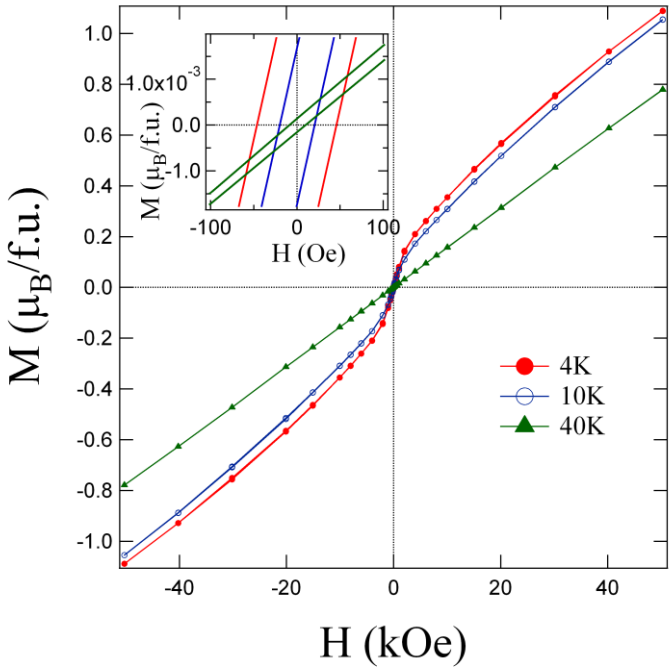

Figure 5.30. Change of magnetization as a function of magnetic field measured at different temperatures for the AP $Mo_{0.3}Cu_{0.7}Sr_2TmCu_2O_y$ material. Inset shows the hysteresis at different fixed temperatures.

However, as it was previously mentioned, there is no presence of long-range magnetic ordering in our studied low temperature NPD profiles. The XPS studies on the AP $Mo_{0.3}Cu_{0.7}Sr_2YCu_2O_y$ and $Mo_{0.3}Cu_{0.7}Sr_2ErCu_2O_y$ materials show the predominance of the paramagnetic Mo^{V} state over the Mo^{VI} one. Therefore, the origin of the ferromagnetic clusters and SG behaviour in the AP $Mo_{0.3}Cu_{0.7}Sr_2ErCu_2O_y$ and $Mo_{0.3}Cu_{0.7}Sr_2TmCu_2O_y$ samples can be understood from the presence of several magnetic and non-magnetic ions with different magnetic moments (Mo^{V}, Mo^{VI}, Cu^{II}, Cu^{III}, Er^{III} or Tm^{III}) and on their distribution in the different crystallographic sites as discussed previously, giving rise to frustration in the lattice. More explicitly, the charge reservoir layer [$(Mo/Cu)O_{1+\delta}$ chain]

contains a mixture of magnetic Mo^V and Cu^{II} ions diluted in a non-magnetic matrix of Mo^{VI} and Cu^{III} ions. Under these circumstances, the Mo^V–O–Mo^V/Cu^{II}–O–Cu^{II} layer gets fragmented into several short–range AFM ordered (as expected from super exchange interaction) parts due to the presence of randomly non-magnetic ions and this precludes the formation of an extended long-range and uniform magnetic ordering. Furthermore, due to the existence of different magnetic interactions (for instance the Mo^V–O–Mo^V super exchange interaction is an AFM interaction and the Mo^V–O–Cu^{II} super exchange interaction is FM), complex magnetic behaviour is expected. Beside the Mo^V–O–Mo^V and Mo^V–O–Cu^{II} magnetic interaction, other regions rich in Cu^{II}–O–Mo^{VI}–O–Cu^{II} pathways with a diamagnetic ion (Mo^{VI}) are also present. Usually, when the angle in this pathway is close to 180°, a weak AFM interaction is originated due to the longer range super-super-exchange interaction. However, in some perovskites[52,-54], when the interaction pathway is much lower than 180°, the super-super-exchange interaction can originate FM interaction, which is indeed not happening here. The existence and competition of FM and AFM interactions can be the origin of magnetic frustration in these systems. It can also be said that frustration in the 1212 compounds can also arise from the Cu-O_5 pyramids.[14,55]

Therefore, it can be proposed that, as a direct consequence of the cation disorder, the $Mo_{0.3}Cu_{0.7}Sr_2ErCu_2O_y$ AP-sample shows ferromagnetic clusters having ferromagnetic domains in a nonmagnetic matrix and it also shows a diffuse FM phase transition since there is no long-range ordering at lower temperature (1.5 K).

Similarly to the case of $IrSr_2(Sm/Eu)Cu_2O_8$ compounds[14] (or Ba_2PrRuO_6[56]), instead of the classical individual spin freezing, a cluster by cluster freezing model could explain the spin glass behaviour of the AP $Mo_{0.3}Cu_{0.7}Sr_2TmCu_2O_y$ sample. According to this model, the spin freezing occurs continuously as the lattice is cooled instead of an abrupt spin freezing at one well defined temperature.[57] Therefore; the spin clusters freeze in random directions that can be aligned by applying a large magnetic field without reaching a finite parallel long range ordering. In the light of our observations, the discussion may be summarized as follows; as the temperature is lowered from T_{CF} (cluster freezing temperature) ~85 K, magnetic ordering starts, followed by a broad maximum at 60 K. Then, at 20 K, the sharp rise in magnetic susceptibility indicates a transition to a weak AFM state. With further decreasing of the temperature, a peak at 16.5 K has been observed. Finally, it enters into a spin frustrated and frozen state at T_f = 13.5 K.

The resistivity (ρ vs T) behaviour for the AP $Mo_{0.3}Cu_{0.7}Sr_2ErCu_2O_y$ measured in the absence of a magnetic field is depicted in figure 5.31. For the AP $Mo_{0.3}Cu_{0.7}Sr_2ErCu_2O_y$ material one can see that the resistance clearly decreases as temperature increases: a semiconducting behaviour is apparent. Resistivity starts to increase at nearly the same temperature where we have found the magnetic irreversibility (27 K), indicating the greater electron localization at low temperature. We can then attribute this increase in resistivity to the forthcoming incipient magnetic interactions.

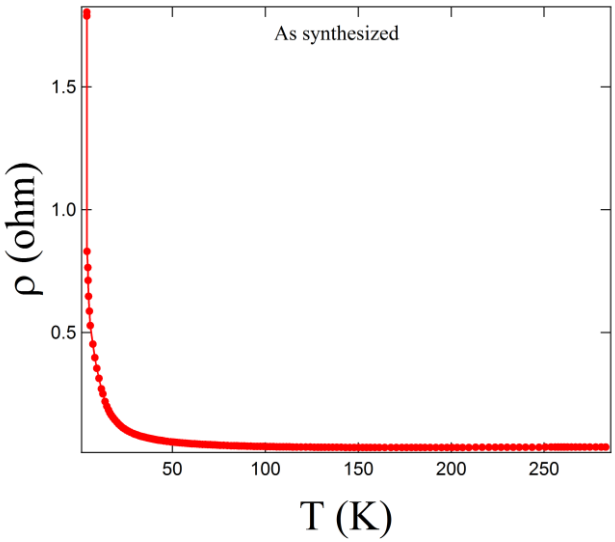

Figure 5.31. Temperature dependence of resistance for the AP $Mo_{0.3}Cu_{0.7}Sr_2ErCu_2O_y$ material.

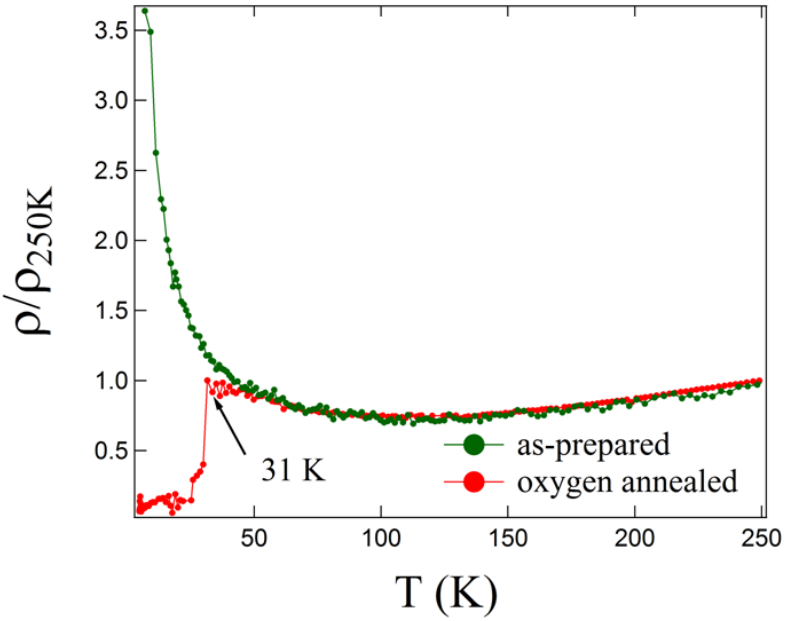

Figure 5.32. Variation of normalized resistivity as a function of temperature for the as-prepared and oxygen annealed $Mo_{0.3}Cu_{0.7}Sr_2TmCu_2O_y$ material. The onset of superconducting transition occurs at 31 K.

For the AP $Mo_{0.3}Cu_{0.7}Sr_2TmCu_2O_y$ material, resistivity (figure 5.32) behaviour shows that the compound is metallic down to 90 K and semiconducting below this temperature. This type of temperature dependence of the resistivity is commonly observed in under-doped cuprates.[58] On the other hand, X-ray photoelectron spectroscopy (at RT) studies on different oxygen annealed $Mo_{0.3}Cu_{0.7}Sr_2RECu_2O_y$ compounds (with RE = Y and Er) indicate that oxygen annealing reduces the average copper valence state by partially oxidizing the molybdenum. As the synthesis conditions and crystal structure of the $Mo_{0.3}Cu_{0.7}Sr_2TmCu_2O_y$ compound are similar to the $Mo_{0.3}Cu_{0.7}Sr_2RECu_2O_y$ compounds (with RE = Y and Er), one would expect the same mechanism. However, it is well known that thermoelectric power (TEP) measurement, S (T), is not only a faithful tool compared to a resistivity one to probe the transport phenomenon in samples with residual distortions arising, for instance, from defects, but can also be used to estimate the hole concentration in high T_C cuprates. Figure 5.33 shows the temperature dependence of the thermoelectric power (TEP), S(T), for both the materials.

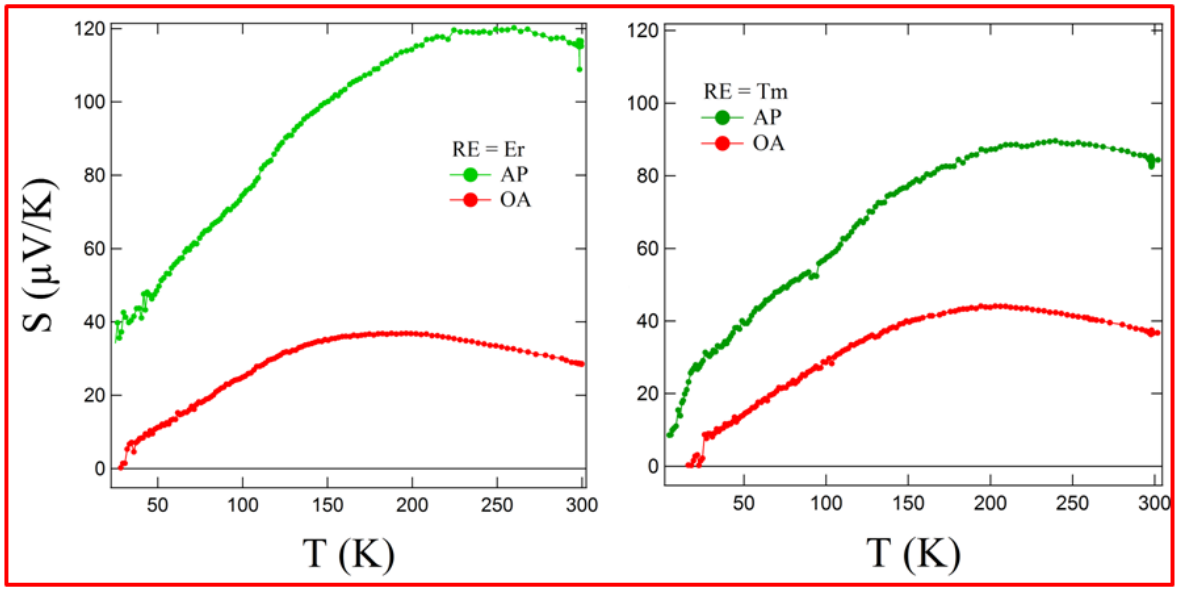

Figure 5.33. The temperature dependence of the thermo electric power (TEP, S) for the as-prepared and oxygen annealed $Mo_{0.3}Cu_{0.7}Sr_2ErCu_2O_y$ (left side) and $Mo_{0.3}Cu_{0.7}Sr_2TmCu_2O_y$ (right side) materials.

The magnitude and shape in both plots are typical for those observed in some other under-doped cuprates. It is found that oxygen annealing leads to a significant change in the room temperature TEP values (S (290K) = 117.5 μV/K and 29.55 μV/K for the AP and OA $Mo_{0.3}Cu_{0.7}Sr_2ErCu_2O_y$ material, respectively and 85 μV/K and 37 μV/K for as-prepared and oxygen annealed $Mo_{0.3}Cu_{0.7}Sr_2TmCu_2O_y$ material, respectively), suggesting that the hole

concentration is increased after oxygen annealing. The hole concentrations (P_h) for different samples can be estimated by universal relations[59] of S (290) with P_h in cuprates.

$$S\ (290\ K) = 372 \exp(-32.4\ P_h) \text{ for } 0.00 < P_h < 0.05,$$
$$S\ (290\ K) = 992 \exp(-38.1\ P_h) \text{ for } 0.05 < P_h < 0.155 \qquad (5.2)$$
$$S\ (290\ K) = -139\ P_h + 24.2 \text{ for } P_h > 0.155.$$

The calculated hole concentrations (P_h) are 0.035 and 0.092 for the AP and OA $Mo_{0.3}Cu_{0.7}Sr_2ErCu_2O_y$ samples, respectively and 0.064 and 0.086 for the as-prepared and oxygen annealed $Mo_{0.3}Cu_{0.7}Sr_2TmCu_2O_y$ samples, respectively. All these studies suggest that oxygen annealing is assisting the Mo to oxidize at the expense of the Cu reduction in the chain site and so the copper plane site is under-doped. In fact, X-ray photoelectron spectroscopy (at RT) studies on $Mo_{0.3}Cu_{0.7}Sr_2RECu_2O_y$ materials (RE = Y and Er, previous section and also *chapter 6*) have shown a reduced copper oxidation state on average (chain and plane) after oxygen annealing.

Superconductivity and structural correlations in the Oxygen annealed sample: The upper panel of the figure 5.34 shows the temperature dependence of the FC and ZFC susceptibility (χ) curves for the OA and HPO $Mo_{0.3}Cu_{0.7}Sr_2ErCu_2O_y$ samples measured at 10 Oe. Both the oxygenated $Mo_{0.3}Cu_{0.7}Sr_2ErCu_2O_y$ samples show superconducting behaviour.

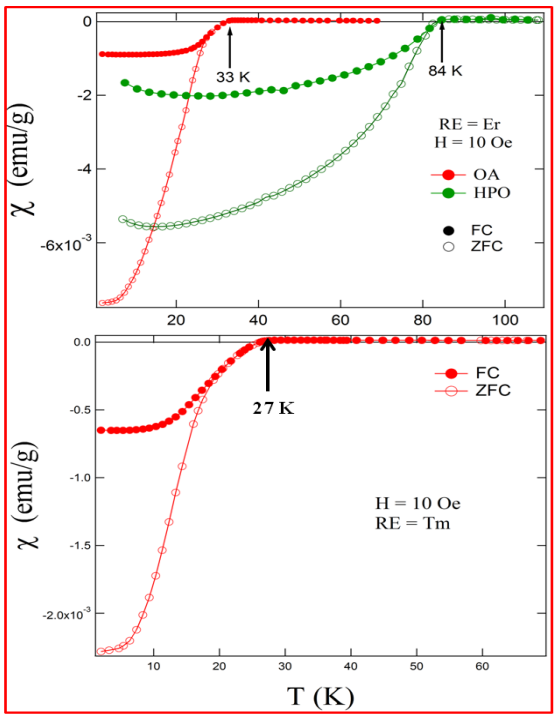

Figure 5.34. Temperature variation of dc-susceptibility for the oxygenated (OA and HPO) $Mo_{0.3}Cu_{0.7}Sr_2ErCu_2O_y$ (upper panel) and $Mo_{0.3}Cu_{0.7}Sr_2TmCu_2O_y$ (OA, lower panel) materials.

The highest transition temperature has been achieved for the high pressure oxygenated sample (HPO). The onset of the diamagnetic signal is seen at 33 K and 84 K for the OA and HPO $Mo_{0.3}Cu_{0.7}Sr_2ErCu_2O_y$ sample respectively. Earlier studies with (Mo, Cu)-1212[36,60-62] compounds, showed similar high T_C (for instance T_C = 87 K for $(Cu_{0.75}Mo_{0.25})Sr_2YCu_2O_{7+\delta}$)[36] when the samples were annealed under high oxygen pressure.

As shown in figure 5.32, the OA $Mo_{0.3}Cu_{0.7}Sr_2TmCu_2O_y$ sample shows superconducting transition at 31 K, which is indeed similar to the transition temperature observed in the magnetic susceptibility (Figure 5.34, T_C = 27K) and TEP (Figure 5.33, T_C = 28K) measurements. Above T_C, the normalized resistivity behaviour of this sample is identical to the behaviour of the as-prepared one.

The shielding fraction is given by the ZFC magnetic data and the Meissner fraction by the FC data. Taking the calculated densities, as suggested by the NPD refinements the calculated shielding fraction and the Meissner fraction are plotted with temperature and shown in figure 5.35 for all the superconducting samples. Though the HPO $Mo_{0.3}Cu_{0.7}Sr_2ErCu_2O_y$ material shows the highest T_C, OA $Mo_{0.3}Cu_{0.7}Sr_2ErCu_2O_y$ material shows highest shielding fraction (65%) at 2 K. But the Meissner fraction is found to be highest for the HPO $Mo_{0.3}Cu_{0.7}Sr_2ErCu_2O_y$ material (11.2% at 4 K).

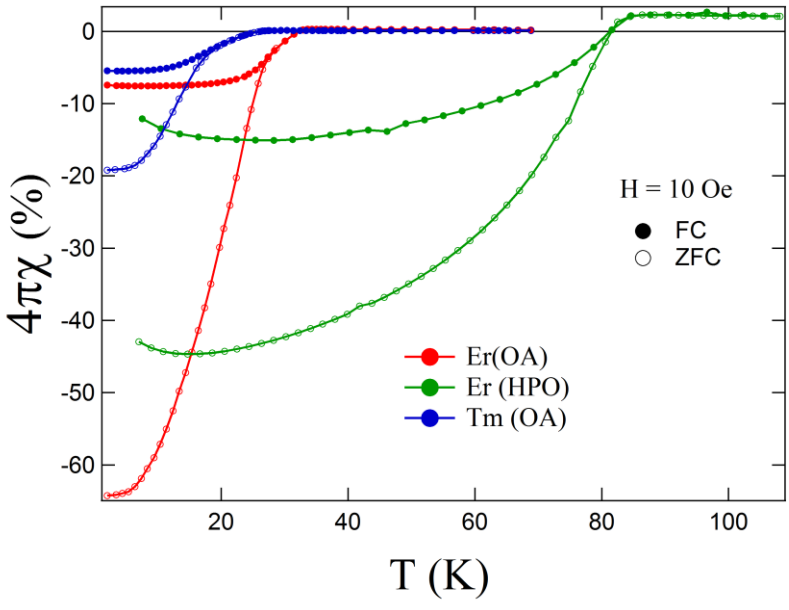

Figure 5.35. Temperature dependence of dc-susceptibility for different oxygen annealed samples, measured at 10 Oe. The figure highlights the shielding fraction is and the Meissner fraction. The susceptibility is normalized to the unit of volume (Volume susceptibility) and multiplied by 100×4π to facilitate the comparison with the expected value of -100 (%) for the ideal superconductor with the demagnetization factor of N = 0.

AC-susceptibility measurements as a function of temperature, measured upon warming the sample from ZFC state at various ac magnetic fields in the absence of dc magnetic field at frequency 200Hz for both the OA samples are shown in Figure 5.36.

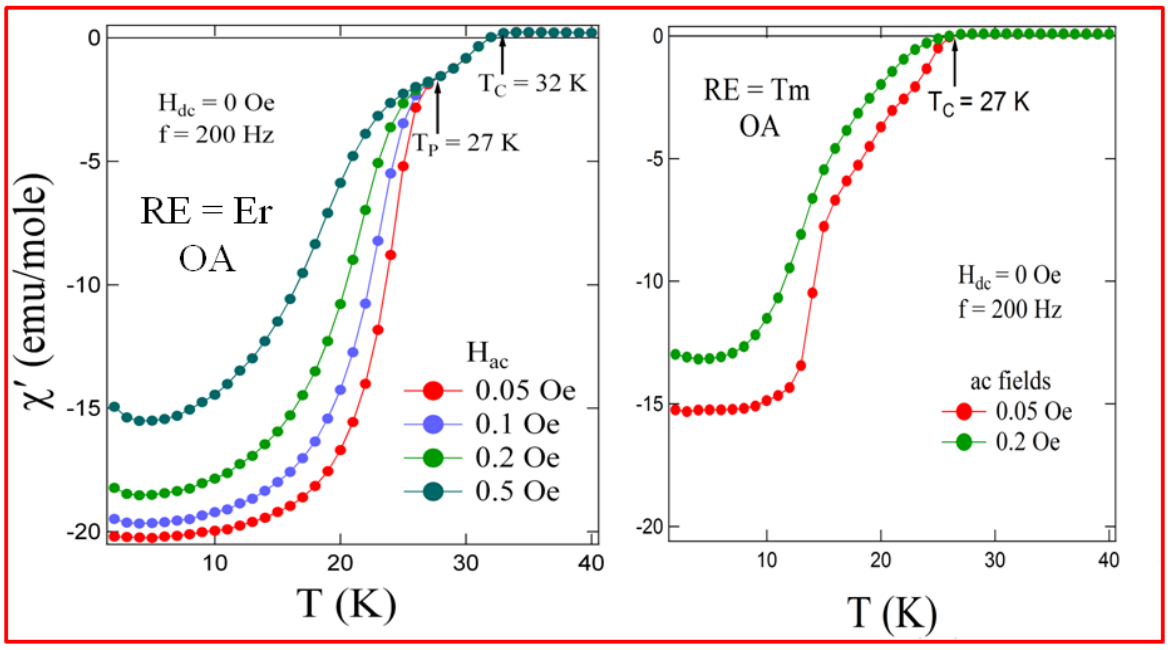

Figure 5.36. Temperature dependence of normalized real ac-susceptibility for the OA $Mo_{0.3}Cu_{0.7}Sr_2ErCu_2O_y$ and $Mo_{0.3}Cu_{0.7}Sr_2TmCu_2O_y$ materials measured in absence of dc magnetic field at various ac fields.

It is found that an ac field of 0.05 Oe is large enough to separate the higher T_C-intragrain and lower T_C-intergrain superconductivity for the OA $Mo_{0.3}Cu_{0.7}Sr_2ErCu_2O_y$ sample. It is clear that two superconducting transitions occur here. The first transition temperature (T_C = 32 K), at which the grains become superconducting, is not affected by H_{ac}; otherwise, at T_P = 27 K, ac susceptibilities are affected by ac field: this is the expected behaviour in a system consist of superconducting clusters linked by Josephson coupling. On the other hand, no such behaviour is observed for the OA $Mo_{0.3}Cu_{0.7}Sr_2TmCu_2O_y$ sample. AC-susceptibility measurements as a function of temperature at different dc magnetic fields for the OA $Mo_{0.3}Cu_{0.7}Sr_2TmCu_2O_y$ sample are shown in figure 5.37. AC- susceptibility is measured upon warming the sample in the presence of different dc fields at 200 Hz. It shows a clear decrease of the superconducting transition temperature with an increasing dc-magnetic field.

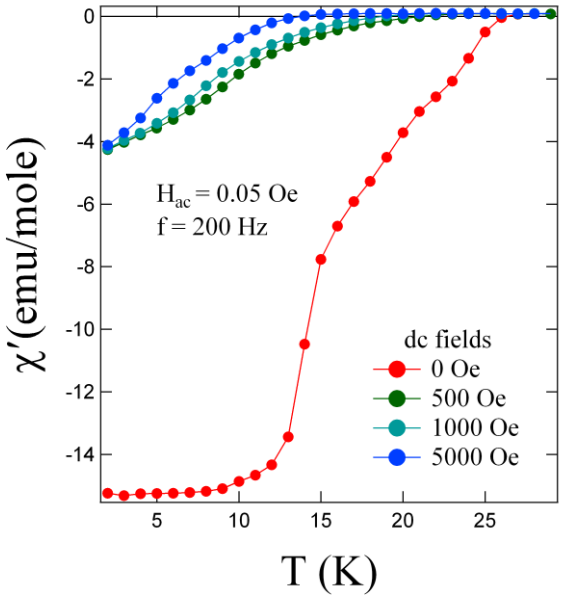

Figure 5.37. Temperature dependence of the real part of ac-susceptibility for the oxygen annealed $Mo_{0.3}Cu_{0.7}Sr_2TmCu_2O_y$ sample measured with various dc fields.

Our structural (NPD pattern refinement) results do offer an explanation of superconductivity for the oxygen annealed samples. In the refinement, it is found that oxygen content increases after annealing under oxygen (Table 5.7 and 5.8). In order to understand the structural details and their effect on superconductivity, we propose a short range ordering model (figure 5.38) for the $(Mo/Cu)O_{1+\delta}$ chain before and after oxygen annealing.

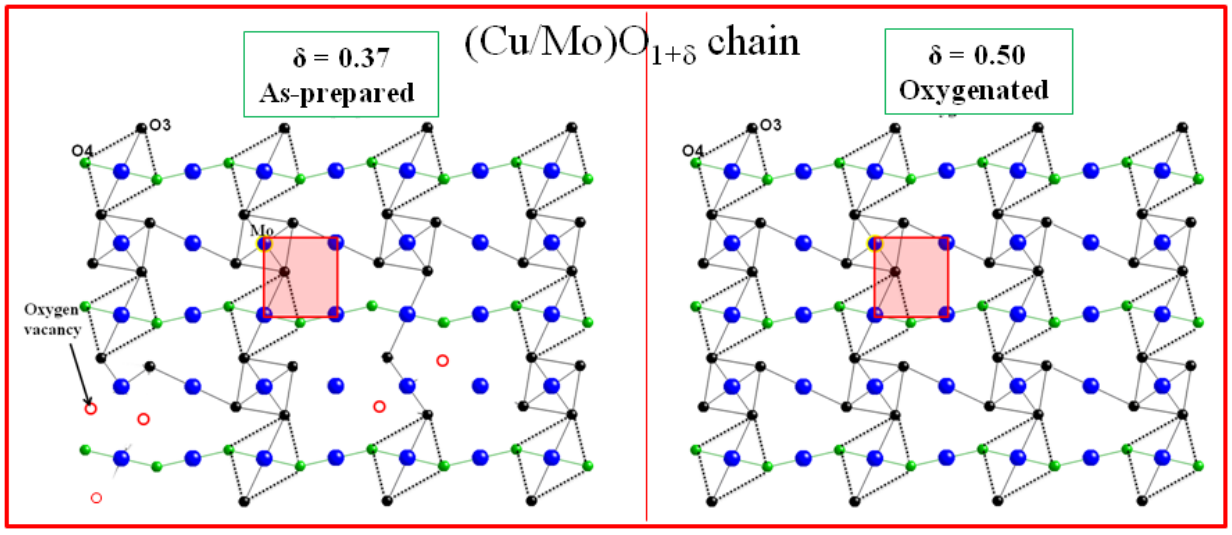

Figure 5.38. View along the (001) direction for the short-range ordered $(Cu1/Mo)O_{1+\delta}$ chain before and after oxygenation. Enhancement of oxygen after oxygen annealing makes the disordered (as-prepared) chain to order at mesoscopic range. The unit cell is indicated by a red square.

For the as-prepared samples the nearly equal distribution of chain oxygens indicates the existence of oxygen vacancies near the Mo atoms and these Mo atoms stay in four fold coordination. Thus, the defect induced by oxygen vacancies in fact makes the chain fragmented and disordered. After annealing under oxygen, the extra oxygen prefers the O3 crystallographic site. This indeed fills up the oxygen vacancies near the Mo atom. And the Mo atoms become six coordinated after oxygen annealing at mesoscopic range. Therefore, the extra oxygen in the O3 site assists in making the $(Mo/Cu)O_{1+\delta}$ chain ordered in a mesoscopic range. Liu at el[63,64] demonstrated that oxygen ordering outside the CuO_2 planes produces strong effects on superconductivity. Their results showed that the ordering associated with the apical oxygen distribution can be an additional tuning factor to enhance T_C in high temperature superconductors. In fact the oxygen ordering correlates with minimized cationic disorder in the CuO_2 planes and within the SrO layer and results in an enhancement of the superconducting transition temperature. A local structural disorder was observed induced by Al doping in the parent $Sm/YCuBa_2Cu_2O_{6+\delta}$ (Cu-1212) compound.[65,66] The disorder seemed not to be confined to the neighbours of the Al dopant, it was extended to the copper plane and therefore was reflected in their physical properties. In light of these observations, we have similarly reflected that in the as-prepared samples, oxygen vacancies neighbouring Mo atoms in the $(Mo/Cu)O_{1+\delta}$ chain site produce a local disorder. The extra oxygen in the $(Mo/Cu)O_{1+\delta}$ chain after oxygen annealing makes the chain ordered in the mesoscopic range. In fact, the existence of orthorhombic crystals as seen in ED patterns for the $Mo_{0.3}Cu_{0.7}Sr_2TmCu_2O_y$ material seems to be an indication of a more ordered chain in a shorter range. This local oxygen-ordering enhances the charge transfer (hole transfer as suggested by TEP measurements) between the reservoir block and the copper plane to assist superconductivity.

It is noteworthy that, contrary to the two-orbital model of *Sakakibara et al*[44] or any other theories that find T_C increases with increasing apical Oxygen (Cu2−O2) distance, the apical Cu2−O2 distance decreases (Figure 5.21) after oxygen annealing while T_C increases for all cases. It is notable that in $Mo_{0.25}Cu_{0.75}Sr_2YCu_2O_y$[36] a similar apical bond length contraction was observed after oxygen annealing. Our structural results then clearly indicate that the apical oxygen is playing an important role in assisting the charge transfer between $(Mo/Cu)O_{1+\delta}$ chain and Cu-O_2 copper plane.

To determine the critical current density (J_C), we have measured the magnetic hysteresis loops at different temperatures. Figure 5.39 shows the hysteresis loop measured at

4K for both the OA samples. The non linear behaviour of the hysteresis curves at higher fields certainly indicates the existence of paramagnetism, arising due to the presence of paramagnetic cations.

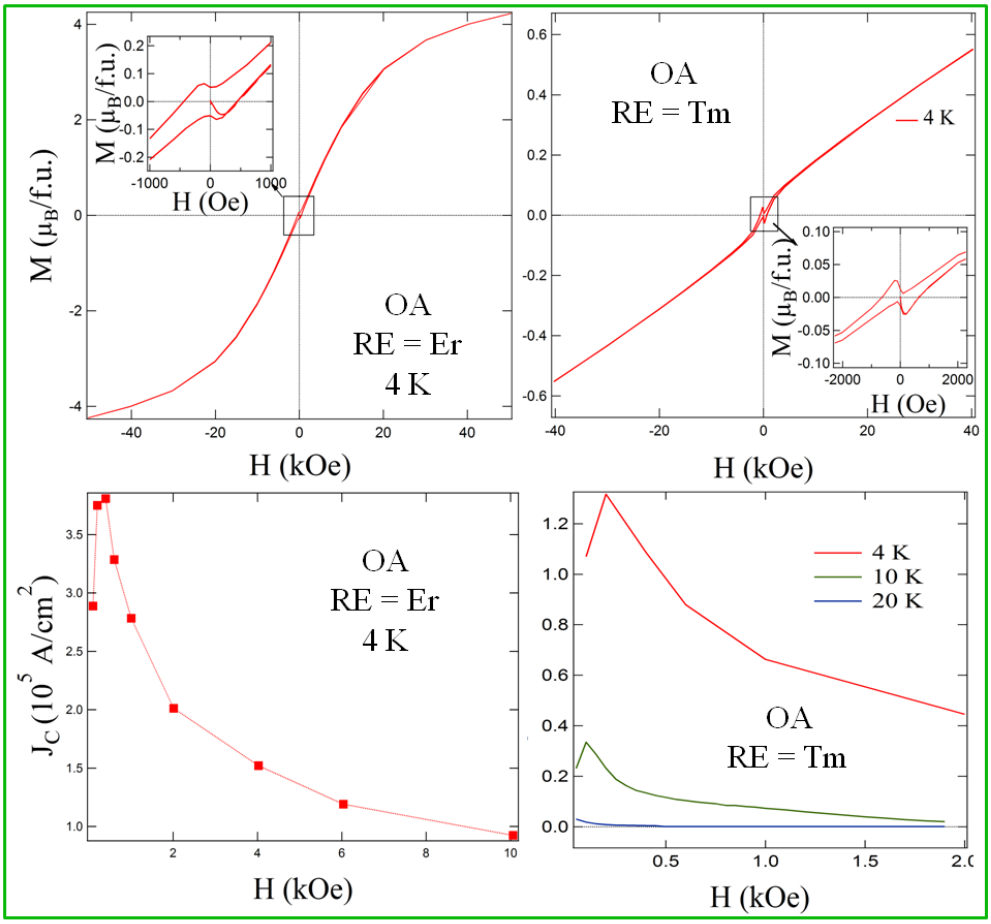

Figure 5.39. Change of magnetization as a function of magnetic field for the OA $Mo_{0.3}Cu_{0.7}Sr_2ErCu_2O_y$ (upper left) and $Mo_{0.3}Cu_{0.7}Sr_2TmCu_2O_y$ (upper right) materials measured at 4 K. Upper insets show the enlarged central part of the hysteresis loop, confirms the irreversibly due to the superconductivity. Lower panels of the figure show the variation of critical current density (J_C) as a function of magnetic field at different fixed temperatures.

However, the irreversibility obtained at lower fields can only be explained in the frame of superconductivity (flux pinning). Following Bean's approach, $J_C(H) = k\partial M/d$, where ∂M in emu/cc, is the difference in magnetic moment (M) at the same magnetic field (H), d is a scaling length in cm and k is a shape coefficient. The intragrain J_C is calculated assuming nearly spherical grains (k = 40) and d = 4 μm (from Electron Microscope measurements). The lower panels of figure 5.39 show J_C as a function of the magnetic field at different temperatures for both the OA samples. It is found that at 4 K, J_C is about 2.9×10^5 A/cm^2 and 1×10^5 A/cm^2 for OA $Mo_{0.3}Cu_{0.7}Sr_2ErCu_2O_y$ and OA $Mo_{0.3}Cu_{0.7}Sr_2TmCu_2O_y$, respectively. The

obtained J_C shows a strong dependence on field with temperature. In addition, a peak is clearly observed in the field dependence of J_C values, from which J_C decreases monotonically. The "peak effect" in the J_C plots is caused by "field induced pins" (FIPs).[67] The FIPs might be coming from the clusters caused by the oxygen vacancies in the Mo/Cu-O chains. These clusters with a lower upper critical field (H_{C2}) than the bulk matrix, describe the weak pins and are disturbed at low applied fields.[67,68] Also the presence of somewhat diluted paramagnetic Mo^V cations even after the oxygenation may provide pinning centres. Therefore, the peak effect can also result from the competition between vortex-vortex and vortex-pin interaction.[69]

5.3. Conclusion

We have investigated the structural and physico-chemical properties of the $Mo_{0.3}Cu_{0.7}Sr_2RECu_2O_y$ (RE = Y, Er and Tm) materials. The as-prepared and oxygenated phases have been characterized by XRD, NPD, TEM, resistivity, TEP and ac and dc magnetization measurements. A joint NPD/XRD refinement yielded more structural detail than either of the two techniques alone. A reliable estimate of the total oxygen content and Cu/Mo distribution over each copper site was obtained. Structural refinements show that the majority of the Mo substitution in the as-prepared sample occurs for the copper in chain sites in the 123-type parent structure.

The influence of oxygenation in the electronic states for the $Mo_{0.3}Cu_{0.7}Sr_2YCu_2O_y$ and $Mo_{0.3}Cu_{0.7}Sr_2ErCu_2O_y$ systems associated to an oxidation reaction from a semiconducting to a superconducting state has been investigated by means of X-ray photoelectron spectroscopy. The XPS studies show the predominance of the Mo^V state over the Mo^{VI} one. Yet, annealing under an oxygen atmosphere enhances the Mo^{VI} state. Quite interestingly, at the same time, a reduction in the copper species is observed.

A combination of ac and dc magnetic measurements is used to study the as-synthesized $Mo_{0.3}Cu_{0.7}Sr_2RECu_2O_y$ (RE = Er and Tm) tetragonal materials. Magnetic measurements on the AP $Mo_{0.3}Cu_{0.7}Sr_2ErCu_2O_y$ sample indicate ferromagnetic interactions through the existence of FM domains in a nonmagnetic matrix. The magnetic state of the AP $Mo_{0.3}Cu_{0.7}Sr_2TmCu_2O_y$ material experiences PM – Weak AFM – SG transitions with a lowering of the temperature. However, instead of a classical individual spin freezing, we suggest a cluster by cluster freezing model to explain the SG nature in this material. The complex magnetic behaviour in these AP materials could be due to the direct consequence of the cation disorder.

On the other hand, all the oxygenated materials are superconducting. The material oxygenated using high pressure shows the highest T_C (84 K). Structural analyses reveal the tendency of short-range oxygen ordering after oxygenation. This increases the effectiveness in the charge transfer to the superconducting layer (CuO_2), resulting in superconductivity. Following our experimental results, we showed that contrary to the two orbital model[44], in association with a shortening in the apical Cu2-O2 distance a decrease in the charge transfer energy favours the enhancement of the apical charge transfer to the CuO_2 plane after oxygenation, which assist the superconductivity. The "peak effect" in the J_C plots has been observed due to "field induced pins" (FIPs).

References

[1]Gagnon R, Lupien C and Teillefer L 1994 Phys. Rev. B **50**, 3458.

[2]Hor P H, Meng R L, Wang Y Q, Gao L, Huang Z J, Bechtold J, Forster K and Chu C W 1987 Phys. Rev. Lett. **58**, 1891.

[3]Chattopadhyay T, Brown P J, Bonnenberg D, Ewert S and Maletta H 1988 Europhys. Lett. **6**, 363, see also Lynn J W, Clinton T W, Li W H, Erwin R W, Liu J Z, Vandervoort K and Shelton R N 1989 ibid. **63**, 2606.

[4]Lee J H, Choi M, Ahmad D, Ahn S S, Park I S, Kim D J, Kim Y C, Jang M S, Sohn M H, Ko Rock-Kil and Jeong D Y 2007 Journal of the Korean Physical Society **50**, No. 4, pp. 1180-1184.

[5]Bauernfeind L, Widder W and Braun H F 1995 Physica C **254**, 151-158.

[6]J. Lynn W, Keimer B, Ulrich C, Bernhard C, and Tallon J L 2000 Phys Rev. B. **61**, R14964.

[7]Papageorgiou T P, Casini E, Skourski Y, Herrmannsdo T, Freudenberger J, Braun H F and Wosnitza J 2007 Physica C, **460–462**, 390–391.

[8]Pringle J D, Tallon J L, Walker B G and Trodahl H J 1999 Phys Rev. B. **59**, R11679.

[9]Rukang L, Yingjie Z, Daoyuang Z, Chen X, Yitai Q, Zuyao C and Guien Z J 1992 Alloy Compd. **185,** 45.

[10]Mclaughlin A C, Morrice D and Sher F 2005 J. Solid State Chem. **178**, 2274.

[11]Adachi S, Kubo K –I, Takano S and Yamauchi H 1992 Physica C **191**, 174.

[12]Eder M H and Gritzner G 2005 Supercond. Sci. Technol. **18,** 87.

[13]Dos santos-Garcia A J, Aguirre M H, Saez Puche R and Alario-Franco M A 2006 J. Solid State Chem. **179,** 1296.

[14]Dos santos-Garcia A J, Van Duijn J and Alario-Franco M A 2008 J. Solid State Chem. **181**, 3317–3321.

[15] Xiong Q, Xue Y Y, Chu J W, Sun Y Y, Wang Y Q, Hor P H and Chu C W 1993 Phys. Rev. B **47**, 11337.

[16]Felner I, Galstyan E, 2004 Phys. Rev. B **69**, p. 024512.

[17]Balchev N, Nenkov K, Mihova G, Kunev B, Pirov J and Dimitrov D A 2009 JMMM **321**, 388–391.

[18]Marik S, Moran E, Labrugere C, Toulemonde O and Alario-Franco M A 2012 J. Solid State Chem. **191,** 40-45.

[19]Hu S F, Liu R S, Su S C, Shy D S and Jefferson D A 1994 J. Solid State Chem. **112**, 203.

[20]Harlow R L, Kwei G H, Suryanarayanan R and Subramanian M A 1996 Physica C **257** 125-136.

[21]Rodriguez-Carvajal J 2001 An introduction to the programme FULL-PROF, Labratoire Leon Brillouin, CEA-CNRS: Saclay, France.

[22]Felner I, Awana V P S, Takayama-Muromachi E 2003 Phys. Rev. B, **68**, p. 094508.

[23]Den T and Kobayashi T 1992 Physica C **196**, 141.

[24]Tsay H L, Shih C R, Chen Y C, Lee W H, Meen T H, Yang H D 1995 Physica C, **252**, 79–86.

[25]William T A, Harrison S R, Vaughey J T, Liu L and Jacobson A J 1995 J. Solid State Chem. **119**, 115-119.

[26]Kambe S, Sato E, Akao T, Ohshima S, Okuyama K, Sekine R 1999 Phys. Rev. B, **60**, 687–697.

[27]Rogacki K, Dabrowski B, Chmaissem O, Jorgensen J D 2000 Phys. Rev. B, **63**, 054501.

[28]Katrib A, Logie V, Peter M, Wehrer P, Hilaire L and Maire G 1997 J. Chim. Phys. Phys.-Chim. Biol. **94**, 1923.

[29]Jalili H, Heinig N F and Leung K T 2009 Phys. Rev. B **79**, 174427.

[30]Larsson S 1976 Chem. Phys. Lett. **40**, 362.

[31]Van der Laan G, Westra C, Haas C and Sawatzky G A 1981 Phys. Rev. B **23**, 4369.

[32]Parmigiani F and Sangaletti L 1994 J. Electron Spectrosc. Relat. Phenom. **66**, 223.

[33]Vasquez R P, Novikov D L, Freeman A J and Siegal M P 1997-I Phys. Rev. B **55**, 21.

[34]Ruiz-Bustos R, Aguirre M. H and Alario-Franco M A 2005 Inorg. Chem. **44**, 3063-3069.

[35]Antipov E V, Abukamov A M and Putilin S N 2002 Supercond. Sci. Technol. **15**, R31-R49.

[36]Grigoraviciute I, Yamauchi H, Karppinen M and Marezio M 2010 Phys. Rev. B **82**, 104507.

[37]Lebedev O I, Tendeloo G V, Licci F, Gilioli E. Gauzzi A, Prodi A, and Marezio M 2002 Phys. Rev. B **66**, 132510..

[38]Jorgensen J D, Beno M A, Hinks D G, Soderholm L, Volin K J, Hitterman R L, Grace J D, Schuller I K, Serge C U, Zhang K and Kleefisch M S 1987 Phys. Rev. B **36**, 3608.

[39]Jorgensen J D, Veal B W, Kwok W K, Crabtree G W, Umezawa A, Nowicki L J and Paulikas A P 1987 Phys. Rev. B **36**, 5731.

[40]Tarascon J M, McKinnon W R, Greene L H, Hull G W and Vogel E M 1987 Phys. Rev. B **36**, 226.

[41]Schuller I K, Hinks D G, Beno M A, Capone D W II, Soderholm L, Locquet J -P, Bruynseraede Y, Segre C U and Zhang K 1987 Solid State Commun. **63**, 385.

[42]Xiao G, Cieplak M Z, Gavrin A, Streitz F H, Bakhshai A and Chien C L 1998 Phys. Rev. Lett. **60**, 1446.

[43]Zhao Y, Shi F, Liu H K, Andrikidis C and Dou S X 1993 Physica C **212,** 451-458.

[44]Sakakibara H, Usui H, Kuroki K, Arita R and Aoki H 2010 Phys. Rev. Lett. **105**, 057003.

[45]Marik S, Dos Santos-Garcia A J, Morán E, Toulemonde O and Alario-Franco M A 2013 Journal of Physics-Condensed Matter **25**, 165704.

[46]Allan K, Campion A, Zhou J and Goodenough J B 1990 Phys. Rev. B **41**, 11572.

[47]Mydosh J A 1993 Spin Glasses: An Experimental Introduction (Taylor and Francis, London).

[48]Cardoso C A, Araujo-Moreira F M, Awana V P S, Takayama-Muromachi E, de Lima O F, Yamauchi H and Karppinen M 2003 Phys. Rev. B **67**, 020407(R).

[49]Binder K and Young A P 1986 Rev. Mod. Phys. **58**, 801.

[50]Myers H P 1997 Introductory Solid State Physics, 2nd. Ed., Taylor & Francis.

[51]Chatterjee S and Nigam A K 2002 Phys Rev. B. **66**, 104403.

[52]Franco D G, Fuertes V C, Blanco M C, Fernadez-Diaz M T, Sanchez R D, Carbonio R E 2012 JSSC **194**, 385–391.

[53]Retuerto M, García-Hernández M, Martínez-Lope M J, Fernández-Díaz M T, Attfield J P and Alonso J A 2007 J. Mater. Chem., **17**, pp. 3555–3561

[54]James M, Attfield J P, Rodríguez-Carvajal J 1995 J. Phys. Chem. Solids, **56**, pp. 1331–1337

[55]Srivastava J K 1998 Phys. Status Solidi (b) **210**, 159–175.

[56]Rao S M, Wu M K, Srivastava J K, Mok B H, Lu C Y, Liao Y C, Hsu Y Y, Y. Hsiue S, Chen Y Y, Neeleshwar S, Tsai S, Ho J C and Liu H L 2004 Phys. Lett. A **324**, 71–81.

[57]Srivastava J K and Rao S M 2003 in: Models and Methods of High-T_C Superconductivity: Some Frontal Aspects, vol. **1**, Nova Science Publishers, Hauppauge, NY, p. 9.

[58]Ando Y, Lavrov A N, Komiya S, Segawa K and Sun X F 2001 Phys. Rev. Lett. **87**, 017001-1.

[59]Tallon J L, Bernhard C, Snaked H, Hitteman R L and Jorgensen J D 1995, Phys Rev. B **51**, 12911.

[60]Grigoravicute I, Karppinen M, Chan T -S, Liu Ru-Shi, Chen Jin-Ming, Chmaissem O and Yamauchi H 2010 JACS **132**, 838-841.

[61]Awanaa V P S, Gupta A, Kishan H, Takayama-Muromachi E, Watanabe T, Karppinen M, Yamauchi H, Malik S K, Yelon W B, Ganesan V and Narlikar A V 2003 Solid State Commun. **129**, 117-121.

[62]Dabrowski B, Rogacki K, Koenitzer J W, Poeppelmeier K R and Jorgensen J D Physica 1997 C **277**, 24-35.

[63]Liu Q Q, Yang H, Yu Y, Yang L X, Yu R C, Li F Y, Jin C Q and Uchida S 2007 Physica C **100**, 463-465.

[64]Yang H, Liu Q Q, Li F Y, Jin C Q and Yu R C 2007 Physica C **467**, 59-66.

[65]Scavini M, Coduri M, Allieta M, Mollica L, Brunelli M, Malavasi L, Lascialfari A, and Ferrero C 2010, J. Phys. chem. C, **114**, 19509.

[66]Brecht E, Schmahl W W, Miehe G, Rodewald M, Fuess H, Andersen N H, Hangmann J, Wolf Th. 1996, Physica C, **265**, 53.

[67]Däumling M, Seuntjens J M and Larbalestier D C 1990 Nature **346**, 332.

[68]Xu X B, Fangohr H, Xu X N, Gu M, Wang Z H, Ji S M, Ding S Y, Shi D Q and Dou S X 2008 Phys. Rev. Lett. **101**, 147002.

[69]Xu X B, Fangohr H, Xu X N, Gu M, Wang Z H, Ji S M, Ding SY, Shi D Q, Dou S X 2008 Phys. Rev. Lett. **101**, 147002.

Chapter 6

Influence of Oxygenation in the superconductivity and electronic states of $Mo_{0.3}Cu_{0.7}Sr_2RECu_2O_y$ (RE = Y and Er)

General Overview

This chapter describes a detailed XPS study on the $Mo_{0.3}Cu_{0.7}Sr_2RECu_2O_y$ materials (RE = Y and Er) having different oxygen contents. The influence of oxygenation in the electronic states for $Mo_{0.3}Cu_{0.7}Sr_2YCu_2O_y$ and $Mo_{0.3}Cu_{0.7}Sr_2ErCu_2O_y$ systems associated to an oxidation reaction from a semiconducting to a superconducting state has been investigated and is discussed. A correlation with the charge transfer mechanism and structural peculiarities is also presented here.

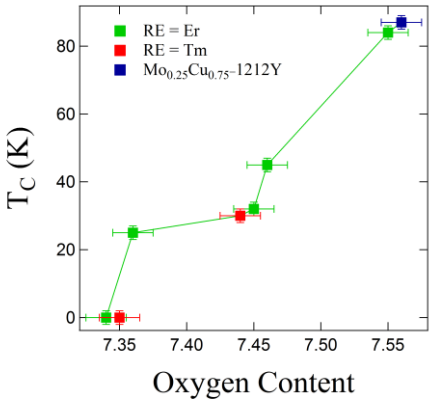

Publication from this chapter

1. Marik S, Moran E, Labrugere C, Toulemonde O and Alario-Franco M A *"Influence of Oxygen Annealing in the Superconductivity and Electronic States of $Mo_{0.3}Cu_{0.7}Sr_2YCu_2O_y$"* 2013 *J. Supercond. Nov. Mag.* **26** 1151.

6.1. Introduction

It is widely accepted, that high temperature superconductivity in cuprates[1] arises from doping of a Mott-Hubbard insulator.[2] The understanding of metal-insulator transitions of doped Mott-Hubbard insulators is one of the outstanding challenges occupying modern Solid State Physics. In particular, in the doped cuprates, there exist a complex interplay between lattice, charge, and spin degrees of freedom. Various phases between the antiferromagnetic charge-transfer insulator and the paramagnetic Fermi-liquid like state have been the subject of discussion. The prominent state of matter in this context is superconductivity.

Materials with the 1212 type-structure[3] ($MA_2RECu_2O_{8-\delta}$ or M – 1212, where M is commonly a transition metal element, A is an alkaline earth metal, and RE is a rare earth ion) have drawn a special interest as they are close to the $YBa_2Cu_3O_y$[4] (YBCO, $CuSr_2YCu_2O_y$, YSCO or Cu-1212) structure having copper in pyramidal coordination with the ligand oxygen. From the Cu-1212-type structures, Mo stabilized $CuSr_2RECu_2O_y$ (RE = rare earth elements) single phase compounds can be prepared at ambient pressure until reaching the composition $Mo_{0.3}Cu_{0.7}Sr_2RECu_2O_y$ ((Mo,Cu)-1212). This is indeed an exciting system to study the superconductivity adjacent to a metal-insulator boundary (see *chapters 4 and 5*).[5-7] Previous work on Mo-stabilized $RESr_2Cu_3O_{7-\delta}$ (RE = Rare earth) phases clearly stated that these compounds display a superconducting transition centering around 30 K associated to an oxidation reaction from a semiconducting state, with the exception for the bigger R = La, Pr and Nd lanthanide-compounds, which are not superconducting.[8] As discussed in the previous chapter (*Chapter 5*) as well as in the reported studies[9-11] the superconducting transition temperature of $Mo_{0.3}Cu_{0.7}Sr_2RECu_2O_y$ materials can be almost as high as YBCO, when the materials were oxygenated under high pressure.

Interestingly, in these compounds, Mo partially adopts the Mo^V oxidation state, which originates magnetic interactions within the charge reservoir layer. As a result, the as-prepared molybdo-cuprate compounds show interesting physical properties.[5-7,12,13] Previous crystal structure studies[5-7,10,14-16] (*chapter 5*) show that all the $Mo_{0.3}Cu_{0.7}Sr_2RECu_2O_y$ compounds adopt a tetragonal structure with the *P4/mmm* space group.

It is noteworthy that contrary to the two-orbital model of *Sakakibara et al*[17], which shows that T_C increases with the increasing apical copper-oxygen (Cu2–O2) distance, the apical Cu2–O2 distance decreases after oxygenation with increasing T_C for all the 1212-type $Mo_{0.3}Cu_{0.7}Sr_2RECu_2O_y$ compounds (*discussed in chapter 5 and in ref. 10*). Moreover, the structural refinement of the as-prepared (non superconducting) and oxidized phases

(superconducting) for the first four members of the homologous series $(Cu_{0.75}Mo_{0.25})Sr_2(Ce,Y)_SCu_2O_{5+2s+\delta}$ by Chmaissem *et. al.*[10] showed that, besides the M-1212 compound, the M-1222 and M-1232 molybdo-cuprate compounds also show the trend of shortening apical oxygen distances after oxygenation. Also, in these compounds, the out-of-plane buckling angle[18] increases with oxygenation in disagreement with the common belief that maximum Tc's are achieved when perfectly flat CuO_2 planes are synthesized as exemplified by mercury cuprate.

High-temperature superconductors have been widely studied with photoemission spectroscopy[19], indeed X-ray photoelectron spectroscopy (XPS) is a powerful tool in studying the mechanism of the 3d element doping in Cu site and can provide information on the electronic structure of the system. The core-level measurements provide information on the electronic states of the compounds, such as oxidation states and doping-induced chemical potential shifts and, in the case of the highly correlated Cu cations, charge-transfer mechanisms and multiplet splitting. The lack of studies on the electronic structure of this interesting molybdo-cuprate family prompted us to investigate the electronic states of 1212-type molybdo-cuprate materials having different oxygen contents and try to relate them to superconductivity, in particular with T_C.

In this chapter, we present and discuss a detailed XPS study of the $Mo_{0.3}Cu_{0.7}Sr_2RECu_2O_y$ materials (RE = Y and Er) having different oxygen contents. The influence of oxygenation in the electronic states for the $Mo_{0.3}Cu_{0.7}Sr_2YCu_2O_y$ and $Mo_{0.3}Cu_{0.7}Sr_2ErCu_2O_y$ systems associated to an oxidation reaction from a semiconducting to a superconducting state has been investigated and is discussed.

6.2. Experimental details

The details of the synthesis procedure have been presented in the previous chapters (*Chapters 3 and 5*). The sample compositions, annealing (oxygenation process) conditions and their naming details are shown in the table 6.1.

The samples purities were checked by powder X-ray diffraction. The oxygen contents were obtained by refining the neutron powder diffraction (NPD, discussed in *chapter 5*) and thermo gravimetric analysis (TGA) using reducing condition (5% H_2 + 95% N_2). Samples were heated to 973 K then isothermally maintained for 15 h, and cooled down to room temperature. The oxygen contents were calculated considering that the final products were RE_2O_3, SrO, $SrMoO_4$ and Cu as observed from the X-ray diffraction.[16]

Table 6.1. Sample compositions, annealing (oxygenation process) conditions and their naming details.

Composition of (Mo,Cu)-1212 materials	Oxygenation process	Name
$Mo_{0.3}Cu_{0.7}Sr_2Y/ErCu_2Oy$	In air at 1273 K for 48 h	AP
$Mo_{0.3}Cu_{0.7}Sr_2Y/ErCu_2Oy$	AP sample annealed under O_2 flow at 873 K for 48 h	OA
$Mo_{0.3}Cu_{0.7}Sr_2Y/ErCu_2Oy$	OA sample annealed under O_2 flow at 673 K for 24 h	OA1
$Mo_{0.3}Cu_{0.7}Sr_2ErCu_2O_y$	AP sample annealed at 673 K for 48 hour under high oxygen pressure (pressure = 100 bar)	OAHP
$Mo_{0.3}Cu_{0.7}Sr_2ErCu_2O_y$	Oxygenation of the AP sample in a Belt Press type apparatus at 5 GPa and 773 K for 30 min in the presence of 33 mol % $KClO_3$	HPO

Physical property measurements were carried out by means of magnetic susceptibility, resistivity and thermoelectric power measurement (TEP) techniques. The resistivity and TEP measurements were carried out in the absence of a magnetic field. And magnetic susceptibility measurements were carried out at 10 Oe magnetic field. The details of the experimental techniques were shown in chapter 3.

The electronic states of all the materials have been investigated by means of X-ray photo electron spectroscopy (XPS) techniques. The details of the instrument and data acquisition process were discussed in the chapter 3.

6.3. Results

6.3.1. Physical properties, oxygen contents and hole concentration

Figure 6.1 shows the temperature variation of resistivity and dc magnetic susceptibility for the $Mo_{0.3}Cu_{0.7}Sr_2RECu_2O_y$ (RE = Y and Er) materials having different oxygen contents. Both AP samples are non-superconducting; as already mentioned, an oxygenation process induces superconductivity in the materials. The weight loss from the TGA measurements for the OA1 and OAHP $Mo_{0.3}Cu_{0.7}Sr_2ErCu_2O_y$ samples are shown in figure 6.2. The superconducting transition temperatures and calculated oxygen contents using different methods, for all the samples, are compared in table 6.2.

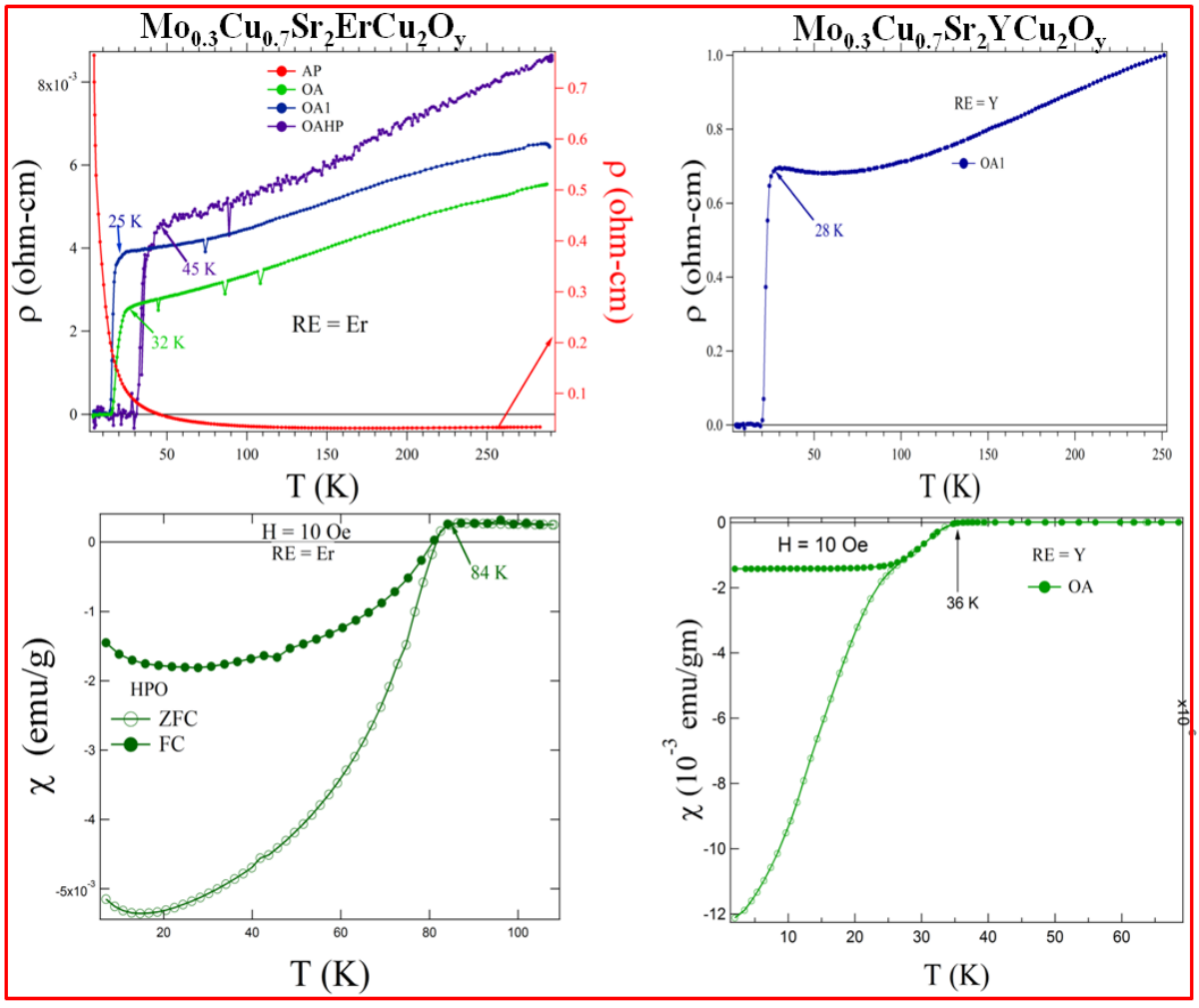

Figure 6.1. Temperature dependence of resistivity and magnetic susceptibility for the $Mo_{0.3}Cu_{0.7}Sr_2RECu_2O_y$ (RE = Y and Er) materials.

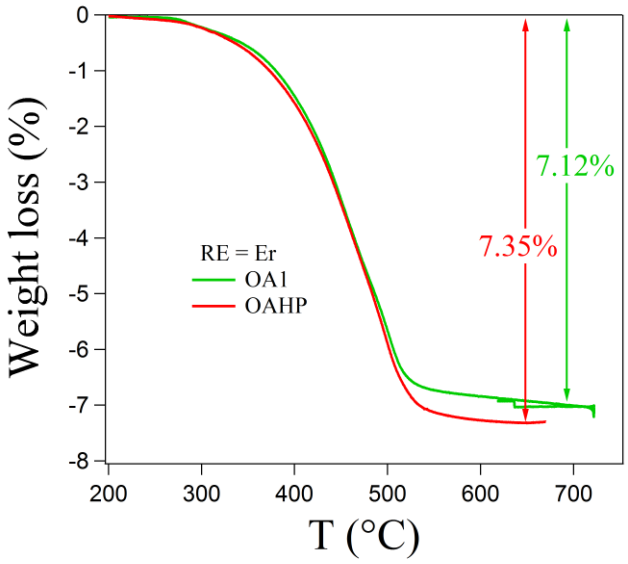

Figure 6.2. TGA measurements for the OA1 and OAHP $Mo_{0.3}Cu_{0.7}Sr_2ErCu_2O_y$ samples.

Table 6.2. Superconducting transition temperatures, calculated oxygen contents, TEP values at 290 K and the calculated hole concentrations for the different $Mo_{1-x}Cu_xSr_2RECu_2O_y$ materials.

Sample Composition	Sample name	T_C (K)	Oxygen content	S (290 K) in μV/K	Hole concentration (P_h)	Remarks
$Mo_{0.3}Cu_{0.7}Sr_2ErCu_2O_y$	AP	NON SC	7.34 (NPD)	117.5	0.035	This Work
	OA	32 K	7.45 (NPD)	29.6	0.092	This Work
	OA1	25 K	7.36 (TGA)	32.8	0.089	This Work
	OAHP	45 K	7.46 (TGA)	24.5	0.097	This Work
	HPO	84 K	7.55 (NPD)	–	–	This Work
$Mo_{0.3}Cu_{0.7}Sr_2YCu_2O_y$	AP	NON SC	–	–	–	This Work
	OA	36 K	–	–	–	This Work
	OA1	28 K	–	–	–	This Work

$Mo_{0.3}Cu_{0.7}Sr_2TmCu_2O_y$	AP	NON SC	7.35 (NPD)	85	0.064	This Work
	OA	30 K	7.44 (NPD)	37	0.086	This Work
$Mo_{0.25}Cu_{0.75}Sr_2YCu_2O_y$	AP	NON SC	7.36 (NPD)	–	–	Ref. 10
	HPO	87 K	7.56 (NPD)	–	–	Ref. 10

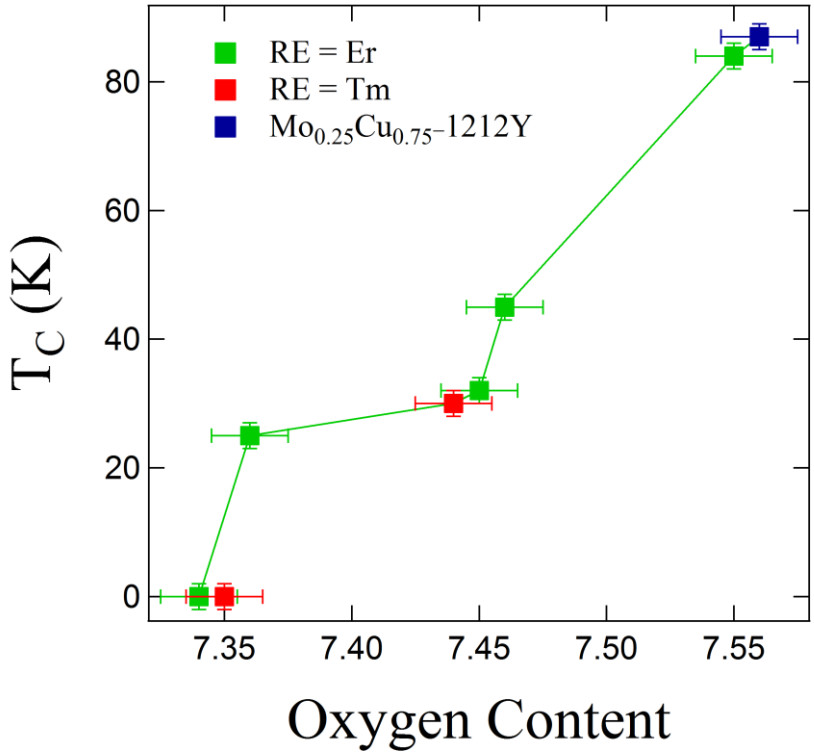

Figure 6.3. Variation of T_C with oxygen content (y) for the different (Mo,Cu)-1212RE (having compositions $Mo_{0.3}Cu_{0.7}Sr_2ErCu_2O_y$, $Mo_{0.3}Cu_{0.7}Sr_2TmCu_2O_y$ and $Mo_{0.25}Cu_{0.75}Sr_2YCu_2O_y$). The data for $Mo_{0.25}Cu_{0.75}Sr_2YCu_2O_y$ ($Mo_{0.25}Cu_{0.75}$-1212Y) material is taken from ref 10.

Figure 6.3 shows the change of T_C with oxygen contents for nine different (Mo,Cu)-1212RE samples (having composition $Mo_{0.3}Cu_{0.7}Sr_2ErCu_2O_y$, $Mo_{0.3}Cu_{0.7}Sr_2TmCu_2O_y$ and $Mo_{0.25}Cu_{0.75}Sr_2YCu_2O_y$). It clearly shows that T_C increases with increasing oxygen content. Figure 6.4a shows the temperature variation of TEP for the $Mo_{0.3}Cu_{0.7}Sr_2ErCu_2O_y$ samples having different oxygen content. However, due to lack of a proper pellet, we were unable to measure either resistivity or TEP for the HP oxidized (HPO) $Mo_{0.3}Cu_{0.7}Sr_2ErCu_2O_y$ material.

The hole concentrations were calculated using the universal formula[20], from the 290 K TEP (S (290 K)) data.

$$S\ (290\ K) = 372 \exp(-32.4\ P_h) \text{ for } 0.00 < P_h < 0.05,$$

$$S\ (290\ K) = 992 \exp(-38.1\ P_h) \text{ for } 0.05 < P_h < 0.155$$

$$S\ (290\ K) = -139\ P_h + 24.2 \text{ for } P_h > 0.155. \qquad (6.1)$$

Figure 6.4b shows the variation of hole concentrations with oxygen contents. The 290 K TEP values and the calculated hole concentrations are shown in table 6.2. In general, the TEP measurements show that the hole concentration increases with increasing oxygen content in the structure, and so does the T_C. Detailed structure, properties and their correlation for different samples have been discussed in the previous chapter (*Chapter 5*). In general, the detailed structural studies, discussed here, show that the variation in the superconducting transition temperature originates from the variation in the hole concentration on the CuO_2 planes and the degree of oxygen ordering in the chain copper sites ($(Mo,Cu)_{1+\delta}$) at the mesoscopic scale.

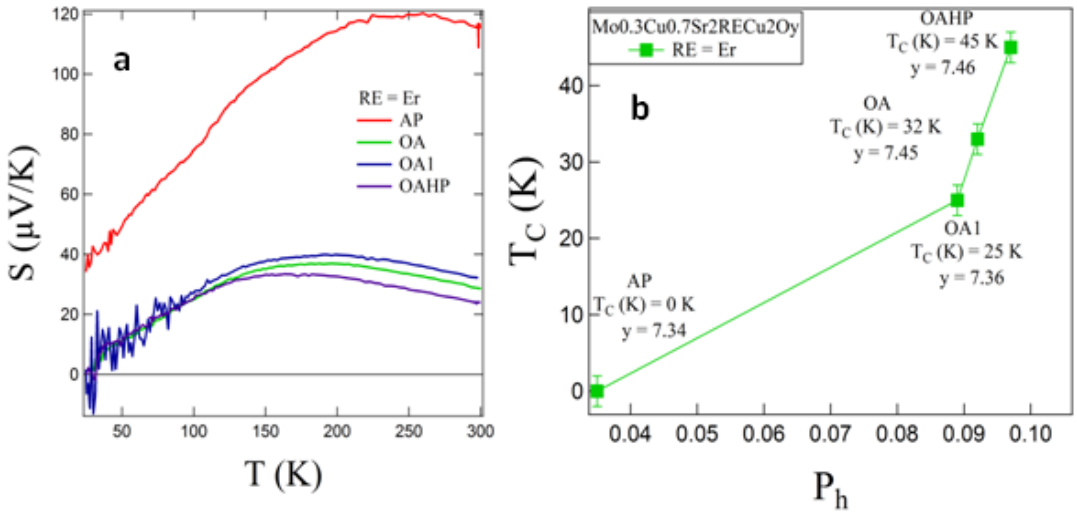

Figure 6.4. (a) The temperature dependence of the thermo electric power (TEP, S) for the $Mo_{0.3}Cu_{0.7}Sr_2ErCu_2O_y$ samples. (b) Variation of T_C with hole concentration (P_h) for the same.

6.3.2. XPS core-level measurements

To get a detailed view of the electronics states and the influence of oxygenation on it, we have studied XPS core level spectra for the $Mo_{0.3}Cu_{0.7}Sr_2RECu_2O_y$ (RE = Y and Er) samples, having different oxygen contents. They are as follows.

C 1s core level spectra: Figure 6.5 shows the C 1s spectra of different $Mo_{0.3}Cu_{0.7}Sr_2RECu_2O_y$ (RE = Y and Er) materials after several scraping in the ultra-high

vacuum. Two intense peaks of C 1s core electrons at 285eV and at 289 eV are observed before scraping. This indicates unambiguously two different states of carbon.[21] The peak at 285 eV corresponds to the normal contamination of the surface by carbon and the second one at 289 eV is due to the formation of carbonates on the surface. The sample was then scraped in vacuum at room temperature with a stainless steel blade. A clean surface, generally, can be obtained after a couple of mild scraping over the surface. The effect of cleaning is evident in the strong attenuation of the C ls signal. We estimate that less than 5% of C is left on the surface after scraping for $Mo_{0.3}Cu_{0.7}Sr_2YCu_2O_y$ samples. For the $Mo_{0.3}Cu_{0.7}Sr_2ErCu_2O_y$ samples no significant C 1s peak at 289 eV has been observed after scraping. The existence of the peak at 285 eV in some samples, even after scraping indicates the carbon left on the surface of the sample is the normal carbon contamination.

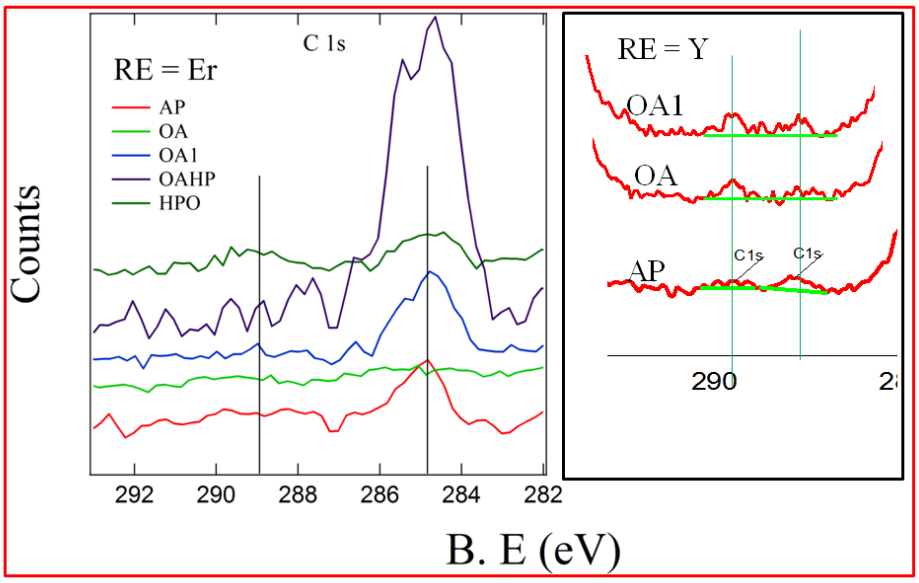

Figure 6.5. Normalized C 1s core level XPS spectra for the $Mo_{0.3}Cu_{0.7}Sr_2RECu_2O_y$ (RE = Y and Er) materials after several scraping at room temperature in the ultra-high vacuum. The other core level XPS spectra have been recorded at the same condition.

Sr 3d core level spectra: The Sr 3d core level spectra for the different $Mo_{0.3}Cu_{0.7}Sr_2YCu_2O_y$ (AP, OA and OA1) samples are shown in figure 6.6. All the samples show a doublet corresponding to the transitions from Sr $3d_{3/2}$ (134 eV) and Sr $3d_{5/2}$ (132.4eV) separated by 1.6 eV.[22] After oxygenation, the samples do show changes in the core level spectra. The intensity of the Sr $3d_{3/2}$ spectra increases after oxygenation.

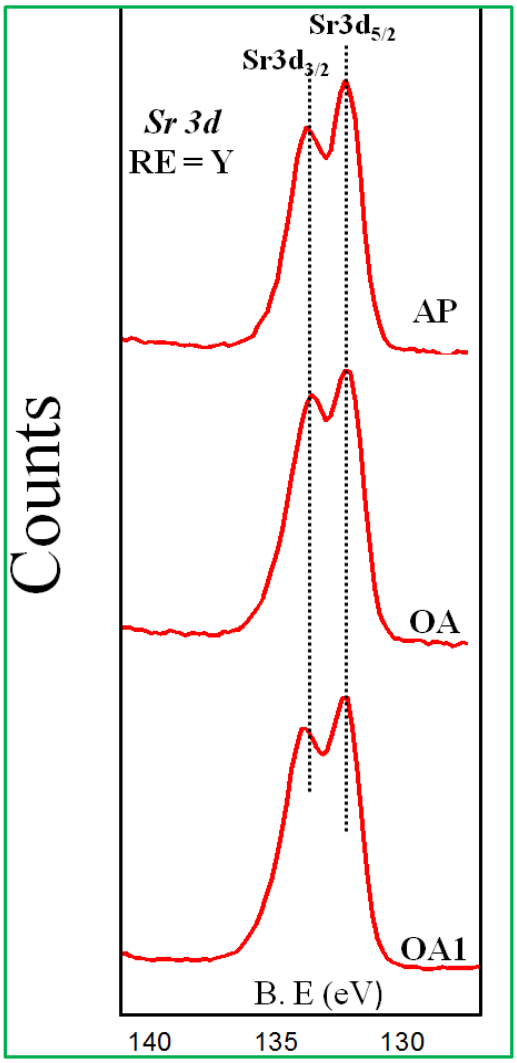

Figure 6.6. Core level XPS spectra of Sr 3d energy region for the $Mo_{0.3}Cu_{0.7}Sr_2YCu_2O_y$ samples.

Figure 6.7a compares the Sr 3d core level spectra for the $Mo_{0.3}Cu_{0.7}Sr_2ErCu_2O_y$ (AP, OA, OA1, OAHP and HPO) samples. Similar to the $Mo_{0.3}Cu_{0.7}Sr_2YCu_2O_y$ samples, they also display the spin-orbit doublet lineshape with a similar energy separation of ~1.6 eV between Sr $3d_{5/2}$ and Sr $3d_{3/2}$. Yet, after oxygenation, they clearly show changes in the core level spectra. Figure 6.7b shows the normalized Sr 3d core level spectra for the $Mo_{0.3}Cu_{0.7}Sr_2ErCu_2O_y$ (AP, OA, OA1, OAHP and HPO) samples. It clearly shows that the intensity of the Sr $3d_{3/2}$ spectra increases after oxygenation. Eventually, for the HPO $Mo_{0.3}Cu_{0.7}Sr_2ErCu_2O_y$ sample, having the highest oxygen content (y = 7.55), Sr $3d_{3/2}$ shows most intense peak among all the samples. Also, the Sr $3d_{3/2}$ spectra are shifted to the lower energy side, with the oxygenation.

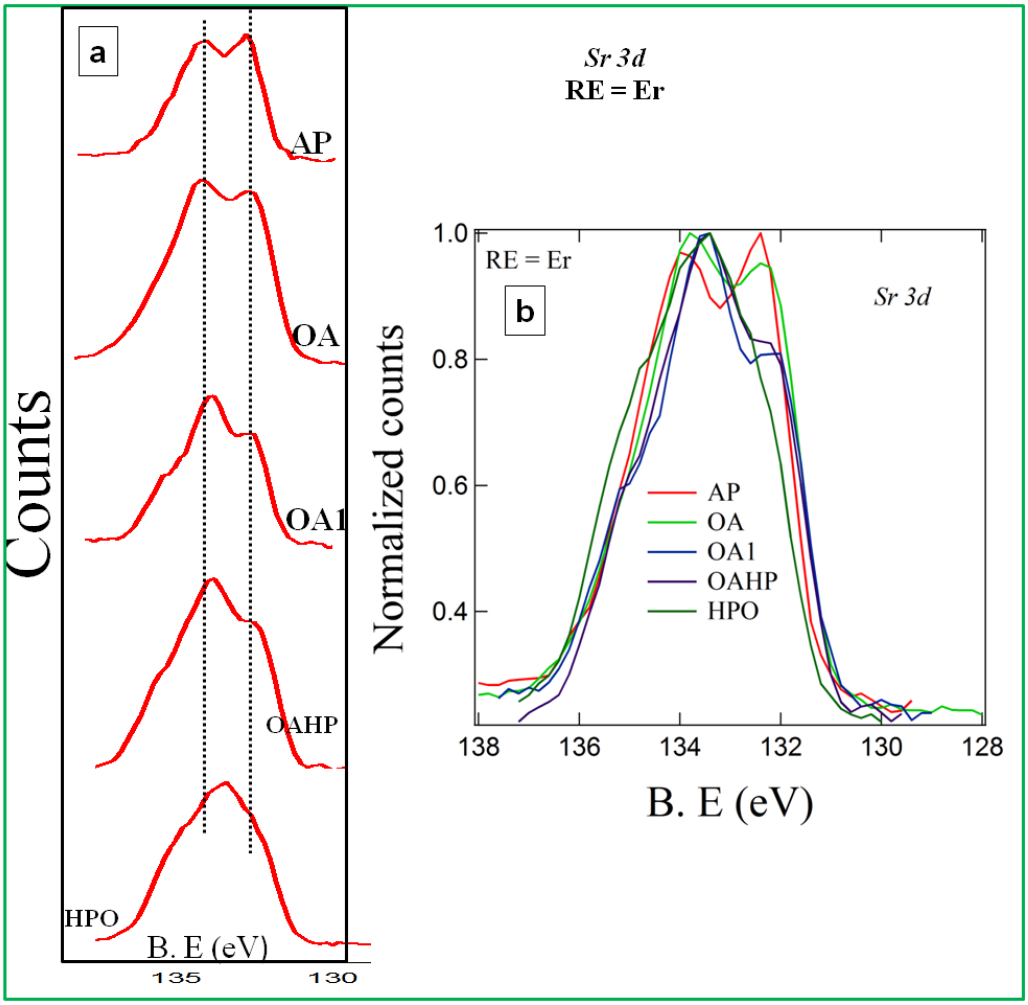

Figure 6.7. (a) Core level XPS spectra and the (b) normalized core level XPS spectra of Sr 3d energy region for the $Mo_{0.3}Cu_{0.7}Sr_2ErCu_2O_y$ samples.

It is worth to recall that the Sr atom (Sr-O) reside between (Cu/Mo)-$O_{1+\delta}$ chain and CuO_2 plane in the (Mo,Cu)-1212 structure (*discussed in chapter 5*). A schematic diagram of (Mo,Cu)-1212 structure is shown in figure 6.8. The changes in the Sr 3d core level spectra after oxygenation may have two possible explanations.

(I) The Sr atom (Sr-O) reside between (Cu/Mo)-$O_{1+\delta}$ chain and CuO_2 plane in the structure, therefore, any changes either in the copper chain site ((Cu/Mo)-$O_{1+\delta}$) or in the copper plane could reflect also in the SrO layer. It may possible that due to the consequence of the extra oxygen in the copper chain site, the Sr 3d core level spectra show changes after oxygen annealing (oxygenation).

(II) Another reason may be due to Sr-Er disorder. In the Bi-1222 ($Bi_2Sr_2CaCu_2O_8$)[22] material, where the Sr- Ca disorder easily occurred, the Sr 3d spectra was deconvulated in

two doublets. The lower binding energy (LBE) doublet represents the Sr atom in the SrO layer between copper chain and CuO_2 plane. And the higher binding energy (HBE) doublet represents the Sr atom in the rare earth (or Ca site for the Bi-1222 material) sandwitched between two CuO_2 layers. Similarly, we have deconvulated the Sr 3d spectra of all the $Mo_{0.3}Cu_{0.7}Sr_2ErCu_2O_y$ samples with two doublets. Figure 6.9 shows the deconvulated spectra and the fitting parameters and the summary of the fitting are shown in table 6.3.

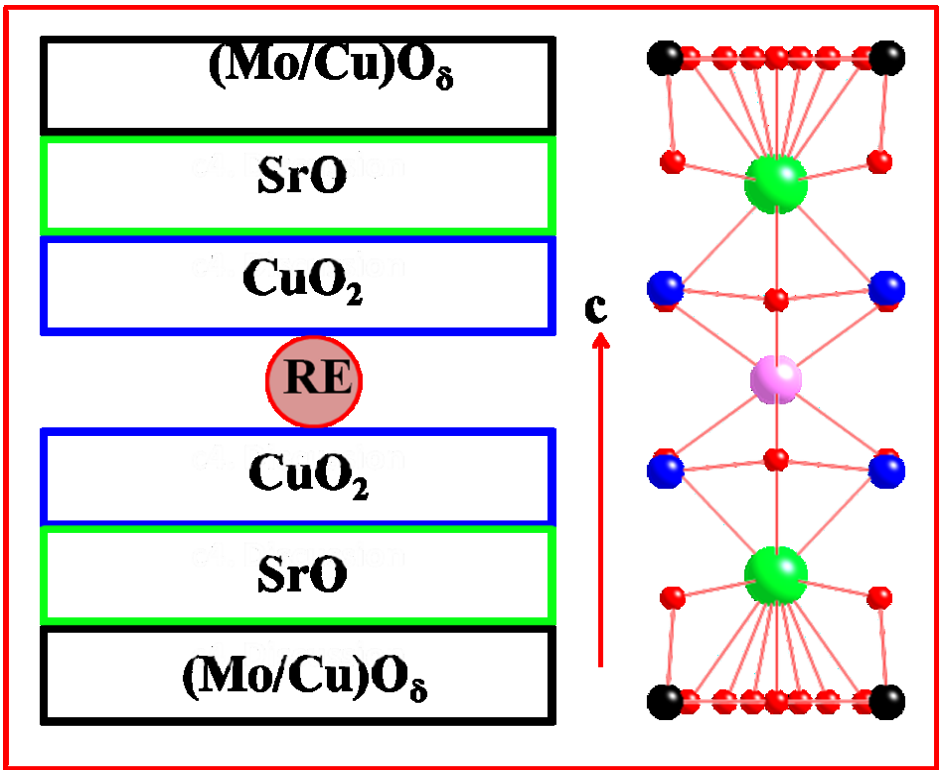

Figure 6.8. Schematic diagram of (Mo,Cu)-1212 structure ($Mo_{0.3}Cu_{0.7}Sr_2RECu_2O_y$ materials, Tetragonal, *P4/mmm*)) along with the proper crystal structure as suggested by NPD refinement.

The fittings (deconvolution) of the Sr 3d core level spectra show that the intensity of the HBE doublet increases with oxygenation. This in fact, points out to the possibility of intermixing between Sr and Er. However, our structural analysis using the joint RT NPD/RT XRD refinement do not show any indication of Sr-Er intermixing.

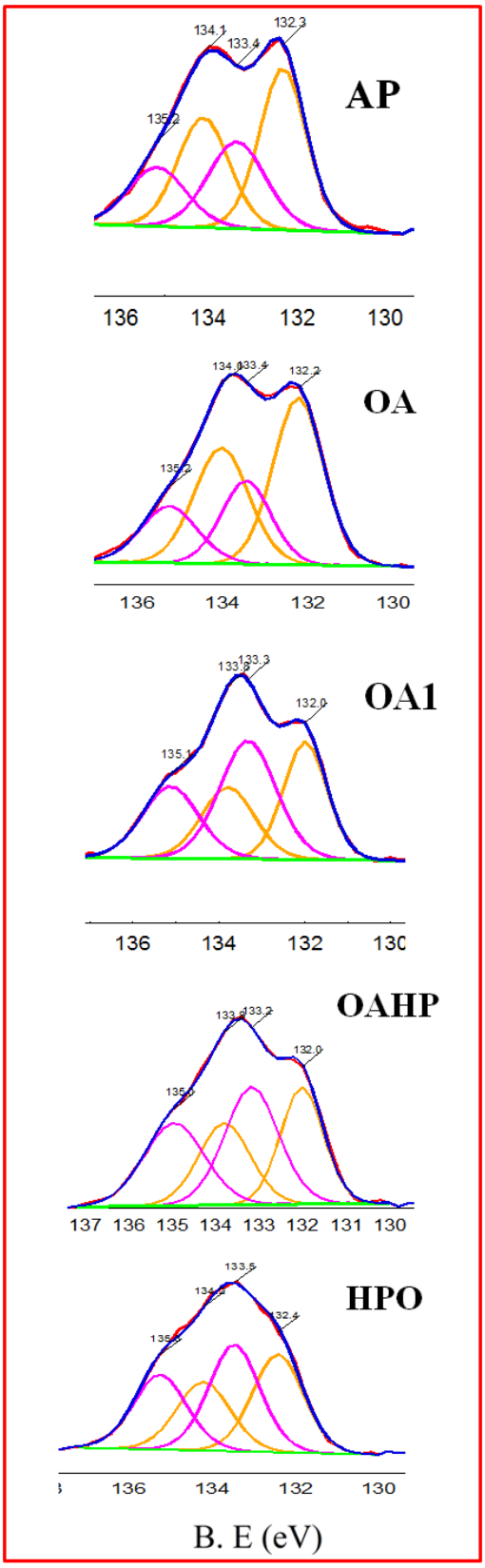

Figure 6.9. Fitted Sr 3d spectra for the $Mo_{0.3}Cu_{0.7}Sr_2ErCu_2O_y$ samples.

Table 6.3. Parameters and summary of fitting of the Sr 3d XPS core level spectra for $Mo_{0.3}Cu_{0.7}Sr_2ErCu_2O_y$ samples.

Sample Name	Core-level spectra	B. E (eV)	FWHM	I (LBE)/I (HBE)
AP	(LBE) Sr $3d_{5/2}$ $3d_{3/2}$ (HBE) Sr $3d_{5/2}$ $3d_{3/2}$	132.3 134.1 133.4 135.2	1.4 1.6	1.00/0.54
OA	(LBE) Sr $3d_{5/2}$ $3d_{3/2}$ (HBE) Sr $3d_{5/2}$ $3d_{3/2}$	132.2 134.0 133.4 135.2	1.5 1.6	1.00/0.50
OA1	(LBE) Sr $3d_{5/2}$ $3d_{3/2}$ (HBE) Sr $3d_{5/2}$ $3d_{3/2}$	132.0 133.8 133.3 135.1	1.5 1.6	0.99/1.00
OAHP	(LBE) Sr $3d_{5/2}$ $3d_{3/2}$ (HBE) Sr $3d_{5/2}$ $3d_{3/2}$	132.0 133.8 133.3 135.1	1.4 1.5	0.99/1.00
HPO	(LBE) Sr $3d_{5/2}$ $3d_{3/2}$ (HBE) Sr $3d_{5/2}$ $3d_{3/2}$	132.4 134.2 133.5 135.3	1.5 1.5	0.91/1.00

Y 3d core level spectra: Figure 6.10a shows the Y 3d core level spectra for the $Mo_{0.3}Cu_{0.7}Sr_2YCu_2O_y$ (AP, OA and OA1) samples. All the spectra exhibit a two peak structure, typical of 3d core levels with spin orbit splitting. The Y $3d_{5/2}$ and $3d_{3/2}$ peaks for the AP sample are at 156.2 eV and 158.3 eV respectively, exhibiting a negative chemical shift of 0.6 eV from the nominal value of 156.8 and 158.9 eV for the Y $3d_{5/2-3/2}$ doublet in Y_2O_3[23]. The intensity ratios of the two components are close to 1.5 in all cases, which is expected from the multiplicity of the spin orbit split feature. However, a small asymmetry in the peak shape is observed after oxygenation. This could be due to more than one electrostatic screening environment for the Y ions upon enhancement of holes after oxygenation in the CuO_2 planes, between which the Y ions are sandwiched.

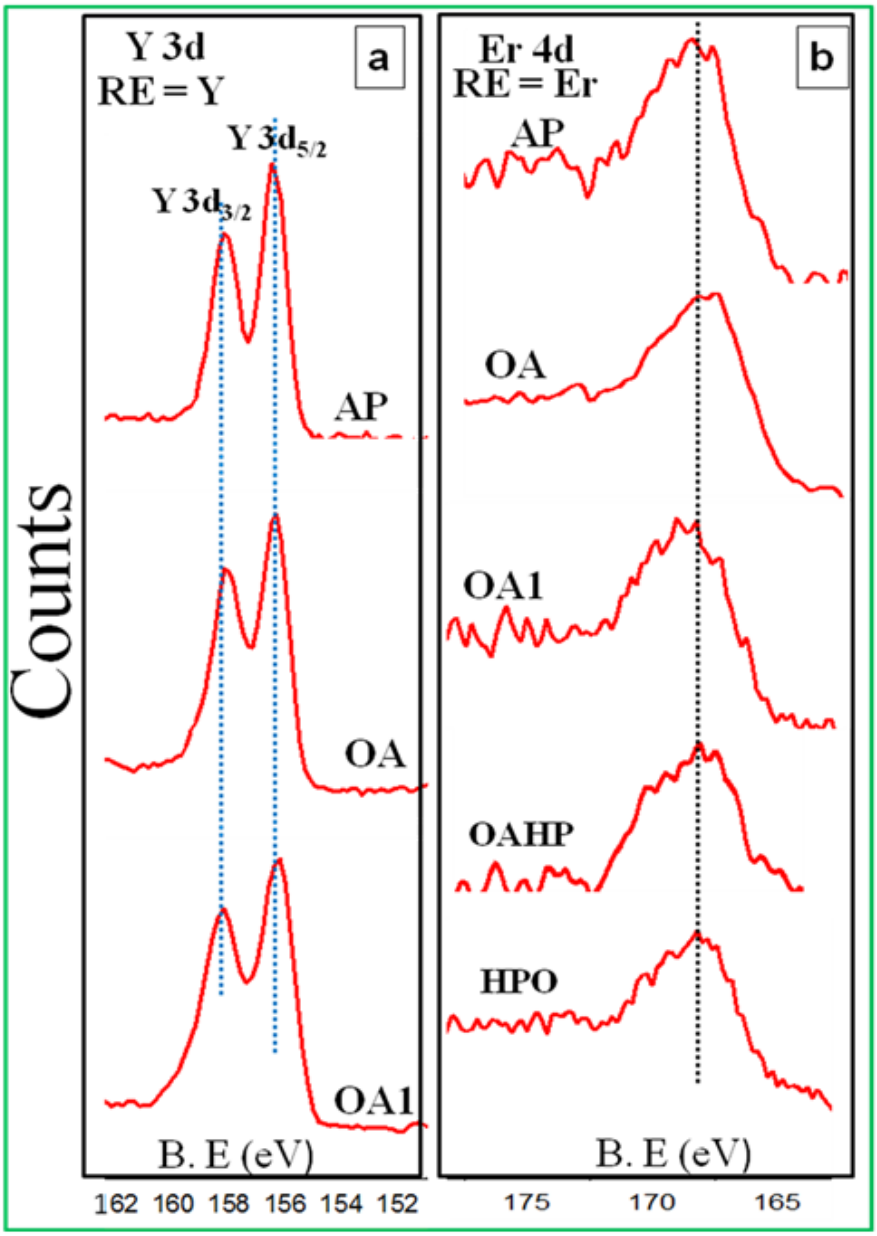

Figure 6.10. Core level XPS spectra of (a) Y 3d energy region for the $Mo_{0.3}Cu_{0.7}Sr_2YCu_2O_y$ samples and (b) Er 4d energy region for the $Mo_{0.3}Cu_{0.7}Sr_2ErCu_2O_y$ samples.

Er 4d core level spectra: The core level Er 4d spectra for all the $Mo_{0.3}Cu_{0.7}Sr_2ErCu_2O_y$ (AP, OA, OA1, OAHP and HPO) samples are shown in figure 6.10b. It shows a peak at 168.2 eV, which is similar to the binding energy of pure erbium oxide[24]. No significant change in the Er 4d spectra has been observed after oxygenation. Moreover, the peak position is found to be the same in all cases. This indeed corroborate the absence of Sr-Er intermixing after oxygenation in the present samples.

Mo 3d core level spectra: Figure 6.11a and 6.11b compares the XPS spectra of the Mo 3d core levels for the different $Mo_{0.3}Cu_{0.7}Sr_2YCu_2O_y$ (AP, OA and OA1) and $Mo_{0.3}Cu_{0.7}Sr_2ErCu_2O_y$ (AP, OA, OA1, OAHP and HPO) samples, respectively. All the spectra exhibit a two peak structure, typical of 3d core levels with spin orbit splitting. The Mo $3d_{5/2}$ and $3d_{3/2}$ peaks for the AP samples are at 232.1 eV and 235.2 eV respectively. We can observ both peak broadening and peak shifting for the oxygenated samples comparing to the AP one. The difference between $3d_{5/2}$ and $3d_{3/2}$ peaks is 3.1 eV for all the samples. The intensity ratios of the two components are close to 1.5 in all cases, which is expected from the multiplicity of the spin orbit split feature.

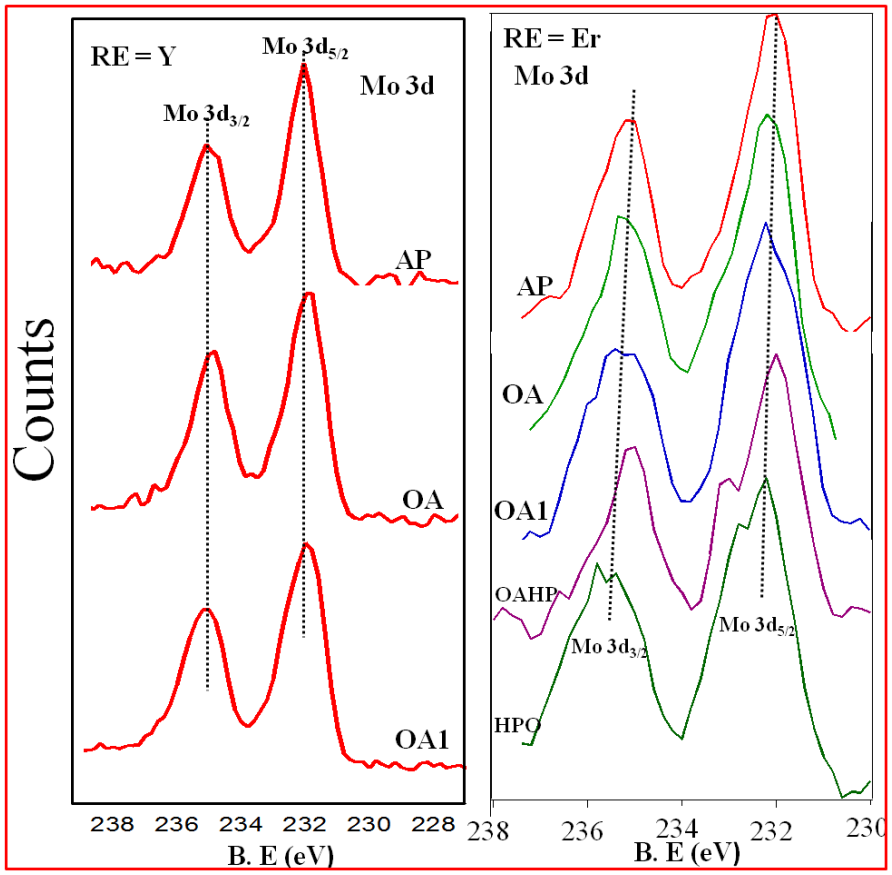

Figure 6.11. Core level XPS spectra of Mo 3d energy region for the $Mo_{0.3}Cu_{0.7}Sr_2RECu_2O_y$ (RE = Y and Er) materials.

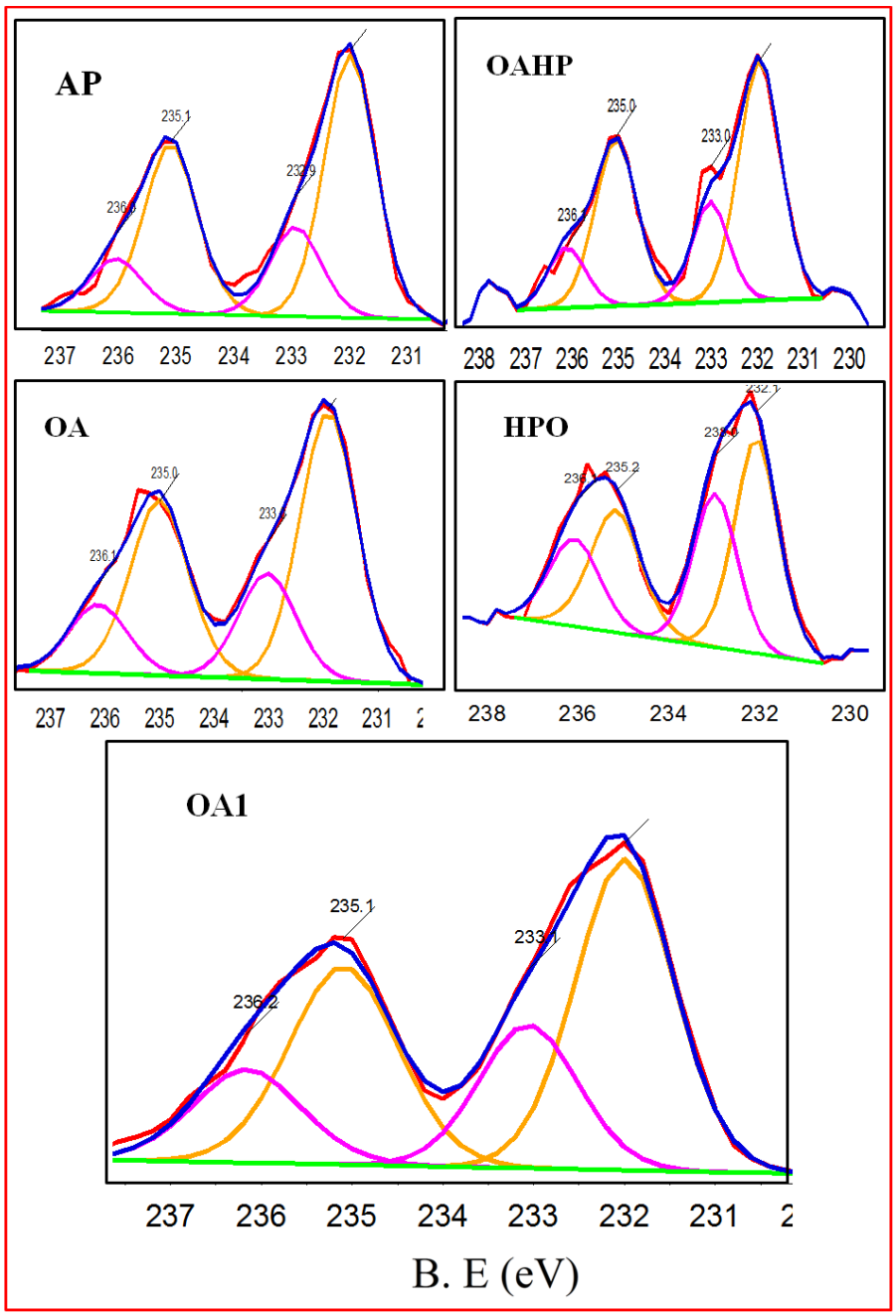

Figure 6.12. Fitted Mo 3d spectra for the $Mo_{0.3}Cu_{0.7}Sr_2ErCu_2O_y$ samples. It shows the co-existence of Mo^{V} and Mo^{VI}. The Mo^{VI} /Mo^{V} ratio increases after oxygenation.

However, to get the idea about the oxidation state of molybdenum, the reason of peak broadening and peak shifting, we have followed the fitting on the Mo 3d core level spectra. A spin-orbit splitting of 3.1 eV[25] and a $3d_{5/2}$:$3d_{3/2}$ intensity ratio of 3:2 have been used for the fitting after appropriate correction of the background with a single Shirley (Gaussian-step) function. The fitted spectra are shown in figure 6.12 and the detailed of the fitting parameters

are shown in table 6.4.

The fitting of the XPS spectra of Mo 3d core levels allow us to confirm the large content of Mo^{V} in the AP samples. Mo^{V} and Mo^{VI} are identified by the energy shifts of their core levels assigning the doublet at 232 eV & 235.1 eV ($3d_{5/2}$ and $3d_{3/2}$) to Mo^{V} and the one at 232.9 eV & 236.0 eV ($3d_{5/2}$ and $3d_{3/2}$) to Mo^{VI} as proposed in the previous chapter (*Chapter 5*). As one could expect, annealing under an oxygen atmosphere increases the amount of Mo^{VI} state. And for the HPO $Mo_{0.3}Cu_{0.7}Sr_2ErCu_2O_y$ sample, having the highest oxygen content (y = 7.55), we have found the highest amount of Mo^{VI} state (42%, and in AP sample Mo^{VI} = 24% and y = 7.34, see Table 6.2 and 6.4).

Table 6.4. Parameters and summary of fitting of the Mo3d XPS core level spectra for $Mo_{0.3}Cu_{0.7}Sr_2RECu_2O_y$ (RE = Y and Er) samples.

Sample	Sample Name	Core-level spectra	B. E (eV)	Mo^{V}/Mo^{VI}	Average oxidation state	Oxygen content (y)
RE = Er	AP	Mo^{V} $3d_{5/2}$ $3d_{3/2}$ Mo^{VI} $3d_{5/2}$ $3d_{3/2}$	232.0 235.1 232.9 236.0	0.76/0.24	5.24	7.34
	OA	Mo^{V} $3d_{5/2}$ $3d_{3/2}$ Mo^{VI} $3d_{5/2}$ $3d_{3/2}$	232.1 235.2 233.0 236.1	0.71/0.29	5.29	7.45
	OA1	Mo^{V} $3d_{5/2}$ $3d_{3/2}$ Mo^{VI} $3d_{5/2}$ $3d_{3/2}$	232.0 235.1 233.1 236.2	0.70/0.30	5.30	7.36
	OAHP	Mo^{V} $3d_{5/2}$ $3d_{3/2}$ Mo^{VI} $3d_{5/2}$ $3d_{3/2}$	231.9 235.0 233.0 236.1	0.69/0.31	5.31	7.46
	HPO	Mo^{V} $3d_{5/2}$ $3d_{3/2}$ Mo^{VI} $3d_{5/2}$ $3d_{3/2}$	232.1 235.2 233.0 236.1	0.58/0.42	5.42	7.55
RE = Y	AP	Mo^{V} $3d_{5/2}$ $3d_{3/2}$ Mo^{VI} $3d_{5/2}$ $3d_{3/2}$	232.0 235.1 233.3 236.4	0.89/0.11	5.11	-
	OA	Mo^{V} $3d_{5/2}$ $3d_{3/2}$ Mo^{VI} $3d_{5/2}$ $3d_{3/2}$	232.0 235.1 233.1 236.2	0.80/0.20	5.20	-
	OA1	Mo^{V} $3d_{5/2}$ $3d_{3/2}$ Mo^{VI} $3d_{5/2}$ $3d_{3/2}$	231.9 235.0 232.8 235.9	0.71/0.29	5.29	-

Cu 2p core level spectra: The Cu 2p core level spectra for the $Mo_{0.3}Cu_{0.7}Sr_2YCu_2O_y$ compounds are shown in figure 6.13. The main peak at 933 eV and the satellite at 942 eV correspond to the Cu $2p_{3/2}$ state and the next two are ascribed to the Cu $2p_{1/2}$.

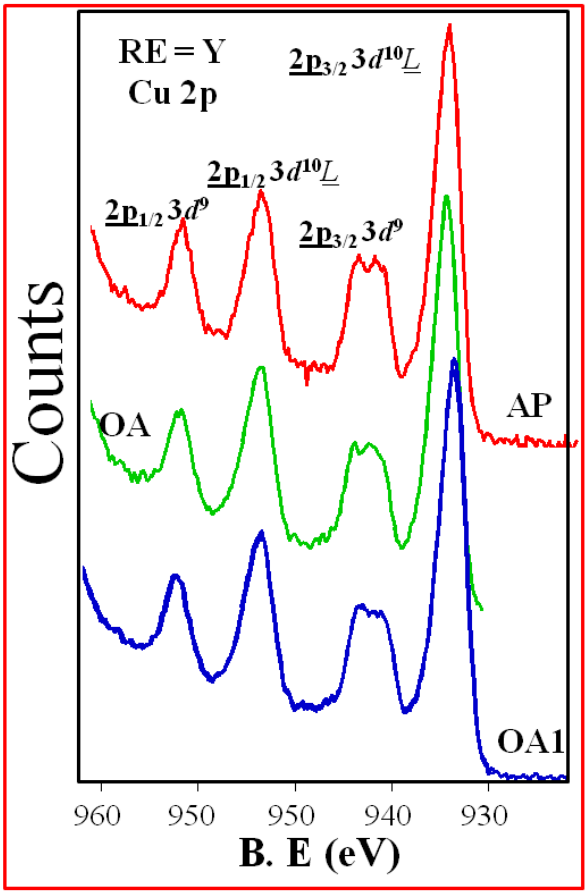

Figure 6.13. Core level XPS spectra of Cu2p energy region for the $Mo_{0.3}Cu_{0.7}Sr_2YCu_2O_y$ materials.

The Cu $2p_{3/2}$ spectra for all the $Mo_{0.3}Cu_{0.7}Sr_2ErCu_2O_y$ samples are shown in figure 6.14. The data have been normalized to the area under Cu $2p_{3/2}$ main line. The Cu $2p_{3/2}$ spectra for all the samples are typical of Cu^{II} compounds. The main peak near 933 eV is attributed to the well-screened $\underline{2p}^5 3d^{10}\underline{L}$ final states resulting from ligand-to-metal (O $2p \rightarrow$ Cu $3d$) charge transfer and the satellite at higher binding energy corresponds to a multiplet of $\underline{2p}^5 3d^9 L$ states, where underbar denotes a hole and L denotes the oxygen ligand.

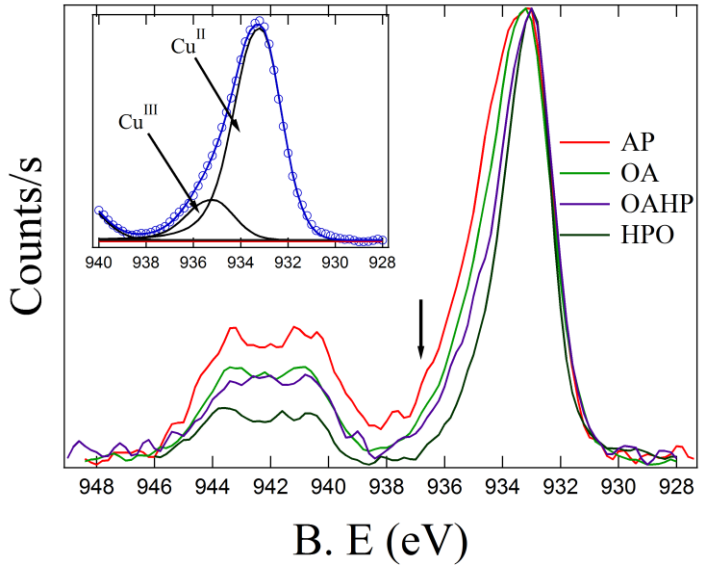

Figure 6.14. Core level XPS spectra of $Cu2p_{3/2}$ energy region for the AP, OA, OAHP and HPO $Mo_{0.3}Cu_{0.7}Sr_2ErCu_2O_y$ samples. The data have been normalized under the $Cu2p_{3/2}$ main peak. A Cu^{III} characteristic shoulder is shown by an arrow. Inset shows the fitted Cu2p spectrum of the OA sample.

In a simplified description of the Cu $2p_{3/2}$ spectrum, to maximize the energy gain, a doped hole first extend out as a symmetric coherent superposition of the four O 2p hole states surrounding the Cu^{II} ion and then hybridizes with the central Cu $d_{x^2-y^2}$ hole to form a Zhang-Rice singlet[30]. The ground state of the neutral CuO_4 cluster integrated in an effective medium in an extended configuration-interaction (CI) model[24,28,31,32] is a superposition of $|3d^9>$ and $|3d^{10}\underline{L}>$ electronic states. The interaction is described by the hybridization integral $T = <d^9|H|d^{10}\underline{L}>$. And the metal to ligand (Cu 3d–O 2p) charge transfer energy $\Delta = <d^9|H|d^9> - <d^{10}|H|d^{10}>$ is a measure of the bonding–antibonding separation in the ground state. According to the CI model, removing a core electron will suddenly switch on a 2p core hole and that will project the system into a two-hole final state configuration. The Coulomb interaction, that exists between the 3d electron and the core hole, could be filled by the charge transfer from the O-2p band. And as a consequence, the locally screened state has the configuration $\underline{2p}^5 3d^{10}\underline{L}$ and constitutes the main peak, while the locally unscreened $\underline{2p}^5 3d^9 L$ state is the shakeup satellite. Moreover, some weak states contribute to the asymmetry of the main peak.[31-35]

However, as shown in figure 6.14, one could see a clear shoulder (shown by an arrow) and broadening of the Cu $2p_{3/2}$ main peak at higher binding energy side for the AP sample, which is characteristic feature of Cu^{III}.[33] Also, the main peak is shifted towards the lower

energy side after oxygenation. We have fitted the Cu $2p_{3/2}$ spectra for all the samples. The fitted spectra are shown in figure 6.15 and 6.16 for the $Mo_{0.3}Cu_{0.7}Sr_2YCu_2O_y$ and $Mo_{0.3}Cu_{0.7}Sr_2ErCu_2O_y$ samples, respectively, and the fitting parameters, the summary of the fitting and the average oxidation state of copper are shown in table 6.5. Quite interestingly, *in parallel to the oxidation of the molybdenum species a reduction of the copper is observed on the XPS spectra of the Cu 2p core levels.* The average oxidation state of Cu goes from 2.19 in the AP $Mo_{0.3}Cu_{0.7}Sr_2ErCu_2O_y$ sample to 2.00 for the HPO $Mo_{0.3}Cu_{0.7}Sr_2ErCu_2O_y$ sample. For the $Mo_{0.3}Cu_{0.7}Sr_2YCu_2O_y$ samples, it goes from 2.27 to 2.19 after oxygenation. A single Gaussian peak (Figure 6.16), which represents the Cu^{II} state, fitted well with the Cu 2p spectra of the HPO $Mo_{0.3}Cu_{0.7}Sr_2ErCu_2O_y$ sample. Besides the peak shift, the satellite peak intensity is found to decrease after oxygenation. The satellite peak and the main peak intensity ratio (I_s/I_m, table 6.5) shows the lowest value for the HPO $Mo_{0.3}Cu_{0.7}Sr_2ErCu_2O_y$ sample, having the highest oxygen content (y = 7.55).

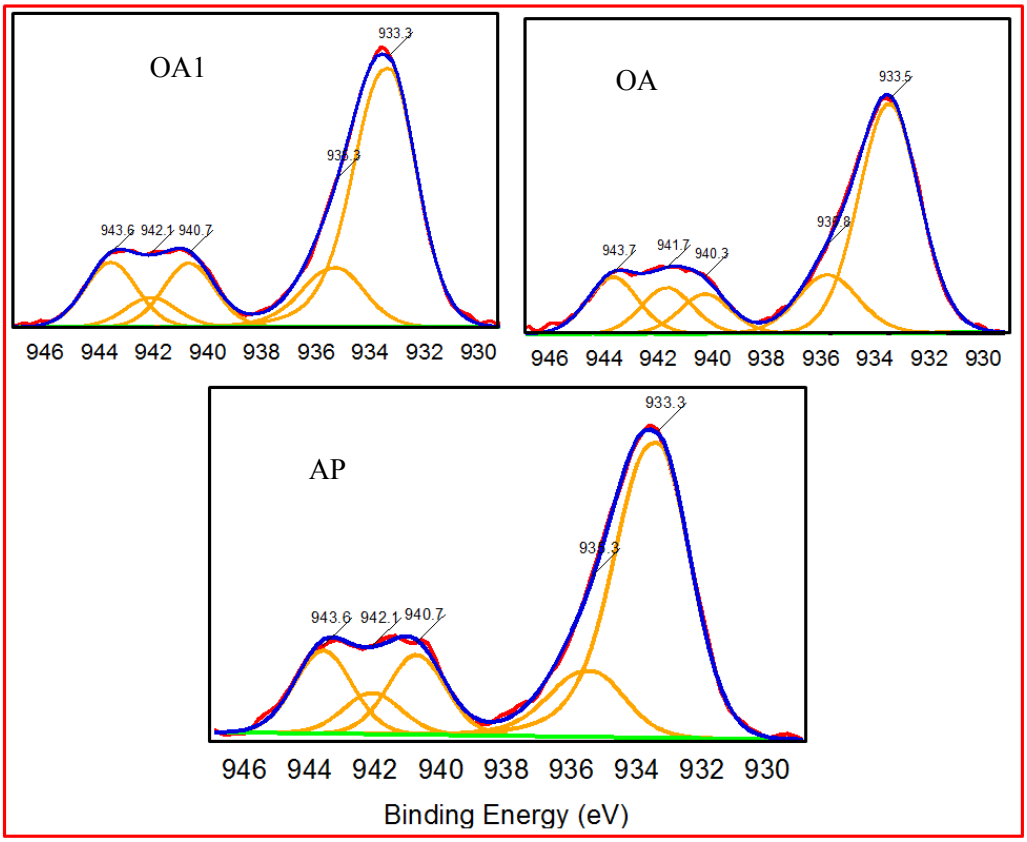

Figure 6.15. Fitted Cu $2p_{3/2}$ spectra for the $Mo_{0.3}Cu_{0.7}Sr_2YCu_2O_y$ samples.

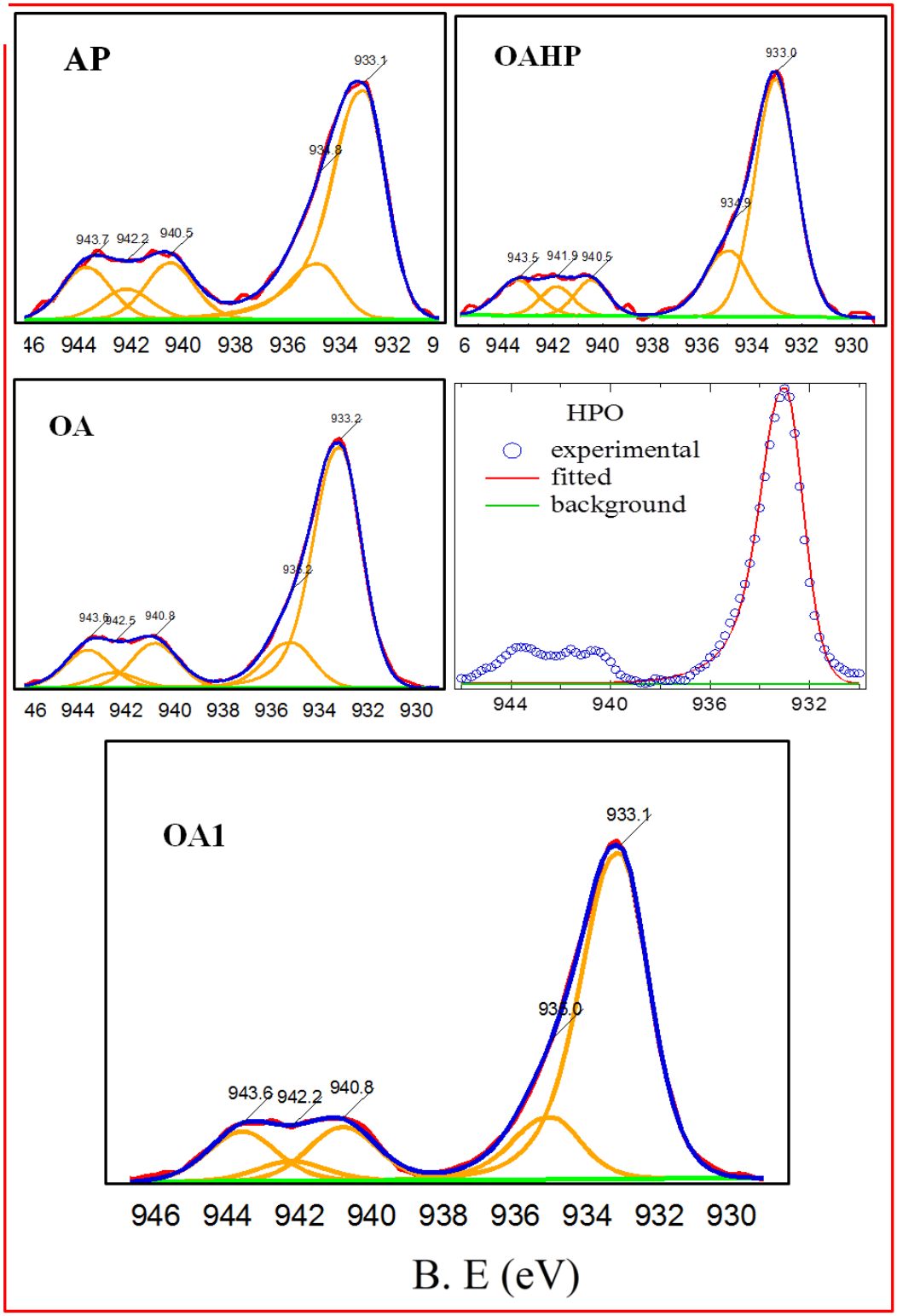

Figure 6.16. Fitted Cu $2p_{3/2}$ spectra for the $Mo_{0.3}Cu_{0.7}Sr_2ErCu_2O_y$ samples.

* All the $Cu2p_{3/2}$ spectra were fitted with a combination of Gaussian-Lorentzian lineshape by the ADVANTAGE software except for the HPO sample. The data of the HPO sample was fitted with a simple Gaussian function, only in the $Cu2p_{3/2}$ main peak by the IGOR-Pro (Wave Metrics) software.

Table 6.5. Parameters and summary of fitting of the $Cu2p_{3/2}$ XPS core level spectra for $Mo_{0.3}Cu_{0.7}Sr_2RECu_2O_y$ (RE = Y and Er) samples. The superconducting transition temperatures (T_C) and the oxygen contents are also included.

Sample	Sample Name with T_C in K	Core-level spectra	B. E (eV)	FWHM	Cu^{II}:Cu^{III}	Average Cu oxidation state	I_S/I_M	Oxygen Content (y)
RE = Er	AP (0 K)	Cu^{II} $2p_{3/2}$ Cu^{III} $2p_{3/2}$	933.1 934.8	2.00 2.00	0.81:0.19	2.19	0.26	7.34
	OA (32 K)	Cu^{II} $2p_{3/2}$ Cu^{III} $2p_{3/2}$	933.2 935.2	2.17 2.17	0.84:0.16	2.16	0.19	7.45
	OA1 (25 K)	Cu^{II} $2p_{3/2}$ Cu^{III} $2p_{3/2}$	933.1 935	2.00 2.00	0.84:0.16	2.16	0.16	7.36
	OAHP (45K)	Cu^{II} $2p_{3/2}$ Cu^{III} $2p_{3/2}$	933 934.8	2.02 2.02	0.88:0.12	2.12	0.16	7.46
	HPO (84 K)	Cu^{II} $2p_{3/2}$	933.0	1.80	1.00:0.00	2.00	0.12	7.55
RE = Y	AP (0 K)	Cu^{II} $2p_{3/2}$ Cu^{III} $2p_{3/2}$	933.3 935.4	2.56 2.56	0.73:0.27	2.27	0.28	—
	OA (36 K)	Cu^{II} $2p_{3/2}$ Cu^{III} $2p_{3/2}$	933.5 935.8	2.73 2.73	0.80:0.20	2.20	0.21	—
	OA1 (28 K)	Cu^{II} $2p_{3/2}$ Cu^{III} $2p_{3/2}$	933.3 935.3	2.56 2.56	0.81:0.19	2.19	0.25	—

O 1s core level spectra: Figure 6.17a and 6.17b show the O 1s spectra for the different $Mo_{0.3}Cu_{0.7}Sr_2ErCu_2O_y$ and $Mo_{0.3}Cu_{0.7}Sr_2YCu_2O_y$ samples, respectively. For the $Mo_{0.3}Cu_{0.7}Sr_2YCu_2O_y$ samples, the data have been normalized to the area under the peak at 529 eV. It is apparent that the O 1s spectra exhibit two broad peaks; one at ~529 eV with higher intensity and another (shoulder) at ~530.8 eV with lower intensity.

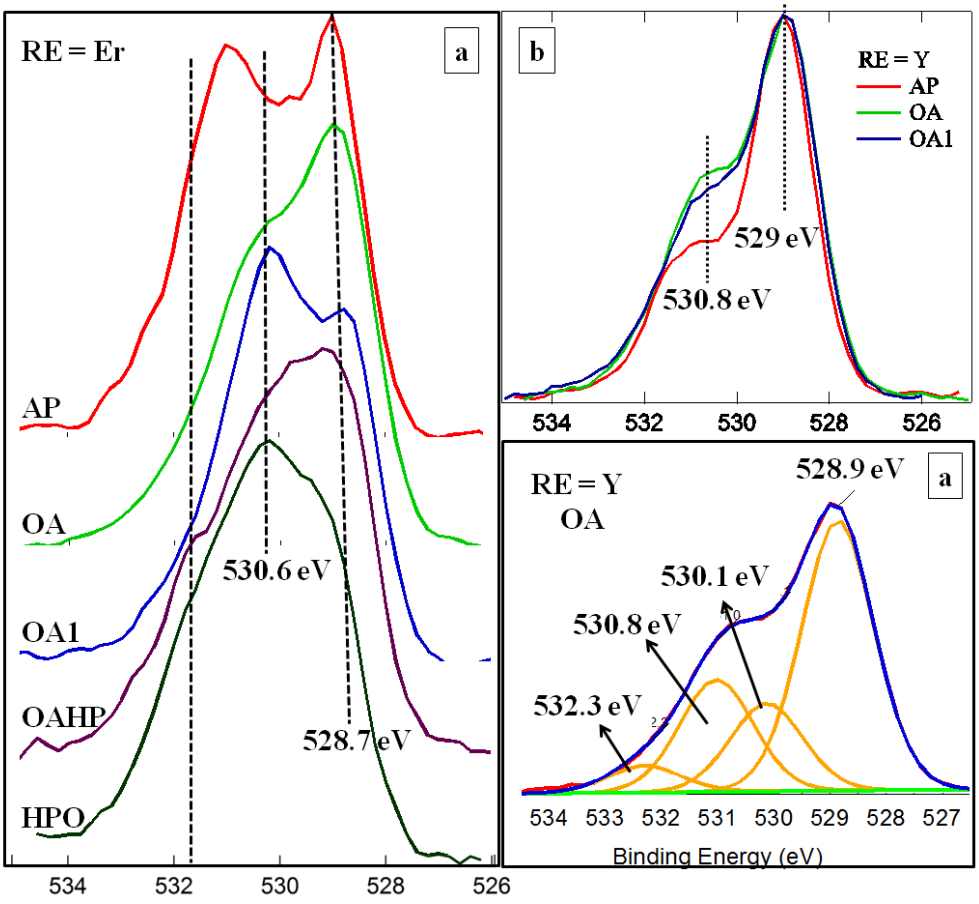

Figure 6.17. (a) Core level XPS spectra of O1s energy region for the $Mo_{0.3}Cu_{0.7}Sr_2ErCu_2O_y$ materials. (b) The data have been normalized to the area under the main peak (=1) at 529 eV for the $Mo_{0.3}Cu_{0.7}Sr_2YCu_2O_y$ materials. It indicates that an oxidation is taking place during annealing under oxygen. (c) Fitted O 1s spectrum for the OA $Mo_{0.3}Cu_{0.7}Sr_2YCu_2O_y$ material.

The AP $Mo_{0.3}Cu_{0.7}Sr_2ErCu_2O_y$ sample shows an intense peak at 531 eV. And for this sample the O1s is dominated by the peak at 531 eV. In fact, the peak (shoulder) at higher binding energy side (~532 eV) is very sensitive to the surface C contamination.[36] As we have observed a little amount of C, even after the scrapping (at the time of data recording), the higher energy side peak for the AP $Mo_{0.3}Cu_{0.7}Sr_2ErCu_2O_y$ sample may have the possibility of a correlation with the surface C contamination, but, certainly not the entire shoulder originates from carbonates.[26] Similarly, the broadening or the enhancement of the peak for

the $Mo_{0.3}Cu_{0.7}Sr_2Y/ErCu_2O_y$ samples, at higher energy side (~532 eV) could be due to the C contamination.[36]Equally, the presence of Mo in both the copper site (83% in Cu1 and 17% in Cu2 site, *Chapter 5*) for the AP $Mo_{0.3}Cu_{0.7}Sr_2ErCu_2O_y$ sample indeed makes the local chemical enviournment complicated, which may have a contribution in the intense peak observed at 531 eV.

However, both of the peaks are considerably broader for all the samples, which suggest the presence of overlapping multi-components in the samples. In the present system, the oxygen component is complex, which includes O1, O2, O3, and O4 at four different sites. O2 and O1 belongs to the SrO layers and CuO_2 planes, respectively and O3 and O4 belongs to the $(Mo/Cu)O_{1+\delta}$ site (Figure 6.8 and Figure 5.14 in the *Chapter 5*). So, the present O 1s emissions corresponds to the emission from O ions bonded to three different metal-oxide planes: O ions bonded to Mo/Cu in $(Mo/Cu)O_{1+\delta}$ planes, to Sr in SrO layers and to Cu in CuO_2 plane. We have fitted the O 1s spectrum for the OA $Mo_{0.3}Cu_{0.7}Sr_2YCu_2O_y$ sample with three different components. The fitted data are shown in figure 6.17c. From this fitting, we can ascribe the peak at 528.9 eV to the O2p-Cu3d bonding; consistent with the studies of other cuprate superconductors[26] while the peak at about 530.1 eV is ascribed to O2p-Mo3d bonding.[5] The peak at 530.8 eV could be due to the O bonding to Sr in the SrO layer. Another peak (fitting peak) at 532.3 eV is likely due to the surface C contamination.

As shown in figure 6.17b, with the normalized O 1s spectra, the shoulder at 530.8 eV (530.6 eV for the $Mo_{0.3}Cu_{0.7}Sr_2ErCu_2O_y$ samples, Figure 6.17a) is increased after oxygen annealing. In fact from the fitting, the peaks at 530.1 eV and 530.8 eV corresponds to the O ions bonded to the $(Mo/Cu)O_{1+\delta}$ and CuO_2 planes, respectively . So the enhancement of the shoulder at ~530.8 eV (530.6 eV for the $Mo_{0.3}Cu_{0.7}Sr_2ErCu_2O_y$ samples) could have a correlation with the extra oxygen ions in the $(Mo/Cu)O_{1+\delta}$ planes, after oxygenation. The oxygenation enhances the amount of oxygen in the $(Mo/Cu)O_{1+\delta}$ plane; this indeed enhances the amount Mo^{VI} state and increases the number of Mo–O bonds, these can reflect in the O 1s line shapes related to the O 2p–Mo 3d bonding. It is noteworthy that, we have also observed significant changes in the Sr 3d core-level spectra after the introduction of extra oxygen ions in the $(Mo/Cu)O_{1+\delta}$ plane. This suggests that the changes in the Sr 3d core level spectra may have a correlation with the enhancement of O 1s spectra at the higher energy side, after oxygenation.

6.4. Discussion and conclusion

Surface electronic structure: At the beginning of this discussion on the electronic states of the scraped $Mo_{0.3}Cu_{0.7}Sr_2RECu_2O_y$ materials, we emphasize that we can only obtain average information from the surface. We did eliminate the surface contamination by repeated scraping in ultra-high vacuum. The effect of cleaning was eventually evidenced in the strong attenuation of the C ls signal.

The Y 3d and Er 4d core level spectra do not show significant changes, after oxidation, as expected. A small asymmetry is observed in the Y 3d core level spectra after oxygenation; this could be due to more than one electrostatic screening environment for the Y ions upon enhancement of holes in the CuO_2 planes, after oxygenation.

The Sr 3d and O 1s core level spectra show a complicated scenario. As discussed earlier, two doublets and the changes in the Sr 3d core level spectra after oxygenation may have two possible explanations. Nevertheless, the structural analysis using the diffraction (NPD and XRD) patterns does not show any indication of the intermixing of Sr and Er in their respective site, in any case. The occupancies of the Sr and Er become negative when they are allowed to share the Er and Sr site, respectively. At the same time, we don't observe any significant change in the Er 4d core level spectra; in fact, the spectra remain same in all cases. Both of these observations rule out the possibility of intermixing of Sr and Er in the structure. The structural studies, discussed in the previous chapter (*Chapter 5*), showed the accumulation of oxygen in the copper chain site ($Cu,Mo–O_{1+\delta}$) after oxygenation; the extra oxygen after oxygen annealing, is introduced in the copper chain site. The amount of extra oxygen in the chain site (δ) changes from 0.34 ($(Cu,Mo)–O_{1.34}$ in AP $Mo_{0.3}Cu_{0.7}Sr_2ErCu_2O_{7.34}$) to 0.55 ($(Cu,Mo)–O_{1.55}$ in HPO $Mo_{0.3}Cu_{0.7}Sr_2ErCu_2O_{7.55}$), after HP oxygenation. As the Sr atom (SrO layer) resides between the $(Cu,Mo)O_{1+\delta}$ chain and CuO_2 plane in the structure, the extra oxygen atoms in the copper chain ($(Cu,Mo)O_{1+\delta}$) site can change the local chemical environment of the Sr atom, which will be reflected in the core level spectra of the Sr 3d.

From the fitting of O1s spectrum, we have found that the O 1s emissions for the present compounds correspond to the emission from O ions bonded to the three different metal-oxygen planes. It shows that the shoulder around 530.1 eV corresponds to the O2p-Mo3d bonding, which in fact increases after oxygenation. As discussed earlier, the introduction of the extra oxygen in the (Cu/Mo)-$O_{1+\delta}$ plane can change the local environment of the Sr atom as it (Sr-O) resides between (Cu/Mo)-$O_{1+\delta}$ and Cu-O plane in the (Mo,Cu)-

1212 structure. Therefore, our study suggests that the observed changes in the Sr 3d and O 1s spectra are correlated. The copper chain site ((Cu/Mo)-$O_{1+\delta}$) changes from (Cu,Mo)–$O_{1.34}$ to (Cu,Mo)–$O_{1.55}$ (HPO $Mo_{0.3}Cu_{0.7}Sr_2ErCu_2O_{7.55}$ sample) with the oxygenation. This indeed increases the number of oxygen bonds with Sr and Mo, which certainly changes the chemical environment of the Sr atom and this is reflected in the core level spectra of the Sr 3d and the O 1s. So, as a consequence of the extra oxygen atoms introduced in the copper chain site ((Cu,Mo)–$O_{1+\delta}$ layer), the Sr 3d and O 1s core level spectra show changes after oxygen annealing (oxygenation).

The extra oxygen after oxygenation, increases the number of Mo–O and Sr-O bonds (also it enhances the amount of the Mo^{VI} state), and has a major contribution to the enhancement of the peak related to the O 2p-Mo 3d bonding. The enhancement of the peak for the AP $Mo_{0.3}Cu_{0.7}Sr_2ErCu_2O_y$ sample, at the higher energy side (~531 eV) could be originated from the presence of Mo in both copper sites (83% in Cu1 and 17% in Cu2 site), which indeed makes the local chemical environment very complicated. However, the enhancement or broadening of the peak at higher energy side (~532 eV) is likely due to the surface contamination, due to the formation of carbonates.

Self doping redox mechanism: Fitting of the Mo 3d and Cu 2p core level spectra allows us to suggest a very interesting doping mechanism upon oxidation. In parallel to the oxidation of the molybdenum species the copper is found to be reduced after oxygenation. As discussed in the previous chapter (*Chapter 5*), a different self-doping mechanism than that observed in $RuSr_2RECu_2O_8$ (RE=rare earth cation) materials can be deduced from our XPS measurements on a set of eight different 1212 molybdo-cuprates ($Mo_{0.3}Cu_{0.7}Sr_2RECu_2O_y$ (RE = Y and Er)) samples.

$$Mo^{V}{}_{x}Mo^{VI}{}_{(0.3-x)} + Cu^{III}{}_{y}Cu^{II}{}_{(2.7-y)} \leftrightarrow Mo^{V}{}_{(x-m)}Mo^{VI}{}_{(0.3-x+m)} + Cu^{III}{}_{(y-n)}Cu^{II}{}_{(2.7-y+n)}$$

Where $0 \leq (x-m) \leq 0.3$ and $0 \leq (y-n) \leq 2.7$

The presence of a high amount of Mo^{V} (76% and 89% for the AP $Mo_{0.3}Cu_{0.7}Sr_2ErCu_2O_y$ and $Mo_{0.3}Cu_{0.7}Sr_2YCu_2O_y$ samples, respectively) may be responsible for the decrease in the oxidation state of copper as it tries to make itself stable in Mo^{VI} oxidation state during the oxidation process and to yield the charge balance the average copper valence state decreases. As we have copper in both sites (Cu1 and Cu2), it is not possible to estimate the accurate hole concentration (and/or the oxidation state of copper for individual site) in the CuO_2 plane from the present XPS results. However, the TEP measurements show the enhancement of the hole concentration with increasing oxygen content. Therefore, it is likely that the oxidation

(reduction)/doping mechanism discussed above is confined to the copper chain site and consequently, the oxidation state of copper, in the CuO_2 plane increases with oxygenation, and so does T_C in an important amount up to 84 K (Table 6.2, Figure 6.3 and 6.4).

Charge transfer energy and orbital admixture: The superconducting transition temperatures as a function of the satellite to main peak (I_s/I_m) intensity ratios is shown in figure 6.18. This shows a decreasing trend of I_s/I_m with increasing superconducting transition temperature.

According to the Configuration Interaction (CI) model[26], the change in the ratio between the satellite peak and the main peak (I_s/I_m) intensity is associated with a charge transfer energy (Δ) from the O 2*p* to the Cu 3*d* state.[27-29] This ratio goes in parallel with the charge transfer energy: it decreases when the charge transfer energy decreases.

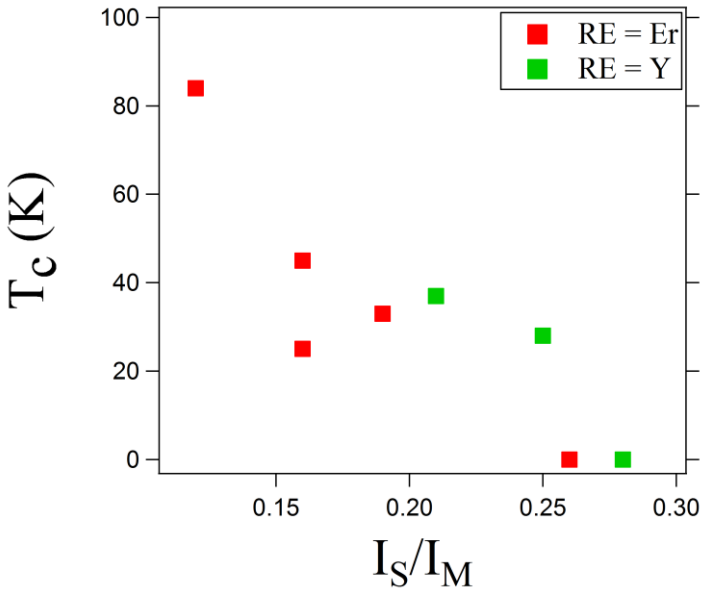

Figure 6.18. Change of superconducting transition temperatures (T_C) with I_s/I_m ratios for the $Mo_{0.3}Cu_{0.7}Sr_2RECu_2O_y$ (RE = Y and Er) samples.

It is well known that the hybridization of Cu 3d orbital with in-plane O 2p orbital dominates the valence-band structure of the cuprate superconductors.[37] Still there is a lively debate whether a multi-band model with other orbitals such as Cu $3d_{3z^2-r^2}$, O$2p_z$ (from apical O sites) should be considered to describe the transport properties and superconductivity in cuprates. Studying the Cu $2P_{3/2}$ core-level spectra of cuprates, *Parmigiani et al.*[28,38] proposed that besides the in plane O $2p_{x,y}$ → Cu $3d_{3x^2-y^2}$ charge transfer the apical O $2p_z$ → Cu $3d_{3z^2-r^2}$ charge-transfer mechanism is also allowed when the Cu ions have the octahedral or pyramidal coordination with the ligand oxygen. As the copper in the copper plane site is in

square pyramidal coordination in the structure of the present materials (indeed, in any 1212-type structure), both charge transfers are allowed here.

Studying the $Bi_2Ca_{1-x}RE_xSr_2Cu_2O_{8+s}$ (RE = Rare Earth materials) series *Rao el. al.*[39] showed that the satellite intensity goes through a minimum around the same composition where the hole concentration as well as the T_C show maxima. But the oxygen contents were assumed to be the same for all compounds in their studies. However, a recent study with YBCO showed that the I_S/I_M ratio (so that charge transfer energy) increases with increasing oxygen content associated with a hike in T_C.[40] It is noteworthy here that our materials have a structure similar to YBCO, this prompted us to compare our results with those of YBCO. Interestingly and contrary to the previous result[40], a decrease in both the I_S/I_M ratio and overall oxidation state of copper has been observed after oxygenation; this is likely correlated with the decrease in the charge-transfer energy. A schematic diagram, highlighting the hybridizations along with the structure of the present materials, is presented in figure 6.19.

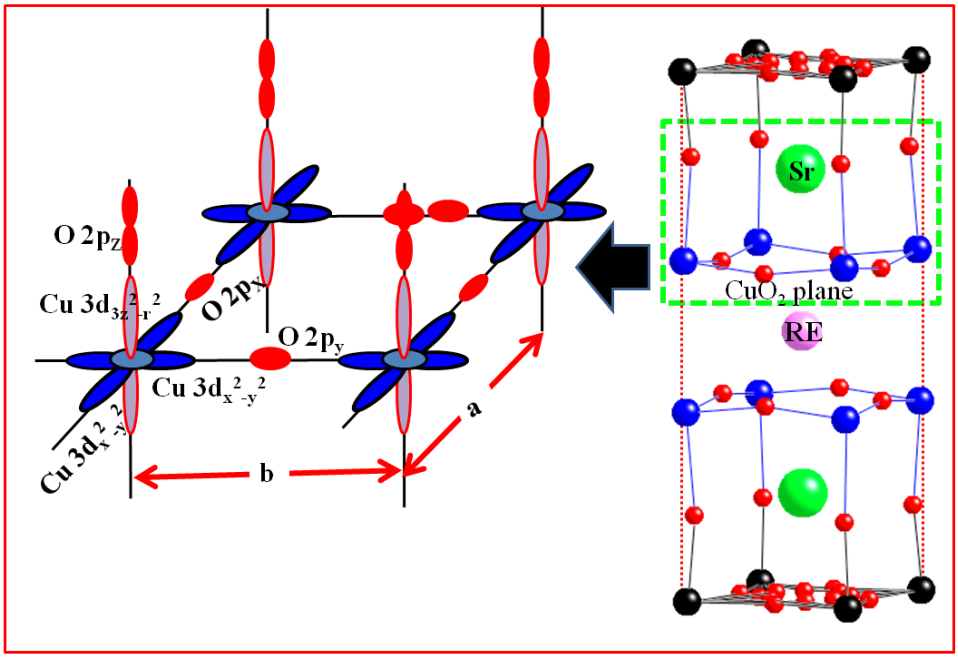

Figure 6.19. In plane and out of plane hybridization of Cu in the CuO_2 plane with oxygen ions having Cu ions in the pyramidal coordination, which highlights the possibility of both the in plane ($O\ 2p_{x,y} \rightarrow Cu\ 3d_{3x^2-y^2}$) and apical ($O\ 2p_z \rightarrow Cu\ 3d_{3z^2-r^2}$) charge-transfer.

Besides the interesting electronic states (and/or in the electronic structure), some remarkable and unconventional structural points have also been observed for the present materials. As discussed earlier (structural part of the *chapter 5*), that similar to the other molybdo-cuprate compounds[10] an unconventional contraction in the apical Cu2–O2 (d_{apical}) bond length is observed after oxygenation (figure 6.20) with increasing T_C. The role of apical

oxygen (O2 in the present materials) in high-T_C superconductivity has been suggested to have a great importance in several experiments and theories.[41-46] For instance, empirically, the presence of apex oxygen atoms makes the CuO_2 plane easier to dope with the holes; the compounds with the square coordination have not been doped successfully but those with the octahedral coordination have been made over-doped.[47] Also, pressure effect on T_C studies show that the T*-phase superconductor with the pyramidal copper coordination (having the apex oxygen atoms) have a very large pressure enhancement of T_C. On the other hand, in the T'-phase superconductor which has no apex oxygen atoms, the pressure coefficient of T, is negligibly small.[42] Our structural results then clearly indicate that the apical oxygen is playing an important role in assisting the charge transfer between the $(Mo/Cu)O_{1+\delta}$ chain and CuO_2 copper plane in the phase transformation (semiconducting to superconducting).

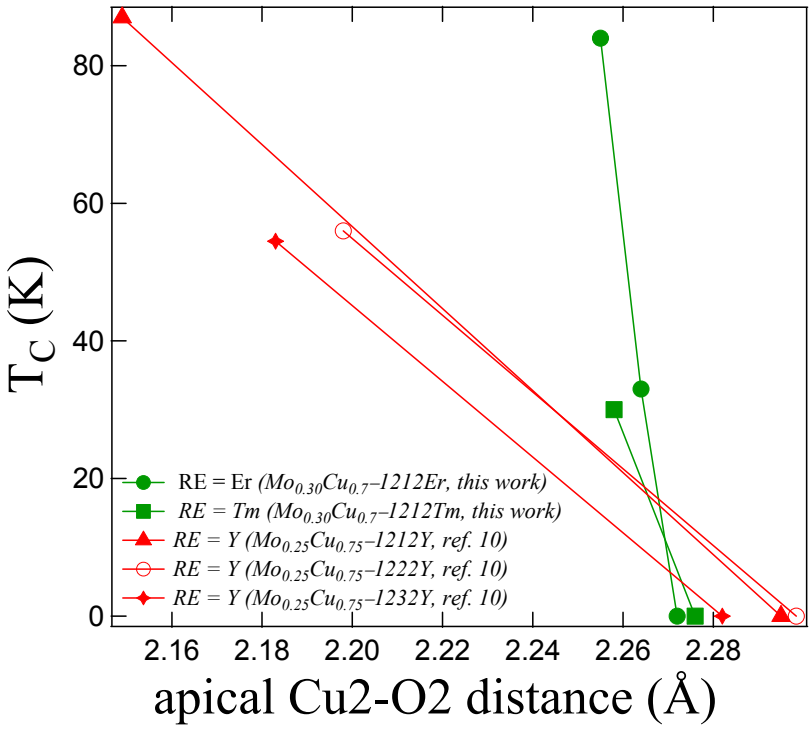

Figure 6.20. Variation of apical Cu2-O2 distances with the superconducting transition temperatures (T_C) for the $Mo_{0.3}Cu_{0.7}Sr_2RECu_2O_y$ (RE = Er and Tm, *Chapter 5*) samples. $(Mo_{0.25}Cu_{0.75})Sr_2YCu_2O_y$ ($Mo_{0.25}Cu_{0.75}$ – 1212Y, ref. 10), $(Mo_{0.25}Cu_{0.75})Sr_2CeYCu_2O_y$ ($Mo_{0.25}Cu_{0.75}$ – 1222Y, ref. 10) and $(Mo_{0.25}Cu_{0.75})Sr_2(Ce_{2/3}Y_{1/3})_3Cu_2O_y$ ($Mo_{0.25}Cu_{0.75}$ – 1232Y, ref. 10) samples are also compared.

On the other hand, Sakakibara et. al.,[48] proposed that shortening of the apical O distance (Cu2–O2) increases the admixture of the Cu $3d_{3z^2-r^2}$ orbital with the in-plane Cu $3d_{x^2-y^2}$ orbital, and this decreases T_C. In fact, in single-layer cuprates, increasing the apical

oxygen distance reduces the charge-transfer energy, which increases the superconducting transition temperature.[48,49] $HgBa_2Ca_2Cu_3O_{8+\delta}$ shows the largest Tc having a large apical distance and almost flat copper plane.[48-52] Therefore, shortening of the apical oxygen distance in our oxygenated superconducting samples may deteriorate the hole transfer (charge transfer) from the copper chain site. Nevertheless, the TEP measurements show that hole concentration in the CuO_2 plane increases after oxygenation in the present materials. A recent theoretical work by Yee at. al.,[53] in contrast with the Sakakibara et. al.,[48] proposed that charge transfer energy controls the strength of correlations and therefore tunes the maximum superconducting transition temperature; starting with the most correlated cuprate La_2CuO_4, reducing charge transfer energy enhances the T_C. Also, *Chmaissem et. al.*[54] showed that the hole concentration per CuO_2 plane to the CuO_2 plane could increase with a movement of apical O distance toward the CuO_2 plane after oxygenation.

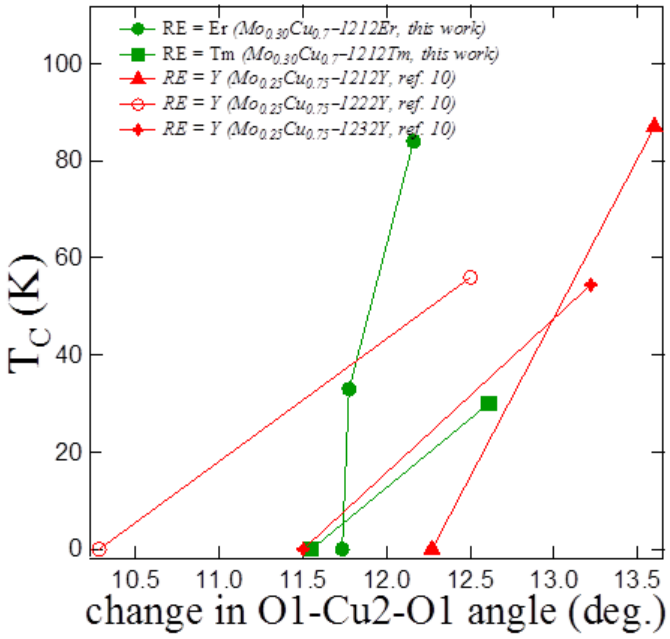

Figure 6.21. Variation of the change in buckling angles (O1-Cu2-O1 angle) with the superconducting transition temperatures (T_C) for the $Mo_{0.3}Cu_{0.7}Sr_2RECu_2O_y$ (RE = Er and Tm, chapter 5). $(Mo_{0.25}Cu_{0.75})Sr_2YCu_2O_y$ ($Mo_{0.25}Cu_{0.75}$ – 1212Y, ref. 10), $(Mo_{0.25}Cu_{0.75})Sr_2CeYCu_2O_y$ ($Mo_{0.25}Cu_{0.75}$ – 1222Y, ref. 10) and $(Mo_{0.25}Cu_{0.75})Sr_2(Ce_{2/3}Y_{1/3})_3Cu_2O_y$ ($Mo_{0.25}Cu_{0.75}$ – 1232Y, ref. 10) materials are also compared here.

At the same time, moving the apical oxygen towards the copper plane makes the copper plane buckled increasing the electron-electron repulsion; this is known to damage the superconducting properties. It is worth recalling here that the structural studies for the present materials (*Chapter 5*) showed the enhancement of buckling in the CuO_2 plane after

oxygenation in parallel with increasing T_C. The change in the buckling angle with T_C for the present materials and for similar molybdo-cuprate materials are shown in figure 6.21.

As discussed earlier, the decrease in the I_S/I_M ratio is likely correlated with the decease in the charge transfer energy. Therefore, in an agreement with Yee et. al.,[53] our experimental results indicate that charge transfer energy is the key factor to tune the superconducting transition temperature (T_C). We have observed that T_C increases with decreasing charge transfer energy. This is occuring in parallel with the shortening of the apical O distance (Cu2–O2) and increasing CuO_2 plane buckling, while the two orbital model[48] predicts the opposite effect. The enhancement of the CuO_2 plane buckling and the shortening of the apical O distance (Cu2–O2) in parallel with increasing T_C for the present molybdo-cuprate materials could be a response to the electronic structure of this family. Thus, similar high T_C´s should be possible, for similar oxygen contents and charge transfer energies, if flatter CuO_2 (less buckling) planes with long apical O distance could be synthesized.

However, as already discussed, the present XPS studies are limited to the surface of these polycrystalline samples. Further investigations, preferably using other analysis techniques that are sensitive to the local chemical environment of the ions and are sensitive to the bulk of the samples (for instance X-ray Absorption spectroscopy) are certainly needed to clarify all these points.

References

[1]Bednorz J G and Muller K A 1986, Phys. Rev. B **50**, 3458.

[2]Imada M, Fujimori A and Tokura Y 1998, Rev. Mod. Phys. **70**, 1039.

[3]Bauernfeind L, Widder W and Braun H F 1995 Physica C **254**, 151-158.

[4]Hor P H, Meng R L, Wang Y Q, Gao L, Huang Z J, Bechtold J, Forster K and Chu C W 1987 Phys. Rev. Lett. **58**, 1891.

[5]Marik S, Moran E, Labrugere C, Toulemonde O and Alario-Franco M A 2012 J. Solid State Chem. **191,** 40-45.

[6]Marik S, Dos Santos-Garcia A J, Morán E, Toulemonde O and Alario-Franco M A 2013 Journal of Physics-Condensed Matter **25**, 165704.

[7]Marik S, Dos Santos-Garcia A J, Morán E, Toulemonde O and Alario-Franco M A (not submitted)

[8]Xiong Q, Xue Y Y, Chu J W, Sun Y Y, Wang Y Q, Hor P H and Chu C W 1993 Phys. Rev. B **47**, 11337.

[9]Awanaa V P S, Gupta A, Kishan H, Takayama-Muromachi E, Watanabe T, Karppinen M, Yamauchi H, Malik S K, Yelon W B, Ganesan V and Narlikar A V 2003 Solid State Commun. **129**, 117-121.

[10]Grigoraviciute I, Yamauchi H, Karppinen M and Marezio M 2010 Phys. Rev. B **82**, 104507.

[11]Grigoraviciute I, Karppinen M, Chan Ting-Shan, Liu Ru-Shi, Chen Jin-Ming, Chmaissem O and Yamauchi H 2010 JACS **132**, 838-841.

[12]Tsay H. L., Shih C. R., Chen Y. C., Lee W. H., Meen T. H. and Yang H. D. *Physica C* **1995**, 252, 79-86.

[13]Tsay H. L., Chen Y. C., Weng S. S., Chang C. F. and Yang H. D. *Phys. Rev. B* **1999-I**, 59, 636-640.

[14]Hu S F, Liu R S, Su S C, Shy D S and Jefferson D A 1994 J. Solid State Chem. **112**, 203.

[15]Harlow R L, Kwei G H, Suryanarayanan R and Subramanian M A 1996 Physica C **257** 125-136.

[16]William T A, Harrison S R, Vaughey J T, Liu L and Jacobson A J 1995 J. Solid State Chem. **119**, 115-119.

[17]Sakakibara H, Usui H, Kuroki K, Arita R and Aoki H 2010 Phys. Rev. Lett. **105**, 057003.

[18]Buchner B, Breuer M, Freimuth A and Kampf A P 1993, Phys. Rev. Lett. **73**, 1841-1844.

[19]Hillebrecht F U, Fraxedas J, Ley L, Trodahl H J, Zaanen J, Braun W, Mast M, Petersen H, Schaible M, Bourne L C, Pinsukanjana P and Zettl A 1989 Phys. Rev. B **39**, 236.

[20]Ando Y, Lavrov A N, Komiya S, Segawa K and Sun X F 2001 Phys. Rev. Lett. **87**, 017001-1.

[21]Moulder J F, Stickle W F, Sobol, P E and Bomben K D *Handbook of X-Ray photoelectron spectroscopy*; Physical Electronics, U.S.A., Inc.: 1995.

[22]Khaled M, Srivastava P, Sekhar B R, Garg K B, Agarwal S K, Nalikar A V and Studer F 1998 J. Phys. Ckem Solids, **59**, No. 5. pp. 771-782.

[23]Uwamino Y, Ishizuka Y, Yamatera H 1984 J. Electron Spectrosc. Relat. Phenom. **34** 67.

[24]Dzhurinskii B F, Gati D, Sergushin N P, Nefedov V I, Salyn Y V, 1975 Russ. J. Inorg. Chem. **20**, 2307–2314.

[25]Katrib A, Logie V, Peter M, Wehrer P, Hilaire L and Maire G 1997 J. Chim. Phys. Phys.-Chim. Biol. **94**, 1923.

[26]Larsson S 1976 Chem. Phys. Lett. **40**, 362.

[27]Van der Laan G, Westra C, Haas C and Sawatzky G A 1981 Phys. Rev. B **23**, 4369.

[28]Parmigiani F and Sangaletti L 1994 J. Electron Spectrosc. Relat. Phenom. **66**, 223.

[29]Vasquez R P, Novikov D L, Freeman A J and Siegal M P 1997-I Phys. Rev. B **55**, 21.

[30]Zhang F C, Rice T M 1988, Phys. Rev., B **37**, 3759.

[31]Hiena T D, Mana N K, Gargb K B 2003, JMMM **262**, 508–513.

[32]Okada K and Kotani A 1989, J. Phys. Soc. Jpn. **58**, 2578–2585.

[33]Allan K, Campion A, Zhou J and Goodenough J B 1990 Phys. Rev. B **41**, 11572.

[34]Yuan C H, Shi L, Wang B M and Zhang Y Q 2007 Solid State Communications **143**, 267–271.

[35]Balzarotti A et al., Characterization of high temperature superconductors by high excitation spectroscopies, Vol. 4, Nova Science, New York, 1989, p. 113.

[36]Kosola A, Putkonen M, Johansson Leena-Sisko, Niinistö 2003, Appl. Surf. Sci., **211**, 102–112.

[37]Yu W J, Mao Z Q, Liu X M, Tian M L, Zhou G E and Zhang Y H 1996, Physica C **261**, 27-32.

[38]Fink J, Niicker N, PeUegrin E, Romberg H, Alexander M and Knupfer M 1994 J. Electron Spectrosc. Relat. Phenom. **66**, 395.

[39]Rao C N R, Rao G. Ranga, Rajumon M K and Sarma D D 1990, Phys. Rev. B, **42**, 1026.

[40]Maiti K, Fink J, Jong S, Gorgoi M, Lin C, Raichle M, Hinkov V, Lambacher M, Erb A and Golden M 2009, Phys. Rev. B, **80**, 165132.

[41]Kaldis E, Fischer P, A. Hewat W, Hewat E A, Karpinski Jand Rusiecki S 1989, Physica C **159**, 668.

[42]Murayama C, Mori N, Yomo S, Takagi, Uchida S and Tokura Y 1989, Nature **339**, 293.

[43]Muller K A 1990, Z. Phys. B **80**, 193.

[44]Matsukawa H and Fukuyama H 1990, J. Phys. Soc. Jpn. **59**, 1723.

[45]Tohyama T and Maekawa S 1990, J. Phys. Soc. Jpn. **59**, 1760; Physica B 1990, **165-166**, 1019.

[46]OhtaY, Tohyama T and Maekawa S 1991, Phys. Rev. B **43**, 2968.

[47]Torrance J B, Bezinge A, Nazzal A I, Huang T C, Parkin S S P, Keane D T, LaPlaca S J, Horn P M and Held G A 1989 Phys. Rev. B **40**, 8872.

[48]Sakakibara H, Usui H, Kuroki K, Arita R and Aoki H 2012 Phys. Rev. Lett. **85**, 064501.

[49]Weber C, Yee C, Haule K and Kotliar G 2012 EPL **100**, 37001.

[50]Chmaissem O, Huang Q, Antipov E V, Putilin S N, Marezio M,. Loureiro S M, Capponi JJ, Tholence J L and Santoro A 1993 Physica C **217**, 265.

[51]Zhang X, Lu W H and Ong C K 1997 Physica C **289**, 99-108.

[52]Chu C W, Gao L, Chen F, Huang Z J, Meng R L and Xue Y Y 1993 Nature **365**, 323-325.

[53]Chmaissem O, Jorgensen J D, Short S, Knizhnik A, Eckstein Y and Shaked H 1999 Nature (London) **397**, 45.

[54]Chmaissem O, Jorgensen J D, Short S, Knizhnik A, Eckstein Y and Shaked H 1999 Nature (London) **397**, 45.

Chapter 7

New 1212–molybdo-cuprate phases using High pressure and high temperature synthesis

General Overview

This chapter describes about the new 1212-molybdo-cuprate compounds with nominal composition $Mo_{0.5}Cu_{0.5}Sr_2RECu_2O_{7.5}$ ($Mo_{0.5}Cu_{0.5}$–1212 RE). High pressure and high temperature technique has been used to synthesize these compounds. Here we describe, the synthesis, structure and microstructure and magnetic properties of the materials corresponding to RE = Gd, Y, Ho and Er.

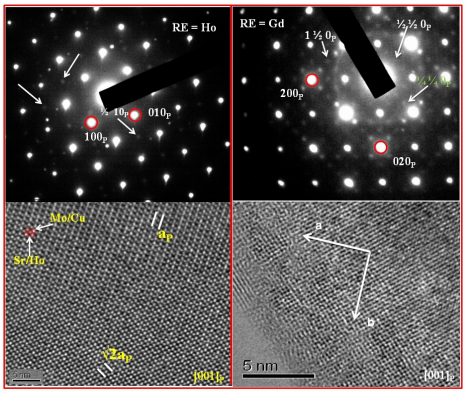

7.1. Introduction

As already mention in this thesis, since the discovery of high temperature superconductivity (SC) in $YBa_2Cu_3O_y$ (YBCO), most of the work devoted to the search of high temperature superconductors has relied upon the synthesis of new materials derived from $YBa_2Cu_3O_y$ and, in particular, upon the substitution of one of the copper atoms located in the so-called charge reservoir layer (CRL).[1] The 1212–type layered cuprates with general formula $MA_2RECu_2O_8$ or M – 1212 (where M is commonly a transition metal element, A is an alkaline earth metal, and RE is a rare earth ion), iso-structural with the classical $YBa_2Cu_3O_y$ (YBCO or Cu–1212) in which Y, Ba, and Cu1 (the chain copper site) are completely or partially replaced with rare earth elements, alkaline earth metal, and transition metal ions, respectively.[2-12]

Obviously, the valance state of substituent cation plays an important role in controlling the effective copper valance (p).[2] In particular; cation substitution at the Cu-sites may change p and affect the physical properties accordingly [see ref. 2 and the references therein]. Coexistence of Weak ferromagnetism (WFM) and superconductivity (SC) have even been discovered in the ruthenocuprate with nominal composition $RuSr_2GdCu_2O_8$.[3,4] Depending on the magnetic state of the substituted transition metal ion, other 1212 compounds show a wide diversity of electronic properties.[3-12] However, at room pressure, not all the members of 1212 type compounds can be made. The use of high pressure has proven very useful in this context.[12-16]

Recently, and contrary to previous claims of coexistence of antiferromagnetism (AFM) and SC in Mo–1212 compounds, as suggested by several groups,[17,18] our work on $Mo_xCu_{1-x}Sr_2YCu_2O_y$[19] (Chapter 3) has revealed that there is no coexistence of magnetism and superconductivity in these compounds. In fact, full replacement of Mo for the copper chain site is not possible at ambient pressure; a pure compound can only form with x = 0.3 nominal composition. Interestingly, in these compounds, Mo partially adopts the Mo^V oxidation state, which is prone to originate magnetic interactions within the charge reservoir layer. And, as a result, other members of the molybdo-cuprate family show interesting and exotic physical properties.[19-24]

However, all attempts were remain unsuccessful for the full replacement of Cu in the CRL by molybdenum at ambient pressure. In an attempt to extend the knowledge this interesting molybdo-cuprate family having octahedra in the CRL, we have prepared a new family with nominal composition $Mo_{0.5}Cu_{0.5}Sr_2RECu_2O_{7.5}$ ($Mo_{0.5}Cu_{0.5}$–1212 RE). The high pressure and high temperature technique has been used to synthesize these compounds. Here

we describe, the synthesis, structure and microstructure and magnetic properties of the materials corresponding to RE = Gd, Y, Ho and Er. The crystal structure is determined using the combination of X-ray/Neutron powder diffraction and electron microscopy. The electronic states have been investigated using X-ray photoelectron spectroscopy.

7.2. Experimental Details

All the samples were prepared in a two step process. The first step corresponds to the synthesis of $SrCuO_2$, which is in fact a useful precursor for the synthesis of 1212-type cuprates in high pressure and high temperature synthesis method. Polycrystalline samples of nominal composition $SrCuO_2$ have been synthesized by the standard solid state reaction method from the starting $SrCO_3$ and CuO products with purity above 99.9%. A mixture of these well homogenized reagents were pressed into pellets and heated at 1273 K for 72 hours in air with further intermediate grindings.

In the second step, this precursor was mixed with the appropriate amount of MoO_3, CuO and corresponding RE_2O_3, which were decarbonized by heating at 1123 K, were placed in a platinum container and heated at 1323 K under a pressure of 50 kbar in a Belt-type apparatus, according to the following equation:

$$2SrCuO_2 + 0.5CuO + 0.5MoO_3 + 0.5RE_2O_3 = Mo_{0.5}Cu_{0.5}Sr_2RECu_2O_{7.5} \quad (1)$$

The reaction pathway was as follows: (i) rising the pressure up to 50 kbar, (ii) increasing the temperature up to 1323 K in 15 minutes, (iii) maintaining the temperature and pressure for 5-30 min, (iv) quenched to room temperature. Afterwards, the pressure was decreased to ambient pressure. The best result was obtained with a reaction time of 15 min.

Powder samples were initially characterized by X-ray powder diffraction (XRD), performed in a PANalytical X'Pert PRO ALPHA1 diffractometer (Cu $K\alpha_1$-radiation, wave length = 1.5406 Å). Further Neutron powder diffraction (NPD) data allows us to determine more precisely the oxygen positions and occupancies. Long scan of NPD at room temperature (RT) was recorded using the D2B diffractometer (λ=1.59 Å) at ILL, Grenoble (France) for RE = Y and Ho materials (~250 mg). The collected diffraction patterns were refined with the Rietveld procedure[25] following the Fullprof suite program. Electron diffraction (ED) and transmission electron microscope (TEM) images were obtained on a Jeol JEM 3000EX microscope. Sample cationic compositions were checked by energy-dispersive spectrometry (EDS, Link Pentafet 5947 Model, Oxford Microanalysis Group) analysis.

DC magnetic susceptibility measurements were performed in zero-field-cooling (ZFC) and field-cooling (FC) conditions over the temperature range 2–300 K, using a Squid

Quantum Design XL-MPMS magnetometer. The specific heat measurements were carried out with a small piece of samples (~12 mg), using the Quantum Design PPMS instrument.

The X-ray photoelectron spectroscopy (XPS) were carried out on a Thermo-VG Scientific ESCALAB 220 iXL spectrometer, equipped with a monochromatic Al K_α X-ray source (1486.6 eV). The detail of the experiment is described in the Experimental section chapter (*chapter3*).

7.3. Results and discussion

7.3.1. Structure, oxygen content and microstructure

Figure 7.1 shows the XRD patterns of four different members of the $Mo_{0.5}Cu_{0.5}$–1212RE family with RE = Gd, Y, Ho and Er.

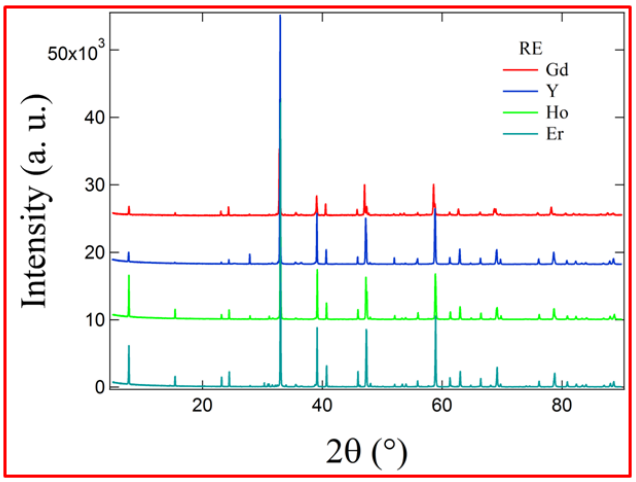

Figure 7.1. XRD patterns for the different members of the $Mo_{0.5}Cu_{0.5}$–1212RE family.

However, all the attempts by varying temperature, pressure and/or reaction time to synthesize pure compounds with RE = Nd, Tb and Lu were unsuccessful. Preliminary Rietveld refinement of XRD patterns of the pure materials with RE = Gd, Y, Ho and Er indicate that all compounds can be isolated as single phases, crystallizing in a tetragonal structure, S. G. *P*4/mmm with a unit cell of ~ $a_p \times a_p \times 3a_p$ type, where a_p indicates the perovskite-type cell parameter. The lattice parameters as a result of the Reitveld refinement of the XRD patterns are shown in table 7.1.

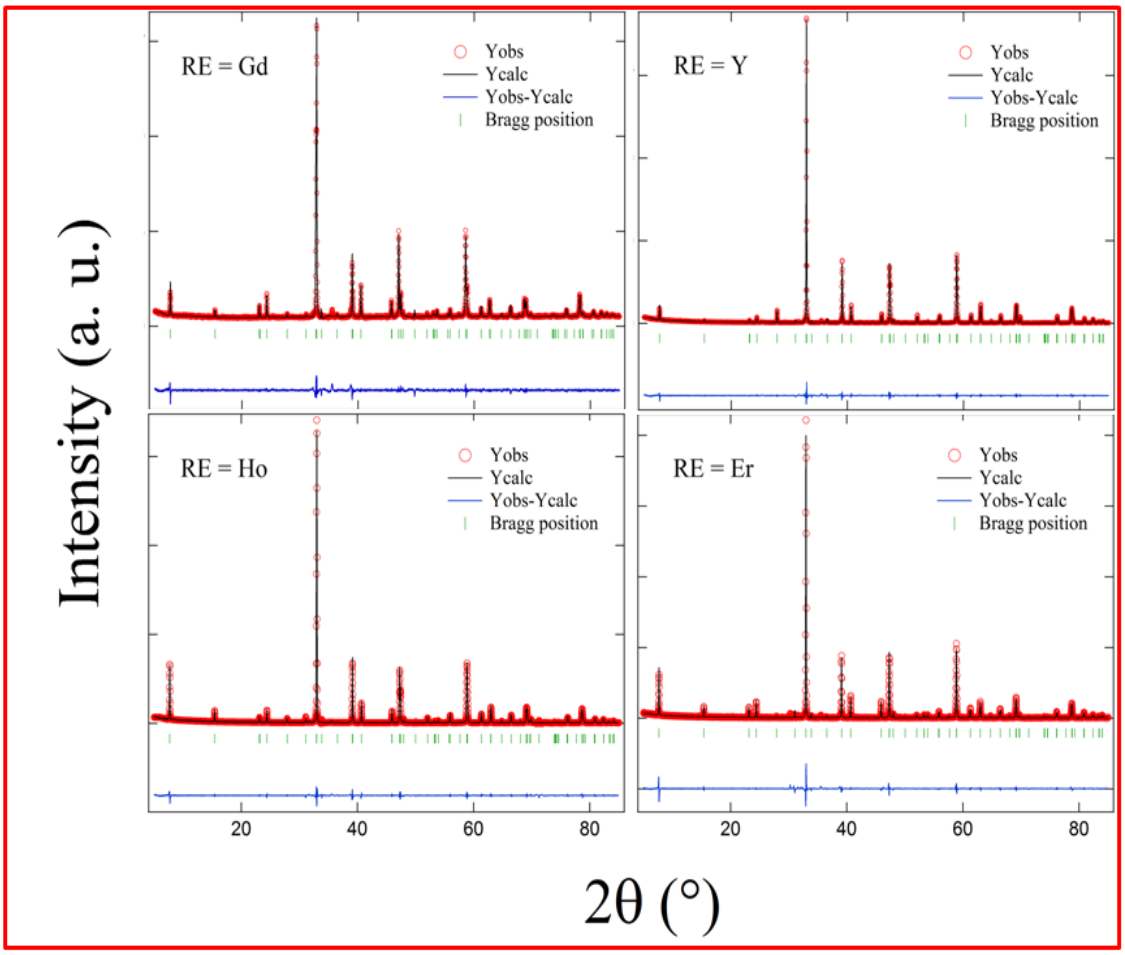

Figure 7.2. Best fitted Rietveld refinement patterns of the XRD collected at RT for the different members of the $Mo_{0.5}Cu_{0.5}$-1212RE family.

Table 7.1: Lattice parameters of the $Mo_{0.5}Cu_{0.5}$–1212RE family and Shannon and Prewitt Ionic Radii[30]

RE	a (Å)	c (Å)	c/a	V (Å)	R (Å)
Gd	3.8644 (1)	11.5147 (3)	2.98	171.951 (6)	1.053
Y	3.8443 (1)	11.5061 (2)	2.99	170.045 (5)	1.019
Ho	3.8428 (1)	11.4941 (2)	2.99	169.736 (4)	1.015
Er	3.8402 (1)	11.4981 (2)	2.99	169.504 (2)	1.004

Figure 7.2 shows the XRD refinement patterns of all the samples. The unit cell parameters (table 7.1) characteristic of the different family members are plotted in figure 7.3. The a and c parameters and, consequently, the unit cell volume show an increasing tendency with increasing ionic radii (in eight coordination) of the rare earth cations. The c/a ratio remains practically constant at ~ 2.99 (1) in all cases. Further Neutron powder diffraction (NPD)

patterns were recorded at RT to determine more precisely the oxygen positions and occupancies for the samples with RE = Y and Ho.

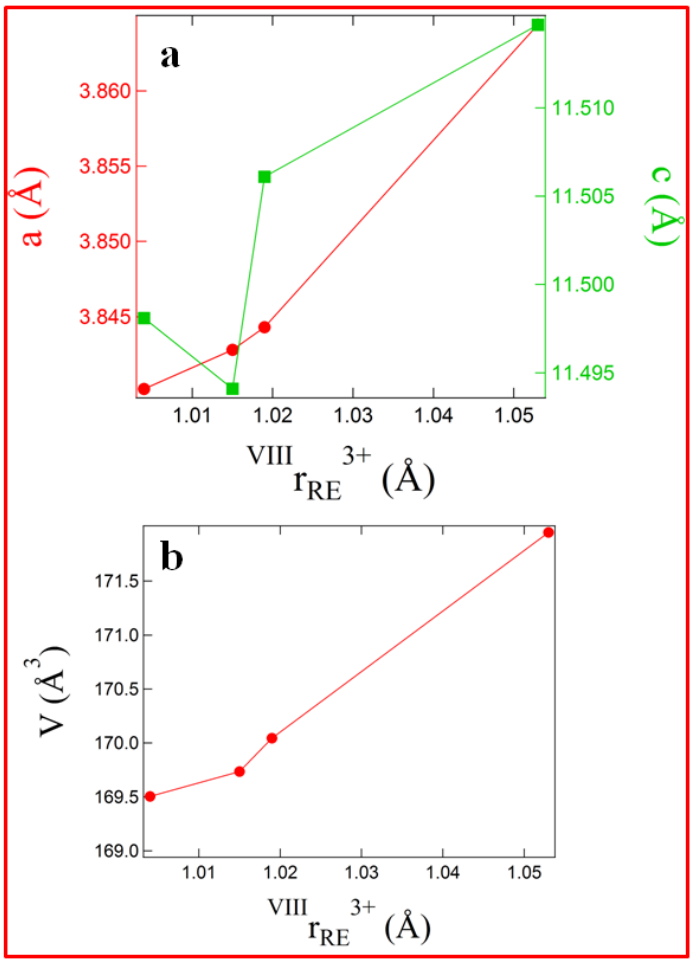

Figure 7.3. Variation of lattice parameters and unit cell volume with the ionic radii of rare earth cations for the different members of the $Mo_{0.5}Cu_{0.5}$–1212RE family.

We have already discussed in chapter 5, that neutron data are highly sensitive to oxygen-atom positions, occupancies and their thermal motions, but no reliable Cu/Mo populations can be established for the Cu1 and Cu2 sites from the neutron data alone. The lack of sensitivity results from the relative similarity in coherent neutron scattering lengths for Cu and Mo (0.772×10^{-12} and 0.695×10^{-12} cm, respectively.). As XRD refinement provides greater sensitivity in determining the Mo and Cu population over Cu1 and Cu2 sites, we have used a joint RT NPD and RT XRD refinement for the samples with RE = Y and Ho. A similar joint powder neutron/X-ray refinements on $Mo_{0.3}Cu_{0.7}Sr_2RECu_2O_y$ (RE = Ho, Er, Tm, *Chapter 5*)[20, 21, 26] provided significant information on Mo population over Cu1 and Cu2 sites, compared to neutron-only measurements on the same phase. Hence, we have discussed

the structural details using the results of the joint NPD/XRD refinements of the $Mo_{0.5}Cu_{0.5}Sr_2RECu_2O_y$ (RE = Y and Ho) materials.

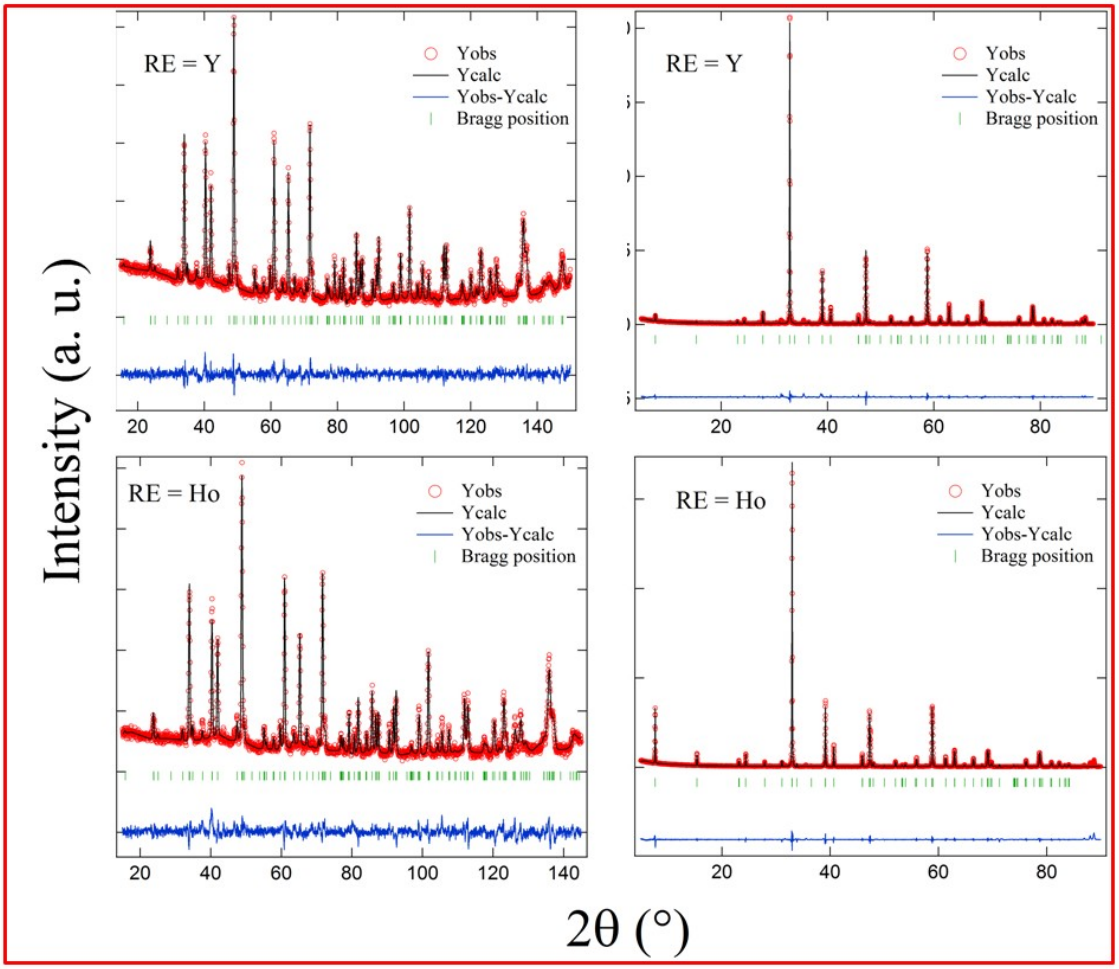

Figure 7.4. Final observed, calculated and difference profiles (Joint Rietveld refinement pattern) of the RT XRD and RT NPD patterns for the $Mo_{0.5}Cu_{0.5}Sr_2RECu_2O_{7.5}$ samples with RE = Y and Ho, respectively.

As a starting model we have used the atomic parameters taken from the previous studies with $Mo_{0.3}Cu_{0.7}Sr_2RECu_2O_y$ (RE = Er, Tm, *Chapter 5*) materials.[20,21] The obtained lattice parameters, agreement factors and selected bond lengths and angles, resulting from the joint refinement of the RT NPD data and RT XRD data, are given in Tables 7.2 and 7.3, respectively for both the $Mo_{0.5}Cu_{0.5}Sr_2RECu_2O_y$ (RE = Y, Ho). Figure 7.4 shows the final plot of the joint Rietveld refinement of the NPD and XRD data for the $Mo_{0.5}Cu_{0.5}Sr_2YCu_2O_y$ and $Mo_{0.5}Cu_{0.5}Sr_2HoCu_2O_y$ samples, respectively.

Table 7.2. Refined structural Parameters and Agreement Factors (from Joint RT XRD/RT NPD refinement) for the $Mo_{0.5}Cu_{0.5}Sr_2RECu_2O_{7.5}$ material with RE = Y and Ho, respectively.

	RE = Y	RE = Ho
a (Å)	3.88452 (4)	3.884425 (6)
c (Å)	11.5171 (2)	11.4945 (1)
V (Cell Volume, $Å^3$)	170.306 (3)	169.868 (3)
RE (0.5, 0.5, 0.5)		
Biso	0.14 (5)	0.98 (2)
Mo1/Cu1 (0, 0, 0)		
Occupancy	0.52 (3)/0.48 (3)	0.51 (4)/0.49 (4)
Biso	0.82 (1)	1.07 (1)
Cu2 (0, 0, z)		
z	0.3607 (2)	0.3589 (2)
Occupancy	0.99 (2)	2.00
Biso	0.18 (5)	0.32 (6)
Sr (0.5, 0.5, z)		
z	0.1988 (3)	0.1970 (2)
Biso	0.92 (2)	0.5 (1)
O1 (0.5, 0, z)		
z	0.3748 (2)	0.3754 (3)
Biso	0.14 (5)	0.8 (1)
O2 (x, y, z)		
x=y	0.048 (2)	0.045 (3)
z	0.1621 (3)	0.1624 (5)
Biso	0.67 (8)	0.1 (2)
O3 (x, y, 0)		
x	0.78 (1)	0.78 (2)
y	0.558 (8)	0.50 (1)
Occupancy	0.106 (5)	0.101 (5)
Biso	0.8 (4)	1.3 (1)
O4 (x, 0.5, 0)		
x	0.098 (3)	0.078 (11)
Occupancy	0.17 (2)	0.18 (1)
Biso	0.4 (2)	1.3 (1)
Total oxygen content	7.54 (2)	7.53 (2)
R_P	2.77	3.28
R_{wp}	3.50	4.86
R_F	2.95	6.85
χ^2	1.99	3.72

The apical oxygen atom O2 has been refined using a displacement from its initial position [from (0, 0, z) to (x, y, z) where x = y] to reduce the initially observed high thermal factor (initial B_{iso} = 2.3 (1)). The oxygen atoms (O1) in the CuO_2 plane show a typical displacement towards the Er site (~0.19 Å). On the other hand, we have found full occupancies for O1 (occupancy = 1.00), O2 (occupancy = 0.25), Sr (occupancy = 1.00) and Er (occupancy = 1.00) and were constrained afterwards.

Site occupancy refinement indicates that the chemical substitution of the Mo ions for the Cu ions occurs only in chain copper site (Cu1). It is noteworthy here that for the as-prepared $Mo_{0.3}Cu_{0.7}Sr_2RECu_2O_y$ (RE = Er and Tm) samples, the chemical substitution of the Mo ions for the Cu ions occurs in both the Cu sites (Cu1 and Cu2) but to a limited extent and interestingly, a redistribution of Mo was found to occur after oxygenation (*Chapter 5*). However, No trace of Mo substitution at Cu2 site is observed in the joint refinement (Mo occupancy becomes negative when Mo is allowed to share the Cu2 site) for the $Mo_{0.5}Cu_{0.5}Sr_2RECu_2O_y$ (RE = Y and Ho) materials.

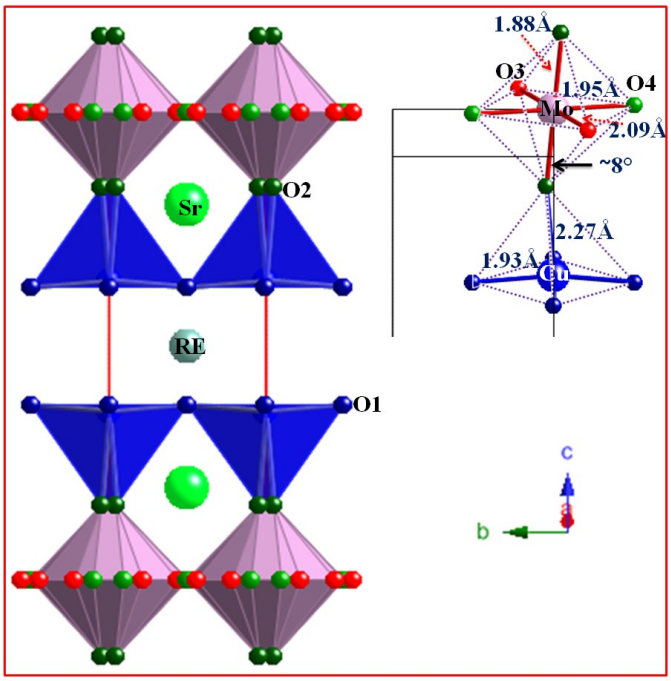

Figure 7.5. Crystal structure of $Mo_{0.5}Cu_{0.5}Sr_2RECu_2O_y$ (Tetragonal, *P4/mmm*).

Table 7.3. Selected bond lengths (Å), angle (°) and the relevant distances (Å) (from Joint RT XRD/RT NPD refinement) for the $Mo_{0.5}Cu_{0.5}Sr_2RECu_2O_{7.5}$ material with RE = Y and Ho, respectively.

Bond length and angle and relevant distances	RE = Y	RE = Ho
(Cu1,Mo)-O2	1.885 (4)	1.883 (6)
(Cu1,Mo1)-O3	1.90 (1)	2.09 (3)
(Cu1,Mo1)-O3	2.30 (4)	2.09 (7)
(Cu1,Mo1)-O4	1.959 (6)	1.95 (4)
Cu2-O1	1.930 (1)	1.932 (2)
Cu2-O2	2.302 (5)	2.27 (2)
RE-O1	2.403 (1)	2.397 (1)
Sr-O1	2.794 (4)	2.811 (1)
$Sr\text{-}O2_{avg}$	2.63 (1)	2.751 (2)
Sr-O3	2.54 (2)	2.51 (3)
Sr-O4	2.763 (3)	2.79 (1)
O1-Cu2-O1	170.345 (3)	168.730 (2)
Cu2-O2-Mo/Cu1	165.619 (4)	166.352 (4)
d(intra)	3.209	3.244
d(inter)	8.308	8.251
d(apical)	2.302 (5)	2.27 (2)
d(block)	3.77	3.766

The Metal-Oxygen octahedra: The $(Mo/Cu)O_{1+\delta}$ chain is situated between two Sr-O layers in the intermediate region of the structure (Figure 7.5). In analogy to the previous studies (*Chapter 5*) we have also found the best fit for these samples using the two different chain oxygen position O3 (x y 0) and O4 (x 0.5 0) giving a minimum thermal factor. These

two positions are partially occupied. The crystal structure of $Mo_{0.5}Cu_{0.5}Sr_2RECu_2O_y$ is shown in figure 7.5. The relative O3/O4 occupancies are 56%/44% and 53%/47% for $Mo_{0.5}Cu_{0.5}Sr_2YCu_2O_y$ and $Mo_{0.5}Cu_{0.5}Sr_2HoCu_2O_y$ compounds, respectively. The nearly equal distributions of relative O3/O4 oxygen contents indicate the random distribution of the chain oxygen in both the O3 and O4 crystallographic sites, which in fact indicates the existence of oxygen vacancies near the Mo atoms and these Mo atoms stay in four-fold planar coordination. Thus, the defect induced by the oxygen vacancies in fact makes the chain fragmented and disordered in a mesoscopic scale. Similar kind of disordered chain was found for the as-prepared $Mo_{0.3}Cu_{0.7}Sr_2RECu_2O_y$ (*chapter 5*)[20,21] materials, which is indeed a reason for the absence of superconductivity in those samples.

The copper plane: The copper polyhedron is elongated along the apical direction (usually attributed to a Jahn-Teller distortion), where the equatorial $d_{Cu2\text{-}O1}$ distances (~1.93 Å) are comparable to those observed in the common HTSC superconductors (1.88–1.97 Å).[15,27] The O2–Cu2–O2 buckling angle, the angle that measures the separation of the copper from the oxygen plane in the copper plane site, is the order of ~170°. It is noteworthy here that the mercury compound with the highest superconducting transition temperature have flat copper-oxygen planes.[28,29] Yet, this is neither a sufficient nor a necessary condition for superconductivity. In the previously studied molybdo-cuprate materials (*chapter 5*) with nominal composition $Mo_{0.3}Cu_{0.7}Sr_2RECu_2O_y$, a similar buckling angle to the present materials was found.

The apical Cu2-O2 distance is similar to those commonly observed in high T_C cuprates (for instance, 2.30 Å for YBCO (T_C = 95 K), 2.824 Å for $HgBa_2Cu_2O_7$ (T_C = 125 K), 2.255 Å in $Mo_{0.3}Cu_{0.3}Sr_2ErCu_2O_{7.54}$ (*chapter 5*, T_C = 84 K)).[15]

Polyhedra Tilt: The tilt of the octahedra in the cooper chain site can be inferred from the (Mo/Cu)–O–Cu angle. For the present materials this angle is ~166° (Table 7.3), which is in fact higher than the $Mo_{0.3}Cu_{0.7}Sr_2RECu_2O_y$ (*Chapter 5*, RE = Er, Tm) materials, where it is ~170°. And the Mo octahedral is rotated by 8° around the c axis, whereas much smaller rotation (4° - 6°) were found in the iso-structural superconducting molybdo-cuprates with nominal composition $Mo_{0.3}Cu_{0.7}Sr_2RECu_2O_y$ (*Chapter 5*, RE = Er and Tm). In non superconducting Cr-1212 compounds, the rotation was about 13°.[15] Similar rotation (~13°) was found also in the corresponding Ru octahedral in Ru-1212 compound.[15]

The total oxygen contents are obtained from the refined oxygen occupancies of the corresponding NPD profiles are 7.54 (2) and 7.53 (2) for the samples with RE = Y and Ho

sample, respectively. Therefore, it could be assumed that all the samples have similar oxygen content (~7.5), which in fact is in a good agreement with the stoichiometry of the synthesis.

Microstructure: The metallic compositions were checked by EDS on several crystals. It shows a good agreement with the nominal composition.

The structural refinements using the combination of XRD and NPD suggest the presence of a tetragonal triple perovskite superstructure with a unit cell of ~ $a_p \times a_p \times 3a_p$ type as the average crystal structure. However, electron microscopy and diffraction clearly show a more complicated scenario.

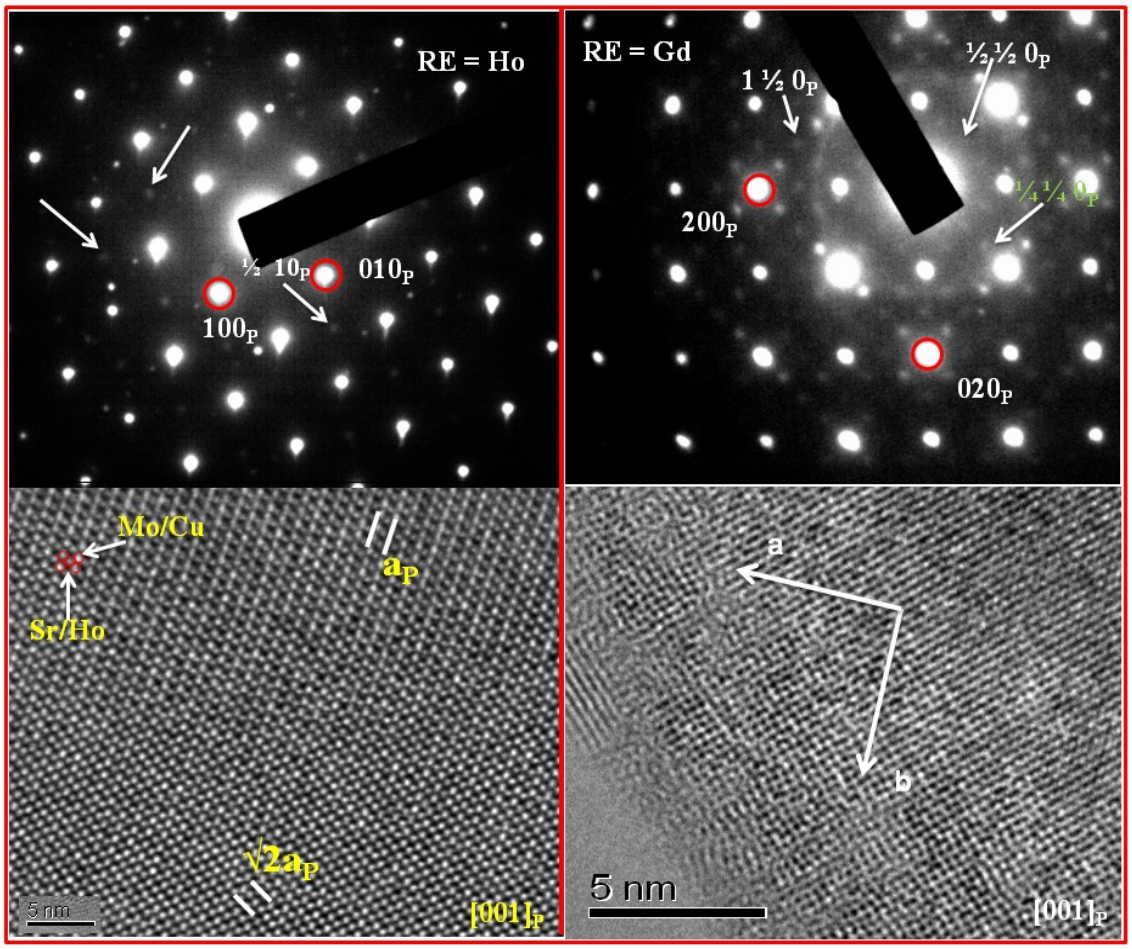

Figure 7.6. Electron diffraction patterns and the HRTEM images for the materials with RE = Gd and Ho recorded along $[001]_p$ zone axis, where both the subcell a_p and the supercell $\sim\sqrt{2}a_p \times \sqrt{2}a_p$ are observed.

Figure 7.6 shows the electron diffraction pattern and the high resolution electron micrograph of the $Mo_{0.5}Cu_{0.5}Sr_2GdCu_2O_{7.5}$ and $Mo_{0.5}Cu_{0.5}Sr_2HoCu_2O_{7.5}$ material along $[001]_P$ zone axis. The strong spots can be indexed on the basis of $[001]_P$ zone axis, where the sub-index p refers the basic perovskite structure. The existence of spots at h/2, k/2, 0 positions indicate the presence of the well known diagonal cell, ~ $\sqrt{2}a_p \times \sqrt{2}a_p \times 3a_p$. A similar superstructure was

also been observed in the iso-structural Chromo-cuprates[15] and Irido-cuprates[11,12]. And this superstructure is due to the tilt of the octahedra. The joint XRD/NPD refinements showed that the octahedral tilting ((Cu/Mo)-O-Cu = 166°) in the present materials are higher than the similar molybdo-cuprate compounds with nominal composition $Mo_{0.3}Cu_{0.7}Sr_2RECu_2O_y$ (chapter 5); there was no evidence of the existence of the diagonal cell in the electron diffraction (ED) patterns of those materials. Therefore, the inclusion of extra molybdenum in the copper chain site enhances the octahedral tilting, which can be visualized in ED patterns. Furthermore, if the tilt is long-range ordered within the crystal, the corresponding maxima can also be observed in X-ray or neutron powder diffraction. However, if this tilt is not regularly ordered one can only see the diagonal cell by means of electron diffraction. The absence of the corresponding extra peak in both the XRD and NPD patterns of these materials confirms that the tilt in the present material is not a regularly ordered phenomenon. It is important to state here that we have an equal amount of two different metal ions (Mo and Cu), randomly distributed in the copper chain site. Moreover, the average metal to oxygen distance ((Mo/Cu)-O) in the copper chain site is ~ 2.01 Å (see table 7.3). The ionic radii of the six-fold coordinated Mo^{V} and Mo^{VI} are 0.61 Å and 0.59 Å, respectively, and then, using the ionic radius of ~1.35 Å for two coordinated O^{-2} gives Mo-O bond lengths of 1.96 Å and 1.94 Å, respectively.[30] And the four-coordinated Cu^{II} has an ionic radius of 0.57 Å, gives Cu-O bond length = 1.92 Å and six-coordinated Cu^{II} has an ionic radius of 0.73 Å, gives Cu-O bond length = 2.08 Å.[30] Therefore, we can say that a molybdenum octahedral is more favourable than the copper octahedral in the copper chain site of the crystal structure. Hence, the absence of regular arrangement of the tilted octahedral is quite expected in the present material.

The electron diffraction patterns along $[100]_P$ and $[010]_P$ zone axes and the HRTEM images along $[100]_P$ and $[110]_P$ zone axes for the $Mo_{0.5}Cu_{0.5}Sr_2HoCu_2O_{7.5}$ material are shown in figure 7.7. It is interesting to note that, no orthorhombic distortion has been observed in any of the diffraction patterns. The lower panel of the figure 7.7 illustrate the HRTEM images along $[100]_P$ and $[110]_P$ zone axes, respectively. They confirm that the layers are regularly stacked along the c direction according to the expected 1212 model.

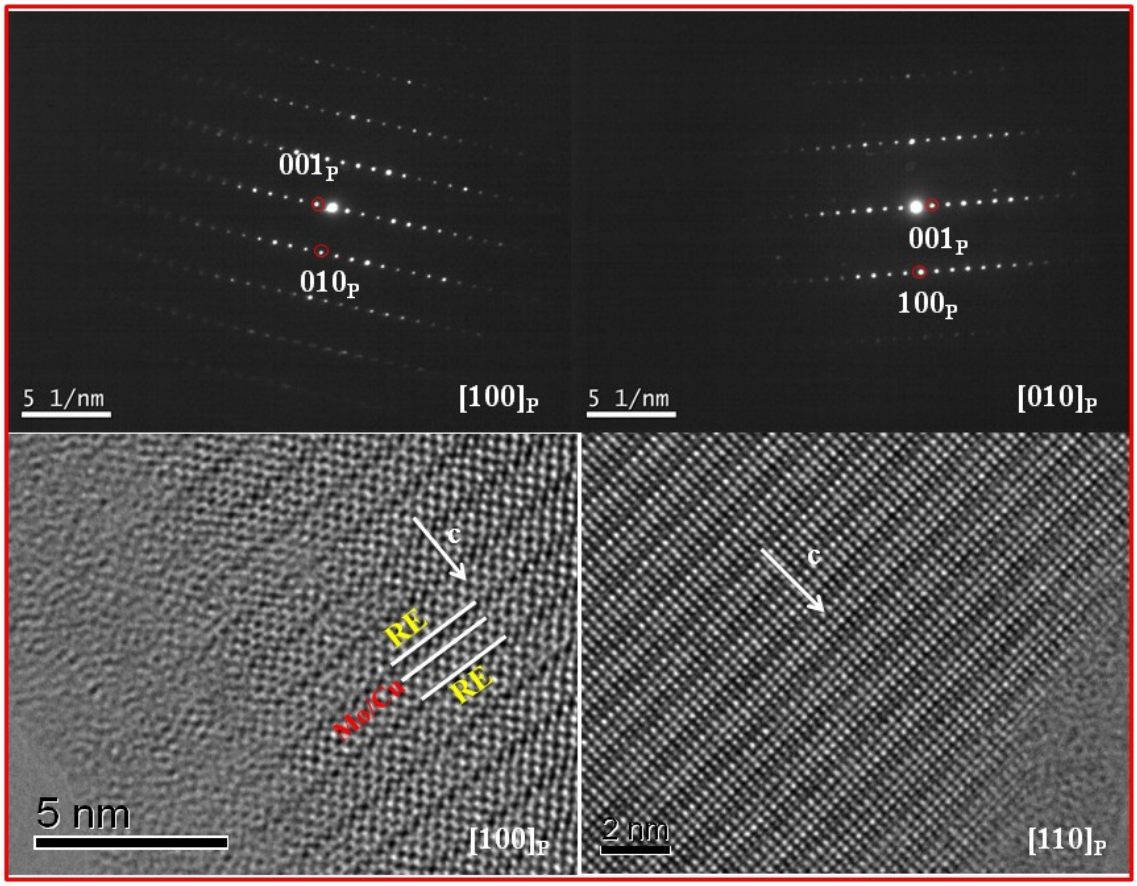

Figure 7.7. Electron diffraction patterns along $[100]_p$ and $[010]_p$ directions for the $Mo_{0.5}Cu_{0.5}Sr_2HoCu_2O_{7.5}$ material. Lower panel of the figure shows the TEM micrograph of the same sample taken along $[100]_p$ and $[110]_p$ directions.

Beside the weak spot at h/2, k/2, 0 positions, there are also spots at h/3, k/3, 0 (figure 7.6), which indicate the presence of microdomain texture. Some weak spots at h/4, k/4, 0 (figure 7.6) position can be attributed to the multiple diffraction due to the presence of domain walls. Figure 7.8 shows the presence of microdomains in which the long c axis changes from domain to domain in one of the three space directions. In fact the image shows a substantial disorder, which is confirmed by the streaking, observed both in the ED pattern

(figure 7.6) and in the Fourier transform (inset of figure 7.8) of the image. This, indeed, is not unusual in perovskites[31] and perovskite related materials.[32-36]

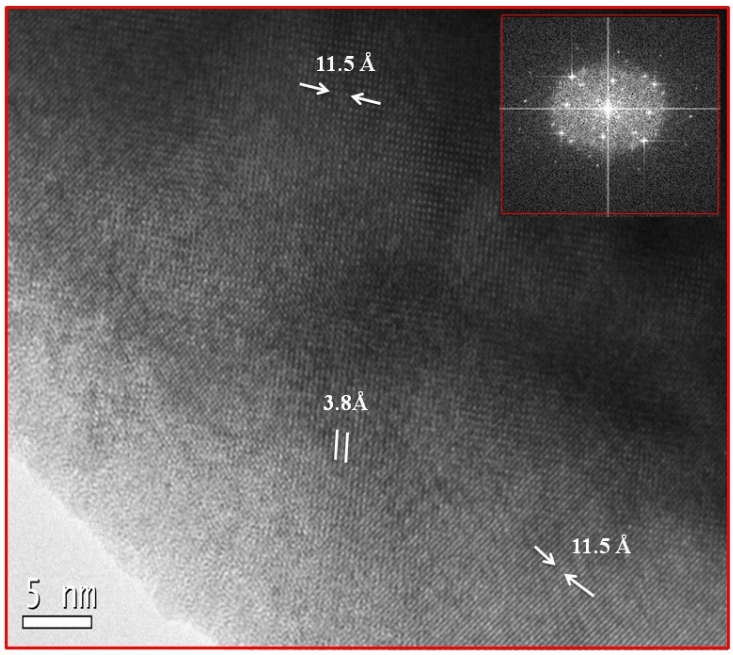

Figure 7.8. [001] zone axis micrograph, showing disordered domains for the $Mo_{0.5}Cu_{0.5}Sr_2HoCu_2O_{7.5}$ material. The Fourier Transform (inset) show streaking, characteristic of disorder.

Not all the crystal studied, showed a clear scenario of microdomain texture. A similar situation is already observed in the HPHT synthesized iso-structural cromo–cuprates[15] and in irido–cuprates[11,12]. The defects and this kind of texture can arise due to the lack of equilibrium in the high pressure synthesis. The presence of the three dimensional microdomains seems to be due to the synthesis conditions. In principle, when a crystal starts to grow, the same choice for it to grow from any point of the mass of the solid. And from there, it can actually grow in any of the three different directions. These growing fronts then commingle to give a microdomain texture. And the size of the domains is very much dependent on the quenching/annealing conditions[37] due to the relative importance of the growth process. Yet, not all the superstructures show this kind of microdomain texture. Their presence appears to be closely related to the amount of distortion from the cubic symmetry of the related sub cell.[32]

In summary we can conclude that the microstructure of these compounds is interpreted by a well-known diagonal cell $\sqrt{2}a_p \times \sqrt{2}a_p \times 3a_p$, distributed in three dimensional domains, as confirmed by the SEAD and HRTEM, while an ideal triple perovskite structure with a "simple" $a_p \times a_p \times 3a_p$ cell is supported from the results found by the NPD/XRD joint

refinements. This could be a consequence of the absence of the long-range ordering in the octahedral tilt due to the random distribution of an equal amount of Mo and Cu in the cooper chain site.

7.3.2. XPS measurements

Figure 7.9 shows the C1s spectra of the $Mo_{0.5}Cu_{0.5}Sr_2HoCu_2O_y$ material before and after scraping in the ultra-high vacuum. Two peaks of C1s core electrons at 285eV and at 289 eV is observed for the sample before scraping. This indicates unambiguously two different states of carbon.

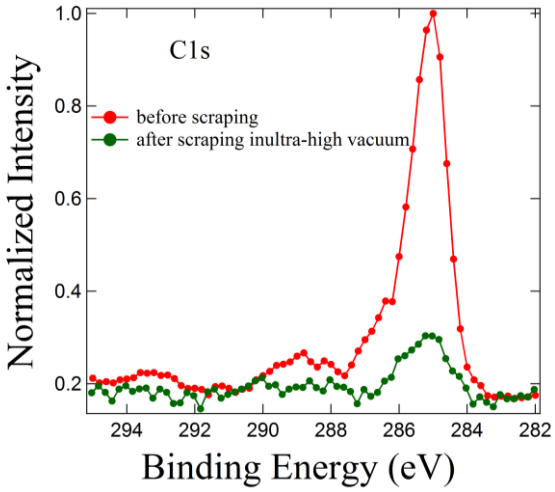

Figure 7.9. XPS C1s spectra of the $Mo_{0.5}Cu_{0.5}Sr_2HoCu_2O_y$ material before and after scraping.

The peak at 285 eV corresponds to the normal contamination of the surface by carbon and the second one at 289 eV is due to the formation of carbonates on the surface. The sample was then scraped in vacuum at room temperature with a stainless steel blade. A clean surface, generally, can be obtained after a couple of mild scraping over the surface. The effect of cleaning is evident in the strong attenuation of the C ls signal (figure 7.9). We estimate that less than 5% of C is left on the surface after scraping; in fact the carbon left on the surface of the sample is the normal carbon contamination. The absence of the peak at 289 eV after scraping confirms that there is no contamination due to the formation of carbonates on the surface.

Sr 3d and Ho 4d core levels: Figure 7.10 shows the spectra of the Sr 3d and Ho 4d core levels for the $Mo_{0.5}Cu_{0.5}Sr_2HoCu_2O_y$ sample. The Sr 3d core level spectrum comprise a doublet corresponding to the transition from Sr $3d_{3/2}$ and Sr $3d_{5/2}$ states.[38] These match well to the expected Sr 3d and Ho 4d core levels from Sr^{II} and Ho^{III} elements.

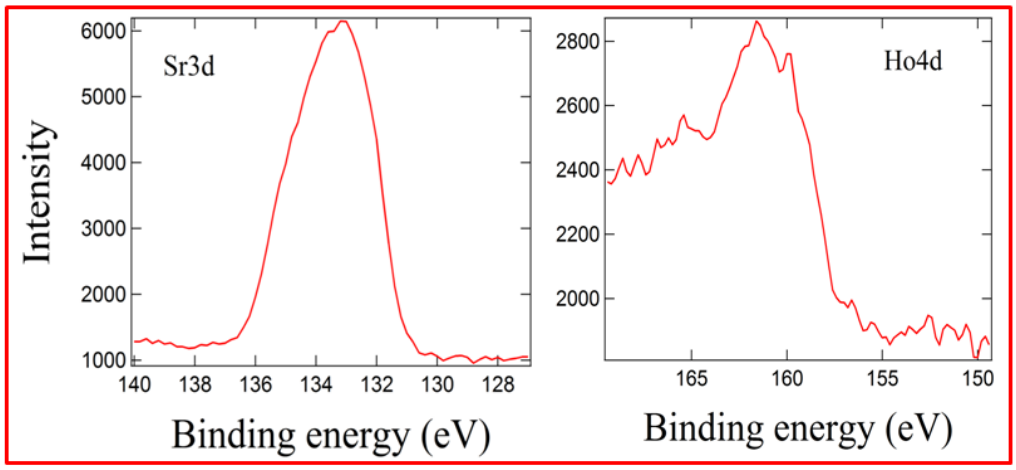

Figure 7.10. Core-level Sr 3d and Ho 4d spectra for the $Mo_{0.5}Cu_{0.5}Sr_2HoCu_2O_y$ material.

Mo 3d core level: Figure 7.11 shows the XPS spectrum of the Mo 3d core levels for the $Mo_{0.5}Cu_{0.5}Sr_2HoCu_2O_y$ sample. A spin-orbit splitting of 3.1 eV[39] and a $3d_{5/2}$:$3d_{3/2}$ intensity ratio of 3:2 have been used for the fitting after appropriate correction of the background with a single Shirley (Gaussian-step) function [Table 7.4]. Fitting of the XPS spectra of Mo 3d core levels allow us to confirm the large content of Mo^{VI}. Mo^{V} and Mo^{VI} are identified by the energy shifts of their core levels assigning the doublet at 232 eV & 235.1 eV ($3d_{5/2}$ and $3d_{3/2}$) to Mo^{V} and the one at 232.9 eV & 236.0 eV ($3d_{5/2}$ and $3d_{3/2}$) to Mo^{VI} as proposed before (*chapter 5 and chapter 6*).[19,20,40] We have found that the Mo^{V}/Mo^{VI} ratio is 0.37:0.63. The relevant parameters of this fit and of other elements are shown in table 7.4.

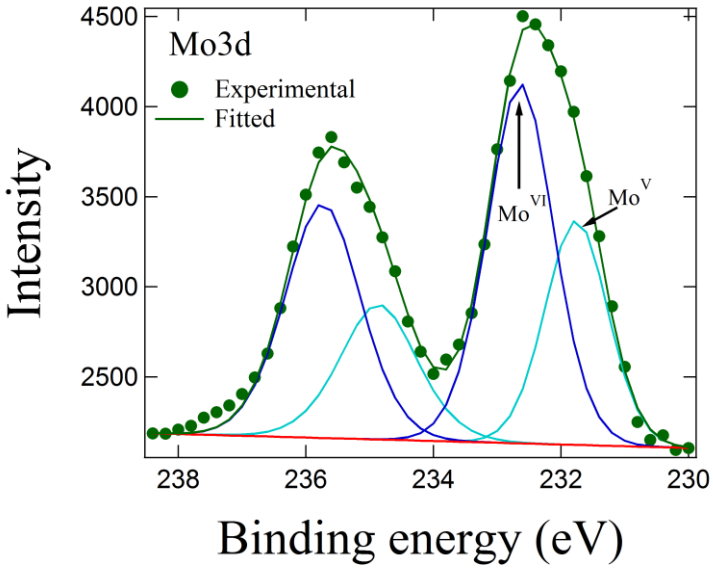

Figure 7.11. Core level XPS spectrum of the Mo 3d energy region with fitting for the $Mo_{0.5}Cu_{0.5}Sr_2HoCu_2O_{7.5}$ material.

It is important to state here that the XPS experiments for as-prepares $Mo_{0.3}Cu_{0.7}Sr_2RECu_2O_y$ materials showed a large content of Mo^V (~80%) in the sample (*chapter 5 and 6*). And due to the presence of high contents of Mo^V, all those compounds showed interesting magnetic properties. It is worth to recall that instead of Mo metal power (used in the preparation of $Mo_{0.3}Cu_{0.7}Sr_2RECu_2O_y$), we have used MoO_3 (Mo^{VI}) as a starting material for the present materials. Then, it could be possible that because of the use of high pressure, higher amounts of Mo remain at Mo^{VI}.

Cu 2p core level: The Cu 2p core level spectrum is shown in figure 7.12. The Cu $2p_{3/2}$ spectrum for the $Mo_{0.5}Cu_{0.5}Sr_2HoCu_2O_{7.5}$ sample is typical of Cu^{II} compounds. The main peak near 932.5 eV is attributed to the well-screened $\underline{2p}^5 3d^{10}\underline{L}$ final states resulting from ligand-to-metal (O $2p \rightarrow$ Cu $3d$) charge transfer and the satellite at higher binding energy corresponds to a multiplet of $\underline{2p}^5 3d^9\underline{L}$ states, underbar denotes a hole and L denotes the oxygen ligand.[41-44] The intensity ratio of the satellite to the main peak is determined by the charge transfer energy from the centre of the valance band to the 3d level.

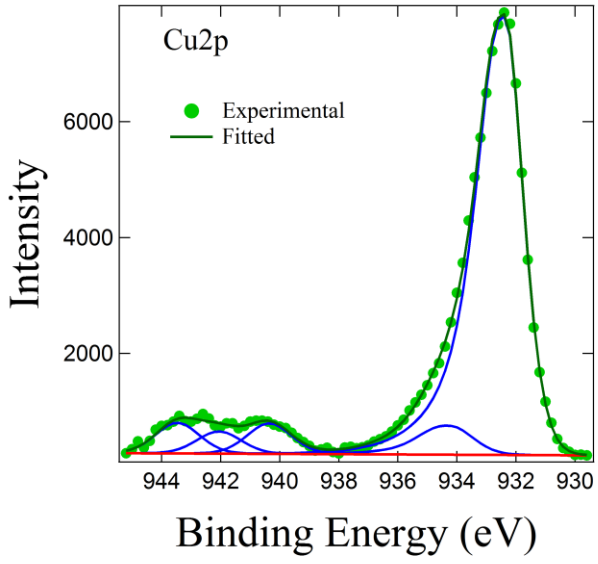

Figure 7.12. Core level XPS spectrum of the Cu 2p energy region with fitting for the $Mo_{0.5}Cu_{0.5}Sr_2HoCu_2O_{7.5}$ material.

Table 7.4. Parameters of fitting for different XPS spectra.

Core level spectra	B.E (eV)	FWHM (eV)	Mo^{V}/Mo^{VI} and Cu^{II}/Cu^{III} Ratio
Mo^{V} $3d_{5/2}$	231.8	1.20	
$3d_{3/2}$	234.9	1.49	
Mo^{VI} $3d_{5/2}$	232.6	1.27	0.37/0.63
$3d_{3/2}$	235.7	1.45	
Cu^{II} $2p_{3/2}$	932.4	1.52	0.93/0.07
Cu^{III} $3p_{3/2}$	934.3	1.90	
O1s	528.9	1.57	
	530.3	1.57	
	531.4	1.60	
	532.8	1.60	

Fitting of the XPS spectra of Cu 2p core level allows us to confirm the large content of Cu^{II} (93%). Almost negligible amount of Cu^{III} (7%) is detected in the fitting. The average oxidation state of the cooper is calculated from the fitting of the Cu 2p core level spectrum is ~ 2.07. The small asymmetry found in the main line shape supports the presence of a small amount of Cu^{III}. Another reason could be due to the hybridization mechanism of apical O $2p_z$–Cu $3d_{z^2-r^2}$. Parmigiani et al proposed that the line shape of the main line has a relation with the Cu–O coordination geometry.[45-48] When the Cu ions have the octahedral or pyramidal coordination with the oxygen ligand, besides the usual O $2p_{x,y}$ – Cu $3d_{x^2-y^2}$ charge transfer, the apical O $2p_z$–Cu $3d_{z^2-r^2}$ charge-transfer mechanism is also allowed. From crystal field theory, the 3d orbitals are splitted into e_g and t_{2g} groups in an octahedral coordination. The energy level of e_g orbitals is higher than the t_{2g} orbitals, since they point directly towards the surrounding ligands. If the symmetry is lower, the e_g orbitals become splitted, and Cu $3d_{x^2-y^2}$ is a higher-energy orbital (related to Cu $3d_{3z^2-r^2}$). The work with X-ray absorption spectroscopy (XAS) in cuprate superconductor showed that there is an unoccupied Cu $3d_{3z^2-r^2}$state, thus the apical O $2p_z$–Cu $3d_{z^2-r^2}$ charge transfer is possible.[46,49] However, as we have copper in both sites (Cu1 and Cu2), it is not possible to estimate the accurate hole

concentration (and/or the oxidation state of copper) in the CuO_2 plane from the present experimental results.

O 1s core level: It is apparent in figure 7.13 that the O 1s spectrum exhibit two broad peaks; one at 528.9 eV with lower intensity and another at 530.5 eV with higher intensity.

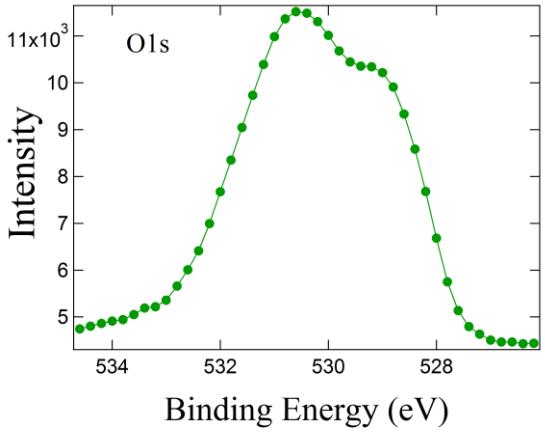

Figure 7.13. Core-level O 1s spectrum for the $Mo_{0.5}Cu_{0.5}Sr_2HoCu_2O_{7.5}$ material.

Both of the peaks are considerably broad, which suggests the presence of overlapping multi-components in samples. In the present system, the oxygen component is complex, which includes O1, O2, O3, and O4 at four different sites. O1 and O2 belongs to the SrO layers and CuO_2 planes, respectively and O3 and O4 belongs to the $(Mo/Cu)O_{1.5}$ planes. So we suggest that the present O 1s emissions correspond to emission from O bonded to Mo/Cu in $(Mo/Cu)O_{1.5}$ planes, O bonded to Sr in SrO layers, O bonded to Cu in CuO_2 plane. We have tried to fit the O 1s spectrum with three different components. The fitted data are shown in figure 7.14.

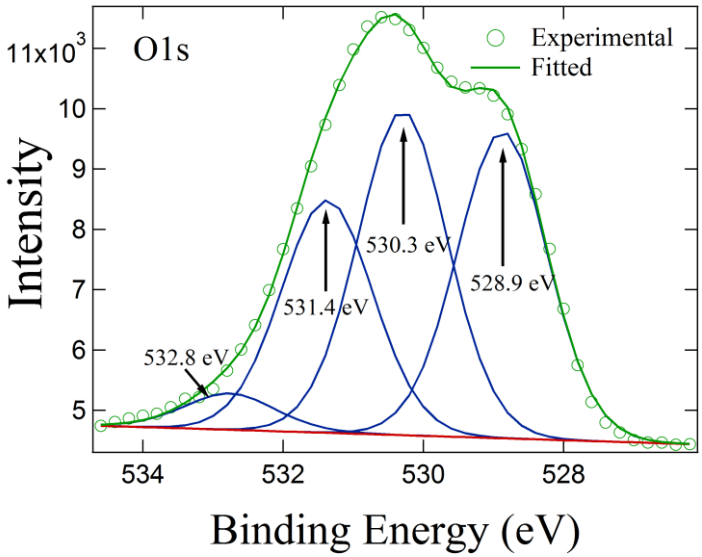

Figure 7.14. Core-level XPS spectrum and the fitting of the O 1s energy region for the $Mo_{0.5}Cu_{0.5}Sr_2HoCu_2O_{7.5}$ material.

And from the fitting we can ascribe the peak at 528.9 eV to the O2p-Cu3d bonding; consistent with the studies of other cuprate superconductors, and the peak at about 530.3 eV is ascribed to O2p-Mo3d bonding.[19] The peak at 531.4 eV could be due to the O bonding to Sr in the SrO layer. Another peak (fitting peak) at 532.4 eV is likely due to the surface contamination (forming carbonate).

Oxygen content: Considering the standard oxidation state of Sr and Ho as 2 and 3, respectively and using the oxidation state of Cu (2.05) and Mo (5.65), as calculated from the corresponding core level XPS spectra, the calculated oxygen content in the sample is 7.50, which is in a good agreement with the NPD refinements.

7.3.3. Physical Properties

Magnetic Properties: The upper panel of the figure 7.15 shows the temperature dependence of the FC and ZFC susceptibility (χ) curves for the samples with RE = Gd, Ho and Er, respectively, measured at 100 Oe. All the susceptibility behaviour is typical of paramagnetic susceptibility.

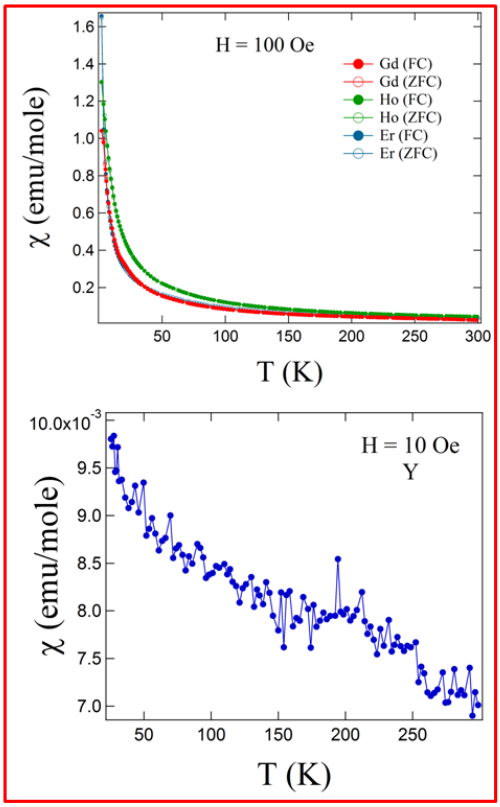

Figure 7.15. Zero field cooled (ZFC) and field cooled (FC) magnetic susceptibility as a function of temperature for the $Mo_{0.5}Cu_{0.5}Sr_2RECu_2O_y$ samples.

The lower panel of the figure shows the susceptibility plot of the $Mo_{0.5}Cu_{0.5}Sr_2YCu_2O_{7.5}$ material measured at 10 Oe. The presence of large noise is due to the small magnetic signal of that material, which is in the order of the lower limit of the SQUID (10^{-6} emu/gm). Figure 7.16 shows the temperature variation of inverse of the FC magnetic susceptibility for the samples with RE = Gd, Ho and Er. However, neither any sign of superconductivity nor any magnetic transition is observed in any of the measurements. The $Mo_{0.5}Cu_{0.5}Sr_2GdCu_2O_{7.5}$ shows two weak transitions at 20 K and at 285 K, which are better visible on the inverse susceptibility plot, corresponds to the secondary phase Gd_2CuO_4[50] (not detected in XRD), which is formed in HPHT.

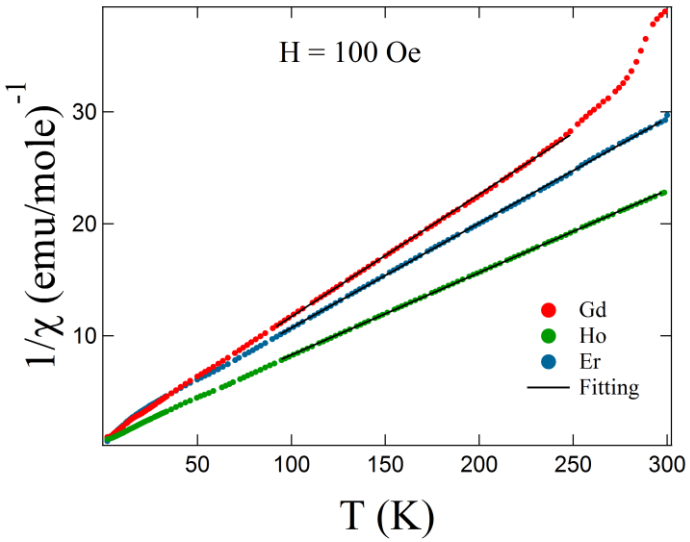

Figure 7.16. Temperature dependence of reciprocal FC susceptibility measured at 100 Oe along with Curie-Weiss fitting (black line).

The Curie-Weiss ($\chi = C/(T-\theta)$, where C = Curie constant and θ is the Weiss temperature) fitting of the inverse of the FC magnetic susceptibility, performed in a wide range of temperature (100 K-300 K, figure 7.16), leads to an effective paramagnetic magnetic moment $P_{eff} = 8.3\mu_B$, $10.37\mu_B$ and $9.45\mu_B$ with $\theta = -7.2$ (1) K, -12.9 (2) K and -14.6 (3) K for the samples with Gd, Ho and Er, respectively. The calculated moments fit quite well with the theoretical value of the Ho^{III} ($P_{eff} = 10.4\ \mu_B$) and Er^{III} ($P_{eff} = 9.5\ \mu_B$) free cation, calculated on the basis of a fully coupled orbital and spin contribution associated with the $^5I_8$ and $^4I_{15/2}$ ground term of Ho^{III} ($P_{eff} = 10.4\ \mu_B$) and Er^{III} ($P_{eff} = 9.5\ \mu_B$), respectively. But for the sample with RE = Gd, due to the presence magnetic transition, originated from secondary phase, the data is fitted between 100 K to 250 K, and the calculated moment is much higher than

expected for Gd^{III} (P_{eff} = 7.94 μ_B) cation. This discrepancy is attributed to the presence of the magnetic secondary phase in that sample. It is noteworthy that iso-structural molybdo-cuprates with nominal composition $Mo_{0.3}Cu_{0.7}Sr_2RECu_2O_y$[19-22] (RE = Rare earth elements, *Chapter 5*), show very interesting physical properties because of the presence of high amount of magnetic Mo^V, which originate short-range magnetic correlations in those materials. And then after oxygenation molybdenum gets oxidized to non magnetic Mo^{VI} and destroys the short-range magnetic correlations. The XPS studies, on the present samples, show the presence of high amount of non magnetic Mo^{VI}; which is the reason for the absence of magnetic correlations in these materials.

Specific heat: Figure 7.17 shows the low temperature variation (2-12 K) of molar specific heat (C-T) for the $Mo_{0.5}Cu_{0.5}Sr_2RECu_2O_{7.5}$ materials with RE = Y, Gd, Ho and Er, respectively.

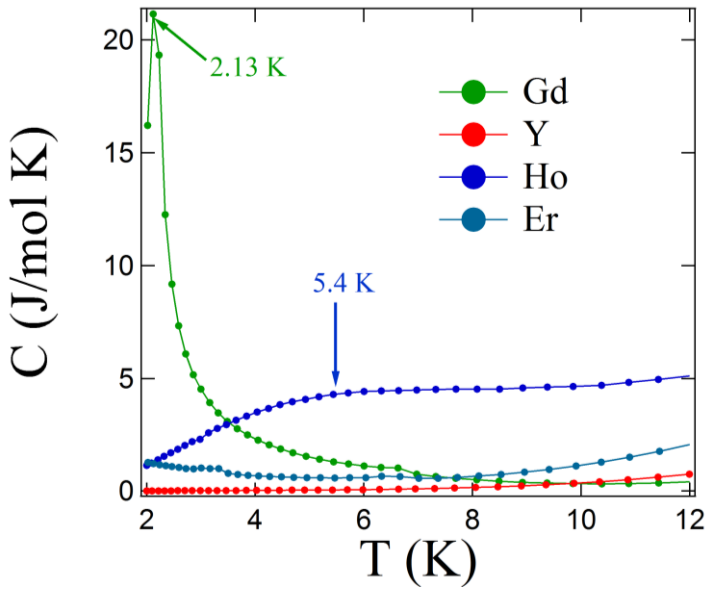

Figure 7.17. Low temperature specific heat for the $Mo_{0.5}Cu_{0.5}Sr_2RECu_2O_{7.5}$ materials with RE = Y, Gd, Ho and Er, respectively.

The magnetic ordering temperatures, determined by the peak in the C-T curves, are 2.13 K and 5.4 K for the samples with RE = Gd and Ho, respectively. No magnetic transition is observed for the materials with RE = Y and Er, down to 2 K. The Gd compound shows a sharp peak at 2.13 K, whereas the Ho compound shows a broad transition at 5.4 K. It could be noted here that the specific-heat curves for the samples with RE = Y and Gd merge together above the ordering temperature, which indicates that these two compounds have the same electronic and lattice contributions to specific heat. This is due to the small crystal-field

splitting of the ground multiplet ^8S of the Gd^{III}, as expected. However, the specific heat for RE = Ho and Er is higher than those of its analogs. This discrepancy indicates the presence of Schottky specific-heat anomalies arising from the interaction of the rare earth ions with the crystalline electric Field. The Curie-Weiss fitting on the magnetic-susceptibility measurements have shown that the effective moments in these compounds are reasonably close to the corresponding values for the RE^{III} free-ions, indicating that the 4f moments of the rare-earth ions are well localized. The sharp peak observed at 2.13 K for the Gd compound is ascribed to the antiferromagnetic (AFM) ordering of the Gd ion. Evidence from the rare earth ordering investigation may be suitable for interpretation at this point. That is, the rare-earth sites are electronically isolated from the neighbouring CuO_2 planes, which prevents the electronic interaction between RE sites and CuO_2 planes, rendering these rare-earth ions free.[51]Previous studies on the Gd ordering in $GdBa_2Cu_3O_{7-\delta}$ revealed that the ordering is a 3-dimensional antiferromagnetic (AFM) order in nature, and independent of the variation of oxygen content.[52,53] Lai et al. reported the same AFM ordering for Gd at the same temperature also in $(Pb_{0.5}Tl_{0.5})Sr_2GdCu_2O_7$, $Pb_2Sr_2GdCu_3O_8$, and $TlSr_2GdCu_2O_8$ with the same shape of specific-heat anomaly.[54] In iso-structural $Mo_{0.3}Cu_{0.7}Sr_2GdCu_2O_7$, a similar specific heat anomaly at the similar temperature (2.27 K) was observed.[23] It seems that the substitutions involving in the cooper chain site and in BaO plane do not affect the Gd-Gd ordering.

The C-T data for $Mo_{0.5}Cu_{0.5}Sr_2YCu_2O_{7.5}$ has been used to subtract the electronic and lattice contributions from C-T for the $Mo_{0.5}Cu_{0.5}Sr_2RECu_2O_{7.5}$ compounds with RE = Gd, Ho and Er in order to characterize the Schottky and magnetic ordering anomalies. The magnetic specific heat (ΔC or C_{mag}) is calculated by subtracting the specific of the materials with RE = Gd, Ho and Er from the $Mo_{0.5}Cu_{0.5}Sr_2YCu_2O_{7.5}$ according to the following equation:

$$\Delta C \text{ (or } C_{mag}) = C (Mo_{0.5}Cu_{0.5}Sr_2RECu_2O_{7.5}) - C (Mo_{0.5}Cu_{0.5}Sr_2YCu_2O_{7.5}) \quad (2)$$

Figure 7.18 shows the temperature variation of $\Delta C/T$ (or C_{mag}/T) together with the change of entropy (S-T) curves for $Mo_{0.5}Cu_{0.5}Sr_2GdCu_2O_{7.5}$ material.

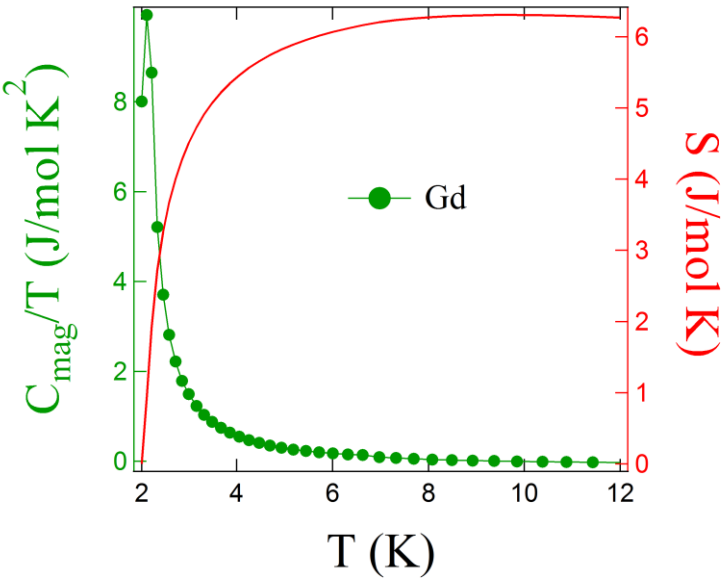

Figure 7.18. C_{mag}/T and the calculated entropy (S) as a function of temperature for the $Mo_{0.5}Cu_{0.5}Sr_2GdCu_2O_{7.5}$ material.

The $\Delta C/T$ (or C_{mag}/T) and the change of entropy of other two materials with RE = Ho and Er is shown in the upper and lower panel of figure 7.19, respectively.

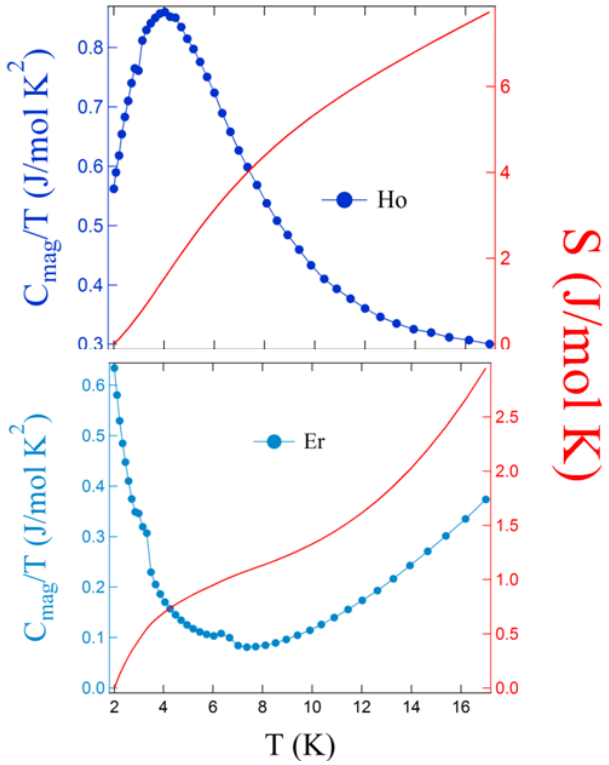

Figure 7.19. C_{mag}/T and the calculated entropy (S) as a function of temperature for the materials with RE = Ho and Er, respectively.

For RE = Gd and Ho a clear peak is observed at 2.13 K and at 5.4 K, respectively. The calculated entropy ($S = \int \Delta C/T$) is much smaller than R ln 8 (17.28 J/mol K) for the $Mo_{0.5}Cu_{0.5}Sr_2GdCu_2O_{7.5}$ material, the value expected for the full degeneracy of the s-type Gd ion. It might be due to incomplete correlation for Gd ions. However, the peak of the Ho compound at 5.4 K is extremely flat. The calculated entropy difference between 2 K and 17 K is less than R ln 3. One might be tempted to correlate the broad peak to the short-range ordering and the sharp peak to the long range ordering. In $HoBa_2Cu_3O_7$, a similar broad peak was observed at the same temperature.[55,56] And similarly, a singlet ground state and three low-lying singlet excited states is producing the broad C-T peak at T~5.4 K for the $Mo_{0.5}Cu_{0.5}Sr_2HoCu_2O_{7.5}$ material. An estimation of the entropy at 17 K yields ~ R ln 2 for the $Mo_{0.5}Cu_{0.5}Sr_2ErCu_2O_{7.5}$ material, i.e., the amount contributed by the ground doublet.

7.4. Conclusion

A new family of cuprates materials with $Mo_{0.5}Cu_{0.5}Sr_2RECu_2O_{7.5}$ (RE = Gd, Y, Ho and Er) has been prepared by HPHT method. However, all the attempts to synthesize a pure compounds with RE = Nd, Tb and Lu by varying temperature, pressure and/or reaction time were unsuccessful. These four new materials are non superconducting. Nevertheless, they show interesting features. Structural analysis using the joint refinement of RT NPD and RT XRD showed that the chain oxygens are randomly distributed in the two different oxygen sites, which are not completely filled and the defect induced by oxygen vacancies in fact makes the chain fragmented and disordered. This disordering seem to be a reason for the absence of superconductivity in these materials. A remarkable microdomain texture has been identified using electron microscopy. The microstructure of these compounds is interpreted by a well-known diagonal cell $\sqrt{2}a_p \times \sqrt{2}a_p \times 3a_p$, distributed in three dimensional domains, as confirmed by the SEAD and HRTEM, while an ideal triple perovskite structure with a "simple" $a_p \times a_p \times 3a_p$ cell is supported from the results found by the RT NPD/XRD joint refinements; which is a consequence of the absence of the long-range ordering in the octahedral tilt due to the random distribution of an equal amount of Mo and Cu in the cooper chain site. XPS studies on the sample with RE = Ho show the predominance of the non magnetic Mo^{VI} state over the Mo^{V} one. At the same time oxidation state of copper is found to be dominated by Cu^{II} and this is, indeed, related to the absence of SC. The presence of higher amount of nonmagnetic Mo^{VI} is found to be a reason for the absence of the magnetic interaction in these materials. Specific heat studies indicate the magnetic ordering at 2.13 K for $Mo_{0.5}Cu_{0.5}Sr_2GdCu_2O_{7.5}$ material is due to the 3-dimensional AFM ordering of the Gd ion.

The heat capacity of the $Mo_{0.5}Cu_{0.5}Sr_2HoCu_2O_{7.5}$ material shows a flat maximum at 5 K due to the separation of the two lowest-lying singlet levels of Ho^{III} ions at that temperature.

References

[1]Tokura Y., Takagi H. and Uchida S. *Nature* **1989**, *337*, 345. See also: Alario-Franco M. A. *Adv. Mater.* **1994**, *7*(2), 229.

[2] Joshi D. G., Subbrarao M. V., Shah A. N., Kuberkar D. G. and Kulkarni R.G. *Applied superconductivity* **1998** 6, 7-9, pp. 471-481.

[3] Bauernfeind L., Widder W. and Braun H. F. *Physica C* **1995,** 254, 151-158.

[4]J. Lynn W., Keimer B., Ulrich C., Bernhard C., and Tallon J. L. *Phys Rev. B.* **2000**, 61, R14964.

[5]Felner I., Asaf U., Reich S. and Tsabba Y. *Physica C* **1999**, 311**,** 163.

[6]Pringle J. D., Tallon J. L., Walker B. G. and Trodahl H. J. Phys Rev. B. **1999**, 59, R11679.

[7]Rukang L., Yingjie Z., Daoyuang Z., Chen X., Yitai Q., Zuyao C. and Guien Z. J. *Alloy Compd.* **1992**, 185**,** 45.

[8]Mclaughlin A. C., Morrice D. and Sher F. *J. Solid State Chem.* **2005**, 178, 2274.

[9]Adachi S., Kubo K –I., Takano S. and Yamauchi H. *Physica C* **1992**, 191, 174.

[10]Eder M. H. and Gritzner G. *Supercond. Sci. Technol*. **2005**, 18**,** 87.

[11]Dos santos-Garcia A. J., Aguirre M. H., Saez Puche R. and Alario-Franco M. A. *J. Solid State Chem.* **2006**, 179**,** 1296.

[12]Dos santos-Garcia A. J., Van Duijn J. and Alario-Franco M. A. *J. Solid State Chem.* **2008**, 181, 3317–3321.

[13]Takayama-Muromachi, E. *Chem. Mater.* **1998**, *10*, 2686.

[14]Ruiz-Bustos R., Gallardo-Amores J. M., Saez-Puche R.; Moran E. and Alario-Franco M. A. *Physica C* **2002**, *382*, 395-400.

[15]Ruiz-Bustos R., Aguirre M. H. and Alario-Franco, M. A. *Inorg. Chem.* **2005**, 44, 3063-3069.

[16]Alario-Franco, M. A., Ruiz-Bustos R. and Dos santos-Garcia A. J. *Inorg. Chem.* **2008**, 47, 6475-6481.

[17]Felner I. and Galstyan E. *Phys. Rev. B* **2004**, 69, 024512.

[18]Balchev N., Nenkov K., Mihova G., Kunev B., Pirov J. and Dimitrov D. A. *JMMM* **2009**, 321, 388–391.

[19]Marik S., Moran E., Labrugere C., Toulemonde O. and Alario-Franco M. A. *J. Solid State Chem.* **2012**, 191**,** 40-45.

[20]Marik S., Dos santos-Garcia A. J., Moran E., Labrugere C., Toulemonde O. and Alario-Franco M. A. (Submitted to Physical chemistry C).

[21]Marik S., Moran E., Dos santos-Garcia A. J., Toulemonde O. and Alario-Franco M. A. *JPCM.* **2013**, 25**,** 165704.

[22]Marik S., Moran E., Dos santos-Garcia A. J., Toulemonde O. and Alario-Franco M. A. *J Supercond Nov Magn* **2013**, 26, 1151–1154.

[23]Tsay H. L., Shih C. R., Chen Y. C., Lee W. H., Meen T. H. and Yang H. D. *Physica C* **1995**, 252, 79-86.

[24]Tsay H. L., Chen Y. C., Weng S. S., Chang C. F. and Yang H. D. *Phys. Rev. B* **1999-I**, 59, 636-640.

[25]Rodriguez-Carvajal J *An introduction to the programme FULL-PROF*, **2001**, Labratoire Leon Brillouin, CEA-CNRS: Saclay, France.

[26]William T. A., Harrison S. R., Vaughey J. T., Liu L. and Jacobson A. J. *J. Solid State Chem.* **1995**, 119, 115-119.

[27]Antipov E. V., Abukamov A. M. and Putilin S. N. *Supercond. Sci.Technol.* **2002**, 15, R31-R49.

[28] Putilin S. N., Antipov E. V., Chmaissem O. and Marezio M. *Nature (London)* **1993**, 362, 226.

[28] Putilin S. N., Antipov E. V., Chmaissem O. and Marezio M. *Nature (London)* **1993**, 362, 226.

[29] Balagurov A. M., Sheptyakov D. V., Aksenov V. L., Antipov E. V., Putilin, S. N., Radaelli P. G. and Marezio M. *Phys. Re*V. *B: Solid State* **1999**, 59(10) 7209.

[30] Shannon R. D. *Acta Crystallogr.* **1976**, A 32, 751.

[31] Poole C., Creswick R. C. and Farach H. *Handbook of Superconductivity*; *Elsevier:* Amsterdam, **1999**, p 136.

[32] Vegas, A., Vallet-Regi M., Gonzalez-Calbet J. and Alario-Franco, M. A . *Acta Cryst*allogr. **1986**, B42, 167.

[33]Alario- Franco M. A., Vallet-Regi, M. and Gonzalez-Calbet, J. *Cryst. Lattice Defects Amorphous Mater.* **1987**, 16, 387.

[34]Alario- Franco M. A., Joubert J. C. and Levi J. P. *Mater. Res. Bull*. **1982**, 21, 733.

[35]Alario-Franco M. A., Henche M. J. R., Vallet M., Calbet J. M., Grenier J. C., Wattiaux, A. and Hagenmuller P. *J. Solid State Chem*. **1983**, 46, 23-40.

[36]Aguirre M., Ruiz-Bustos R. and Alario-Franco M. A. *J. Mater. Chem*. **2003**, 13, 1156-1160.

[37]Garcia-Martin S., Alario-Franco M. A., Ehrenberg H. and Amador U. *J. Am. Chem. Soc.* **2004**. 224 3587.

[38]Hiena T. D., Mana N. K. and Gargb K.B. *JMMM.* **2003**, 262, 508-513

[39]Katrib A., Logie V., Peter M., Wehrer P., Hilaire L. and Maire G. *J. Chim. Phys. Phys.-Chim. Biol.* **1997**, 94, 1923.

[40]Jalili H., Heinig N. F. and Leung K. T. *Phys. Rev. B* **2009**, 79, 174427.

[41]Larsson S. *Chem. Phys. Lett*. **1976**, 40, 362.

[42]Van der Laan G., Westra C., Haas C. and Sawatzky G. A. *Phys. Rev. B* **1981**, 23, 4369.

[43]Parmigiani F. and Sangaletti L. *J. Electron Spectrosc. Relat. Phenom.***1994**, 66, 223.

[44]Vasquez R. P., Novikov D. L., Freeman A. J. and Siegal M. P. *Phys. Rev. B* **1997-I**, 55, 21.

[45]Parmigiani F., Depero L. E., Minerva T. and Torrance J. B. J. *Electron Spectrosc. Relat. Phenom.* **1992**, 58, 315.

[46]Parmigiani F. and Sangaletti L. *J. Electron Spectrosc. Relat. Phenom*. **1994**, 66, 223.

[47]Parmigiani F., Pacchioni G., Illas F. and P.S. Bagus *J. Electron Spectrosc. Relat. Phenom.* **1992**, 59, 255.

[48]Parmigiani F., Shen Z. X., Mitzi D. B., Lindau I., Spicer W.E. and Kapitulnik A. *Phys. Rev. B* **1991**, 43, 3085.

[49]Fink J., Niicker N., PeUegrin E., Romberg H., Alexander M. and Knupfer M. *J. Electron Spectrosc. Relat. Phenom.* **1994**, 66, 395.

[50]Martinho H., Martin A. A., Moreno N. O., Sanjurjo J. A., Rettori C., Oseroff S. B., Fisk Z., Pagliuso P. G. and Sarrao J. L. *Physica B* **2001**, 305, 48–55.

[51]Alp E. E., Solderholm L., Shenoy G. K., Hinks D. G., Capone II D. W., Zhang K. and Dunlap B. D. *Phys. Rev. B* **1987**, 36, 8910.

[52]Den T. and Kobayashi T. *Physica C* **1992**, 196, 141.

[53]Bachmann R., Disalvo F. J., Geballe T. H., Greene R. L., Howard R. E., King C. N., Kirsch H. C., Lee K. N., Schwall R. E., Thomasand H. U. and Zuback R. B. *Rev. Sci. Instrum*. **1972**, 43, 205.

[54]Lai C. C., Shieh J. H., Chiou B. S., Ho J. C. and Ku H. C. *Phys. Rev. B* **1994**, 49, 1499.

[55]Simizu S., Friedberg S. A., Hayri E. A. and Greenblatt M. *Phys. Rev. B* **1987**, 36, 7129-7132.

[56]Ferreira J. M., Lee B. W., Dalichaouch Y., Torikachvili M. S., Yang K. N. and Maple M. B. *Phys. Rev. B* **1988**, 37, 1580-1586.

Chapter 8

Summary and concluding remarks

In the present thesis, we have presented systematic studies on the composition-structure-property correlation for the (Mo,Cu) – 1212 (1212-molybdo-cuprate) materials. The crystal structure and electronic state studies provide us important information on this interesting cuprate family. Eventually, the interesting physical properties have been discussed on the frame of structural studies.

The study of the $Mo_xCu_{1-x}Sr_2YCu_2O_y$ ($0.3 \leq x \leq 1$) solid solution emphasizes the ability of this phase to incorporate foreign cations. It shows that contrary to the previous claims, the square-planar copper in the chains in the $CuSr_2YCu_2O_{7-\delta}$ (YSCO, Cu-1212, Y-123) structure is not completely replaced by [Mo-O_6] octahedra at ambient pressure. We have checked the solubility of Mo in YSCO. Secondary phases start to form when $x \geq 0.35$. Anti-ferromagnetism in all superconducting multiphase samples is due to the secondary phase $Y_2Cu_2O_5$. In fact, a material of composition "$MoSr_2YCu_2O_8$" does not exist at room pressure and, indeed, can not show any coexistence of antiferromagnetism and superconductivity.

All the pure $Mo_{0.3}Cu_{0.7}Sr_2RECu_2O_y$ compounds show a tetragonal structure with the space group P4/mmm. The crystal structure of all the materials is investigated by means of XRD, NPD and ED techniques. Crystal structure studies based on XRD refinement on the $Mo_{0.3}Cu_{0.7}Sr_2YCu_2O_y$ materials indicates an interesting site selection scenario of the dopant Mo cation. The chemical substitution of the Mo ions for the Cu ions in $CuYSr_2Cu_2O_{7-\delta}$ is found to occur in both Cu sites in the structure, but up to limited extent. We have determined that the majority of the Mo substitution in these samples occurs for copper in [Cu1] chain sites in the 123-type parent structure. However, Cu/Mo populations are established for the Cu1 and Cu2 sites from the joint refinement using the XRD/NPD data for the $Mo_{0.3}Cu_{0.7}Sr_2RECu_2O_y$ (RE = Er and Tm) materials. A joint NPD/XRD refinement yielded more structural detail than either of the two techniques alone. A reliable estimate of the total oxygen content and Cu/Mo distribution over each copper site was obtained. Site occupancy refinement for both the as-prepared samples indicates that the chemical substitution of the Mo ions for the Cu ions occur in both Cu sites (Cu1 and Cu2) but up to a limited extent. We have found that the majority of the Mo [0.25 (2), ~83% of the total Mo content and 0.23 (2), ~77% of the total Mo content for the samples with RE = Er and Tm, respectively] substitution in these samples occur for the copper in the chain sites (Cu1). Interestingly, no trace of Mo substitution at the Cu2 site is observed in the Joint XRD/ NPD refinement for both the oxygen annealed samples (occupancy becomes negative when Mo is allowed to share Cu2 site). A model for the Mo diffusion to the copper chain site during the oxidation process has been presented. And the splitting observed in the NPD patterns of the OA Tm

sample is due to the increased c/a ratio after oxygenation.

A combination of ac and dc magnetic measurements, resistivity and TEP measurements are used to study the $Mo_{0.3}Cu_{0.7}Sr_2RECu_2O_y$ (RE = Er and Tm) tetragonal materials. Magnetic measurements on the AP $Mo_{0.3}Cu_{0.7}Sr_2ErCu_2O_y$ sample indicate ferromagnetic interactions through the existence of FM domains in a nonmagnetic matrix. The magnetic state of the AP $Mo_{0.3}Cu_{0.7}Sr_2TmCu_2O_y$ material experiences PM – Weak AFM – SG transitions with a lowering of the temperature. However, instead of a classical individual spin freezing, we suggest a cluster by cluster freezing model to explain the SG nature in this material. The complex magnetic behaviour in these AP materials seems to be the direct consequence of the cation disorder. On the other hand, all the oxygenated materials are superconducting. The material oxygenated using high pressure shows the highest T_C (84 K). Structural analyses reveal the tendency of short-range oxygen ordering after oxygenation. A short-range oxygen ordering model at the mesoscopic scale, in the chain copper site is proposed and discussed. This increases the effectiveness in the charge transfer to the superconducting layer (CuO_2), resulting in superconductivity. Following our experimental results, we found that contrary to the two orbital model and common wisdom, the apical Cu2-O2 distance decreases with increasing T_C, in association with an oxidation reaction. The "peak effect" in the current density (J_C) plots has been observed due to "field induced pins" (FIPs).

The influence of oxygenation in the electronic states for the $Mo_{0.3}Cu_{0.7}Sr_2YCu_2O_y$ and $Mo_{0.3}Cu_{0.7}Sr_2ErCu_2O_y$ systems associated to an oxidation reaction from a semiconducting to a superconducting state has also been investigated by means of X-ray photoelectron spectroscopy. The XPS studies show the predominance of the Mo^V state over the Mo^{VI} one in the AP samples. Yet, annealing under an oxygen atmosphere enhances the Mo^{VI} state. Quite interestingly, at the same time, a reduction in the copper species is observed. A novel self doping equilibrium is proposed here for the 1212-molybdo-cuprate compounds, after oxygenation. Equally, a detailed study on the electronic states is presented. The hole concentration on the copper plane is calculated using the room temperature TEP value; this shows an increasing tendency with increasing T_C, after oxygenation. Following our experimental results, we have found that charge transfer energy is the key factor to tune the superconducting transition temperature (T_C). We have observed that T_C increases with decreasing charge transfer energy. This is occurring in parallel with the shortening of the apical O distance (Cu2–O2) and increasing CuO_2 plane buckling, while the two orbital model

predicts the opposite effect. The enhancement of the CuO_2 plane buckling and the shortening of the apical O distance (Cu2–O2) in parallel with increasing T_C for the present molybdo-cuprate materials could be a response to the electronic structure of this family.

Eventually, in an attempt to extend the knowledge on this interesting molybdo-cuprate family having octahedra in the charge reservoir layer (copper chain, Cu1), a new family of 1212-molybdo-cuprate materials with composition $Mo_{0.5}Cu_{0.5}Sr_2RECu_2O_{7.5}$ (RE = Gd, Y, Ho and Er) has been prepared by the HPHT method. These four new materials are non superconducting. Nevertheless, they show interesting features. Structural analyses using the joint refinement of RT NPD and RT XRD showed that the chain oxygen ions are randomly distributed in the two different oxygen sites, which are not completely filled and the defect induced by oxygen vacancies in fact makes the chain fragmented and disordered. This disordering could be a reason for the absence of superconductivity in these materials. A remarkable microdomain texture has been identified using the electron microscopy. The microstructure of these compounds is interpreted by a well-known diagonal cell $\sqrt{2}a_p \times \sqrt{2}a_p \times 3a_p$, distributed in three dimensional domains, as confirmed by the SEAD and HRTEM, while an ideal triple perovskite structure with a "simple" $a_p \times a_p \times 3a_p$ cell is supported from the results found by the RT NPD/XRD joint refinements; this is a consequence of the absence of the long-range ordering in the octahedral tilt due to the random distribution of an equal amount of Mo and Cu in the cooper chain site. XPS studies on the sample with RE = Ho show the predominance of the non magnetic Mo^{VI} state over the Mo^{V} one. At the same time oxidation state of copper is found to be dominated by Cu^{II}. The presence of a higher amount of nonmagnetic Mo^{VI} is found to be a reason for the absence of the magnetic interactions in these materials. Specific heat studies indicate the magnetic ordering at 2.13 K for $Mo_{0.5}Cu_{0.5}Sr_2GdCu_2O_{7.5}$ material is due to the 3-dimensional AFM ordering of the Gd ion. The heat capacity of the $Mo_{0.5}Cu_{0.5}Sr_2HoCu_2O_{7.5}$ material shows a flat maximum at 5 K due to the separation of the two lowest-lying singlet levels of Ho^{III} ions at that temperature.